

Cardiff University

School of Engineering

Influence of Solidity on the Performance, Swirl
Characteristics, Wake Recovery and Blade
Deflection of a Horizontal Axis Tidal Turbine

A Thesis submitted to Cardiff University,
for the Degree of Doctor of Philosophy

By

Ceri Morris

Abstract

The main focus of this thesis was to investigate the influence of solidity on the performance, swirl characteristics, wake length and blade deflection of a Horizontal Axis Tidal Turbine (HATT) using the simulation software package Ansys. An existing laboratory scale prototype HATT was modified to improve upon previously gathered experimental data and provide further confidence of the validity of the numerical models. The solidity was varied by altering the number of blades in the numerical models.

The work presented in this thesis shows that, for this blade profile, increasing the solidity increases the peak C_θ and peak C_p and reduces the λ at which these occur. C_t was found to be approximately the same at peak C_p , which was assumed to be the normal operating condition. At λ above peak C_p , near freewheeling, C_t continued to increase for the 2 bladed turbine, remained approximately constant for the 3 bladed turbine and decreased for the 4 bladed turbine, due to the change in pitch angle required to maintain optimum power. This indicates that higher solidity rotors would have to withstand lower loads in the event of a failure. In addition, the thrust per blade was shown to increase with reducing number of blades.

The swirl characteristics in the wake were found to agree with swirl theory and the swirl was found to increase with solidity whilst being weak or very weak in each case. Swirl number was found to be dependent on solidity only up to distances of 10 diameters downstream.

At higher turbulent intensities, the wake recovery was only influenced by solidity up to 15 diameters downstream of the HATT but at low turbulence intensities the wake length increased with solidity indicating that low solidity rotors may offer higher overall array efficiencies in areas of low turbulent intensity.

Blade deflection was shown to increase with a reduction in the number of blades, due to the increased thrust per blade. The power output of the 3 bladed turbine was shown to decrease by 0.4% with a deflection of 0.12 m. However, the power output of the 2 and 4 bladed turbines was found to increase with deflections as it was subsequently found that the pitch settings found in a previous study were not fully optimised for a rigid blade. At deflections above 0.20 m the power output of the 4 bladed turbine was found to decrease. It is expected that the power output of the 2 bladed turbine would eventually decrease with further deflections but no decrease was found for the maximum deflection considered, of 0.35m.

This thesis therefore shows that the optimum number of blades may vary from site to site and even from one location within an array to another. It also shows that blade deflection will alter the power output and that blades could be designed so as to reach their optimum setting at a given blade deflection.

Table of Contents

Table of Contents	i
List of Figures	vi
List of Tables	xi
Nomenclature	xii
1 Introduction	1
1.1 Current Status of Renewables	1
1.2 Tidal Energy	3
1.2.1 Tidal Stream Resource	3
1.2.2 Current Status of the Sector and Research Drivers	5
1.3 Thesis aims and objectives	6
1.4 Thesis Layout	6
2 Literature Review	8
2.1 Types of device	8
2.1.1 Horizontal Axis Tidal Turbines.....	8
2.1.2 Vertical Axis Tidal Turbines (VATTs).....	10
2.1.3 Oscillating hydrofoil	12
2.1.4 Venturi Effect devices	12
2.1.5 Other types of device	13
2.1.6 Rotor design used in this work.....	14
2.2 Environmental Impacts	14
2.3 Securing, Installation and Maintenance.....	16
2.4 Design Considerations of a HATT	17
2.4.1 Solidity.....	17
2.4.2 Interaction with Stanchion.....	20
2.4.3 Wake Length	21
2.4.4 Blade Loading	22

2.5	Modelling.....	23
2.5.1	Physical Modelling	23
2.5.2	Numerical Modelling.....	23
2.6	Summary of Literature Review	28
3	Theory.....	29
3.1	Performance Characteristics	29
3.2	Solidity	30
3.3	Swirl	31
3.4	CFD.....	34
3.4.1	RANS.....	35
3.4.2	Turbulence Models	36
3.4.3	Wall Functions.....	40
3.4.4	Simulating Rotation.....	42
3.5	FEA.....	43
4	Numerical Methodology	45
4.1	CFD Geometry Creation.....	45
4.1.1	Turbine Geometry	45
4.1.2	Cylindrical Subdomain (MRF).....	47
4.1.3	Main domain	48
4.2	Mesh for CFD models	49
4.2.1	Global mesh settings.....	49
4.2.2	Turbine Domain.....	50
4.2.3	Surrounding Domain	52
4.2.4	Named Selections.....	52
4.3	CFD Solver Settings.....	53
4.3.1	Viscous Models	54
4.3.2	Inlet	55
4.3.3	Outlet	55
4.3.4	Wall conditions.....	55
4.3.5	Material Properties of fluid.....	55

4.3.6	Rotation of Turbine Using MRF	56
4.3.7	Convergence Monitoring	56
4.4	Post processing.....	56
4.4.1	Extracting Torque	56
4.4.2	Calculating turbine power	56
4.4.3	Extracting Axial Loads	56
4.4.4	Calculation of Swirl Number	57
4.5	FSI models.....	57
4.5.1	Modifications to CFD models	57
4.5.2	FEA models	59
4.5.3	System Coupling.....	61
5	Flume Testing and Model Validation	65
5.1	Flume Specifications.....	65
5.2	Improvements made to turbine design	66
5.3	Blade Design	67
5.4	Pitch Angle Setting	68
5.5	Location of HATT within Flume	69
5.6	Flume Velocity	69
5.7	Thrust Load measurement	70
5.8	Test Procedure	70
5.9	Reduction in Scatter	72
5.10	Power Measurements	73
5.11	Thrust Measurements	75
5.12	Summary of Flume Testing and Model Validation	75
6	Performance Characteristics.....	77
6.1	Torque	77
6.2	Power.....	82
6.3	Thrust.....	87
6.4	Summary of Performance Characteristics.....	93
6.5	Effect of Different Turbulence Decay	94

7	Swirl Characteristics	100
7.1	Swirl Number	100
7.2	Swirl Decay	110
7.3	Tangential velocity decay, W_m/W_{m0}	122
7.4	Type of Vortex	124
7.5	Dynamic Pressure	127
7.6	Summary of Swirl Characteristics in Wake.....	131
8	Wake Recovery	133
8.1	Centre Line Velocity.....	133
8.2	Swept Area Average Velocity	138
8.3	Comparison of centre line and swept area average velocity.....	143
8.4	Summary of Wake Study	145
9	Blade Deflection	147
9.1	Torque	147
9.2	Thrust.....	150
9.3	Blade Deflection	152
9.4	Change in Power with Deflection	154
9.5	Change in Pitch Angle.....	158
9.6	Change in Twist	160
9.7	Summary of Blade Deflection.....	162
10	Conclusions and recommendations	164
10.1	Conclusions.....	164
10.2	Specific Observations	165
10.2.1	Validation Data.....	165
10.2.2	Performance Characteristics.....	165
10.2.3	Swirl.....	166
10.2.4	Wake	167

10.2.5 Blade Deflection	167
10.3 Recommendations and future work	168
References	170
Appendix A Performance Characteristics with SST model.....	182
Appendix B Swirl Characteristics with SST model.....	184
Appendix C Dynamic Pressure Profiles with SST model	186

List of Figures

Figure 1.1 Progress in renewable electricity, heat and transport (Source: UK Renewable Energy Roadmap Update, 2013)	2
Figure 1.2 Renewable electricity share of total generation (Source: Renewable Energy Roadmap Update, 2013)	3
Figure 1.3 UK Tidal Stream Resource (BERR, 2008)	4
Figure 2.1 Marine Current Turbines' SeaGen Device (Taylor, 2007)	9
Figure 2.2 HATT devices under development	10
Figure 2.3 Examples of VATTs	11
Figure 2.4 Examples of Oscillating Hydrofoils	12
Figure 2.5 Venturi Effect Devices	13
Figure 2.6 Other types of tidal stream device	13
Figure 2.7 Power coefficient curves for wind turbines with increasing numbers of blades (Hau, 2006)	18
Figure 2.8 Marine Current Turbines' SeaFlow Device (Murdoch University, 2008) ..	19
Figure 3.1 Turbine configurations	30
Figure 3.2 Qualitative representation of a Rankine vortex (Gupta et al., 1984)	33
Figure 3.3 Layers of the near wall boundary layer (Adapted from ANSYS, 2010)	40
Figure 4.1 Three Bladed Turbine Geometry	45
Figure 4.2 Two Bladed Turbine Geometry	46
Figure 4.3 Four Bladed Turbine Geometry	47
Figure 4.4 Turbine with surrounding cylindrical sub-domain	48
Figure 4.5 Turbine geometry surrounded by cylindrical sub-domain and main domain	49
Figure 4.6 Mesh on surface of blade	51
Figure 4.7 Mesh on outer surface of MRF	51
Figure 4.8 Mesh on inner surface of main domain	52
Figure 4.9 Named Selections for Turbine Blades	53
Figure 4.10 Blade surface mesh in FEA models	59
Figure 4.11 Constraints and Loads	61
Figure 4.12 General Grid Interface Mapping (ANSYS, 2011b)	63

Figure 4.13 Example of poor mapping where unmapped cells are shown in red.	64
Figure 4.14 Mapping achieved in FSI models where unmapped cells are shown in red.	64
Figure 5.1 Schematic of Recirculating Flume at the University of Liverpool	65
Figure 5.2 Previous turbine design	66
Figure 5.3 Couplings used to connect the previous turbine to the motor	66
Figure 5.4 Improved turbine design during testing	67
Figure 5.5 FX 63-137 profile and profile of HATT used in this work	68
Figure 5.6 Precision machined blocks with blade tip chord aligned with 6° block....	68
Figure 5.7 measured free-stream water-channel velocity (U_{ADV}) versus the nominal free-stream water-channel velocity (U_f) as per the dial setting	70
Figure 5.8 Current vs time from experimental testing	71
Figure 5.9 Angular velocity v time from experimental testing	71
Figure 5.10 Comparison of experimental data with that from the previous turbine design	73
Figure 5.11 C_p vs λ from experimental data	74
Figure 5.12 C_p vs λ from blockage corrected experimental data and from CFD models.....	75
Figure 5.13 C_t vs λ from blockage corrected experimental data and from CFD models.....	76
Figure 6.1 C_θ vs λ for the 2 bladed turbine	78
Figure 6.2 C_θ vs λ for the 3 bladed turbine	79
Figure 6.3 C_θ vs λ for the 4 bladed turbine	79
Figure 6.4 C_θ vs λ for the 2,3 and 4 bladed turbines	81
Figure 6.5 Normalised C_θ vs normalised λ for the 2, 3 and 4 bladed turbines	82
Figure 6.6 C_p vs λ for the 2 bladed turbine	83
Figure 6.7 C_p vs λ for the 3 bladed turbine	84
Figure 6.8 C_p vs λ for the 4 bladed turbine	84
Figure 6.9 C_p vs λ for the 2, 3 and 4 bladed turbines	86
Figure 6.10 Normalised C_p vs normalised λ for the 2, 3 and 4 bladed turbines	87
Figure 6.11 C_t vs λ for the 2 bladed turbine	88

Figure 6.12 C_t vs λ for the 3 bladed turbine	89
Figure 6.13 C_t vs λ for the 4 bladed turbine	90
Figure 6.14 C_t vs λ for the 2, 3 and 4 bladed turbines	91
Figure 6.15 Normalised C_t vs normalised λ for the 2, 3 and 4 bladed turbines.....	92
Figure 6.16 Thrust per blade vs λ for the 2, 3 and 4 bladed turbines.....	93
Figure 6.17 Contours of Turbulent Intensity with the RSM model.....	95
Figure 6.18 Contours of Turbulent Intensity with the SST model	95
Figure 6.19 C_θ vs Number of Blades at peak C_p (normal operating condition).....	96
Figure 6.20 C_p vs Number of Blades at peak C_p (normal operating condition).....	97
Figure 6.21 C_t vs Number of Blades at peak C_p (normal operating condition)	98
Figure 7.1a Variation of swirl number with downstream distance for the 2 bladed turbine.....	101
Figure 7.1b Recirculation zones behind turbine blades at $\lambda=0.49$	101
Figure 7.2 Swirl Number vs λ at $x/D=0.1$ with RSM and SST for the 2 bladed turbine	102
Figure 7.3 Variation of swirl number with downstream distance for the 3 bladed turbine.....	104
Figure 7.4 Variation of swirl number with downstream distance for the 4 bladed turbine.....	104
Figure 7.5 Swirl Number vs λ at $x/D=0.1$ with RSM and SST for the 3 bladed turbine	105
Figure 7.6 Swirl Number vs λ at $x/D=0.1$ with RSM and SST for the 4 bladed turbine	106
Figure 7.7 Swirl Number vs λ at $x/D=0.1$ for the 2, 3 and 4 bladed turbines	107
Figure 7.8 λ at which peak swirl occurs for each downstream location for the 2, 3 and 4 bladed turbines	108
Figure 7.9 Peak swirl number vs number of blades for each model	109
Figure 7.10 Swirl at peak power vs number of blades for each model	110
Figure 7.11 Swirl decay at peak swirl and peak power for the 2 bladed turbine	111
Figure 7.12 Swirl decay at peak swirl and peak power for the 3 bladed turbine	112
Figure 7.13 Swirl decay at peak swirl and peak power for the 4 bladed turbine	113

Figure 7.14 Difference between peak swirl and swirl at peak power vs number of blades at $x/D=0.1$	113
Figure 7.15 Swirl decay at peak swirl for the 2 bladed turbine with each model ...	114
Figure 7.16 Swirl decay at peak swirl for the 3 bladed turbine with each model ...	116
Figure 7.17 Swirl decay at peak swirl for the 4 bladed turbine with each model ...	116
Figure 7.18 Swirl decay at peak swirl for the 2, 3 and 4 bladed turbines.....	117
Figure 7.19 Swirl decay at peak power for the 2 bladed turbine with each model	118
Figure 7.20 Turbulent Intensity downstream of the 2 bladed turbine at peak swirl (top) and peak power (bottom)	118
Figure 7.21 Swirl decay at peak power for the 3 bladed turbine with each model	120
Figure 7.22 Swirl decay at peak power for the 4 bladed turbine with each model	121
Figure 7.23 Swirl decay at peak power for the 2, 3 and 4 bladed turbines.....	122
Figure 7.24 Decay of maximum tangential velocity along axis of swirling jets (Chigier & Chervinsky, 1967) & in the wake of 2, 3 and 4 bladed turbines at peak swirl & peak power.....	123
Figure 7.25 Decay of maximum tangential velocity along axis of swirling jets (Chigier & Chervinsky, 1967) and in the wake of the 3 bladed turbine at peak swirl and peak power with the RSM and SST models	124
Figure 7.26 Tangential velocity profile at $x/D=1$ downstream of the 2 bladed turbine on x and y axes	125
Figure 7.27 Tangential Velocity Contours at $x/D=1$ downstream of the 2 bladed turbine.....	125
Figure 7.28 Tangential velocity profile at $x/D=1$ downstream of the 3 bladed turbine on x and y axes	126
Figure 7.29 Tangential velocity profile at $x/D=1$ downstream of the 4 bladed turbine on x and y axes	127
Figure 7.30 Dynamic pressure profiles downstream of the 2 bladed turbine.....	128
Figure 7.31 Dynamic pressure profiles downstream of the 3 bladed turbine.....	129
Figure 7.32 Dynamic pressure profiles downstream of the 4 bladed turbine.....	130
Figure 7.33 Dynamic pressure profiles downstream of the 3 bladed turbine with the RSM and SST models	131

Figure 8.1 Normalised centre line axial velocity downstream of the 2 bladed turbine	134
Figure 8.2 Normalised centre line axial velocity downstream of the 3 bladed turbine	136
Figure 8.3 Normalised centre line axial velocity downstream of the 4 bladed turbine	136
Figure 8.4 Normalised centre line axial velocity downstream of the 2, 3 and 4 bladed turbines	138
Figure 8.5 Normalised swept area average axial velocity downstream of the 2 bladed turbine	140
Figure 8.6 Normalised swept area average axial velocity downstream of the 3 bladed turbine	141
Figure 8.7 Normalised swept area average axial velocity downstream of the 4 bladed turbine	142
Figure 8.8 Normalised swept area average axial velocity downstream of the 2, 3 and 4 bladed turbines	143
Figure 8.9 Normalised centre line and swept area average axial velocity downstream of the 2, 3 and 4 bladed turbines	144
Figure 9.1 Torque vs E for the 2 bladed turbine	148
Figure 9.2 Torque vs E for the 3 bladed turbine	149
Figure 9.3 Torque vs E for the 4 bladed turbine	149
Figure 9.4 Thrust vs E for the 2 bladed turbine	150
Figure 9.5 Thrust vs E for the 3 bladed turbine	151
Figure 9.6 Thrust vs E for the 4 bladed turbine	151
Figure 9.7 Deflection vs E for the 2 bladed turbine	152
Figure 9.8 Deflection vs E for the 3 bladed turbine	153
Figure 9.9 Deflection vs E for the 4 bladed turbine	153
Figure 9.10 Deflection vs E for the 2, 3 and 4 bladed turbines	154
Figure 9.11 Power vs deflection for the 2 bladed turbine	155
Figure 9.12 Power vs deflection for the 3 bladed turbine	156
Figure 9.13 Power vs deflection for the 4 bladed turbine	156

Figure 9.14 Normalised power vs deflection for the 2, 3 and 4 bladed turbines	158
Figure 9.15 Normalised power vs change in pitch angle for the 2, 3 and 4 bladed turbines	159
Figure 9.16 Normalised power vs change in pitch angle for the 2, 3 and 4 bladed turbines	160
Figure 9.18 Twist required to maintain a constant angle of attack at λ for peak power found in this study	162

List of Tables

Table 1.1 UK Renewable Energy Targets for 2020	1
Table 3.1 Turbine solidity values.....	30
Table 3.2: General characteristics of vortices.....	33

Nomenclature

A = rotor swept area, m^2

A_1 = area of control surface 1 for GGI mapping, m^2

A_2 = area of control surface 2 for GGI mapping, m^2

A_3 = area of control surface 3 for GGI mapping, m^2

B = number of blades

$[B]$ = strain-displacement matrix, $1/m$

C = average chord length, m

C_p = power coefficient

C_t = thrust coefficient

C_θ = torque coefficient

C_μ = empirically derived constant

$[D]$ = elasticity or stiffness matrix, N/m^2

E = Young's modulus, N/m^2

E_c = empirical constant

G = shear modulus, N/m^2

G_θ = axial flux of angular momentum, Nm

G_x = axial flux of linear momentum, N

G_k = production of kinetic energy, m^2/s^2

F = axial load, N

\vec{F} = external body force, N

F_1 = blending function

$\{F_e^{nd}\}$ = nodal forces, N

$\{F_e^{pr}\}$ = element pressure force vector, N

k = turbulent kinetic energy, m^2/s^2

$[K_e]$ = element stiffness matrix, N/m

$[K_e^f]$ = element foundation stiffness matrix, N/m

k_p = turbulent kinetic energy at point p, m^2/s^2

$[M_e]$ = element mass matrix, kg

P = power, W

p = hydrostatic pressure, Pa

r = radius, m

\vec{r} = position vector from the origin of the rotating frame, m

R1 = Sub-face on surface receiving data

R2 = Sub-face on surface receiving data

S = swirl number

S1 = Sub-face on surface sending data

S2 = Sub-face on surface sending data

T = torque, Nm

U_p = mean velocity of the fluid at a point P, m/s

u = free stream velocity, m/s

\bar{u} = time averaged component of velocity, m/s

u' = fluctuating component of velocity, m/s

\vec{u}_r = relative velocity, m/s

U_t = velocity in flume, m/s

u_τ = friction velocity, m/s

U^* = dimensionless velocity

$\{u\}$ = nodal displacement vector, m

$\{\ddot{u}\}$ = acceleration vector, m/s²

w = tangential velocity, m/s

w_1 = mapping weight 1

w_2 = mapping weight 2

x = downstream distance, m

y_p = distance from wall to point P, m

y^+ = near wall flow resolution factor

y^* = near wall flow resolution factor

Greek Symbols

λ = tip speed ratio

κ = von Karman constant (0.4187)

μ = dynamic viscosity of the fluid

δ_{ij} = Kronecker delta

ε = dissipation rate of turbulent kinetic energy, m²/s³

ε_p = dissipation rate of turbulent kinetic energy at point p, m²/s²

ε_x = normal strain in the x direction

ε_y = normal strain in the x direction

ε_z = normal strain in the x direction

ε_{xy} = shear strain in the x-y plane

ε_{xz} = shear strain in the x-z plane

ε_{yz} = shear strain in the y-z plane

$\{\varepsilon^{el}\}$ = strains that cause stresses

ω = specific dissipation rate

$\vec{\omega}$ = rotational velocity, rad/s

σ = solidity

σ_k = Prandtl number

σ_x = normal stress in the x direction, N/m²

σ_y = normal stress in the x direction, N/m²

σ_z = normal stress in the x direction, N/m²

σ_{xy} = shear stress in the x-y plane, N/m²

σ_{xz} = shear stress in the x-z plane, N/m²

σ_{yz} = shear stress in the y-z plane, N/m²

$\sigma_{\omega,2}$ = empirical constant

$\{\sigma\}$ = stress vector, N/m²

ρ = density, kg/m³

Ω = vorticity, 1/s

ν = kinematic viscosity, m²/s

$\bar{\tau}$ is the stress tensor

$\vec{\omega}$ is the specified rotational velocity

τ_w = wall shear stress,

Acronyms

ADV- Acoustic Doppler Velocimeter

BEMT- Bladed Element Momentum Theory

CFD- Computational Fluid Dynamics

DECC- Department of Energy and Climate Change

DES- Detached Eddy Simulation

DHRL- Dynamic Hybrid RANS/LES

EMEC- European Marine Energy Centre

FEA- Finite Element Analysis

FRP- Fibre Reinforced Plastic

FSI- Fluid Structure Interaction

GGI- General Grid Interface

HATT- Horizontal Axis Tidal Turbine

HAWT- Horizontal Axis Wind Turbine

LES- Large Eddy Simulation

MCT- Marine Current Turbines

MRF- Moving Reference Frame

PV- photovoltaic

RANS- Reynolds Average Navier Stokes

RSM- Reynolds Stress Model

SST- Shear Stress Transport

TI- Turbulent Intensity

VATT- Vertical Axis Tidal Turbine

VAWT- Vertical Axis Wind Turbine

1 Introduction

1.1 Current Status of Renewables

It is widely understood and accepted that in order to ensure security of supply, the energy mix must diversify to include a wider variety of resources (DECC, 2013). There is also a drive to reduce the emissions that contribute to global warming in an attempt to mitigate the effects of climate change. The current targets for the EU are set at a 20% reduction from the 1990 baseline level by 2020, with 20% of total energy consumption derived from renewable sources (European Union Committee, 2008). Each member state has an individual renewable energy target based on the proportion of energy provided by renewables when the targets were set and the potential for increasing this proportion. The UK's renewable energy target is 15% of the total annual energy consumption (DECC, 2011). In addition to this 2020 target, the UK has also set a longer term target to achieve an 80% reduction in greenhouse gas emissions from the 1990 baseline level by 2050 (National Archives, 2008). Continued research and investment into emerging technologies and sectors which may not have a significant impact on the 2020 target is therefore vital if the UK is to meet its longer term objective.

The amount of energy from renewables required to meet these targets depends on the total energy consumption. The Department of Energy and Climate Change (DECC) projected a renewable energy supply in 2020 of 234 TWh in their UK Renewable Energy Roadmap (DECC, 2011), but this has since been revised downwards in their Annual updates (DECC 2012, 2013) to give the estimations shown in Table 1.1.

Table 1.1. UK Renewable Energy Targets for 2020 (DECC, 2013)

Year	Renewable Energy Target/ TWh
2011	234
2012	223-230
2013	216-225

The progress towards the 2020 target is given in Figure 1.1. Clearly the largest contribution towards the target has so far been from the electricity sector and this sector has also shown the most growth since 2008 (DECC, 2013).

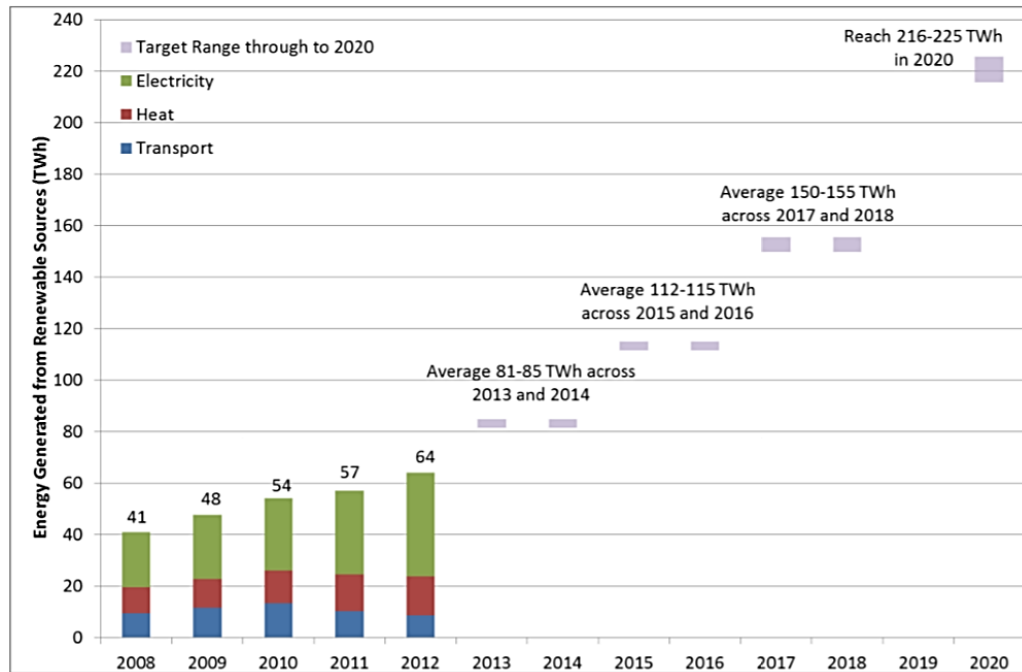


Figure 1.1 Progress in renewable electricity, heat and transport (Source: UK Renewable Energy Roadmap Update, 2013)

A breakdown of the renewable sources that have been exploited to produce this electricity is given in Figure 1.2 for each quarter from the start of 2010 to the second quarter of 2013, (DECC, 2013). The most recent data show that the largest contribution is from bioenergy, followed by onshore wind and offshore wind, with relatively small contributions from solar PV, wave and tidal and hydro power. None of the renewable sources are completely carbon free due to the infrastructure required to exploit them. However, there is particular debate regarding energy from biomass and whether it truly contributes to significant emissions reductions (Cho, 2011; Environment Agency, 2009), but this is outside the scope of this work and will not be discussed further. Other renewables such as wind and solar photovoltaic (PV), whilst providing a valuable contribution to the energy mix, are unpredictable in the medium to long term and therefore cannot replace conventional fossil fuelled power plants. The energy in the tides can be accurately

predicted weeks, months and even years in advance. This predictability is the main advantage of tidal energy. Another advantage is the limited visual impact when compared with, for example, wind turbines.

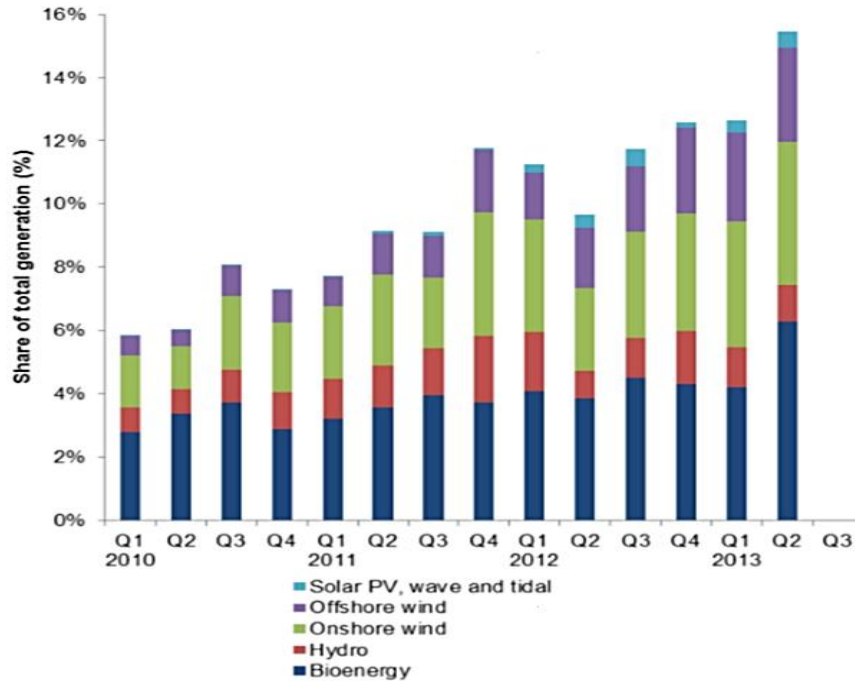


Figure 1.2 Renewable electricity share of total generation (Source: Renewable Energy Roadmap Update, 2013)

1.2 Tidal Energy

Tidal energy technologies generally fall into two categories; tidal range and tidal stream. Tidal range schemes extract energy by using a barrage or impoundment to create a head difference and then releasing water through turbines to generate electricity whereas tidal stream devices extract energy directly from the currents. Since this thesis is based on tidal stream devices, tidal range schemes will not be covered. The technologies used to exploit the tidal stream resource discussed here are described in Chapter 2.

1.2.1 Tidal Stream Resource

The UK is ideally situated to exploit tidal stream energy, with 10-15% of the global resource and around 50% of the European resource located in its national waters (Black and Veatch, 2005). A study by Black and Veatch (2005) found that within the

UK, 58% of the national resource is found off the coast of Scotland, in the Pentland region, 15% around Alderney, 4% around Rathlin Island and 3.7% around the Mull of Galloway, as shown in Figure 1.3. However, they have since revised these estimates to give approximately the same proportion of the resource in England, Scotland and Wales (Black and Veatch, 2011). Variability in topography, ratio of flow velocity in flood to ebb tide, depth requirement due to shipping and velocity profile are all site specific and optimum device spacing guidelines have not yet been established, hence it is difficult to estimate the total potential extractable energy. Quoted figures for the total exploitable resource in the UK range from 18 TWh/yr (Black and Veatch, 2005) to 29 TWh/yr (Black and Veatch, 2011), with ABP mer (2007) estimating figure of 27 TWh/yr for the top 10 sites combined. Salter (2005) and Mackay (2007), however, argue that these estimates should be far higher by considering the flow as a tidal wave and including the potential as well as the kinetic energy.

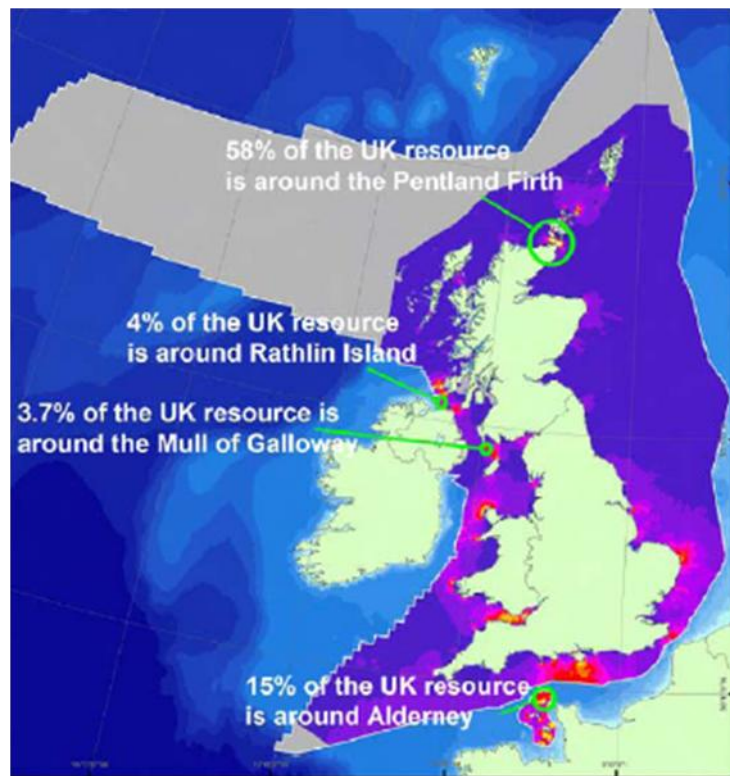


Figure 1.3 UK Tidal Stream Resource (BERR, 2008)

1.2.2 Current Status of the Sector and Research Drivers

Currently there is only one prototype with a rated power of over 1MW situated within UK waters, which is the Seagen device installed in 2008 in Strangford Lough, Northern Ireland by Marine Current Turbines (MCT). Many other devices have been tested in the European Marine Energy Centre (EMEC) in the Pentland Firth, as well as in other parts of the UK (Renewable UK, 2011) and some of these are described in Chapter 2. To reach the required contribution toward the renewable energy targets, arrays of multiple devices must be installed. This stage has not yet been reached but MCT plan to begin installation of a 9 device array, in the Anglesey Skerries in the summer of 2014.

The performance of a tidal stream device is crucial in determining its financial viability and length of payback and will be affected by factors including blade or hydrofoil design and solidity. Any changes in performance with blade deflection under loading will also affect the overall efficiency of a device and its energy extraction over a tidal cycle, again influencing the economics of an installation. In addition to the performance of each individual device, the amount of energy that can be extracted from an array of devices will determine whether tidal stream energy can contribute sufficient electricity to the grid to play a significant role in meeting the UK's long term renewable energy and emissions reduction targets. This will depend upon the spacing of the devices, which will in turn depend on the velocity recovery in the wake of each device. Since the power is proportional to the cube of the velocity, a relatively small reduction in incoming flow velocity will result in a large reduction in power output so the devices must be located where the velocity has recovered sufficiently.

The performance of a device, the change in performance under loading and the wake recovery may all be related to the solidity, which is a function of the chord length of the blade and the number of blades, as will be discussed in Chapter 3. The wake recovery may also depend on the swirl characteristics of the wake which again may be a function of solidity. As such, this work investigates the effect of solidity on the performance, swirl characteristics, wake length and blade deflection of a tidal stream turbine.

1.3 Thesis aims and objectives

The aim of this work was to investigate the effect of solidity of the performance, swirl characteristics, wake length and blade deflection of a horizontal axis tidal stream turbine. This was met by the following objectives:

- To modify the existing laboratory scale prototype Horizontal Axis Tidal Turbine (HATT) to reduce data scatter and improve model validation using a controlled environment.
- To compare the performance characteristics of the 2, 3 and 4 bladed turbines using Computational Fluid Dynamics (CFD) modelling.
- To investigate the swirl characteristics in the wake of each turbine.
- To compare the velocity recovery in the wake of each turbine based on the centre line velocity and the velocity over the swept area of a downstream turbine.
- To develop a fully 2 way coupled Fluid Structure Interaction (FSI) model of each turbine and use these models to assess blade deflection and change in performance characteristics for 2, 3 and 4 bladed turbines.

1.4 Thesis Layout

- Chapter 1 introduces the drivers for research into tidal energy and the current status of the sector along with the aims and objectives of this work.
- Chapter 2 reviews the relevant literature, outlining the devices under development and some of the key design considerations.
- Chapter 3 presents the applicable theory used to model the turbine and assess its performance and swirl characteristics.
- Chapter 4 describes the numerical methodology used to apply the theory presented in Chapter 3.
- Chapter 5 explains the experimental methodology and validation of the numerical models.
- Chapter 6 presents and discusses the performance characteristics of each of the turbine configurations considered.

- Chapter 7 analyses the swirl characteristics in the wake of each turbine.
- Chapter 8 compares the velocity recovery in the wake of each of turbine.
- Chapter 9 investigates the effect of blade deflection on the performance characteristics.
- Chapter 10 summarises the main conclusions from the work and makes recommendations for further work.

2 Literature Review

Tidal Stream technology has seen a rapid expansion in recent years with over 50 devices now in development, several devices at the commercial deployment stage and arrays of devices in the planning stage. This chapter outlines the different types of device under development and identifies some of the design considerations and areas in which research is being undertaken to ensure that tidal stream becomes a full commercial reality and contributes towards the renewable energy targets discussed in Chapter 1.

2.1 Types of device

There are many types of device in development, most of which can be categorised based on whether they produce a rotational or linear motion, the direction of the rotational axis or linear motion and the inclusion of any flow acceleration mechanism. The main categories into which most devices fall are horizontal axis tidal turbines (HATTs), vertical axis tidal turbines (VATTs), venturi effect devices and oscillating hydrofoils.

2.1.1 Horizontal Axis Tidal Turbines

The main feature which identifies a HATT is that the rotational axis of the turbine is parallel to the tidal flow (EMEC, 2012). In comparison with VATTs, HATTs tend to have higher efficiencies but are more complex in design; requiring blades which incorporate twist and taper to achieve this (Khan et al., 2009). Typical peak efficiencies range from around 39% to 48% (Mason-Jones, 2010; Jo et al., 2013; Faudot et al., 2013; Walker et al., 2013). The direction of the flow is of importance meaning that the rotor or the blades must be rotated between the ebb and flood tides or bi-directional blades used (Liu and Veitch, 2012; Nicholls-Lee, 2011). Along with the higher efficiency, HATTs also tend to have higher rotational velocities than VATTs, which although still significant, reduces the problem of generator matching (Khan et al., 2009).

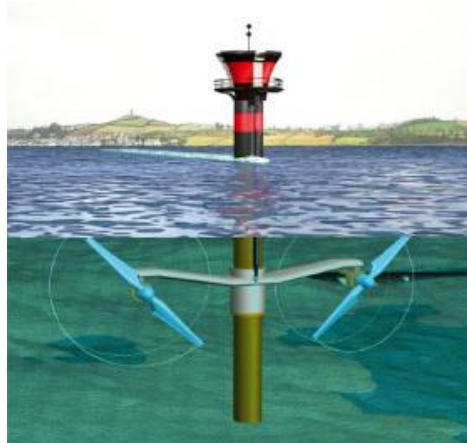
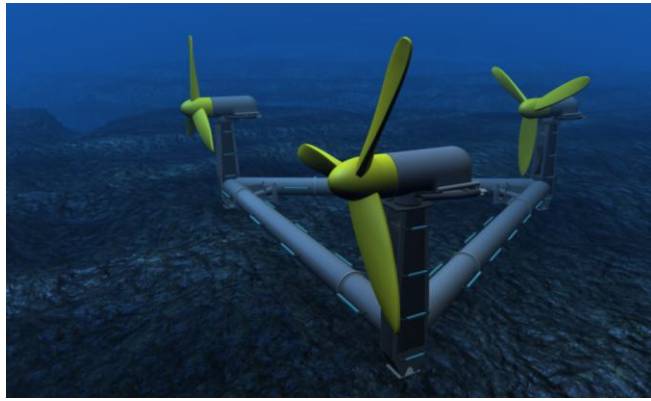


Figure 2.1 Marine Current Turbines' SeaGen Device (Taylor, 2007)

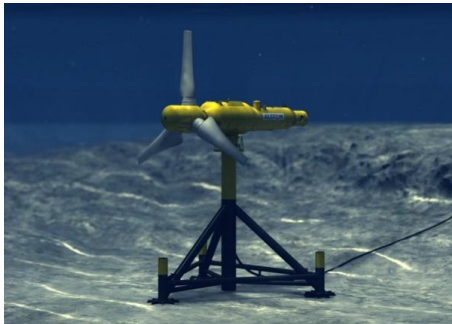
There are many forms of HATT, differing on how many blades the rotor has and how the device is fixed in position. The most developed HATT is the 1.2 MW SeaGen developed by Marine Current Turbines (MCT), shown in Figure 2.1, which is pile driven and has two rotors, each with 2 blades. Installed in 2008, it is the first commercial scale tidal stream turbine to generate power in UK waters (Sea Generation Ltd., 2007). Other devices at varying degrees of development are the 1 MW TidEl from SMD (SMD, 2012), Open Hydro (Open Hydro, 2012), the 500 kW Deep Gen from Tidal Generation Ltd (Tidal Generation, 2010) (now Alstom) and the 1.2 MW Delta Stream from Tidal Energy Ltd scheduled to be deployed at Ramsey Sound in Pembrokeshire in the near future (Tidal Energy, 2012a). Like SeaGen, TidEl also has two, 2 bladed rotors, Figure 2.2a, whereas Delta Stream, Figure 2.2b, and Deep Gen, Figure 2.2c, have 3 bladed rotors and Open Hydro has many blades and an open centre, Figure 2.2d. Prior to developing the Delta Stream device, Tidal Energy Ltd also undertook trials on a 4 bladed rotor, Figure 2.2e, under the previous company name of Tidal Hydraulic Generators Ltd (Tidal Energy, 2012b).



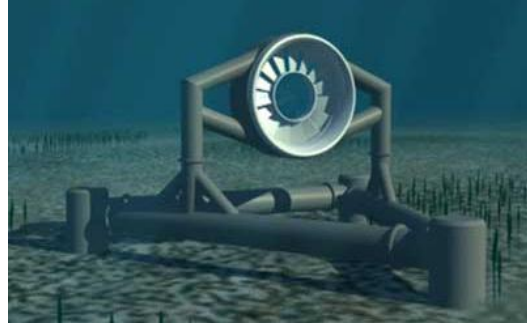
(a) TidEl (SMD, 2012)



(b) DeltaStream (Tidal Energy, 2012a)



(c) DeepGen (Alstom, 2013)



(d) OpenHydro (OpenHydro, 2012)



(e) Tidal Hydraulic Generators Ltd (Tidal Energy, 2012b).

Figure 2.2 HATT devices under development

2.1.2 Vertical Axis Tidal Turbines (VATTs)

VATTs extract energy from the flow in a similar way to HATTs, but the rotational axis of the turbine is perpendicular to the tidal flow (Renewable UK, 2011). There are very few VATTs in development in comparison to HATTs. The main advantage of a VATT is that it can operate regardless of the direction of tidal flow without loss of operational efficiency and without the need for any pitch or yaw mechanism to rotate the blades or rotor (Eriksson et al., 2008). A VATT can have straight blades,

reducing the design and manufacturing costs when compared with the more complex HATT blades (Khan et al., 2009). In addition, since the rotational velocity of a VATT tends to be lower, they produce less noise (Riegler, 2003) and pose a reduced risk of collision (Eriksson et al., 2008) which may be beneficial for marine life. However, a reduction in noise may result in marine life coming in closer proximity to the device which would counteract the reduced collision risk due to lower blade velocity. The disadvantages of a VATT include lower efficiency (Khan et al., 2009), with typical peak values of around 37% to 40% (Han et al., 2013; Eriksson et al., 2008), although Eriksson et al. (2008), state that the lower efficiencies could be a result of more research based on horizontal turbines than on vertical turbines in the wind industry. Other disadvantages of VATTs include the low starting torque, meaning that unlike most HATTs they may need a starting mechanism (Khan et al., 2009), and the torque ripple due to the changing angle of attack through the rotation cycle (Eriksson et al., 2008).



(a) Kobold Turbine (University of Naples, 2012) (b) Gorlov Turbine (Appleyard, 2012)

Figure 2.3 Examples of VATTs

VATTs can be divided into two main groups depending on the blade design. The first type is a straight bladed VATT known as a Darrieus turbine, for example the Kobold Turbine, Figure 2.3a, (University of Naples, 2012) and the second type has helically shaped blades, an example of which is the Gorlov Turbine, Figure 2.3b (Appleyard, 2012).

2.1.3 Oscillating hydrofoil

Oscillating Hydrofoils use an oscillating motion rather than a rotary motion to extract energy from the flow and consist of a hydrofoil mounted on a pivoting arm. The tidal flow over the hydrofoil causes the arm to reciprocate in either a vertical or horizontal plane due to the hydrodynamic lift and drag forces on the wing. Examples of such devices include the seabed mounted Stingray (The Engineering Business Ltd., 2003), bioSTREAM (BioPower Systems, 2013) and Pulse Stream (Renewable UK, 2011). Stingray, Figure 2.4a, and Pulse Stream, oscillate in the vertical plane whereas bioSTREAM, Figure 2.4b, oscillates in the horizontal plane.



(a) Stingray (BBC, 2002)



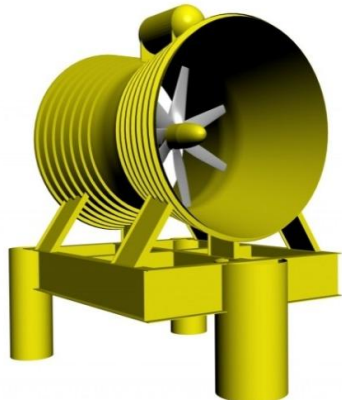
(b) bioStream (BioPower Systems, 2013)

Figure 2.4 Examples of Oscillating Hydrofoils

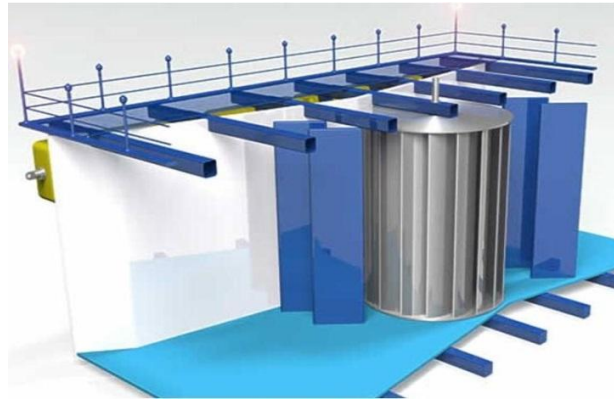
2.1.4 Venturi Effect devices

There are two general types of Venturi Effect devices. The first is essentially a HATT or VATT with a duct around the turbine which increases the flow velocity, such as the Lunar Tidal Turbine (Lunar Energy, 2012) and the Neptune Proteus (Renewabl, 2010), shown in Figure 2.5a and Figure 2.5b.

The second utilises a venturi and uses the reduced fluid pressure at the throat to draw a secondary fluid through a separate turbine, for example the Spectral Marine Energy Converter (VerdErg, 2012).



(a) Lunar Tidal Turbine
(Lunar Energy, 2012)

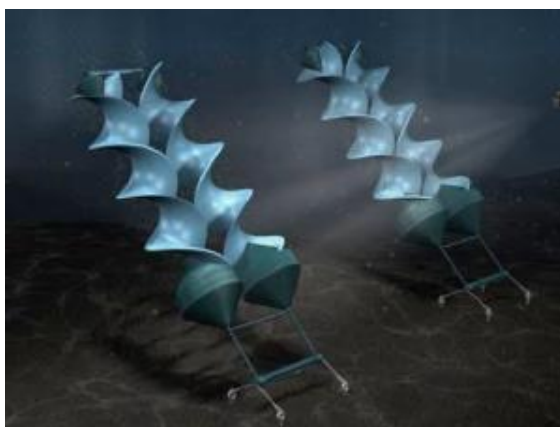


(b) Neptune Proteus (Renewabl.com)

Figure 2.5 Venturi Effect Devices

2.1.5 Other types of device

There are some tidal stream devices which cannot be placed into any of the categories described above. Examples of these are the Flumill Power Tower, Figure 2.6a, and the DeepGreen developed by Minesto, Figure 2.6b. The Flumill Power Tower consists of two counter-rotating helical screws mounted parallel to each other (Flumill, 2012). The device is buoyant and is fixed to the seabed using a flexible mooring system. It can generate in tidal flows as low as 0.5 m/s.



(a) Flumill Power Tower (Flumill, 2012)



(b) Deep Green Device (Minesto,

2012)

Figure 2.6 Other types of tidal stream device

The Deep Green device is essentially a wing with a turbine attached to the underside. The device is tethered to the seabed and moves through the water with a motion similar to that of a kite, due to the hydrodynamic lift created by the flow over the wing. The Deep Green also has the advantage of being able to operate in low velocity flows as the device can move at up to ten times the speed of the current; which creates sufficient flow through the turbine (Minesto, 2012).

2.1.6 Rotor design used in this work

Since most of the commercial prototypes in development are HATTs and the majority have 2, 3 or 4 bladed rotors, this work is based on these configurations.

2.2 Environmental Impacts

The characteristic behaviour of the ocean depends on many factors such as depth, bathymetry and weather. These factors contribute to the decision of where to locate devices and in fact what type of device, with each device having a minimum rated flow velocity and a securing mechanism that may only be suitable for a given depth of bathymetry.

Construction and operation of one or more tidal stream devices will have direct and indirect effects on the surrounding environment and on the life within it. The protection of the environment, of species and human health, as well as the prevention of interference with legitimate uses of the sea, such as shipping, are the main factors that a government has to consider when assessing a marine licence application. In some cases, getting the necessary consent and licence imposes great difficulties and huge time delays for developers.

Many tidal stream devices are still in various stages of development and hence there have been few studies into the environmental effects of these technologies. The studies which have been carried out to date are mostly either based on predictions or are unverified (US Department of Energy, 2009), with the exception

of Marine Current Turbines who have had an independent study conducted, led by Royal Haskoning, for the deployment of SeaGen (Royal Haskoning, 2011). This study found that there were no major environmental impacts as a result of the project.

The quality of the water surrounding tidal stream devices could change significantly. For example, a change in turbidity is possible due to the effects on sediment transport and deposition caused by the altered tidal flows and current streams which may occur due to these devices (Sustainable Development Commission, 2007). The effect of this on marine life is uncertain. Thriving species could be negatively affected and vacate the area whereas the opposite is also a possibility; where new species are attracted. Although, water quality was not included in the SeaGen environmental monitoring programme; a species of mussel not found in the area prior to deployment was subsequently found on the mono-pile structure and was considered a positive addition to the biodiversity (Royal Haskoning, 2011).

The effect on shipping is a concern and this may limit the location and size of device arrays. Pollution from the machinery used should also be considered such as the release of hydraulic fluids, lubricants, etc. (Sustainable Development Commission, 2007). No evidence has yet been found that Electromagnetic fields from generators and cables affect the migratory and feeding habits of marine mammals and fish – however, this is still a controversial area (Switzer and Meggitt, 2010).

There is a small possibility of creatures such as fish, mammals or even diving birds, striking turbines. There are also concerns of the cavitation effects causing sudden pressure changes that could harm fish (Byrne et al, 2011). Some device developers have attempted to mitigate the risk to marine life in their designs such as the Open Hydro and the Alstom Hydro, which both incorporate an open centre allowing safe passage for fish and marine mammals (Renewable UK, 2011; Open Hydro, 2012).

Installation of tidal stream devices can have an effect on the surrounding environment, from mooring systems such as anchors and foundations to the laying of transmission cables and pipes. In the case of SeaGen this was found to be temporary and the structure has since become a thriving habitat for marine

creatures (Royal Haskoning, 2011). There is also likely to be a temporary issue with the high noise levels during construction (Frid and Andonegi, 2012), though operational noise is a different issue and could act to keep marine creatures away. Royal Haskoning estimate that the operational noise of SeaGen is audible to marine mammals up to 1.4km from the device and have found a local avoidance of around 250m from the device, although this may not be due to noise as the same observation was made when the turbine was not operating (Royal Haskoning, 2011).

2.3 Securing, Installation and Maintenance

Devices can be secured through a number of methods and Fraenkel (2002) described a number of techniques from piled through to floating structures, which include:-

1. Gravity base, where the device is attached to a weighted structure, as used by OpenHydro, Figure 2.2b;
2. Piled devices, either mounted to single or multiple piles, as used by SeaGen, Figure 2.1;
3. Flexible Moorings which consist of a tether using chains, cables or ropes and anchor to secure the device to the seabed allowing alignment with oncoming waves or tidal flows. Some devices include contra-rotating rotors, either with separate but parallel rotational axes, such as TidEl, Figure 2.2a, or on the same rotational axis, as investigated by Clarke et al. (2008). This results in zero net torque and hence the device stays aligned with the flow.

Other methods of securing devices have been proposed including multiple hydrofoils mounted to the structure which hold the device in place using down forces created by tidal flows (EMEC, 2012). Whichever system is chosen, all aspects relating to safety and reliability must be considered, and it must be cost effective (Harris et al., 2004). Piled foundations are likely to be expensive and with current technology are limited to depths of 40 m or less (Clarke et al. 2010).

The installation procedure must also be thoroughly planned and well executed as poorly installed devices could result in large unforeseen costs. For example, the estimated cost to rectify 164 poorly installed offshore wind turbines was ~£13M (Renewable Energy World, 2010).

Economic viability of marine energy devices requires lengthy life spans, leading to the requirement of costly maintenance procedures due to the remote locations and harsh environments. There are several proposed methods for maintenance, including detachment from moorings and towing ashore and removal of the turbine and generation unit as one leaving the main structure on the seabed (Lunar Energy, 2010). Piled devices offer relatively easy access for maintenance as submerged devices can be raised out of the water and maintenance undertaken in situ. However, the time frame for maintenance undertaken in situ is limited by the duration of slack water.

2.4 Design Considerations of a HATT

The tidal stream turbine modelled in this study is of the HATT type. Therefore, the main design considerations discussed will focus on this type of device.

2.4.1 Solidity

For a given rotor diameter, solidity is a function of chord length and the number of blades. It has been shown by Hau (2006) that increasing the number of blades on the rotor of a wind turbine increases its power output but with diminishing returns so that there is a smaller benefit for each additional blade, as shown in Figure 2.7. An increase in the number of blades also reduces the operational range and the optimum tip speed ratio (λ), also shown in Figure 2.7 (Hau, 2006). The increased power and reduction in both operational range and optimum λ was shown by (Consul et al., 2009) to also be true for a VATT but only two blade configurations were modelled and therefore the diminishing returns could not be confirmed. Shiono et al. (2000) found that for a fixed number of blades the power output of a VATT increased with solidity from a solidity of 0.108 to 0.179 and then decreased with further increases in solidity.

The majority of horizontal axis wind turbines (HAWTs) are 3 bladed and the reasons for this include aesthetics, noise and engineering considerations. It is generally thought that 3 bladed rotors are more aesthetically pleasing than 2 bladed rotors and are quieter due to a lower rotational speed (Cottrell, 2002). Although aesthetics will not be an issue for tidal stream turbines, noise generation may be a problem for marine life (DTI, 2007). In addition to noise, higher rotational speeds may also increase the risk of cavitation and injury or death to marine mammals.

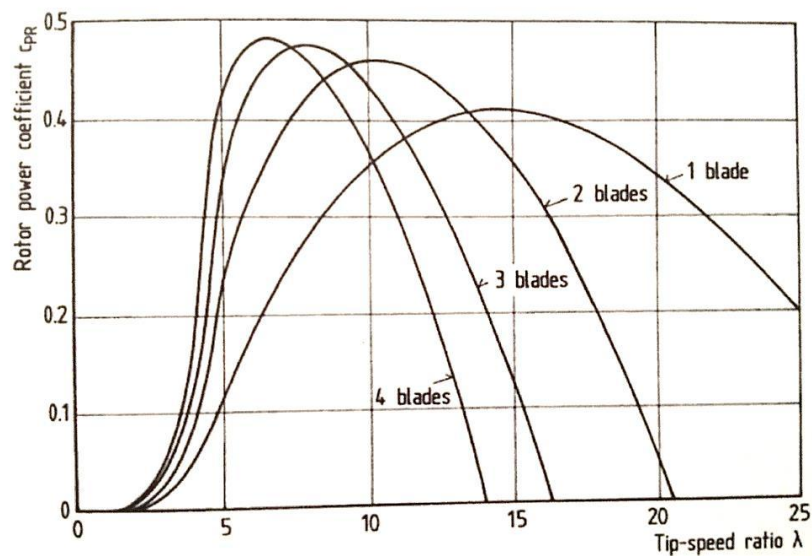


Figure 2.7 Power coefficient curves for wind turbines with increasing numbers of blades (Hau, 2006)

The number of blades is a particular concern for pile driven and gravity based structures since as a blade passes in front of the support stanchion, or behind for some designs, tower shadow effects occur, leading to a reduction in torque and thrust (Mason-Jones et al., 2013). According to Jo et al. (2012) a 2 bladed rotor would suffer from unacceptable tower shadow effects but a 3 bladed rotor can maintain stable disk characteristics and therefore more blades are unnecessary, since they will increase the cost of the rotor. However, an increase in the number of blades would reduce the overall tower effects for designs where only one blade passes in front of the support stanchion at a time, such as the MCT Seagen device,

since the ratio of blades affected by the tower to the total number of blades would be lower. For designs where 2 blades pass in front of the support stanchion at the same time, this may not be the case. For example, with MCTs SeaFlow device, Figure 2.8, a 4 bladed rotor would result in 2 out of 4 blades in the tower shadow at one time, in comparison with 1 out of 3 for a 3 bladed rotor. A reduced overall tower effect would be beneficial from a generation point of view, since the output would be more consistent. However, depending on the design of support stanchion, reducing the overall tower effect may have a negative effect on the drive train components due to misalignments caused by imbalances of the forces on the rotor. A tethered mooring system may alleviate problems associated with tower shadow.



Figure 2.8 Marine Current Turbines' SeaFlow Device (Murdoch University, 2008)

Although there have been few studies on solidity for HATTs, findings from work on HAWTs may be transferable. Duquette et al. (2003a) investigated the effect of solidity on a HAWT by changing both the chord length of each blade and the number of blades. The study was based on numerical predictions with solidity values ranging from 0.05 to 0.45 and blade numbers of 3, 6 and 12. The findings showed that for a fixed solidity, maximum power output increased with the number of blades. For a fixed number of blades the maximum power output varied with

solidity but to a differing extent depending on the number of blades. However, experimental work by Duquette et al. (2003,b) contradicted the numerical predictions and showed a reduction in power output for an increased number of blades at a constant solidity. The authors suggest that this may be due to low Reynolds number and blockage effects in the experimental set-up. Mason-Jones et al. (2012) and Tedds et al. (2011) have shown that low Reynolds number can reduce the power output but it is likely that this would affect all of the results. In addition the constant solidity would result in the same blockage ratio throughout the experiments so these explanations may not be justified.

When considering the design of a theoretical turbine for a study on composite blades, Wadia et al. (2011) state that higher solidity rotors will be less prone to blade erosion and cavitation since the optimum λ is lower and therefore the flow velocity over the blades is lower. They also assert that a lower λ should result in a reduced effect from the drag caused by marine fouling.

While it is stated above that fewer blades can reduce the cost of the rotor, it can also reduce the cost of the gearbox, since the operating λ is higher and therefore closer to that of a generator (Jo et al., 2013). However, other factors such as tower shadow effects, installation, maintenance and lifespan will contribute to the economic considerations; all of which may be dependent on the number of blades.

2.4.2 Interaction with Stanchion

As discussed above, the interaction with the stanchion can affect the performance and loading on a tidal stream turbine. In addition to the number of blades, the magnitude of the effect is also influenced by the geometry of the stanchion (Mason-Jones et al., 2013) and the distance between the rotor and the stanchion (Frost et al., 2014). The former study found that the power output of a turbine with an elliptical or hydrofoil shaped stanchion is around 20% higher than with a square stanchion and the total thrust around 35% lower. The latter work showed that the power output increased by around 10% when the rotor to stanchion distance was increased from 1 to 2 hub diameters with the turbine upstream of the stanchion.

Furthermore, although the average power output was found to reduce by only around 7% when the rotor was downstream of the stanchion, the fluctuations in power over the rotational cycle increased from around 2.5% to around 30% and the fluctuations in thrust from 1% to 15%.

2.4.3 Wake Length

There are little published data regarding the wake of a full-scale tidal turbine and none could be found in the public domain. Small scale experiments have been undertaken by Myers et al. (2008, 2010), using mesh disks to simulate rotors. These studies showed a recovery to 90% of the upstream flow velocity along the centre line of the disk at a downstream distance of ~ 20 diameters. The representation of rotors as mesh disks neglects the swirl imparted on the flow but the authors state that these effects dissipate rapidly and only affect the near-wake region, the end of which is defined as “the point at which the shear layer reaches the centre line”. The results of this work suggest that the thrust on a turbine affects only the near wake with the far wake depending mainly on ambient turbulence, proximity to the surface and sea bed and local bathymetry.

In contradiction to the assumptions of Myers et al. (2008, 2010), McCombes et al. (2008) predict that the vortices shed from the blade will have a significant effect on the wake recovery and state that traditional CFD may underestimate wake length due to the diffusion of vorticity.

Research in the wind industry has shown that in wind tunnel experiments the velocity at $x/D=16$ is less than 90% of the upstream value (Vermeer et al., 2003). However, Helmis et al. (1995) argue that the length of the near wake region is overestimated by wind tunnel experiments with their field measurements showing negligible velocity deficit at $x/D=10-12$. This could be due to differences in the physical surroundings which cannot be accurately modelled in a wind tunnel and could also be applicable to tidal stream turbine wakes. Masters et al. (2013) investigated the effect of flow acceleration on wake recovery by including a sloping surface in their models and found that a surface gradient of -0.01 reduced the distance to 80% velocity recovery by almost 50%. In addition to this, Olczak et al.

(2013) found that surface waves can improve velocity recovery and reduce wake length, with larger waves having a greater effect. These findings highlight the necessity of extensive field data for a site prior to installation and the inclusion of as many physical features as practical in a physical or numerical model of a proposed site.

2.4.4 Blade Loading

The loads which the blades must withstand are a critical design requirement, with expensive and embarrassing blade failures occurring for several prototype turbines in recent years. While the failure of the Atlantis AR1000 blades was due to a manufacturing defect, both the OpenHydro and Verdant Power failures were caused by a larger than expected incoming velocity and hence load (Liu and Veitch, 2012), again underlining the importance of accurate site specific field data including turbulence and wave effects.

The dynamic loading on a tidal stream turbine can be separated into periodic loads, caused by velocity shear and rotor-stanchion interaction, and stochastic loads caused by turbulence and waves. Collier et al. (2013) showed that the fatigue loading is dominated by the stochastic loads. Most full scale prototypes have composite blades and according to Wadia et al. (2011) fatigue is unlikely to be critical for glass/carbon laminates but can be significant for metal parts. This would include, for example, bolts used to secure the blades to the hub.

Wadia et al. (2011) also state that seawater saturation reduces the fibre strength of a composite by ~10% and the resin-based strength by 25% which must be accounted for in the design process. They also found that a longitudinal web along the length of the blade reduced the bending moment by a factor of 4. Additional material combined with a longitudinal web will limit the minimum thickness of the blade but Liu and Veitch (2012) found that increasing the thickness of the blades by a small amount to improve the strength has little effect on the power output of the turbine. In addition to external loads, Wadia et al. (2011) also considered the internal loads at the tips if the blades are water filled, due to the increase in pressure caused by centripetal acceleration. Their findings led them to conclude

that the blades of a TST could be approximately 50% lighter than those of a wind turbine with the same rated power but at 75% of the cost.

2.5 Modelling

Modelling of a full scale turbine, either by scaled prototype or numerically, is an essential part of the design process, providing developers and investors with estimates of power, loads, and flow characteristics. This section considers published modelling in the field, focussed on HATTs, since the tidal stream turbine used for the work in this study is of this type.

2.5.1 Physical Modelling

Physical scale modelling has been undertaken in towing tanks, recirculating flumes, rivers and harbours and offshore. Towing tank experiments have been carried out by, for example, Faudot et al. (2013) in their work on runaway situations and Clarke et al (2008). when developing their contra-rotating prototype. Towing tank tests can provide a controlled environment but can only be used with plug flows and cannot simulate velocity profiles. Recirculating flume testing has been undertaken by several research groups and can include velocity profiles (Tedds et al., 2013) and waves (Olczak et al. 2013). However, recirculating flumes tend to have a smaller cross section than towing tanks and therefore rotor diameters can be limited by blockage effects.

River, harbour and offshore testing include work by Orme and Masters (2004), Starzmann et al. (2013) and Clarke et al. (2008). Unlike towing tanks and recirculating flumes, river, harbour and offshore testing does not provide a controlled environment. It is therefore less suitable for validating numerical models but does give an insight into the effects of variable flow velocity and turbulence and provides valid information regarding turbine performance in a more realistic environment.

2.5.2 Numerical Modelling

In order to minimise the time and cost taken to move from initial concept to commercial deployment, numerical modelling can be used to reduce the number of design iterations in the physical prototype. The approach taken depends on time

and computational constraints and is often based on one or more of the following methods.

2.5.2.1 Blade Element Momentum Theory

Blade Element Momentum theory (BEMT) is based on a combination of momentum theory and the lift and drag coefficients of a blade profile. It is faster and less computationally expensive than other numerical methods such as Computational Fluid Dynamics (CFD) and is therefore the basis for commercial wind and tidal design tools such as Garrad Hassan's Bladed and Tidal Bladed due to the number of design iterations that can be performed in a short period of time (Bahaj et al., 2007). However, it does not account for any flow perpendicular to the blade profile, along the length of the blade and assumes the forces on the rotor are rotationally averaged (Malki et al., 2013; Batten et al., 2013).

Malki et al. (2013) have developed a coupled BEM-CFD model which is based on momentum source terms from a BEM model being fed into a RANS model. The authors state that where the incoming flow is non-uniform, as is likely in most practical cases, this method can give more realistic predictions than the classical BEM method.

Batten et al. (2013) have also used this method and state that it is suitable for assessing the interactions of wakes in an array but not for obtaining predictions for the loading on each individual blade since the time-averaged nature of the actuator disk still applies. The results of this work also indicate that this method over predicts overall loading and under predicts performance which could contribute to over engineering and unfavourable economics if used for the final design of an individual turbine.

2.5.2.2 Computational Fluid Dynamics

CFD can give more detailed information on the forces on an individual turbine and can be used for optimising a turbine, after initial blade design. For example, Mason-Jones (2010) found that a blade which was predicted to have an optimum pitch angle of 7° using BEM was later found to have an optimum of 6° using CFD.

CFD involves solving the Reynolds Averaged Navier Stokes (RANS) equations by Finite Volume method, using semi-empirical turbulence models. Several turbulence models have been developed and range in complexity and applicability. The majority of CFD studies in the field have used either the $k-\epsilon$ model (Gant and Stallard; 2008, Malki, 2013) or the $k-\omega$ Shear Stress Transport (SST) model (McSherry et al.; 2011, Afgan et al.; 2013, Fleming et al., 2013), although Mason-Jones et al. (2008) used the Reynolds Stress Model (RSM). Those used in this work are discussed in Chapter 3.

Early CFD work in the field of tidal stream turbines was based on extracting energy from the flow by modelling the turbine as a porous disk (Gant and Stallard, 2008). Unlike the coupled BEM-CFD method, no swirl is introduced to the flow and hence this is a highly simplified representation of a tidal stream turbine. It has limited use in estimating wake lengths and their interactions in arrays, but again does not give detailed information about the turbine, such as blade loading. It therefore cannot be used in the development of Fluid-Structure Interaction (FSI) models, discussed later in this chapter.

In 2008, Mason-Jones et al. (2008) modelled a horizontal axis tidal turbine using the full turbine geometry and this method is now being used by several research groups (McSherry, 2011; McNaughton, 2013; Fleming, 2013). One issue that has become apparent through these studies is the decay in turbulence from the inlet through the length of the domain (Gant and Stallard, 2008; Mason-Jones, 2010). Velocity profiles and bed shear have been included in attempt to mitigate this problem (Fleming et al, 2013), but this again relies on accurate field data to give realistic results.

Further complexity in the flow field can be modelled using Large Eddy Simulation (LES). LES involves filtering the Navier-Stokes equations to remove eddies which are smaller than the grid spacing, and resolving the large eddies which remain. The small scale turbulence is then modelled assuming an isotropic eddy viscosity (ANSYS, 2010). LES requires a very fine mesh and is therefore very computationally expensive.

A study on LES and RANS was conducted by Afgan et al. (2013). They concluded that the LES models did not offer significant advantages over the RANS models for mean and instantaneous power and load predictions but did capture unsteady loads which were not captured by the RANS models. It is therefore likely that a LES would offer useful fatigue and life prediction data toward the end of the design process. However, this study showed the computational expense of LES with 2048 processors used for these models.

A compromise between RANS and LES can be achieved using hybrid RANS/LES models such as the Detached Eddy Simulation (DES) available within ANSYS FLUENT (2010) and the Dynamic Hybrid RANS/LES (DHRL) model developed by Bhushan et al (2013). These models operate in RANS mode in the boundary layer near walls and in LES mode in the free stream flow.

Due to the requirement to develop a 2-way coupled Fluid Structure Interaction (FSI) model, as discussed in Section 1.3, the RANS modelling approach was taken for the work in this thesis. This was because details on the loads on each blade were required and therefore an actuator disk model would be insufficient, but the computational expense of DES or LES would result in an unreasonable run time when coupled with FEA.

2.5.2.3 Fluid-Structure Interaction

In recent years, Fluid Structure Interaction (FSI) modelling has been used for analysis of wind turbine blades, although much of this research involves the coupling of BEM codes with FEA, as in the work by Lee et al. (2012) in their work on FSI of FRP (fibre reinforced plastic) wind turbine blades.

Previous FSI studies of marine turbines include Nicholls-Lee et al. (2011). In their work a surface panel code was used for the CFD and ANSYS 12.1 for the FEA. Matlab was used as the FS interface to enable the transfer of force and displacement data between the CFD and FEA codes. This work gives a valid insight to the effects of fluid structure interaction and its consequences on cavitation, power attenuation and stresses on the structure. While it is stated by Nicholls-Lee et al. (2011) that the panel method performs well for undeviating flows it is clear

that where it becomes necessary to include intricacy in the hydrodynamic flow field, the use of RANS, DES and LES solvers are required to model the hydrodynamics. Moreover, with an increased knowledge of a hydrodynamic flow field under extreme conditions such as an upstream velocity profile and rotor stanchion interaction it becomes necessary to consider the strong coupling effects between the fluid and the structure.

Another approach to FSI is to use a RANS solver for the hydrodynamics and a simplified solver for the structural analysis such as that employed by Arnold et al. (2013), where the Simpack multibody method was coupled with ANSYS CFX. This method is less computationally expensive than FEA but relies on a reduced number of degrees of freedom and does not offer the same level of accuracy as an FEA solver.

Furthermore, simplified models can be used for both the fluid and structural analyses, such as in the work by Bercin et al. (2013) on an efficient method for analysing FSI of HATT blades, which is based on coupling a BEM code with beam theory and modal decomposition.

While the above methods all provide valid approximations required at an early stage of development, at a more advanced design stage the coupling of CFD and FEA solvers can provide detailed predictions for the flow field, performance, deformation and loading, and can help to minimise the number of physical prototypes and modifications to these prototypes that are required for successful deployment.

Research based on coupling of CFD and FEA solvers includes that by Jo et al. (2013), who investigated the performance of a horizontal axis tidal turbine with blade deformation and found a 2.2% drop in the power output with a maximum blade tip deflection of 0.216m. However, this work was based on a one-way coupling where the results from a CFD study were exported to a FEA model and the deformed structure was fed back to the CFD model to find the change in power output for a given blade deflection. However, the single coupling iteration does not account for the change in blade deflection associated with the altered flow field.

A fully coupled 2-way FSI using a symmetry boundary and single blade was undertaken by Park et al. (2013). In this 2-way study ANSYS CFX 13.0 and ANSYS Transient Structural were used. From the results it was suggested by Park, et al. (2013) that although the deflection of the blades was relatively small in their study it was still necessary to consider blade deformation due to a 1.7% drop in maximum power extraction. Moreover, the latter research indicated that a possible over estimate of the maximum negative pressure on the suction side of the blade, as was found with a rigid blade, has the potential to lead to a corresponding over prediction on the initiation of cavitation.

The FSI work in this thesis is based on fully-coupled two-way FSI models of a horizontal turbine hub and all blades.

2.6 Summary of Literature Review

There are various different types of tidal stream devices and various methods of securing them to the sea bed. This work is based on a HATT rotor. The design considerations of a HATT include solidity, wake length and blade loading which are all investigated in this study. Other areas of research include interaction with the support stanchion, securing, installation and maintenance and environmental impacts but these are beyond the scope of this work.

Research methods in the field include numerical and physical modelling. The methods used for this work are based on CFD and FSI numerical modelling. Scaled prototype testing in a recirculating flume is used to validate the CFD models.

To the author's knowledge, there are no data published using RANS based CFD to compare tidal stream turbines with different numbers of blades of the same blade design. Also, no published work could be found which involves a fully coupled 2 way FSI analysis of a complete tidal stream turbine rotor.

3 Theory

In order to compare devices of different physical sizes subjected to different flow conditions, non-dimensional coefficients are used. This chapter gives an overview of the relevant theory used to assess the performance of a HATT, define its solidity and analyse the swirl it imparts to the flow. Details of the underlying theory of the numerical modelling are also given.

3.1 Performance Characteristics

The performance of a HATT can be described by the non-dimensional performance characteristics below, which are based on Froude's Momentum Theory for an actuator disk (Hansen, 2001). The power coefficient (C_p) is the ratio of the extracted energy to the available energy over the swept area of the turbine and is given by Equation 3.1.

$$C_p = \frac{2P}{\rho A u^3} \quad 3.1$$

Equation 3.2 gives the torque coefficient (C_θ), which is the ratio of the torque generated by the turbine to the maximum theoretical torque.

$$C_\theta = \frac{2T}{\rho A u^2 r} \quad 3.2$$

The thrust coefficient (C_t), given by Equation 3.3 is the ratio of the axial load on the turbine to the axial load over the swept area of the turbine.

$$C_t = \frac{2F}{\rho A u^2} \quad 3.3$$

The tip speed ratio (λ) is the ratio of the tangential velocity of the blade tip to the upstream velocity of the flow and is given by Equation 3.4. Plotting the above performance characteristics against λ enables different devices to be compared regardless of the turbine diameter or flow conditions.

$$\lambda = \frac{\omega r}{u} \quad 3.4$$

3.2 Solidity

The Solidity of a turbine is given by the ratio of the total blade area to the swept area of the rotor and is represented by Equation 3.5 (Duquette and Visser, 2003).

$$\sigma = \frac{BC}{\pi R} \quad 3.5$$

where B is the number of blades and C is the average chord length.

The solidity values used for the work presented in this thesis and the associated number of blades are shown in Table 3.1 and Figure 3.1 below.

Table 3.1 Turbine solidity values

No of Blades,	Solidity, σ
2	0.14
3	0.21
4	0.28

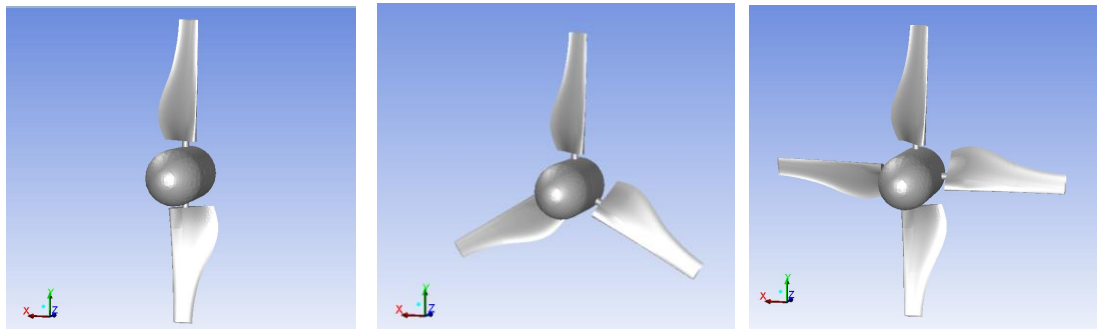


Figure 3.1 Turbine configurations

3.3 Swirl

Swirl flows are observed in natural flows, such as tornadoes and typhoons, and have been widely used, for various reasons, in technical applications, such as aeronautics, heat exchange, spray drying, separation, combustion, etc. Their importance and complexity have been the subject of many research investigations for decades and a full review of the complex nature of the research into swirl and vortex breakdown can be found in Lucca-Negro and O'Doherty (2001) and Syred (2006).

In aeronautics, leading-edge vortices shed from a delta wing induce a velocity field that results in increased lift and stability of the wing. However, under certain conditions related to the angle of attack of the wing, these vortices can undergo a sudden and drastic change in structure, known as vortex breakdown, which can adversely alter the aerodynamic characteristics of the wing. A similar bursting phenomenon has been observed for trailing wing-tip vortices, which is, this time, desirable as these vortices represent a hazard to smaller aircraft in areas of dense air traffic (Spall et al., 1987). An understanding of the vortices shed from TSTs and the ensuing swirl flow is therefore important if these turbines are to operate under optimal conditions whilst minimising their spacing within an array.

A swirl flow is defined as one undergoing simultaneous axial and vortex motions. It results from the application of a spiralling motion, a swirl velocity component (tangential velocity component) being imparted to the flow, axial-plus-tangential entry swirl generators or by direct tangential entry (Gupta et al, 1984). The vorticity of such flows is the curl or simply the distortion of the velocity field. This distortion, when it exists, results from the different angular velocities of different rings of particles. It therefore causes an object travelling on a circular path to rotate about its own axis as it goes along. Vorticity is defined as the ratio of the circulation round an infinitesimal circuit to the area of that circuit (Massey, 2006) and is given by: -

$$\text{vorticity } \Omega = \frac{\text{circulation}}{\text{area}} = \nabla \times \underline{U}_p \quad 3.6$$

$$\text{Where } \underline{U}_p = \underline{u} + \underline{v} + \underline{w}$$

Flows with a tangential or swirl velocity w of type $w = C/r$ are called *potential* or *free* vortices. The vorticity of such flows tends to zero and the local flow rotates as a fixed body, that is, each element of the moving fluid undergoes no *net* rotation (with respect to chosen coordinate axes) from one instant to another. Hence such flows are called *irrotational*. Flows with solid-body rotation such that the tangential velocity is given by $w = c'r$ are called *forced* vortices. In this case the vorticity does not tend to zero and such flows are called *rotational*, that is each element of the moving fluid travels along a circular path and simultaneously rotates about its own axis.

In practice there may be rotational motion in one part of a flow field and irrotational motion in another part. In addition, all free vortices in real fluids have a central vortex core in which the vorticity is non-zero (Gupta et al, 1984). Conservation of angular momentum tends to create a free vortex flow, in which the circumferential velocity increases sharply as the radius decreases, w finally decaying to zero at $r = 0$ as viscous forces begin to dominate.

The free and forced vortices can be distinguished by the radial position of the maximum value of the tangential velocity component: in a free vortex, the maximum is found near the axis of symmetry while in the forced vortex, the maximum is found at the outer edge of the vortex. In some cases, a combined or Rankine vortex exists where the forced vortex equation is satisfied at small radial distances and the free vortex equation for large radial distances (Figure 3.2). This type of vortex has been shown to develop, for example, when the flow is introduced tangentially at the periphery of a cylindrical chamber and exhausted at an axial nozzle (Keyes, 1960; Roschke et al.; 1965, Sozou and Swithenbank, 1969). The central forced vortex region exhibits flow field and turbulence characteristics, which appear to be significantly different from those seen in the surrounding irrotational vortex flow field. This central region is often referred to as the inner or vortex core. It is described as being shear free, but not vorticity free. The core is generally limited to that region of the solid-body rotating flow (Sloan et al., 1986), but can also be extended to the radius of maximum tangential velocity.

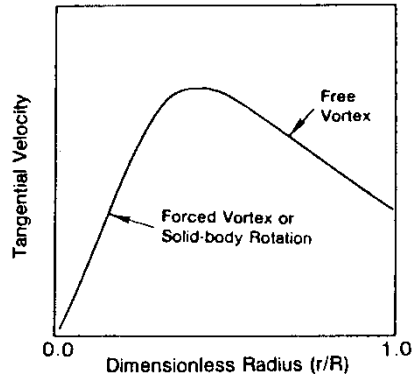


Figure 3.2 Qualitative representation of a Rankine vortex (Gupta et al., 1984)

The characteristics of each type of vortex can be uniquely defined as summarised in Table 3.2.

Table 3.2: General characteristics of vortices (Gupta et al., 1984)

	Forced vortex (solid-body rotation)	Free vortex (potential vortex)	Combined vortex (Rankine vortex)
Tangential Velocity Distribution, w	$wr^n = \text{constant}$ where $n < 0$	$wr^n = \text{constant}$ where $n > 0$	$w = \frac{C'}{r} \left[1 - \exp\left(-\frac{r^2}{R^2}\right) \right]$
Angular velocity, ω	c' (constant)	$\frac{C}{r^2}$ (function of r)	function of r
Circulation, Γ	$2\pi\omega r^2$	$2\pi C$	$2\pi C' \left[1 - \exp\left(-\frac{r^2}{R^2}\right) \right]$
Vorticity, Ω	$4\pi\omega = \text{constant}$	0	$\frac{4\pi C'}{R^2} \left[1 - \exp\left(-\frac{r^2}{R^2}\right) \right]$

In addition to classifying a swirl flow based on its type of vortex, it is common to characterise the degree or intensity of the swirl using the dimensionless local swirl number. This is because the degree of swirl has large-scale effects on the flow fields (Gupta et al., 1984). For example, introducing swirl into turbulent jets causes an

increase in jet growth, rate of entrainment and rate of decay of the jet. The swirl number is defined as follows (Lilley, 1973):

$$S = \frac{G_\phi}{G_x r} \quad 3.7$$

Where

$r = R$, the rotor radius since r is normally defined as the distance from the axis of rotation to the geometry edge;

G_ϕ is the axial flux of angular momentum and is given by

$$G_\phi = \int_0^R (wr) \rho u 2\pi r dr = \frac{2}{3} \pi R^3 \overline{uw} \quad 3.8$$

G_x is the axial flux of linear momentum is given by

$$G_x = \int_0^R u \rho u 2\pi r dr + \int_0^R p 2\pi r dr = \pi \rho R^2 \overline{u}^2 \quad 3.9$$

assuming the static pressure is constant over the R , and consequently that the pressure term can be omitted (Lucca-Negro, 1999).

The swirl number is typically used to define the level of swirl, such that very weak swirl is when $S \leq 0.2$, weak swirl corresponds to $0.2 < S \leq 0.5$ and strong swirl is when $S > 0.5$ (Gupta et al, 1984).

3.4 CFD

The commercial software ANSYS FLUENT was used for all CFD models discussed in this thesis. Continuity and momentum equations are solved for all types of flow via a finite-volume method. To account for the effects of turbulence, a variety of models are available, ranging in complexity from one-equation models to LES. The turbulence models used in this work fall into the Reynolds Averaged Navier-Stokes (RANS) category, as discussed previously, in Chapter 2. These models are described in further detail below.

Within ANSYS FLUENT various methods are available to simulate rotation. These include 2-D axisymmetric models, Moving Reference Frame (MRF) and dynamic meshing. The 2-D axisymmetric models can be used for simple problems where an external boundary is rotating. In situations where the rotating body moves through the fluid, a MRF or dynamic mesh model is required. As will be discussed in Chapter 4, a MRF was used for this work and the applicable theory is included below.

3.4.1 RANS

The RANS equations are derived by splitting the velocity term in the instantaneous Navier-Stokes equations into the time averaged and fluctuating components, Equation 3.10.

$$\mathbf{u} = \bar{\mathbf{u}} + \mathbf{u}' \quad 3.10$$

The resulting Reynolds Averaged Navier-Stokes equation for incompressible flow, such as that of water flowing around a tidal turbine, is given below in Cartesian tensor form (Versteeg and Malalasekara, 2007):

$$\rho \left(\frac{\partial \bar{u}_i}{\partial t} + \frac{\partial}{\partial x_j} (\bar{u}_i \bar{u}_j) \right) = -\frac{\partial P}{\partial x_i} + \frac{\partial}{\partial x_j} \left(\mu \frac{\partial \bar{u}_i}{\partial x_j} \right) + \frac{\partial}{\partial x_j} \left(-\rho \overline{u'_i u'_j} \right) \quad 3.11$$

where P is the hydrostatic pressure, $-\rho \overline{u'_i u'_j}$ are the Reynolds stresses which are present due to turbulence and must be evaluated to close the equation

Many turbulence models, including the k - ω SST model used in this work and discussed in Section 3.4.2.2, rely on the Boussinesq hypothesis which relates the Reynolds stresses to the mean velocity gradients by assuming an isotropic turbulent viscosity, μ_t . This is given by Equation 3.12, (ANSYS, 2010) where k is the turbulent kinetic energy and δ_{ij} is the Kronecker delta which is 1 if $i=j$ and 0 otherwise. This assumption is reasonable for many types of flow, including boundary layers and round jets (ANSYS, 2010) and has been shown to give acceptable predictions for HATTs (McSherry et al, 2011; Afgan et al, 2013; Fleming et al, 2013).

$$-\rho \overline{u'_i u'_j} = \mu_t \left(\frac{\partial \overline{u_i}}{\partial x_j} + \frac{\partial \overline{u_j}}{\partial x_i} \right) - \frac{2}{3} \left(\rho k + \mu_t \frac{\partial \overline{u_k}}{\partial x_k} \right) \delta_{ij} \quad 3.12$$

An alternative approach is to evaluate the individual stress components, as in the Reynolds Stress Model (RSM), also used in this work and outlined in Section 3.4.2.1.

For all turbulence models available within ANSYS FLUENT, the turbulent kinetic energy, k , and turbulence dissipation rate, ε , are obtained via Equations 3.13, 3.14 and 3.15 respectively and the specific dissipation rate ω is approximately equal to the ratio of the two (ANSYS, 2010).

$$k = \frac{1}{2} \overline{u'_i u'_i} \quad 3.13$$

$$\varepsilon = \nu \overline{\frac{\partial u'_i}{\partial x_j} \left(\frac{\partial u'_i}{\partial x_j} + \frac{\partial u'_j}{\partial x_i} \right)} \quad 3.14$$

$$\omega \sim \frac{\varepsilon}{k} \quad 3.15$$

3.4.2 Turbulence Models

3.4.2.1 RSM

As stated above, the RSM evaluates the individual stress components to close the RANS equations, rather than assuming an isotropic turbulent viscosity. This gives the RSM the potential to more accurately predict the flow field variables in complex flows involving high levels of swirl and rotation (ANSYS, 2010), such as those which may occur in the vicinity of a tidal stream turbine. It also more closely represents the turbulence near solid walls which is anisotropic since it is dominated by shear due to wall friction (Versteeg and Malalasekara, 2007).

The transport equations of the Reynolds stresses may be written in the following form:

$$\frac{\partial}{\partial t} \left(-\rho \overline{u'_i u'_j} \right) + C_{ij} = D_{t,ij} + D_{l,ij} - P_{ij} + \varphi_{ij} - \varepsilon_{ij} \quad 3.16$$

Where

$$C_{ij} = \frac{\partial}{\partial x_k} \left(\rho \bar{u}_k \overline{u'_i u'_j} \right) \text{ is the convective transport} \quad 3.17$$

$$D_{t,ij} = - \frac{\partial}{\partial x_k} \left(\overline{\rho u'_i u'_j u'_k} + \overline{p'(\delta_{kj} u'_i + \delta_{ik} u'_j)} \right) \text{ is the turbulent diffusion} \quad 3.18$$

$$D_{l,ij} = \frac{\partial}{\partial x_k} \left(\mu \frac{\partial}{\partial x_k} \left(\overline{u'_i u'_j} \right) \right) \text{ is the viscous diffusion} \quad 3.19$$

$$P_{ij} = \rho \left(\overline{u'_i u'_k} \frac{\partial \bar{u}_j}{\partial x_k} + \overline{u'_i u'_k} \frac{\partial \bar{u}_i}{\partial x_k} \right) \text{ is the stress production} \quad 3.20$$

$$\varphi_{ij} = \overline{p' \left(\frac{\partial u'_i}{\partial x_j} + \frac{\partial u'_j}{\partial x_i} \right)} \text{ is the pressure strain} \quad 3.21$$

And

$$\varepsilon_{ij} = 2\mu \overline{\frac{\partial u'_i}{\partial x_k} \frac{\partial u'_j}{\partial x_k}} \text{ is the dissipation, giving the full transport equation as:} \quad 3.22$$

$$\begin{aligned} \frac{\partial}{\partial t} \left(-\rho \overline{u'_i u'_j} \right) + \frac{\partial}{\partial x_k} \left(\rho \bar{u}_k \overline{u'_i u'_j} \right) = & - \frac{\partial}{\partial x_k} \left(\overline{\rho u'_i u'_j u'_k} + \overline{p'(\delta_{kj} u'_i + \delta_{ik} u'_j)} \right) + \\ & - \frac{\partial}{\partial x_k} \left(\mu \frac{\partial}{\partial x_k} \left(\overline{u'_i u'_j} \right) \right) - \rho \left(\overline{u'_i u'_k} \frac{\partial \bar{u}_j}{\partial x_k} + \overline{u'_i u'_k} \frac{\partial \bar{u}_i}{\partial x_k} \right) \overline{p' \left(\frac{\partial u'_i}{\partial x_j} + \frac{\partial u'_j}{\partial x_i} \right)} + p' \left(\frac{\partial u'_i}{\partial x_j} + \right. \\ & \left. \frac{\partial u'_j}{\partial x_i} \right) - 2\mu \overline{\frac{\partial u'_i}{\partial x_k} \frac{\partial u'_j}{\partial x_k}} \end{aligned}$$

3.23

To close the equations the turbulent diffusion ($D_{t,ij}$), pressure strain (φ_{ij}), and dissipation (ε_{ij}) must be modelled, using approximations for the unknown terms.

These approximations are as follows:

$$D_{t,ij} = - \frac{\partial}{\partial x_k} \left(\frac{\mu_t}{\sigma_k} \frac{\partial \overline{u'_i u'_j}}{\partial x_k} \right) \quad 3.24$$

where $\sigma_k = 0.82$ and

$$\mu_t = \rho C_\mu \frac{k^2}{\varepsilon} \quad 3.25$$

Equation 3.24 is a simplified form of a generalized gradient-diffusion model (Daly and Harlow, 1970) where the value of σ_k was derived by Lien and Leschziner (1994).

$$\varphi_{ij} = -C_1 \rho \frac{\varepsilon}{k} \left(\overline{u'_i u'_j} - \frac{2}{3} \delta_{ij} k \right) - C_2 \left(p_{ij} - \frac{2}{3} \delta_{ij} p_{ij} \right) \quad 3.26$$

where $C_1 = 1.8$ and $C_2 = 0.6$

The first term on the right hand side of Equation 3.26 is known as the slow pressure-strain term and the second term on the right hand side is known as the rapid pressure-strain term where the constants are empirically derived. This approach was proposed by Gibson and Launder (1978). The slow pressure-strain term is due to mutual interactions of turbulent eddies and the rapid pressure-strain term is due to interactions between turbulent eddies and the mean flow. Both terms act to reduce the anisotropy of Reynolds stresses (Versteeg and Malalasekara, 2007). The actual expression used is modified to include corrections to the rapid pressure-strain term to ensure independence from the co-ordinate system and a wall reflection term which counteracts the reduction of anisotropy in near-wall regions (Versteeg and Malalasekara, 2007; ANSYS, 2010)

$$\varepsilon_{ij} = \frac{2}{3} \delta_{ij} \rho \varepsilon \quad 3.27$$

The dissipation rate of Reynolds stresses, Equation 3.27, is modelled by assuming that the small dissipative eddies are isotropic.

3.4.2.2 k- ω SST

The transport equations for the standard k- ω model, developed by Wilcox (1998) are given below, Equations 3.28 and 3.29.

$$\frac{\partial}{\partial t} (\rho k) + \frac{\partial}{\partial x_i} (\rho k u_i) = \frac{\partial}{\partial x_j} \left(\Gamma_k \frac{\partial k}{\partial x_j} \right) + G_k - Y_k \quad 3.28$$

$$\frac{\partial}{\partial t} (\rho \omega) + \frac{\partial}{\partial x_i} (\rho \omega u_i) = \frac{\partial}{\partial x_j} \left(\Gamma_\omega \frac{\partial \omega}{\partial x_j} \right) + G_\omega - Y_\omega \quad 3.29$$

Where Γ_k , G_k and Y_k are the diffusivity, generation and dissipation of turbulent kinetic energy and Γ_ω , G_ω and Y_ω are the diffusivity, generation and dissipation of ω . Full expressions for these terms are given in the ANSYS FLUENT theory guide (ANSYS, 2010).

The standard k- ω model accounts for low Re effects in the inner region of the boundary layer but is highly sensitive to the values of k and ω in the free stream. The SST k- ω model couples the standard k- ω model with a modified version of the k- ϵ model via a blending function so that in the near wall region the standard k- ω model solely applies and in the free stream the modified version of the k- ϵ model solely applies with a smooth transition in the region between (ANSYS, 2010).

The transport equations for the SST k- ω model were developed by Menter (1994) and are of a similar form to Equations 3.28 and 3.29. The expressions for the terms Γ_k , G_k , Y_k , Γ_ω , G_ω and Y_ω are different, with different constants and limiters for the turbulent viscosity and production of kinetic energy. The revised model constants are based on experience. The limitations on turbulent viscosity and production of kinetic energy improve predictions in adverse pressure gradients and prevent build-up of turbulence in stagnation regions (Versteeg and Malalasekara, 2007). These expressions are again given in the ANSYS FLUENT theory guide (ANSYS, 2010).

There is also an additional cross-diffusion term in the equation for ω which arises from the modification of the k- ϵ model into equations based on k and ω by substitution of ϵ with $k\omega$. This term is given in Equation 3.30.

$$D_\omega = 2(1 - F_1) \frac{1}{\omega \sigma_{\omega,2}} \frac{\partial k}{\partial x_j} \frac{\partial \omega}{\partial x_j} \quad 3.30$$

where F_1 is a blending function and the empirical constant $\sigma_{\omega,2} = 1.17$.

Through blending both models the SST k- ω model incorporates the advantages from both the standard k- ω model and the k- ϵ model, giving more accurate and reliable predictions for many types of flow, including the flow over an airfoil. It is therefore recommended by ANSYS to use the SST k- ω model rather than the standard k- ω model (ANSYS, 2010).

Further improvements in predictions can be achieved with the Transition SST model which couples the SST k- ω model with two other transport equations, for intermittency and transition onset (Menter et al, 2004). However, use of the Transition SST model requires a very fine mesh to capture the transition correctly and when used with the mesh described later, in Chapter 4, negligible difference was found between this and the SST k- ω model. In addition, the transition region usually constitutes a very small proportion of the flow field and therefore errors from neglecting it are small (Versteeg and Malalasekara, 2007). The SST results presented in this thesis are therefore based on the principles of the SST k- ω model.

3.4.3 Wall Functions

The inner boundary layer near the walls can be divided into three layers, as shown in Figure 3.3. In order to avoid a very fine mesh resolution required to fully resolve the boundary layer near the walls, semi-empirical wall functions based on the work of Launder and Spalding (1974) are used.

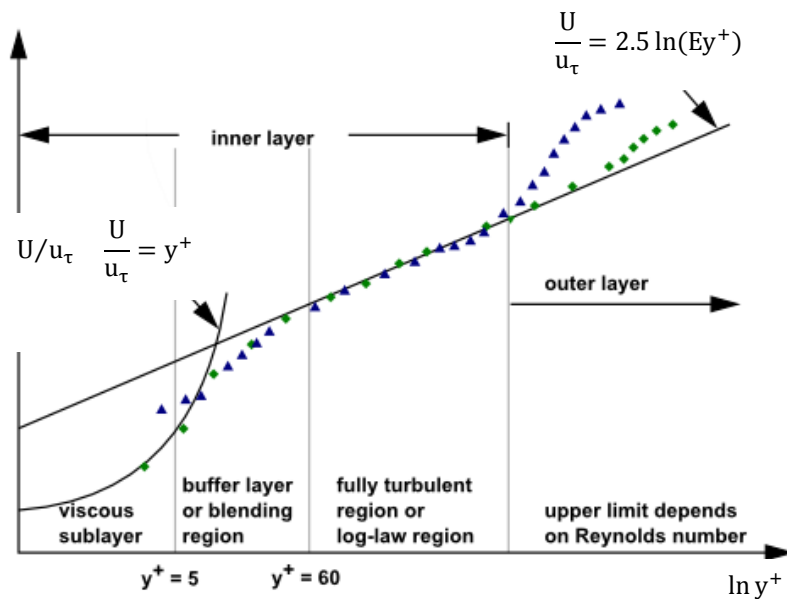


Figure 3.3 Layers of the near wall boundary layer (Adapted from ANSYS, 2010)

The value of y^+ in Figure 3.3 is given by

$$y^+ = \frac{\rho u_\tau y}{\mu} \quad 3.31$$

where u_τ is the friction velocity and is given by

$$u_\tau = \sqrt{\frac{\tau_w}{\rho}} \quad 3.32$$

although the law-of-the-wall for mean velocity is based on y^* since this is approximately equal to y^+ in equilibrium turbulent boundary layers (ANSYS, 2010).

Equations 3.33, 3.36 and 3.37 give the standard wall function for momentum and turbulence which are based on the work of Launder and Spalding (1974). These functions assume a constant shear stress, which is equal to the wall shear stress, and a local equilibrium between the production and dissipation of k , resulting in a logarithmic velocity profile near the wall.

The mean velocity is given by

$$U^* = \frac{1}{\kappa} \ln(Ey^*) \quad 3.33$$

Where U^* is the dimensionless velocity and is given by

$$U^* \equiv \frac{U_p C_\mu^{1/2} k_p^{1/2}}{\tau_w / \rho} \quad 3.34$$

y^* is the dimensionless distance to the wall, given by

$$y^* \equiv \frac{\rho C_\mu^{1/4} k_p^{1/2} y_p}{\mu} \quad 3.35$$

And E is a constant where $E = 9.8$ for smooth walls.

The production of turbulent kinetic energy is calculated from

$$G_k \approx \tau_w \frac{\partial U}{\partial y} = \tau_w \frac{\tau_w}{\kappa \rho C_\mu^{1/4} k_p^{1/2} y_p} \quad 3.36$$

And the dissipation of turbulent kinetic energy is calculated from

$$\varepsilon_p = \frac{C_\mu^{3/4} k_p^{3/2}}{y_p} \quad 3.37$$

These wall functions are applicable to the k-ε models and the RSM model and allow a relatively coarse mesh in the near wall region with an upper limit for y^+ of around 400-500 (Hinze, 1987; Versteeg and Malalasekara, 2007). However, if the mesh is too fine the accuracy of the solution will deteriorate and enhanced wall treatment is required. Enhanced wall treatment is default for the k-ω models as the ω equation can be integrated through the viscous sub-layer. The enhanced wall treatment works by blending the log-law layer formulation with the viscous layer formulation, giving a single wall law for the entire near wall region and therefore maintaining accuracy independent of mesh refinement. The mesh size used for this work means that the standard wall functions are sufficient.

3.4.4 Simulating Rotation

The momentum equation for a non-accelerating frame is given below:

$$\frac{\partial}{\partial t}(\rho \vec{u}) + \nabla \cdot (\rho \vec{u} \vec{u}) = -\nabla p + \nabla \cdot (\vec{\tau}) + \vec{F} \quad 3.38$$

Where an MRF is used to simulate rotation, a rotational component is added to the velocity to give:

$$\vec{u} = \vec{u}_r + \vec{\omega} \vec{r} \quad 3.39$$

Using the absolute velocity formulation, the momentum equation for the flow within the MRF is given in Equation 3.40 (Ansys, 2010) where an additional acceleration term has been added.

$$\frac{\partial}{\partial t}(\rho \vec{u}) + \nabla \cdot (\rho \vec{u}_r \vec{u}) + \rho(\vec{\omega} \vec{u}) = -\nabla p + \nabla \cdot (\vec{\tau}) + \vec{F} \quad 3.40$$

All of the results discussed in this thesis are based on steady state models where density is constant and therefore the first term in Equation 3.40 is neglected.

3.5 FEA

The Static Structural component within ANSYS Workbench was used for the Finite Element Analysis (FEA) models that were coupled with CFD models to create FSI models, as is described in Chapter 4. The Static Structural component calculates the stresses, strains and displacements of a structure under steady loading conditions, using the stress-strain relationships and structural matrices via the finite element method.

The stress-strain relationships for an isotropic linear material at a constant temperature are based on Hooke's Law for elastic behaviour (Ashby and Jones, 1980) and are given below for the x, y and z directions:

$$\varepsilon_x = \frac{\sigma_x}{E} - \frac{\nu}{E}(\sigma_y + \sigma_z) \quad 3.41$$

$$\varepsilon_y = \frac{\sigma_y}{E} - \frac{\nu}{E}(\sigma_x + \sigma_z) \quad 3.42$$

$$\varepsilon_z = \frac{\sigma_z}{E} - \frac{\nu}{E}(\sigma_x + \sigma_y) \quad 3.43$$

$$\varepsilon_{xy} = \frac{\sigma_{xy}}{G} \quad 3.44$$

$$\varepsilon_{xz} = \frac{\sigma_{xz}}{G} \quad 3.45$$

$$\varepsilon_{yz} = \frac{\sigma_{yz}}{G} \quad 3.46$$

E, ν and G are related by:

$$G = \frac{E}{2(1+\nu)} \quad 3.47$$

Linear deformations of elastic materials can be described by the principle of virtual work, which states that the net of internal strain energy and external work due to applied loads must be zero. Therefore, it can be shown that:

$$([K_e] + [K_e^f])\{u\} = [M_e]\{\ddot{u}\} + \{F_e^{pf}\} + \{F_e^{nd}\} \quad 3.48$$

Where $[K_e]$ is the element stiffness matrix, $[K_e^f]$ is the element foundation stiffness matrix, $\{u\}$ is the nodal displacement vector, $[M_e]$ is the element mass matrix, $\{\ddot{u}\}$ is

the acceleration vector, $\{F_e^{pr}\}$ is the element pressure vector and $\{F_e^{nd}\}$ are the nodal forces applied to the element. Full expressions and derivations for these vectors and matrices are given in the ANSYS Theory Reference (ANSYS, 2011a).

The stresses and strains at the integration points are calculated from Equations 3.49 and 3.50 respectively:

$$\{\sigma\} = [D]\{\varepsilon^{el}\} \quad 3.49$$

$$\{\varepsilon^{el}\} = [B]\{u\} \quad 3.50$$

Where $\{\sigma\}$ is the stress vector, $[D]$ is the elasticity or stiffness matrix, $\{\varepsilon^{el}\}$ are the strains that cause stresses, $[B]$ is the strain-displacement matrix and $\{u\}$ is the nodal displacement vector, as before.

4 Numerical Methodology

A series of CFD models were created within ANSYS Workbench to represent the 2, 3 and 4 bladed turbine configurations. These models were used to assess the performance, swirl characteristics and wake recovery and were then coupled with FEA models to investigate the effect of blade deflection on the performance characteristics.

4.1 CFD Geometry Creation

4.1.1 Turbine Geometry

All turbine geometries were created by first importing the .igs file, created by Egarr (et al, 2004) of a 3-bladed turbine with a blade pitch angle of 6° and a diameter of 10 m, shown in Figure 4.1. The number of blades and blade pitch angle were modified to suit, based on previous work carried out at Cardiff University, and the fluid domain was then built around the turbine. The original file was created by joining several faces to form each blade and, rather than merge these faces to form a single face, they were retained to allow additional control when creating the mesh.

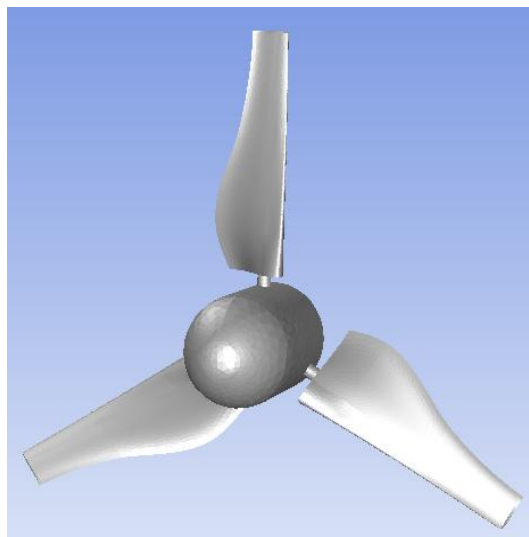


Figure 4.1 Three Bladed Turbine Geometry

4.1.1.1 Two Blades

In the case of the 2-bladed turbine, two of the original blades were removed by highlighting all of their faces and using the function “face delete”. The pin at the root of the remaining blade was also removed in the same way. The remaining blade was then rotated by -3° about the axis through the centre of its pin to give a blade pitch angle of 3° but the same blade profile and twist as the original 3 bladed turbine. The pitch angle of 3° was based on previous work carried out at Cardiff University. A copy of this blade was made and rotated by 180° about the rotational axis of the turbine. Finally the pins were formed by creating a cylinder which extended from the root of the original blade, through the hub, to the root of the copied blade. This merged the blades with the pins and the hub, forming a single body which could be used to represent the 2-bladed turbine, shown in Figure 4.2.

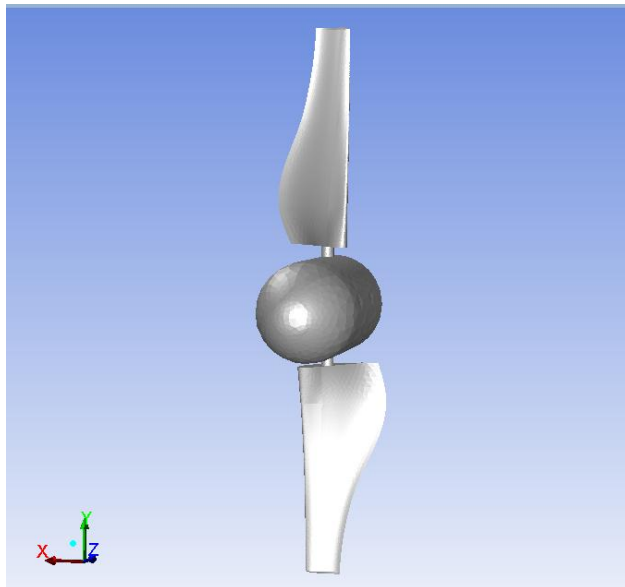


Figure 4.2 Two Bladed Turbine Geometry

4.1.1.2 Three Blades

As stated above, the 3 Bladed turbine geometry was already available from previous work by (Egarr et al, 2004) and no changes were required.

4.1.1.3 Four Blades

The 4-bladed turbine geometry was created in a similar manner to that of the 2-bladed turbine. In this case, the remaining blade was rotated by 3° about the axis through the centre of its pin to give a blade pitch angle of 9° , again with the same blade profile and twist as the 2 and 3 bladed configurations. The pitch angle was again based on previous work. Three copies of the blade were made and spaced evenly about the rotational axis of the turbine, at 90° apart, using the pattern function. Two cylinders were created to form the pins and again, the blades were merged with the pins and hub to create a single body representing the 4-bladed turbine, shown in Figure 4.3.

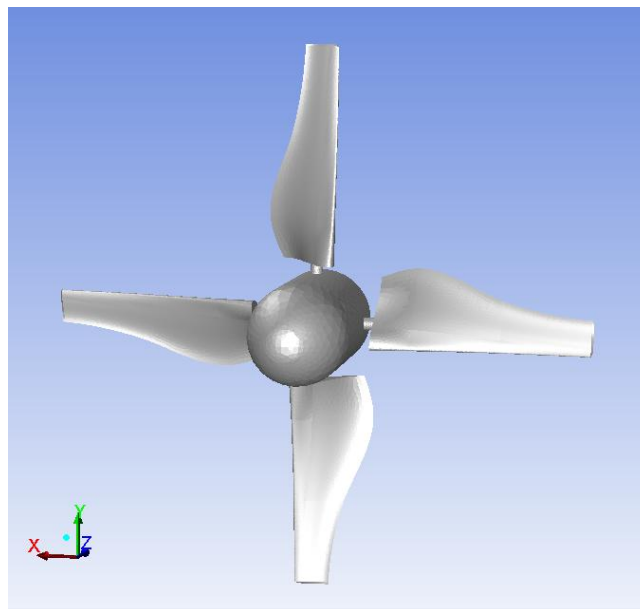


Figure 4.3 Four Bladed Turbine Geometry

4.1.2 Cylindrical Subdomain (MRF)

To simulate rotation of the turbine, a cylindrical sub-domain of 14 m in diameter and 5 m in length was created around the turbine, as shown in Figure 4.4. The turbine was then subtracted from the cylindrical sub-domain using the Boolean function but was suppressed rather than deleted, so that it could be used later for the FSI modelling discussed in Chapter 3.

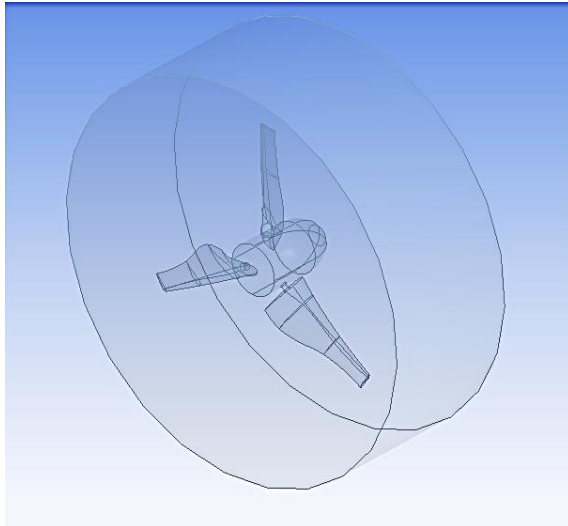


Figure 4.4 Turbine with surrounding cylindrical sub-domain

4.1.3 Main domain

The main domain, surrounding the cylindrical sub-domain, was a 400 m long channel with a square cross section 50 m in width and 50 m in depth. These dimensions were based on previous work by Mason-Jones (2010) which showed that a domain of this size was adequate to isolate the turbine from boundary effects. The cylindrical sub-domain was located within the main domain such that the centre of rotation of the turbine was 100 m downstream of the inlet, 25 m from each side, 35 m from the top and 15 m from the bottom. This location was chosen to allow for future comparisons with previous work where a velocity profile was included (Mason-Jones, 2010). The rotational axis was aligned with the z-axis and also with the direction of the flow. This is shown in Figure 4.5. Additional cylinders were created upstream and downstream of the cylindrical subdomain for the purpose of mesh refinement in these areas. The cylindrical sub-domain was subtracted from the main domain, again using the Boolean function.

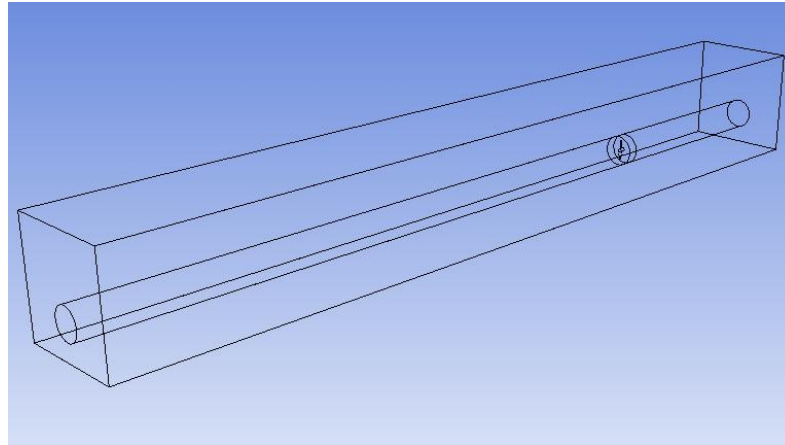


Figure 4.5 Turbine geometry surrounded by cylindrical sub-domain and main domain

4.2 Mesh for CFD models

4.2.1 Global mesh settings

The domain was split into the required control volumes by creating a mesh. The physics preference was set to CFD, with the solver preference set to Fluent. This sets defaults for meshing controls which are most suited to the solver being used, in this case Fluent. When CFD is selected as the physics preference the option to Use Advanced Size Function defaults to “On: Curvature” which refines the mesh based on the change in angle over a surface or edge. This was changed to “On: Proximity and Curvature” where, in addition to changes in angle, the mesh is also refined in areas between two edges, faces or bodies, based on the distance between them. The smoothing setting options are low, medium and high and this determines the number of iterations where nodes are moved to improve the quality of the cells. For the meshes created in this work the setting was medium. The Transition setting affects the rate at which adjacent cells grow and was set to slow to prevent large cells immediately next to small cells which could result in large gradients of flow variables. The Span Angle Centre setting affects the angle each element can span in areas where the mesh is refined based on curvature. The options are coarse, medium and fine and the medium option was selected. The default growth rate of 1.2 was used resulting in an edge length in each layer of cells of 1.2 times the edge length in the preceding layer. Small features in the geometry are removed

according to the defeaturing tolerance which was set to be smaller than the minimum cell size. The mesh metric skewness was used to determine the quality of the mesh where a value of 0 indicates a perfect cell with equal edge lengths, face sizes and internal angles. ANSYS (2010) classifies cells as excellent if they have a skewness of 0-0.25, good with a skewness of 0.25-0.5, fair with a skewness of 0.5-0.75, poor with a skewness of 0.75-0.9 and bad with a skewness of above 0.9. It is recommended by ANSYS (2010) that for 3D modelling, “most cells should be good or better, but a small percentage will generally be in the fair range and there are usually even a few poor cells”.

4.2.2 Turbine Domain

The original .igs file of the turbine geometry consisted of several faces. Each blade comprised 19 faces. These faces were maintained in order to give more control when meshing. Due to the complex geometry of the turbine blades, tetrahedral cells were used. Face sizing was used to specify the cell size on the surfaces of the blades. A size of 0.03m was applied to approximately the outer third of each blade (nearest the tip). The middle third was set at 0.06m and the inner third (nearest the root) was set at 0.09m. These sizes were selected to give a cell density equivalent to that created by Mason-Jones (2010) and shown to be sufficient for mesh independency. This is illustrated in Figure 4.6. The increase in cell density from root to tip allows for a greater number of cells on the faces in the outer third of the blade, where the greatest proportion of pressure differential is present. Typical Y^+ values on the blade surfaces of approximately 300-500 were achieved, which is within the limit for the use of wall functions, as discussed in Chapter 3. The size of the cells on the faces of the hub and the outer faces of the cylindrical sub-domain, Figure 4.7, were also controlled using face sizing, both with a size of 0.1m. These mesh settings, together with the global mesh setting discussed previously in Section 4.1.4.1, resulted in a cell count within the cylindrical subdomain of $\sim 0.9M$ for the 2 bladed turbine models, $\sim 1.4M$ for the 3 bladed turbine models and $1.8M$ for the 4 bladed turbine models.

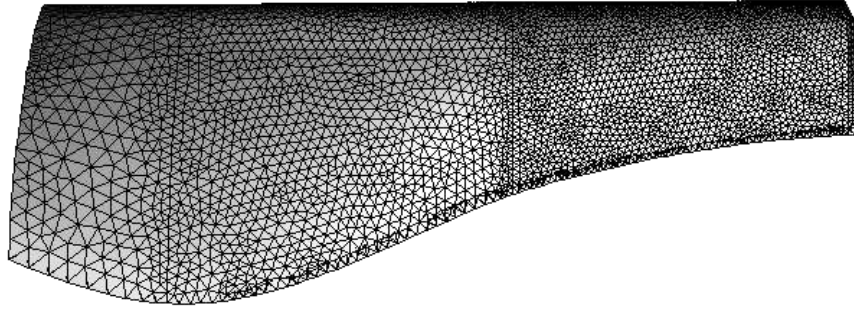


Figure 4.6 Mesh on surface of blade

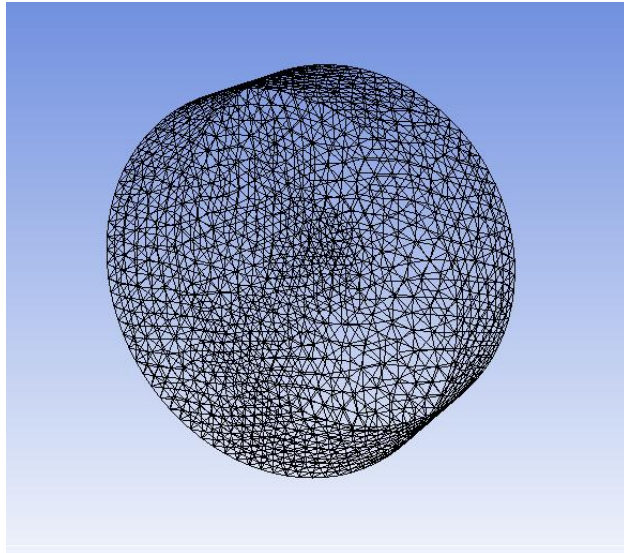


Figure 4.7 Mesh on outer surface of MRF

4.2.3 Surrounding Domain

The main domain was meshed with hexahedral cells which were aligned with the direction of the free stream flow. Face sizing was applied to the inner faces of the main domain, which share a physical location with the outer faces of the cylindrical domain, Figure 4.8. The same size of 0.1m was used to limit poor numerical diffusion across the interface, which is discussed in Section 4.2.4. The cell count for the surrounding domain was $\sim 0.5M$.

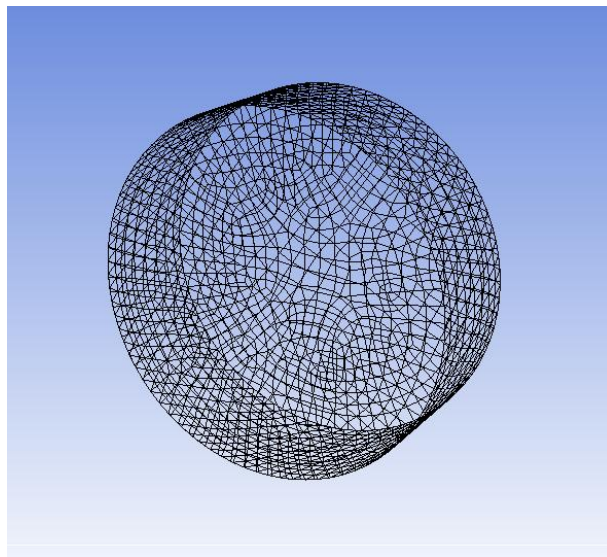


Figure 4.8 Mesh on inner surface of main domain

4.2.4 Named Selections

During meshing, named selections were created to allow boundary conditions to be applied and results to be reported. Each turbine blade was named blade followed by the number 1, 2, 3 or 4, with blade 1 being the blade vertically above the hub and the number increasing with position in an anti-clockwise direction, as shown in Figure 4.9. These names enabled the forces on each blade to be reported. Some of the named selections included key words which are recognised by ANSYS and result in defined boundary conditions being applied to these faces within ANSYS FLUENT. This was the case for the inlet and outlet to the domain which were named inlet and outlet and hence defined as these boundary types. The outer faces of the cylindrical sub-domain were named turbine_interface and the inner faces of the

main domain were named sea_interface. The inclusion of the key word interface in these named selections meant that they were defined as interfaces within FLUENT and could then be easily matched up. The remaining named selections were the turbine hub, named hub, and the outer faces of the domain, named top, bottom and sides.

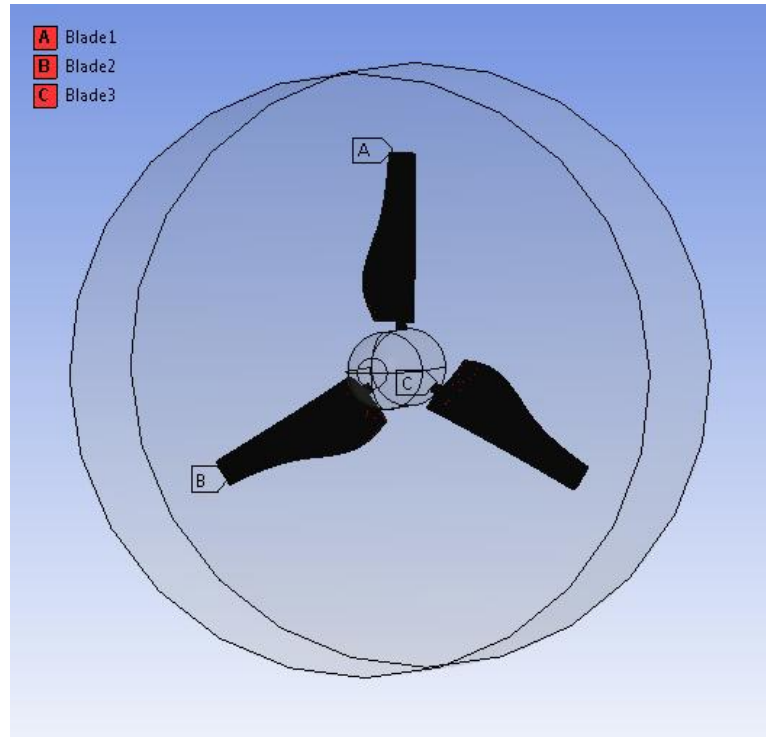


Figure 4.9 Named Selections for Turbine Blades

4.3 CFD Solver Settings

ANSYS FLUENT offers both pressure-based and density-based solvers. Pressure-based solvers were initially developed for low speed, incompressible flows and hence a pressure based solver was used for the work discussed in this thesis.

The gradients of the variables were evaluated using the Least Squares Cell Based method which is more accurate than the Green-Gauss cell-based method and less computationally expensive than the Green-Gauss node-based method. The standard pressure interpolation scheme was used, which interpolates the pressure

at the cell faces using momentum equation coefficients and according to ANSYS (2010), is acceptable for most cases.

The values of the flow variables at the cell faces are interpolated from the cell centre values. The values of momentum were interpolated using the second order upwind scheme, where the face values are found using a Taylor series expansion of the cell centre values. The turbulent kinetic energy, specific dissipation rate, intermittency and momentum thickness Re were found using the first order upwind scheme, where the face values are equal to the cell centre value of the upstream, or upwind, cell.

When iterating the model solution, the difference between the calculated value and the previous value of each variable is multiplied by the under-relaxation factor and added to the previous value to give the solution for the next iteration. The under-relaxation factors, found within the solution controls menu were left at the default values where possible. These were pressure 0.3, density 1, body forces 1, momentum 0.7, turbulent kinetic energy 0.8, specific dissipation rate 0.8, intermittency 0.8, momentum thickness Re 0.8, Turbulent Viscosity 1. Where convergence was not easily achieved, the under-relaxation factors were reduced to improve stability and then increased once the model had stabilised to reduce the computational time required to obtain a full solution.

4.3.1 Viscous Models

The RSM model was shown by Mason-Jones (2010) to be more suitable than the $k-\epsilon$ models and the Spalart-Allmaras model for the application of modelling the HATT also used in this research. The $k-\omega$ SST model has also been widely used for the modelling of HATTs and hence the RSM and $k-\omega$ SST were the viscous models selected for use within this research.

4.3.2 Inlet

The inlet to the domain was set as a velocity inlet with the velocity specification method set as magnitude, normal to boundary, which resulted in the flow being aligned with the rotational axis of the turbine. The velocity magnitude for all models presented in this thesis was 3.086 m/s, or 6 knots, as this is at the higher end of the ideal velocity range (Black and Veatch, 2005). The turbulence specification method was left at the default of k and ϵ with the turbulent kinetic energy and the turbulent dissipation rate both left at the default values of $1 \text{ m}^2\text{s}^{-2}$ for the former and $1 \text{ m}^2\text{s}^{-3}$ for the latter. This was due to the lack of turbulence data available and the knowledge that the turbulence would likely decay significantly from the inlet to the turbine location.

4.3.2.1 Reynolds Specification Method for Inlet

Where the RSM was used as the viscous model and hence a Reynolds-stress specification method was required, this was set as k or turbulent intensity as the individual values of the Reynolds stresses were unknown.

4.3.3 Outlet

The outlet from the domain was set as a pressure outlet with a gauge pressure of 0 Pa. The backflow direction specification method was set as normal to boundary and the turbulence specification method and related values were the same as for the inlet. Again where the RSM was used, the Reynolds-stress specification method was set as k or turbulent intensity.

4.3.4 Wall conditions

The outer boundaries of the models were set as stationary walls with default roughness values but the shear condition was set to specified shear with shear stress components of 0 Pa in all directions for all boundaries.

4.3.5 Material Properties of fluid

In addition to the default of air, the material water-liquid was created by copying it from the ANSYS FLUENT database. The density was changed to 1025 kgm^{-3} to represent sea water. The material for use was then specified by changing the material name from air to water-liquid for each zone in the cell zone conditions.

4.3.6 Rotation of Turbine Using MRF

Rotation of the turbine was simulated by selecting frame motion in the cell zone conditions for the cylindrical sub-domain named turbine. The rotation-axis origin was set as 0, 0, 0 and the rotation-axis direction was along the z axis. The rotational velocity was varied to cover the operational range of the turbine while the translational velocity was set to 0 ms⁻¹ in all 3 directions. The frame motion simulates rotation by imparting a rotational acceleration component to the fluid within the domain to which it is applied, as discussed in Chapter 3.

4.3.7 Convergence Monitoring

All steady state models were iterated until the residuals had stabilised rather than setting a convergence target. In addition to the residuals, convergence was also monitored by creating a point downstream of the turbine and plotting the axial component of velocity at this point using the area weighted average methodology.

4.4 Post processing

4.4.1 Extracting Torque

The torque was extracted from each model by setting up a force report and selecting the moments option. The moment centre was set as 0, 0, 0 and the moment axis was set as the z axis. Each blade and the hub were selected as the wall zones and the results were printed to the text user interface where the torque resulting from each blade and the hub was displayed separately as well as the net torque for the whole turbine.

4.4.2 Calculating turbine power

The power was then calculated by multiplying the total torque by the rotational speed of the turbine. It should be noted that the theoretical maximum extractable power is 59% of the available upstream power, as shown by Betz (1966).

4.4.3 Extracting Axial Loads

The axial load was extracted by setting up a force report and selecting the forces option. The direction vector was set as the z axis and again the blades and the hub

were selected as the wall zones. Again the results were printed to the text user interface and the axial load on each blade and the hub was given as well as the net axial load.

4.4.4 Calculation of Swirl Number

Planes were created at a range of downstream distances from the turbine, over which the swirl number was calculated. These planes were perpendicular to the rotational axis of the turbine. Plots of axial and tangential velocity were created for each of these planes. These plots were then opened in Microsoft Excel and a simple formula was used to determine whether each cell was within the swept area of the turbine based on its x and y coordinates. Values of axial and tangential velocity for those cells determined to be within the swept area of the turbine were then used to calculate the swirl number using Equation 3.7.

4.5 FSI models

The hydrodynamic forces acting on the blades, whilst also resulting in a torque which causes the turbine to rotate, may also cause the blades to deform. The deformation of the blades will change the flow field around the turbine which in turn will alter the hydrodynamic forces. The CFD models were coupled with FEA models to predict the deformation of the blades and the resulting change in hydrodynamic forces.

The hydrodynamic forces calculated by the CFD were transferred to the FEA models where the blade deformations were then calculated. The models were two-way coupled to allow the blade deformations calculated by the FEA to be transferred back to the CFD where the flow field was updated. This process was iterated until the changes in the flow field and the blade deformations were within the defined convergence criteria.

4.5.1 Modifications to CFD models

Existing CFD models, discussed in Sections 4.1-4.4 were used with dynamic meshing enabled. The turbine blades were selected and set as dynamic mesh zones with the System Coupling option. The cylindrical MRF was also set as a dynamic mesh zone but with the Deforming Zone option. These settings allowed the mesh on the

surface of the blades to move and also the surrounding mesh to deform to allow for the movement. The updated fluid mesh was controlled using both smoothing and remeshing to prevent negative cell volumes within the proximity of the turbine blades. Depending on model convergence either the Spring smoothing method or the Diffusion smoothing method was used. With the spring smoothing method the displacement of each node is opposed by a force which is proportional to the distance. The damping of the springs is controlled by the spring constant factor which is between 0 and 1 with 0 being no damping. This was set to 1. Diffusion smoothing offers more control over which areas of the mesh are allowed to deform. Areas with low diffusivity are allowed to deform more. A diffusion parameter is specified which determines the diffusivity of a cell based on either its distance from the moving boundary or its volume. This means that a higher mesh quality can be preserved near the moving boundary or in areas of high cell density and therefore generally results in a better mesh than when the spring smoothing method is used, but at a higher computational cost. Where the Diffusion method was used the boundary-distance option was selected for the diffusion function with a diffusion parameter of 1.5. When achieving convergence was problematic remeshing was also enabled, where local cell remeshing was selected with the minimum and maximum length scales taken from the mesh scale information panel. This instructs ANSYS FLUENT to mark any cells which have length scales outside minimum and maximum values specified or skewness above the maximum allowable skewness. The marked cells are then remeshed if their quality is improved. If remeshing the marked cells would not produce a mesh with improved cell quality, then local zone remeshing is performed where the entire zone adjacent to the moving boundary is remeshed (ANSYS, 2010).

4.5.2 FEA models

4.5.2.1 Geometry

The geometries used in the FEA models were the 2, 3 and 4 bladed turbine geometries created in preparation for the CFD models and described in Section 4.1.1.

4.5.2.2 Mesh

The mesh for the FEA models was again controlled by the use of face sizing. Since the mapping was dependent on having cells of a similar size on the coupled faces, the mesh on the surface of each blade was assigned a face size of 0.09, Figure 4.10.

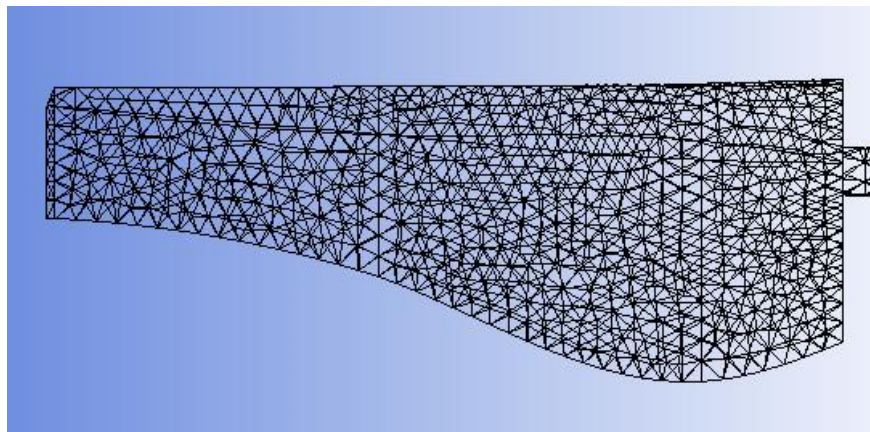


Figure 4.10 Blade surface mesh in FEA models

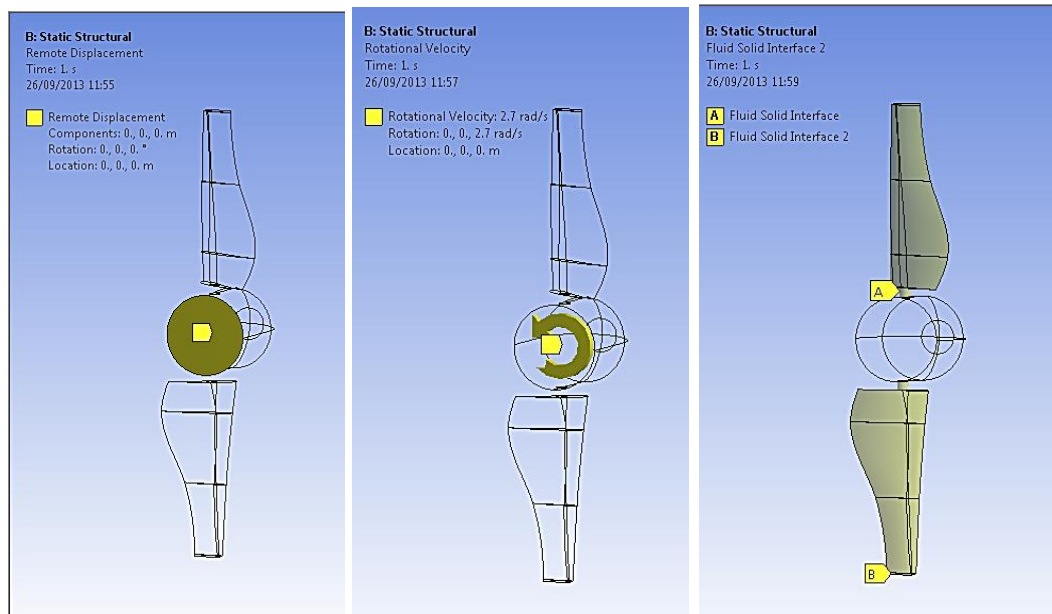
4.5.2.3 Materials

Although it is unlikely that the blades of full size turbines will be a solid, homogeneous material, no information on blade construction was available for this

research. Hence, the blades were modelled as solid bodies for simplicity of the FEA models. The materials used for blade construction are likely to include composites but since no information on material properties was known, materials available for use within ANSYS, such as steel and aluminium, were selected and the Young's modulus changed to vary the stiffness and allow a change in deflection. Therefore the stresses and strains calculated may be unrealistic. However, the main area of interest was the predicted effect of blade deflection on the performance characteristics of the turbine and as such these limitations were deemed acceptable.

4.5.2.4 Constraints and Loads

The model was constrained by applying a remote displacement to the rear face of the hub as illustrated in Figure 4.11a. This was set with a displacement of 0 m in the x, y and z directions and a rotation of 0° about the x, y and z axes. A rotational velocity matching that of the MRF in the CFD model was applied to the whole body of the turbine so that although the turbine did not physically rotate, the effect of the centrifugal forces was still accounted for, Figure 4.11b. To enable the loads to be transferred from the fluid model to the structural model, the surfaces of each blade were assigned as Fluid Solid Interfaces, Figure 4.11c.



(a) Remote displacement (b) Rotational Velocity (c) Fluid Solid Interfaces

Figure 4.11 Constraints and Loads

4.5.3 System Coupling

To enable a 2-way coupling analysis the ‘System Coupling’ procedure was used within ANSYS. This process solves the CFD model to an acceptable or predefined residuals convergence tolerance and provides the hydrodynamic forces exerted on the blades via the fluid-solid interfaces. Following convergence of the CFD model the structural model is started within the system coupling and the hydrodynamic forces are transferred to the structural model, which in turn iterates the solution to convergence and, for the specified material properties, provides the displacement of the blades. The displacement results were then fed back to the CFD model where the mesh is once again deformed via system coupling mesh deformation and the spring damping/smoothing options as previously discussed. This process is then re-iterated via the system coupling (ANSYS, 2011b).

4.5.3.1 Data Transfers

Two data transfers were created for each turbine blade. One of these was to transfer the forces from the fluid model to the structural model and the other was to transfer the displacement from the structural model to the fluid model. The

ANSYS component system from which the data are transferred is known as the “source” and the component to which it is transferred is known as the “target”. The data transfers involved three steps; mapping, interpolation and interpolated data post-processing (ANSYS, 2011b).

4.5.3.2 Mapping

Mapping is the first step in the process of transferring data from one ANSYS component system, e.g. FLUENT, to another, e.g. Mechanical. It involves matching nodes within each mesh to generate weights. ANSYS uses the Bucket Surface mapping algorithm for transferring displacement from Mechanical to FLUENT and the General Grid Interface (GGI) mapping algorithm for transferring forces from FLUENT to mechanical.

The Bucket Surface algorithm divides the target mesh into a relatively coarse grid of groups of cells, known as buckets. Each node on the source mesh is then assigned to a bucket. It is then mapped to an element within the bucket based on a proximity tolerance and the weighting is obtained by evaluating the shape function associated with the element. Any nodes which do not fit the proximity tolerance are reported as unmapped but are still in reality mapped to the nearest node.

The GGI algorithm splits each element face on the surfaces to be mapped into sub faces. The number of sub faces is equal to the number of nodes on the face. The sub faces from the source and target surfaces are intersected and the overlapping areas create a number of control surfaces as shown in Figure 4.12, where S1 and S2 are sub faces on the surface which is sending data, R1 and R2 are sub faces on the surface receiving data, and A1, A2 and A3 are control surfaces. The areas of the control surfaces are used to calculate the mapping weights. The weights associated with sub face R1 are found according to Equations 4.1 and 4.2, taken from ANSYS (2011b) with similar equations used to find the weights for all of the other sub faces. Unlike the Bucket Surface mapping algorithm, any areas of the target mesh that are unmapped are assigned a value of 0.

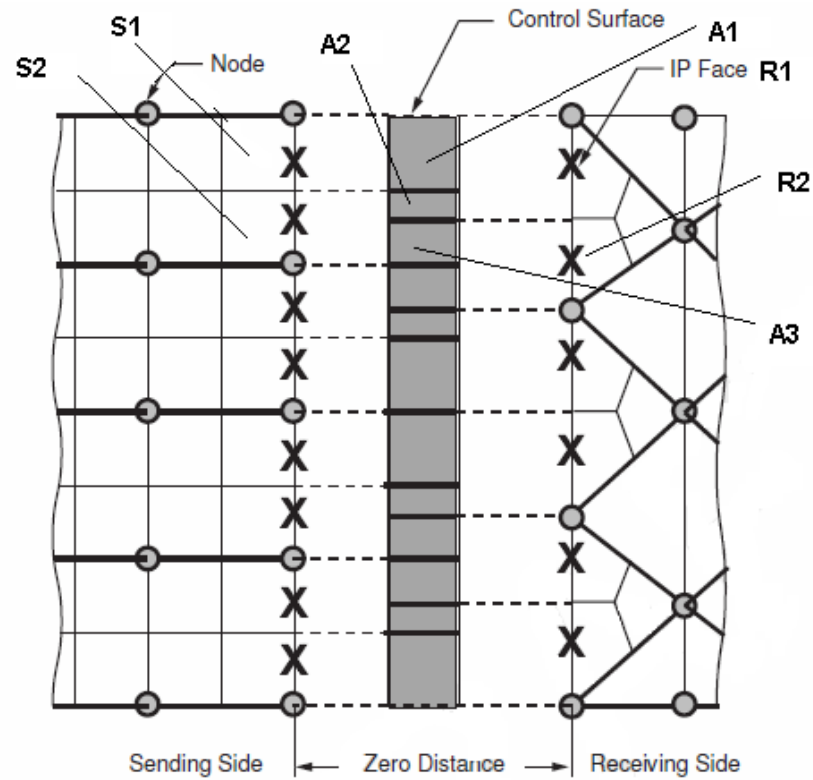
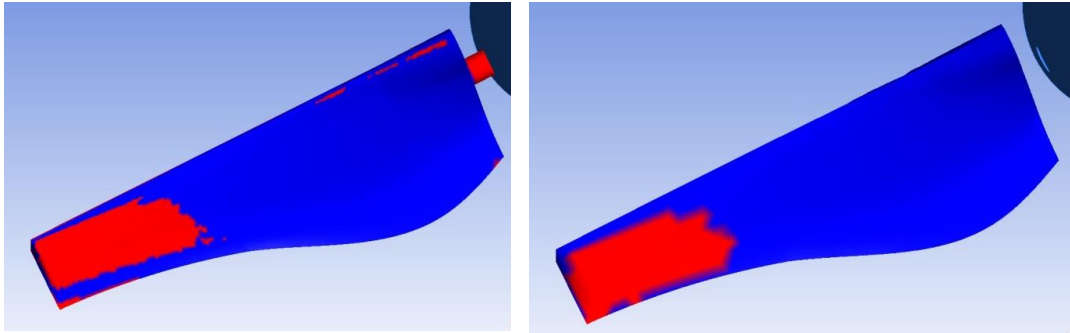


Figure 4.12 General Grid Interface Mapping (ANSYS, 2011b)

$$w1 = \frac{A1}{A1} \quad 4.1$$

$$w2 = \frac{A2}{A2+A3} \quad 4.2$$

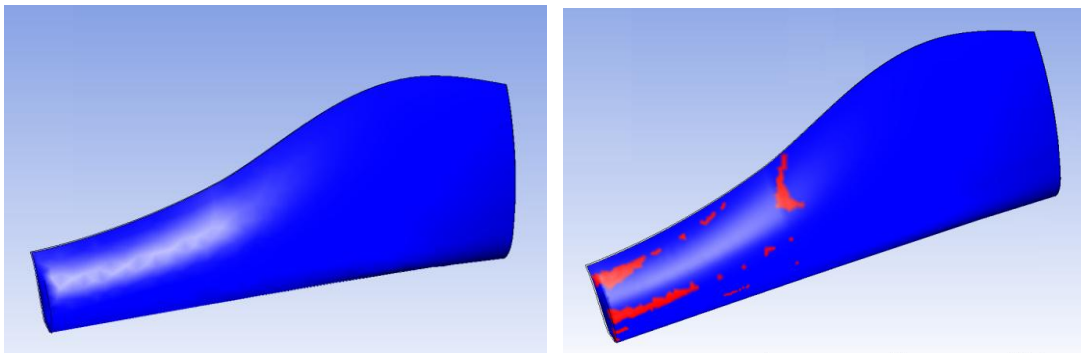
A mapping summary was provided at the beginning of each analysis, stating both the percentage of nodes and the percentage of the area that were mapped. A visual assessment of the mapping was also possible via the beta feature “DumpInterfaceMeshes”. This allowed the mapped and unmapped areas of each blade to be displayed in CFD post. Figure 4.13 shows an example of poor mapping where the mesh settings used for the CFD model were those discussed in Section 4.2 and the cell size in the FEA model was 0.2. The FEA mesh used for the models discussed in this thesis resulted in 95% of the area being successfully mapped, as shown in Figure 4.14. This was considered sufficient since the actual magnitude of deflection was not the main focus but rather the effect of the deflection on the performance characteristics of the turbine.



(a) Source

(b) Target

Figure 4.13 Example of poor mapping where unmapped cells are shown in red.



(a) Source

(b) Target

Figure 4.14 Mapping achieved in FSI models where unmapped cells are shown in red.

4.5.3.3 Analysis Settings

The coupling sequence was set up such that the FEA model was solved first, followed by the CFD model.

5 Flume Testing and Model Validation

In order to validate the CFD models described in Chapter 4, a prototype turbine was developed and tested in a recirculating flume. This chapter describes the prototype turbine and the testing undertaken. Although the prototype was designed and developed at Cardiff University and the author participated in testing; flume calibration, dynamometer calibration and blockage correction calculations were undertaken by Sian Tedds at the University of Liverpool.

5.1 Flume Specifications

All testing was carried out in the recirculating flume at the University of Liverpool.

Figure 5.1 gives a schematic of this flume.

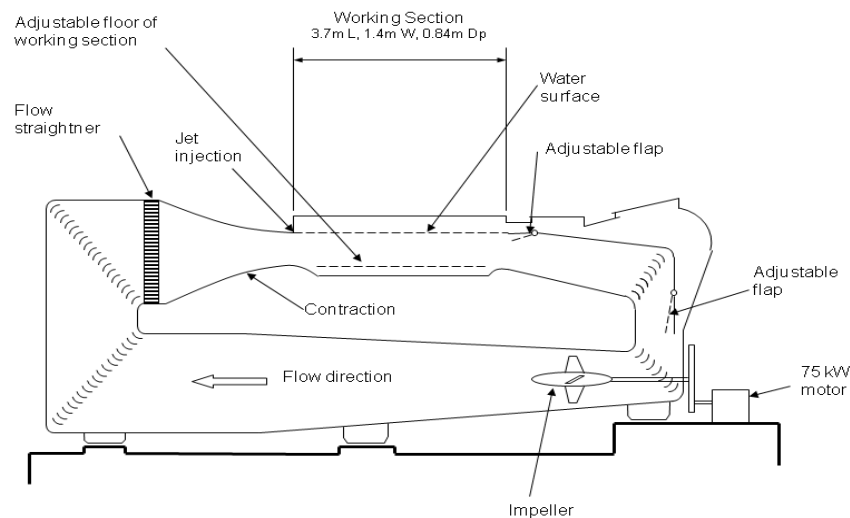


Figure 5.1 Schematic of Recirculating Flume at the University of Liverpool

The working section of the flume is 1.4 m in width and 4 m in length with a depth range up to 0.85 m and can be operated as an open channel or an enclosed channel. All of the tests were carried out with the open channel set-up, at the maximum depth of 0.85 m. To remove the water surface velocity deficit caused by air drag, a plane jet is used at the entrance to the working section. This jet is located at the water surface and spans the width of the working section. At the inlet to the working section there is a flow straightener to ensure that the flow is uniform.

5.2 Improvements made to turbine design

Following previous testing of the turbine described in Mason-Jones (2010) and shown in Figure 5.2, an improved turbine was developed. The data from the tests using the initial turbine showed a high level of scatter and the main causes of this were given by Mason-Jones (2010) as insufficient distance between the rotational plane of the turbine and the support stanchion and the two types of coupling used to connect the turbine to the motor (Figure 5.3), which was located above the surface of the water.



Figure 5.2 Previous turbine design

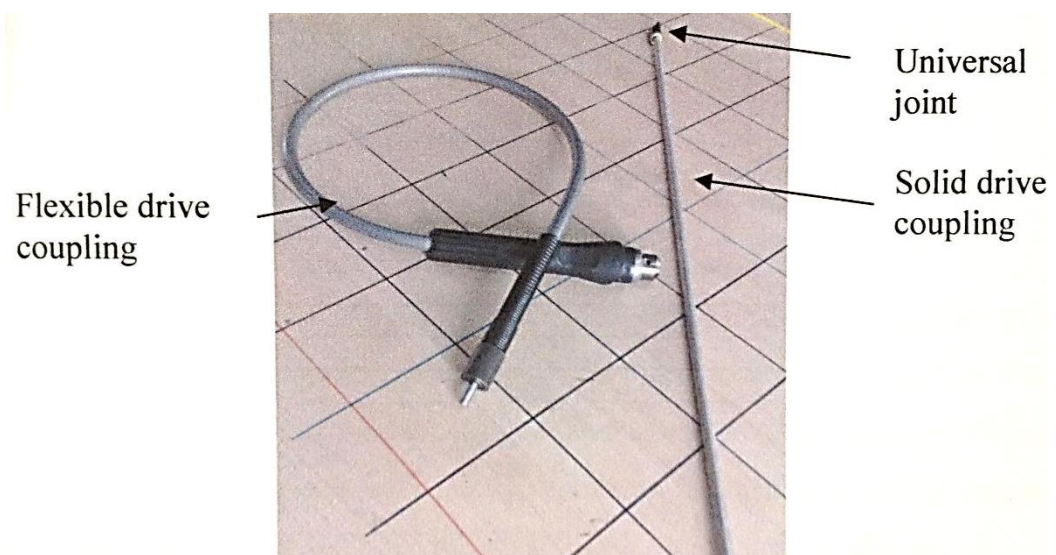


Figure 5.3 Couplings used to connect the previous turbine to the motor

Therefore, during the development of the improved turbine, the length of the nacelle was increased so that the distance between the rotational plane of the turbine and the front of the support stanchion was 3 hub diameters. Also, a new, physically smaller motor was used and housed within the nacelle to allow for a fixed drive shaft to be used due to the alignment of the turbine and the motor (Figure 5.4). The power and encoder cables were connected through the rear of the nacelle using gland seals to prevent water ingress. The replacement motor was a Baldor Brushless AC Servomotor. This motor was selected as its physical size allowed it to be housed within the nacelle. However, it was subsequently found that it cut out at a lower torque than the peak torque generated by the turbine due to overheating. As such data for the entire operating range of the turbine could not be obtained. The control system was the same used with the original turbine and is described in detail in (Mason-Jones, 2010).

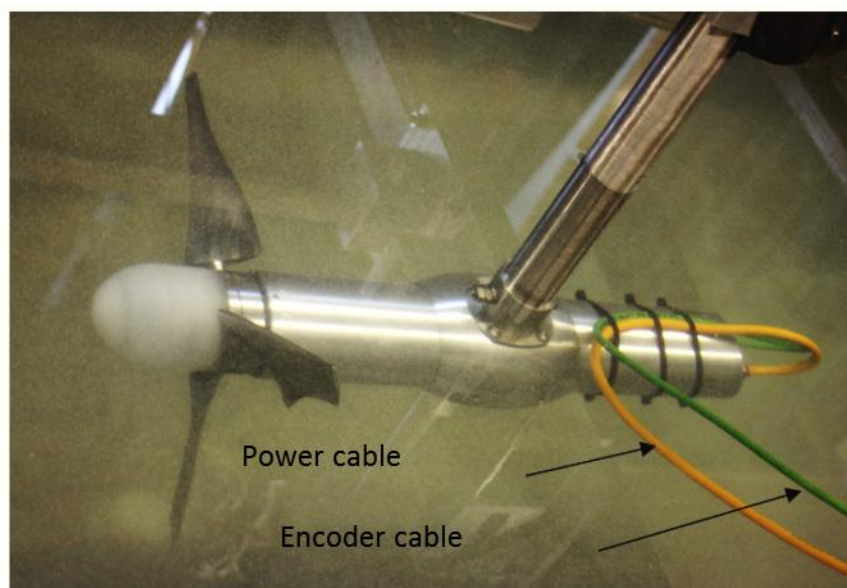


Figure 5.4 Improved turbine design during testing

5.3 Blade Design

The blades used during testing were those used by (Mason-Jones, 2010). The profile of the blade is a variant on the Wortman FX63-137, shown in Figure 5.5. The chord length is 0.03 m at the blade tip and 0.08 m at the root with a twist of 35° along

the length of the blade. The length of the blade is 0.2 m giving a turbine diameter of 0.5 m and a blockage ratio of 0.17. A pin of 32 mm in length and 15 mm in diameter allows the blades to be clamped to the hub in configurations of 1,2,3,4 and 6 blades. The 3 bladed configuration was used for testing. The centre of the pin is 22 mm from the leading edge.

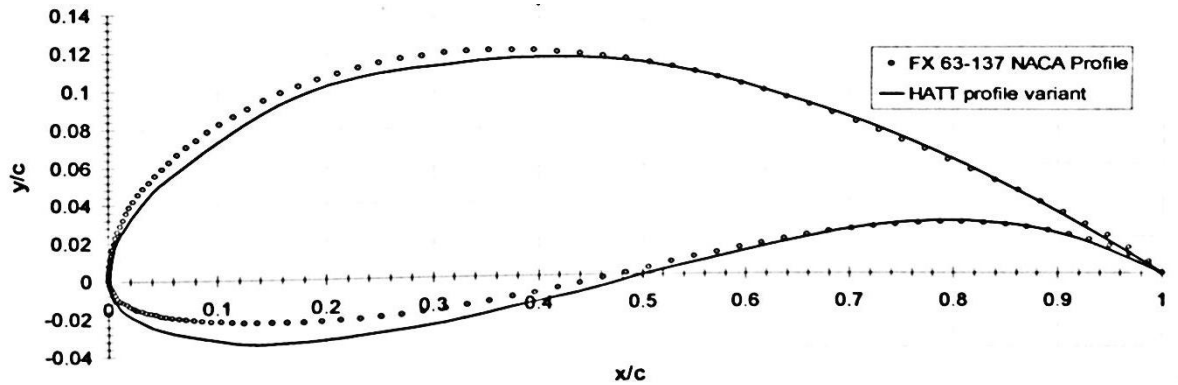


Figure 5.5 FX 63-137 profile and profile of HATT used in this work

5.4 Pitch Angle Setting

The pitch angles were set using the precision machined blocks described by Mason-Jones (2010) and shown in Figure 5.6. The optimum pitch angle setting had been calculated and verified by Maon-Jones, (2010) as 6° for the 3 Bladed turbine, hence this was the setting used for the testing.

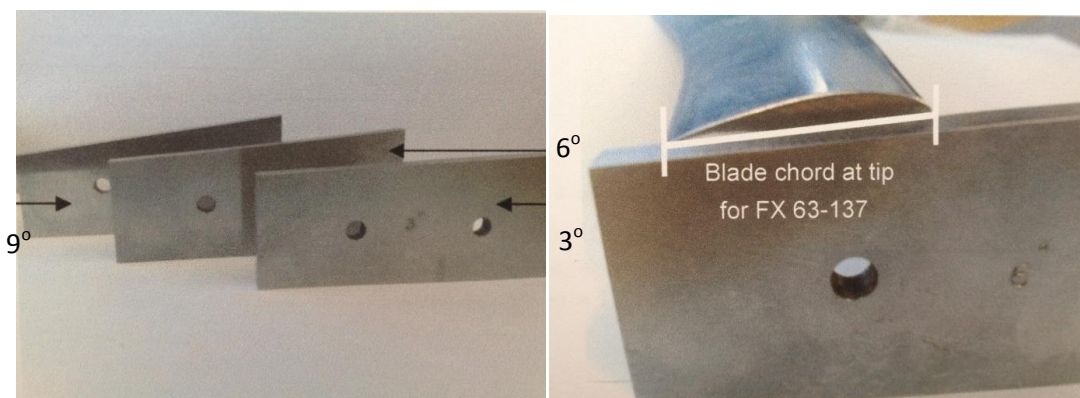


Figure 5.6 Precision machined blocks with blade tip chord aligned with 6° block

5.5 Location of HATT within Flume

The turbine was located at the centre of the flume cross-section i.e. midway through the depth and midway across the width and approximately half-way along the length of the working section.

5.6 Flume Velocity

The maximum flow velocity of the flume is 6ms^{-1} with the tests described here carried out at the dial setting which equates to 1m/s . At this flow velocity, the performance characteristics of this turbine have been shown to be independent of Reynolds number (Mason-Jones et al, 2012). An Acoustic Doppler Velocimeter (SonTek/YSI 10-MHz ADV) was used to measure the free-stream velocity within the flume. This was done with the channel empty and with the turbine in place to determine any reduction in velocity due to the extra resistance caused by the turbine. Measurements were taken at 1.5 m (3 turbine diameters) upstream of the turbine at freewheeling and at the maximum power measured. The sampling rate was 25 Hz and approximately $10\,000$ velocities were measured with an estimated statistical uncertainty of 1% , although ADV system is accurate to approximately $\pm 5\%$ of the resultant velocity (Tedds et al, 2011). Figure 5.7 shows the measured free-stream water-channel velocity (U_{ADV}) versus the nominal free-stream water-channel velocity (U_f) as per the dial setting.

The empty channel data is slightly higher than the dial setting with a least squares fit giving a slope of 1.03 . In addition it can be seen that the presence of the turbine reduces the velocity in the channel to around 94% of the dial setting.

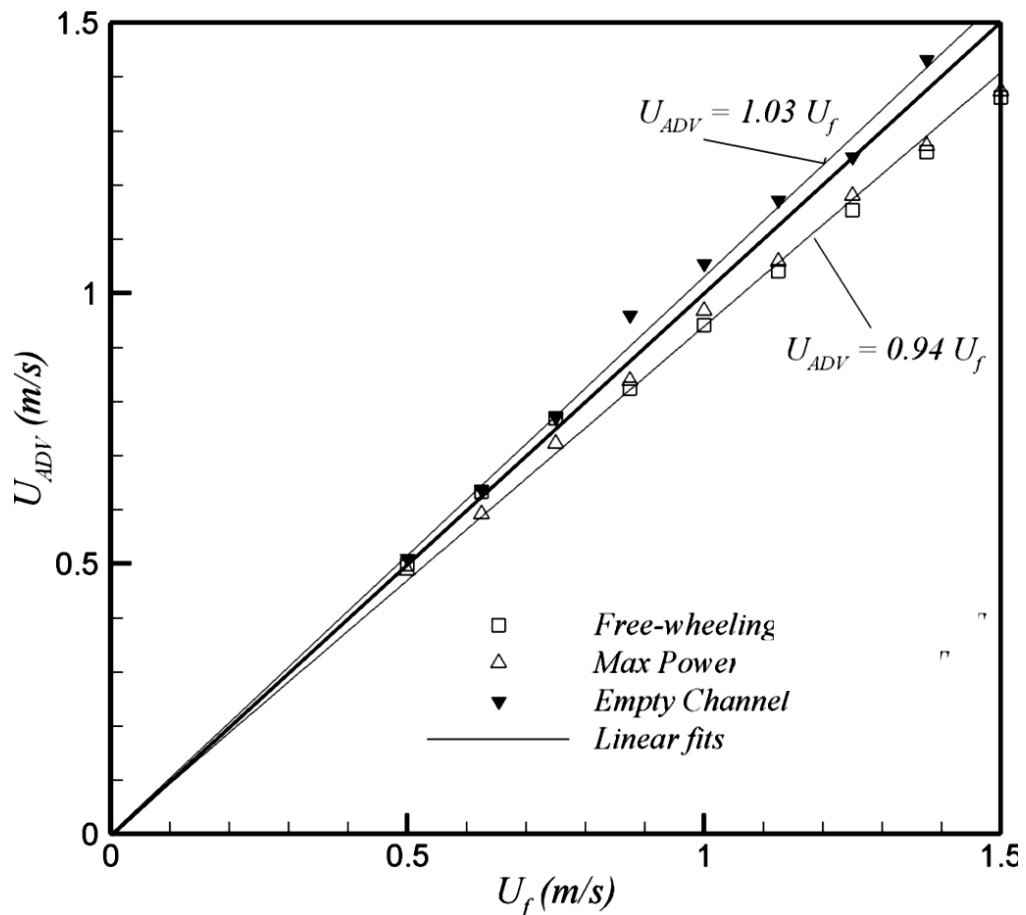


Figure 5.7 measured free-stream water-channel velocity (U_{ADV}) versus the nominal free-stream water-channel velocity (U_f) as per the dial setting

5.7 Thrust Load measurement

The thrust on the HATT was measured using a 50 kg strain gauge dynamometer. The design of this dynamometer is described in detail in Milward and Rossiter (1983). The force block was calibrated by applying a mass with an Instron model 5582 machine. Mass was applied from 5 kg to 50 kg in steps of 5 kg. It is estimated that this produced a calibration which is accurate to about 1%.

5.8 Test Procedure

During testing the turbine was first allowed to freewheel before an opposing torque was applied via the programme written by Mason-Jones (2010) using the software package MintMT within WorkBench v5. This programme allowed the opposing torque to be increased incrementally whilst capturing the rotational speed of the

turbine via the encoder at each torque setting. To ensure the rotational speed of the turbine had stabilised at each setting, the torque was held constant for a period of 5 s before data was collected for a period of 120 s. The sample rate was 0.92 Hz, giving 110 data points at each torque setting. Figure 5.8 and Figure 5.9 show the measured current and angular velocity, demonstrating the incremental increases in current, and hence torque, and the associated incremental reductions in angular velocity.

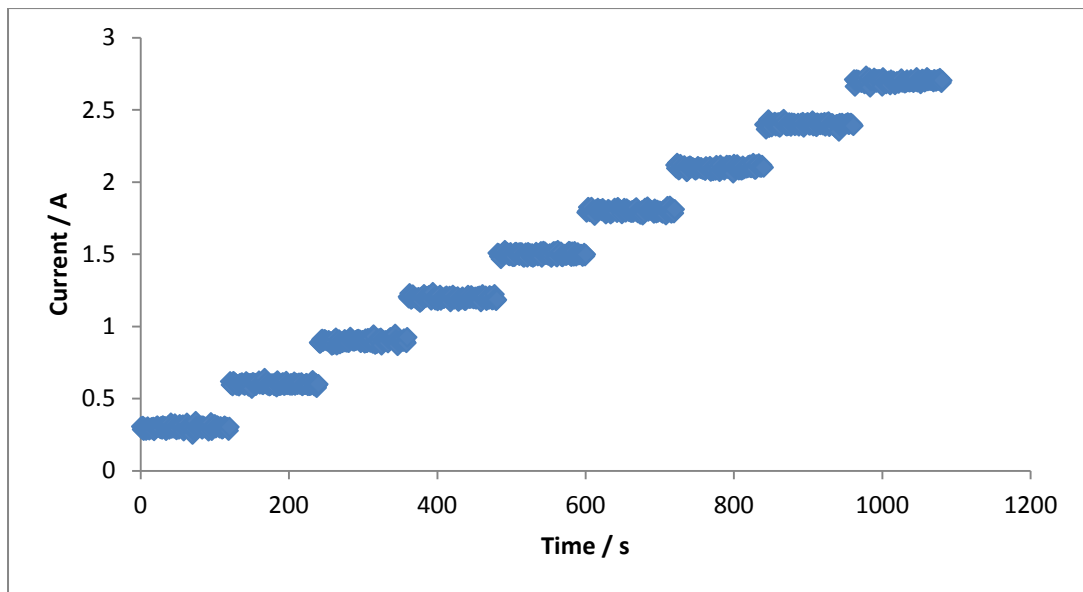


Figure 5.8 Current vs time from experimental testing

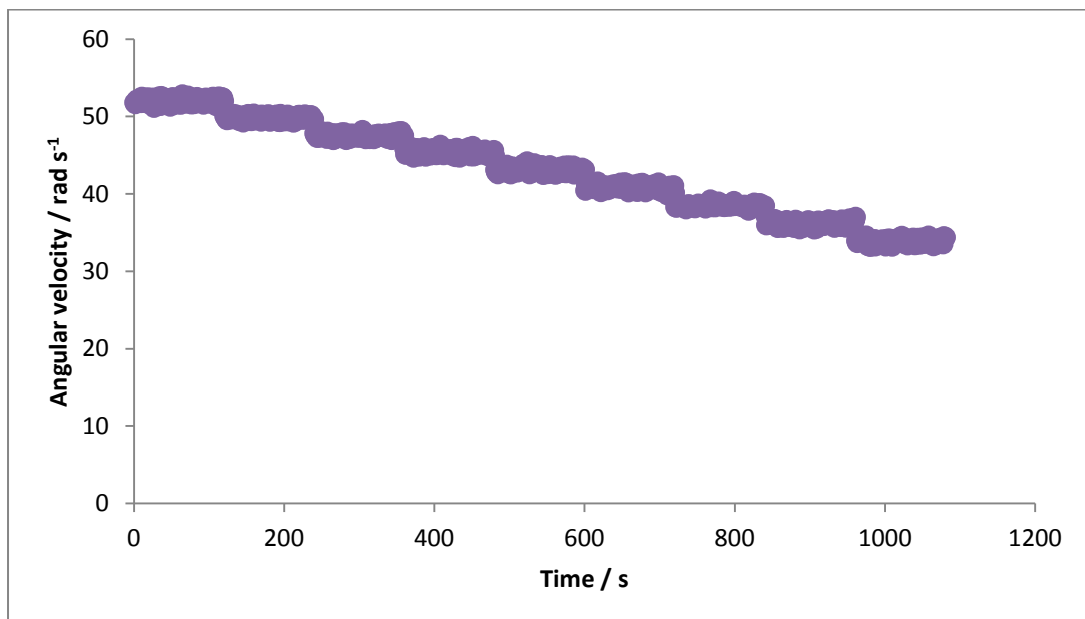


Figure 5.9 Angular velocity v time from experimental testing

5.9 Reduction in Scatter

Figure 5.10 compares the raw data from these tests (referred to as new data) with those from the tests using the previous prototype HATT (referred to as old data) as undertaken by Mason-Jones (2010). The electrical current data follows the same trend although the new data begins at a lower electrical current. The increments in electrical current are the same and the increasing separation of the data sets is simply due to the differing test duration since it was possible to run these tests for a far longer time period as the drive shaft issues discussed previously had been overcome. However, the old data reaches a maximum electrical current of around 3.6 A, whereas the new data ends at around 2.7 A. This is because the motor cut out above this current due to overheating.

The new angular velocity data show greatly reduced scatter in comparison with the old data. As discussed above, this is due to the increased distance between the rotor and the support stanchion and the fixed drive shaft. The minimum angular velocity is higher for the new data due to the lower electrical current at which the motor cut out. In addition, the torque constant of the motor is smaller meaning a larger electrical current would be required to achieve the same reduction in angular velocity.

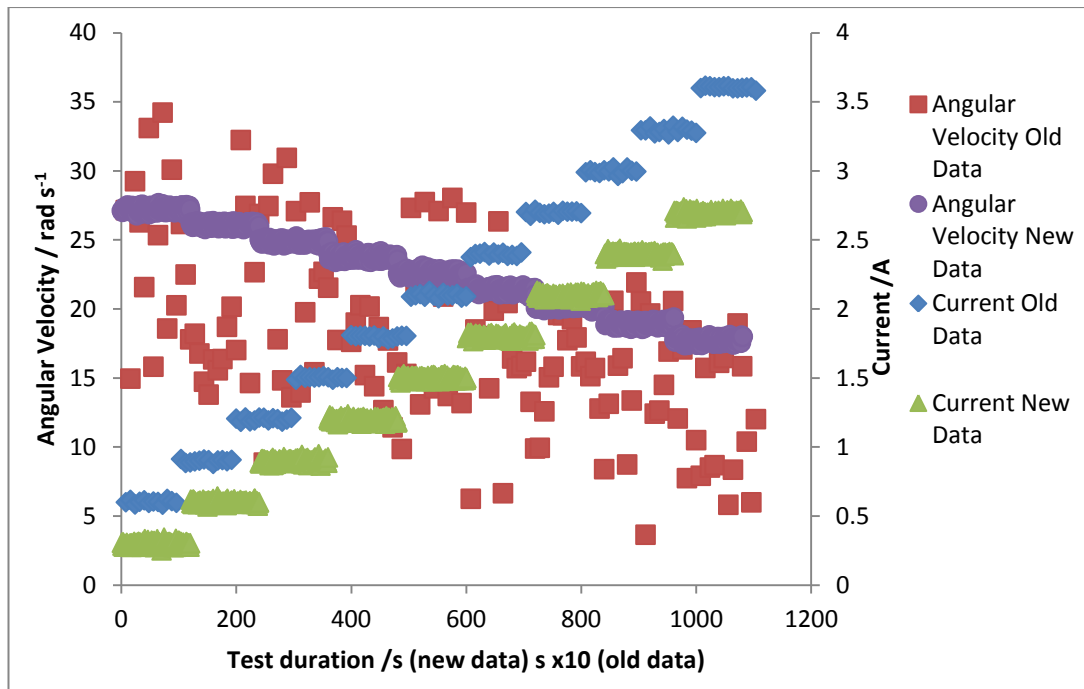


Figure 5.10 Comparison of experimental data with that from the previous turbine design

5.10 Power Measurements

The experimental data were used to calculate the power output of the turbine. The power and angular velocity were then non-dimensionalised to give C_p and λ , based on the upstream value given by the ADV. Figure 5.11 gives the mean C_p for each sample period, based on the mean ADV value and free stream velocities of 1% above and below this value. It is clear that C_p is very sensitive to the free stream velocity, with a maximum difference of 5% in C_p for a 2% difference in U due to the available power being proportional to the cube of the flow velocity.

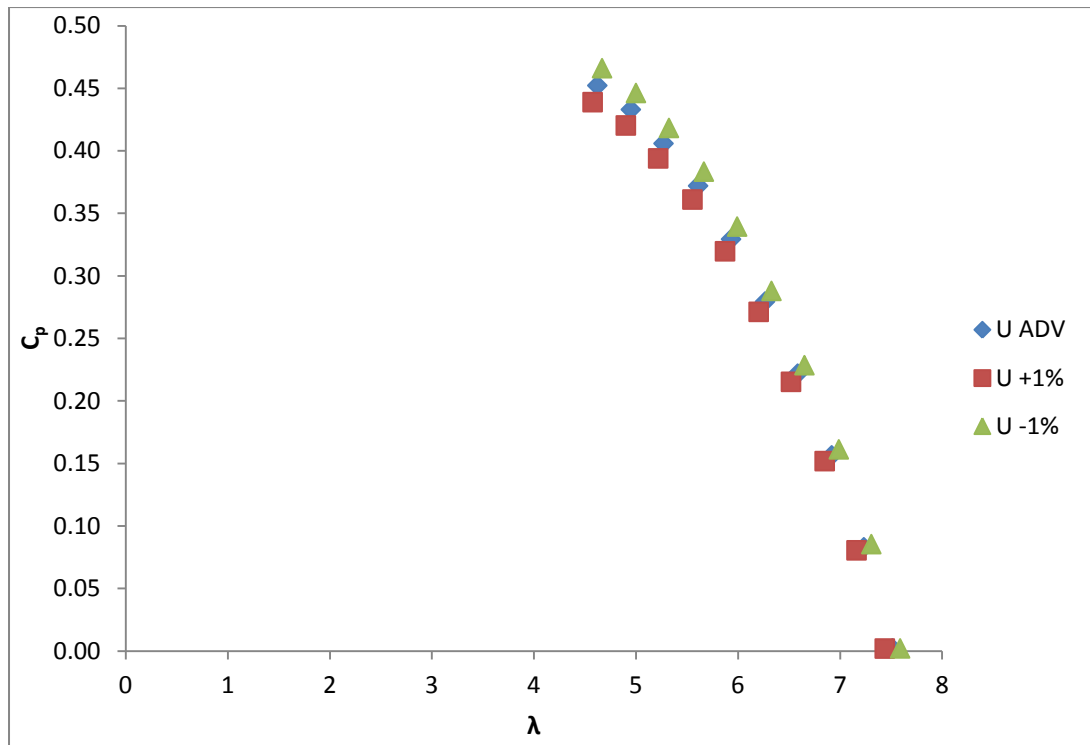


Figure 5.11 C_p vs λ from experimental data

The C_p values given in Figure 5.11 do not account for the blockage effects of the flume. A blockage correction factor U_t/u of 0.96 was calculated for this HATT and flume, based on the work of Bahaj et al (2007b). When corrected for blockage the experimental C_p values reduce to those given in Figure 5.12.

The results of the CFD models developed in this work are also given in Figure 5.12 and show very good correlation with the experimental data, although a comparison is only possible at $\lambda = 4.4$ and above which does not include peak C_p . The results of the RSM model show particularly close correlation with a difference at $\lambda = 4.4$ of 0.1%. Given the inherent error within the ADV system, the results of the SST model are also considered good and at $\lambda = 4.4$ the difference is 6.3%. The differences between the CFD results will be discussed later, in Chapter 6. The experimental data from these tests also compare well with the experimental data of Bahaj et al (2007b), which are based on cavitation tunnel and towing tank tests of a 0.8 m diameter, 3 bladed HATT and give a peak C_p of between 0.41 and 0.46 for optimum pitch angle.

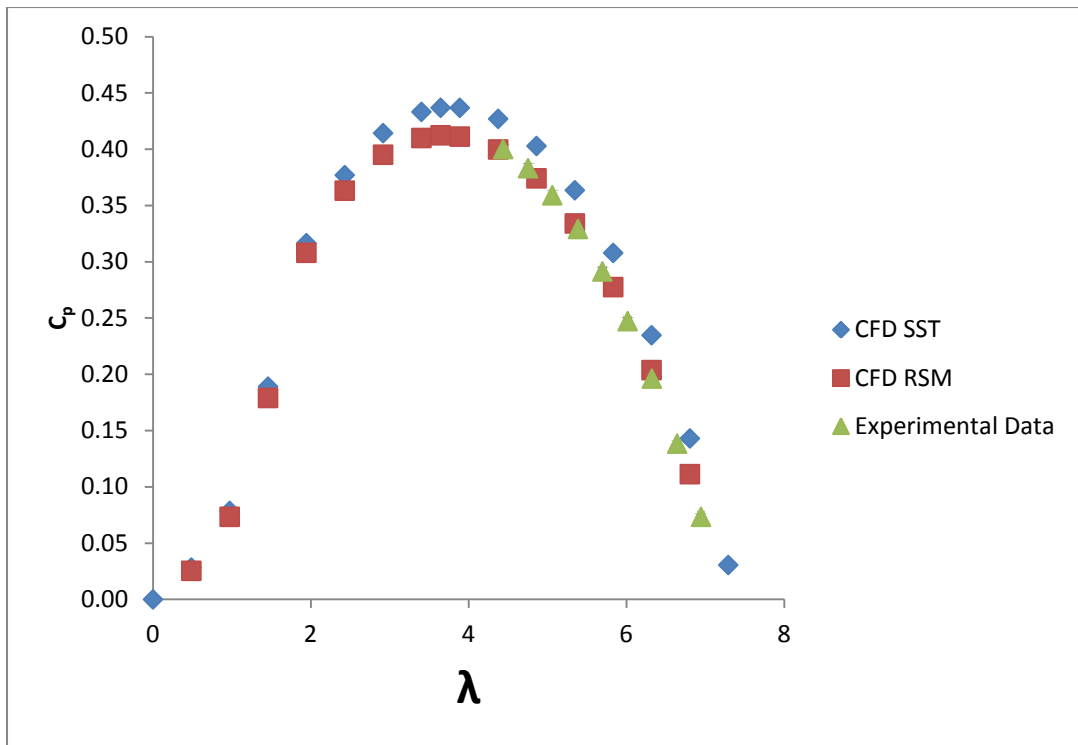


Figure 5.12 C_p vs λ from blockage corrected experimental data and from CFD models

5.11 Thrust Measurements

Figure 5.13 shows the experimental thrust data and the CFD predictions. Although the correlation is not quite as close as for C_p , it is still reasonable, with a maximum difference of 10%. Again, a comparison is only possible at $\lambda = 4.4$ and above. The predictions from the SST CFD model shows a closer correlation to the experimental thrust data but again, given the inherent error within the ADV system, both models are considered to correlate reasonably well with the experimental data.

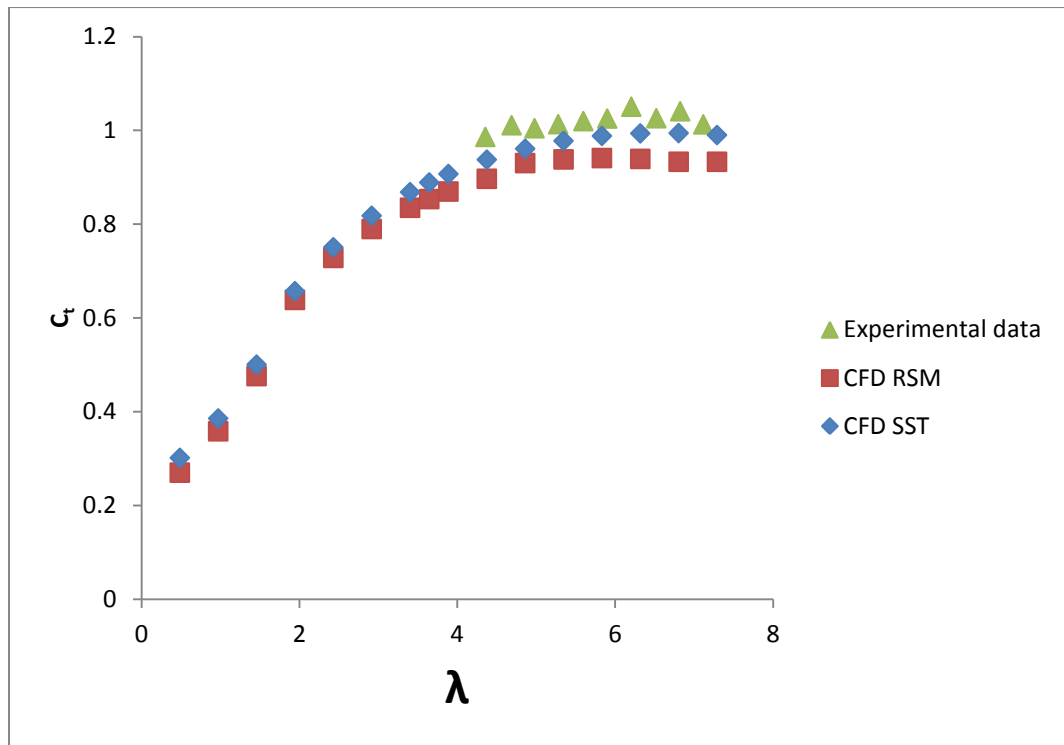


Figure 5.13 C_t vs λ from blockage corrected experimental data and from CFD models

5.12 Summary of Fume Testing and Model Validation

The improvements to the prototype turbine design significantly reduced the scatter in the experimental data which was the first objective of this work. However, due to the motor overheating, the experimental measurements were limited to $\lambda = 4.4$ and above and therefore peak power could not be captured. When corrected for blockage, the experimental data showed good correlation with the results from the CFD giving confidence in the numerical modelling.

6 Performance Characteristics

As discussed and defined in Chapter 3, the main performance characteristics, by which a TST can be described, are the torque coefficient, C_θ , the power coefficient, C_p , and the thrust coefficient, C_t . This chapter considers the variation in these coefficients with λ , also defined in Chapter 3, for the 2, 3 and 4 bladed turbines with each of the viscous models used, and then compares the results for each configuration. The effect of differing turbulence decay is also investigated by comparing the performance characteristics under normal operating conditions, taken as peak power generation, with models with fixed minimum turbulence.

6.1 Torque

Figure 6.1 shows that with the RSM model the cut-in C_θ of the 2 bladed turbine is 0.025. The C_θ then increases, reaching a peak of 0.114 at a λ of 2.43. The increase is approximately linear from a λ of 1 until peak C_θ (at a rate of 0.052). After the peak, C_θ decreases, again linearly but at a slower rate (0.020), until it reaches 0 at a λ of around 8.1, which is the freewheeling λ . This is the maximum velocity at which the turbine would rotate due to the hydrodynamic forces imparted on the blades by the tidal current. For the turbine to rotate at a λ greater than this, it would have to be driven by a motor and would effectively act as a pump.

The SST model is shown to predict a slightly higher C_θ than the RSM model over the range of λ studied, with a peak of 0.116 compared with a peak of 0.114 for the RSM model. The maximum torque for the 2 bladed turbine predicted by the SST model is therefore 1.8% higher than the RSM model. Since CFD only provides an estimate of the field and the forces on the blades, with potential errors from truncation and numerical diffusion, this difference is considered to be small and is of little significance. Most importantly, both models show the same trend, which is typical of a horizontal axis turbine (Orme and Masters, 2004, Mason-Jones, 2010) and the λ at which peak C_θ is predicted to occur is the same.

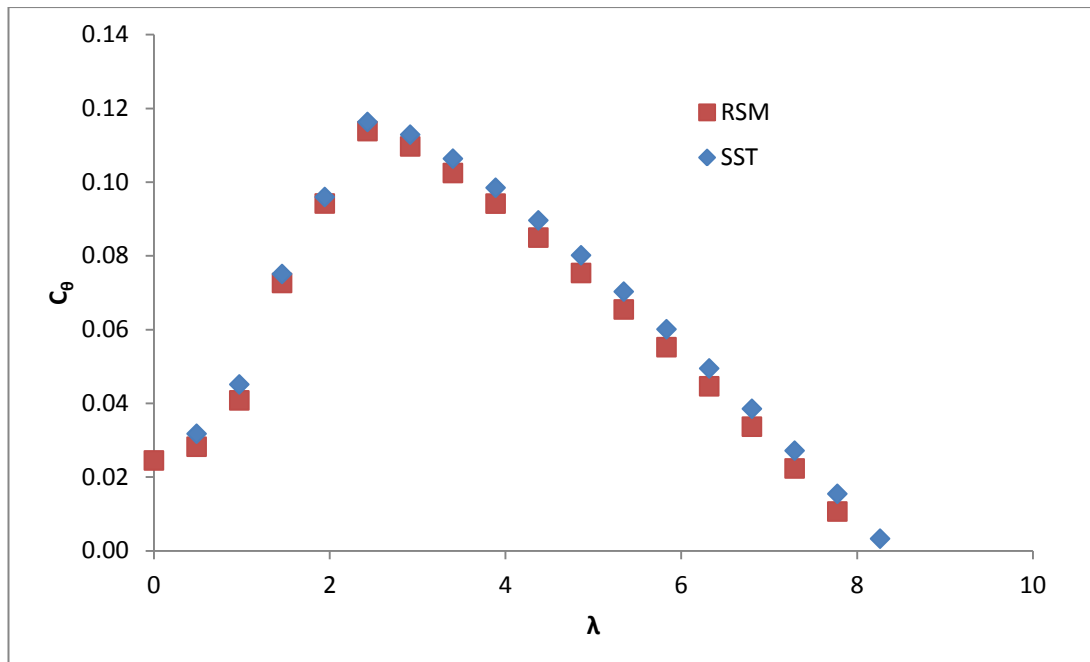


Figure 6.1 C_p vs λ for the 2 bladed turbine

The C_p curves for the 3 and 4 bladed turbines are shown in Figures 6.2 and 6.3. They follow the same general trend as those of the 2 bladed turbine, with an almost linear increase from $\lambda = 1$ to peak C_p and a linear but slower decrease from peak C_p to freewheeling.

For the 3 bladed turbine, the RSM predicts a cut-in C_p of 0.05, and a peak C_p of 0.158, both higher than those of the 2 bladed turbine. The curve can be seen to increase from $\lambda = 1$ with a rate of 0.105 to the peak which occurs at a λ of 1.94. Freewheeling λ occurs at around 7.1, lower than the 2 bladed turbine, with the rate of decrease being 0.031.

For the 4 bladed turbine, the RSM prediction of cut-in C_p has again increased, to 0.07, and the peak C_p has increased to 0.188. The λ at which peak C_p occurs has further decreased, to around 1.8, and the freewheeling λ has reduced to 6.4. The linear increase from $\lambda = 1$ to the peak has a rate of 0.125 and the rate of decrease from the peak is 0.042.

As with the 2 bladed turbine, the SST model predicts a higher C_p than the RSM model for the 3 and 4 bladed turbines at all of the λ considered. The peak C_p for the

3 bladed turbine is 0.163 for the SST compared with 0.158 for the RSM, or an increase of 3.0%. For the 4 bladed turbine the peak C_{θ} predicted by the SST model is 5.7% higher than the RSM, at 0.199 compared with 0.188.

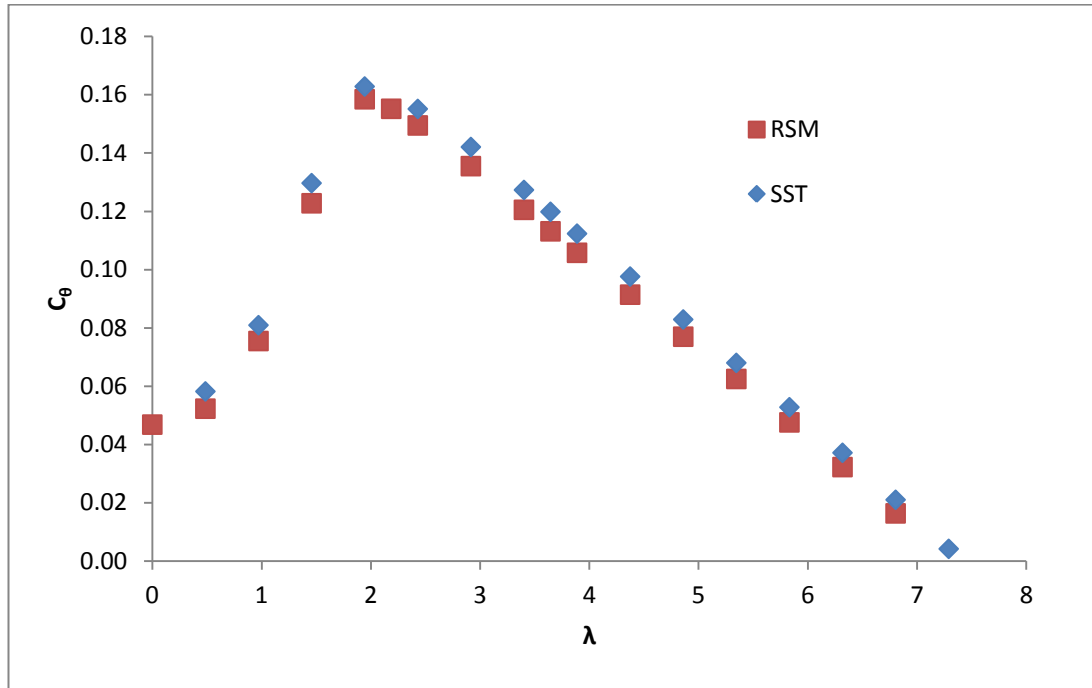


Figure 6.2 C_{θ} vs λ for the 3 bladed turbine

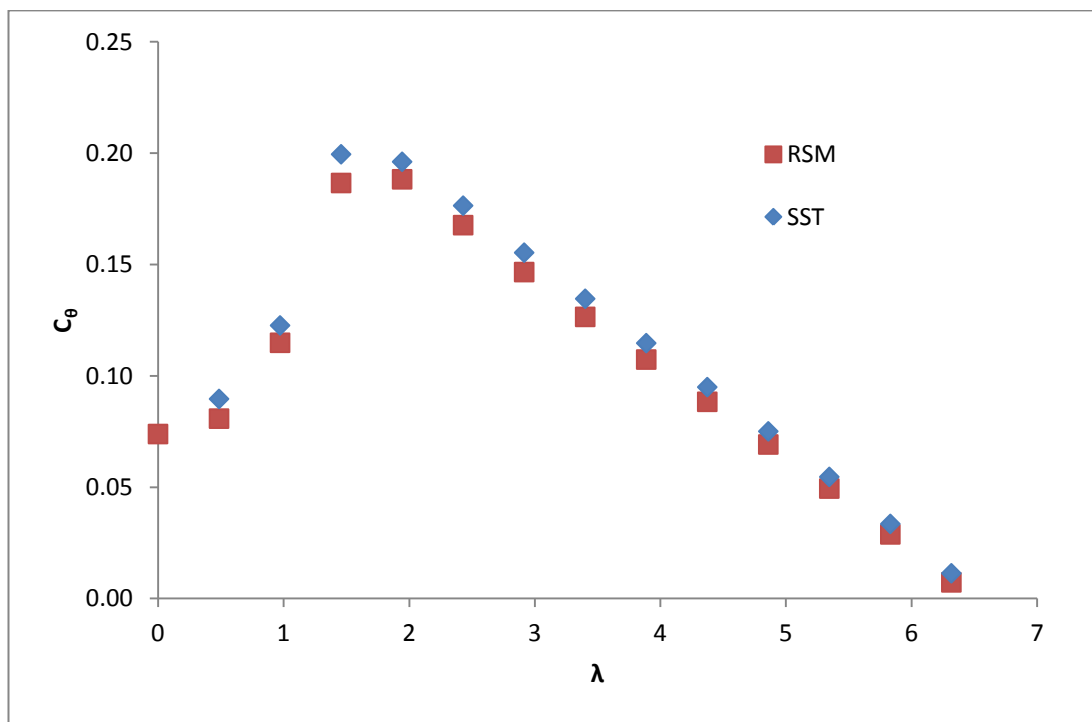


Figure 6.3 C_{θ} vs λ for the 4 bladed turbine

The SST models give slightly higher values than the RSM models for C_θ for all three turbine configurations at all values of λ considered. It is thought that this is partly due to the difference in turbulence intensity immediately upstream of the turbine, as will be discussed in Section 6.4. It may also be a result of the improved ability of the RSM model to give accurate predictions in complex flows such as those with swirl, due to its ability to model anisotropic turbulence, as discussed in Chapter 3. However, since the values are all within 1.7% to 6.5% at peak power and follow the same trends for each performance characteristic of each turbine, a comparison is only shown here for the RSM model. Similar observations are found for the SST model and these are given in Appendix A.

Figure 6.4 compares the C_θ curves for the 2, 3 and 4 bladed turbine configurations. It is clear that the cut-in C_θ increases with the number of blades due to the resultant force on each blade being multiplied by the number of blades. The rate of increase of cut-in C_θ also increases with the number of blades with a larger difference between 3 and 4 blades than between 2 and 3 blades. Near $\lambda = 0$, there is little to no flow over the rear surface of the blade (upper portion of the hydrofoil) and hence there is very little lift and the torque is dominated by the reaction force as the fluid is deflected around the blade. The increase in pitch angle with the number of blades means that the resultant force per blade also increases.

The increase in peak C_θ with the number of blades is in agreement with the findings for a Vertical Axis Wind Turbine by Roh and Kang (2013), who found that peak C_θ increased with solidity for σ between 0.033 and 0.08. One consequence of this is that the 4 bladed turbine would require the largest diameter of drive shaft and the 2 bladed turbine the smallest, implying that the cost of the drive shaft could increase with the number of blades. Based on these results, maintaining a constant shear stress would require a ~25% increase in the shaft diameter from the 2 bladed turbine to the 4 bladed turbine. This is based on a simplistic consideration that $\tau = 16T/\pi D^3$.

It is also clear from Figure 6.4 that the λ at which both peak C_θ and freewheeling occur decrease with an increase in the number of blades. This is because the

optimum pitch angle increases with the number of blades and hence a lower value of λ is required to achieve the optimum lift to drag ratio. If a traditional mechanical power train were used, this may result in additional stages within the gearbox for a higher number of blades, with the increased costs and losses associated. All of the turbines have a torque curve typical of a HATT, (Orme and Masters 2004, Mason-Jones, 2010).

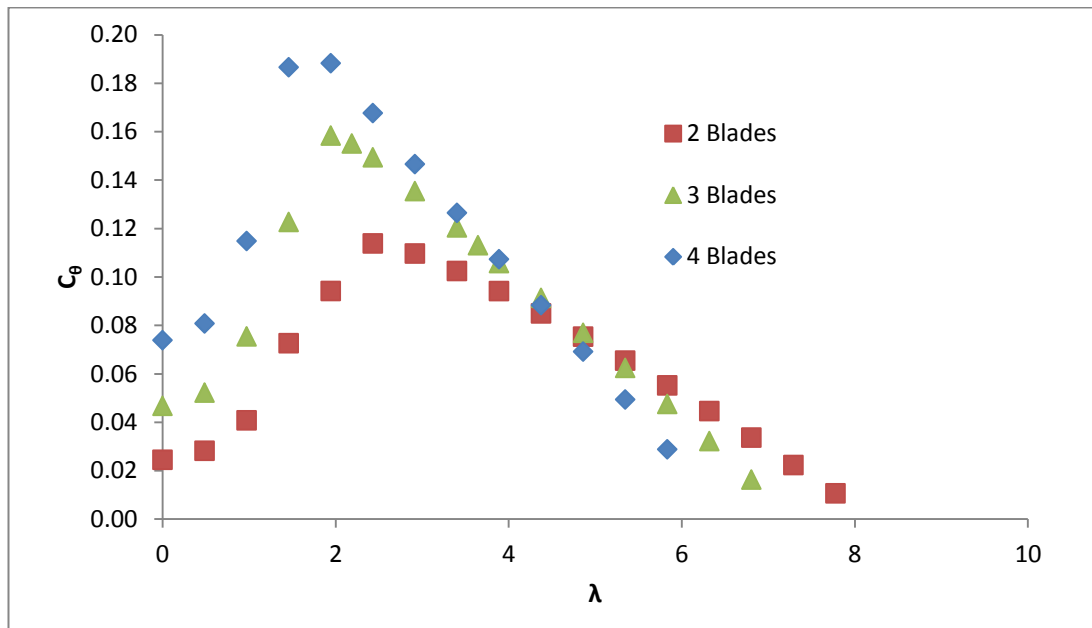


Figure 6.4 C_θ vs λ for the 2,3 and 4 bladed turbines

Figure 6.5 shows the C_θ curves with the RSM for all three turbine configurations, normalised with respect to maximum C_θ and maximum λ for each turbine. Aside from at start up and at very low values of λ , the curves of the 3 and 4 bladed turbines show very good correlation. The 2 bladed turbine data do not compare as well but still fall within 10% of the values for the other turbine configurations at λ from peak $C_\theta / C_\theta \text{ max}$ to freewheeling. Therefore, for this blade design, with knowledge of the torque characteristics of one turbine configuration, a reasonable estimation of the torque characteristics of another configuration over the majority of its operational range could be made. In practical terms, once the freewheeling λ had been established, the λ at which peak C_θ occurs could be estimated to within 7% and vice versa.

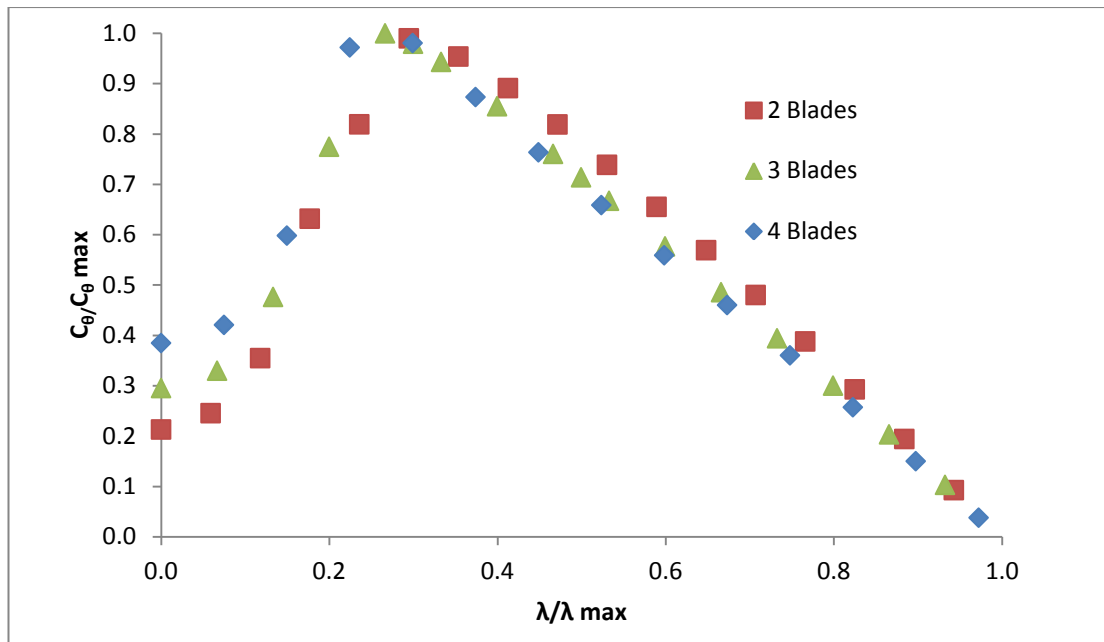


Figure 6.5 Normalised C_{θ} vs normalised λ for the 2, 3 and 4 bladed turbines

6.2 Power

Figure 6.6 shows the power curves for the 2 bladed turbine. With the RSM, peak C_p was found to be 0.37, occurring at a λ of 4.4. Again, freewheeling occurs around 8.1. Since the power is calculated from the torque and the rotational speed, and the model was run at the same rotational speeds, it follows that if the C_{θ} is higher with the SST model than with the RSM, the C_p must also be higher. Figure 6.6 shows that this is the case, with the SST model predicting a higher C_p than the RSM model at all of λ considered. However, whereas the difference between the C_{θ} predicted by each model is fairly constant, the difference in C_p varies with λ . This is because the torque is multiplied by the rotational speed, which is less than 1 for values of λ below 1.5, thereby reducing the difference, and at higher λ is greater than 1, therefore increasing the difference. The maximum C_p predicted by the SST model is 0.39 which is 0.02 greater than that predicted by the RSM model. This is a difference of 5.4%. Given that the experimental data is based on a free stream velocity measured with an ADV system that is estimated to be accurate to $\pm 5\%$, the difference between the models is considered small.

The SST model also predicts a slightly larger operational range, with freewheeling occurring at a λ of around 8.3 compared to around 8.1 for the RSM model, a difference of 2.5%. The λ at which peak power occurs is only slightly increased by the SST model, with 4.4 being the closest λ modelled for both the RSM and SST models.

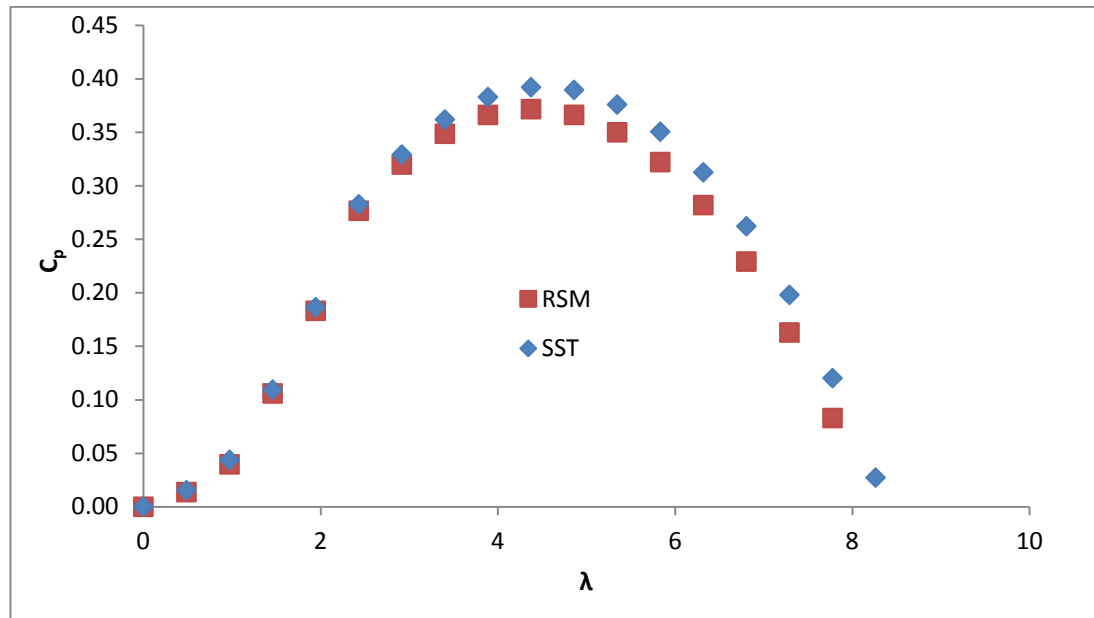


Figure 6.6 C_p vs λ for the 2 bladed turbine

The C_p curves of the 3 and 4 bladed turbines, Figures 6.7 and 6.8, also follow the same general trend as those of the 2 bladed turbine. With the RSM, peak C_p for the 3 bladed turbine, Figure 6.7, is 0.41 compared with 0.37 for the 2 bladed turbine. It occurs at a lower λ of around 3.65. Peak C_p predicted by the RSM for the 4 bladed turbine, Figure 6.8, is 0.43, which is higher than both the 2 and 3 bladed turbines. It occurs at a λ of around 3.4, lower than both other turbine configurations.

For the 3 and 4 bladed turbines the values of predicted C_p are again slightly higher for the SST model at all values of λ considered. The maximum C_p predicted by the SST model for the 3 bladed turbine is 0.44 which is 0.03 greater than that predicted by the RSM model. This is an increase of 5.9%. The operational range predicted by the SST model is 4.2% larger, with freewheeling occurring at a λ of 7.4 compared to

7.1 for the RSM model. The λ at which peak power occurs for the 3 bladed turbine is 3.65 for both the RSM and SST models.

The peak C_p predicted by the SST model for the 4 bladed turbine is 6.5% higher than that predicted by the RSM at 0.46 compared with 0.43. The difference is again very small at values of λ below 1.5 and increases with λ .

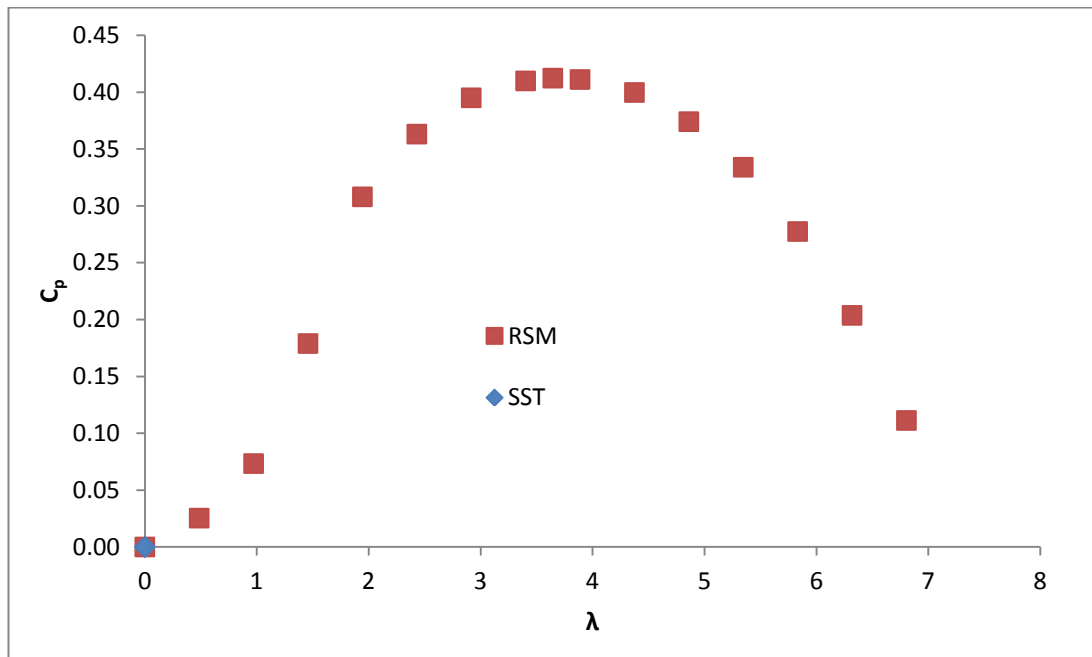


Figure 6.7 C_p vs λ for the 3 bladed turbine

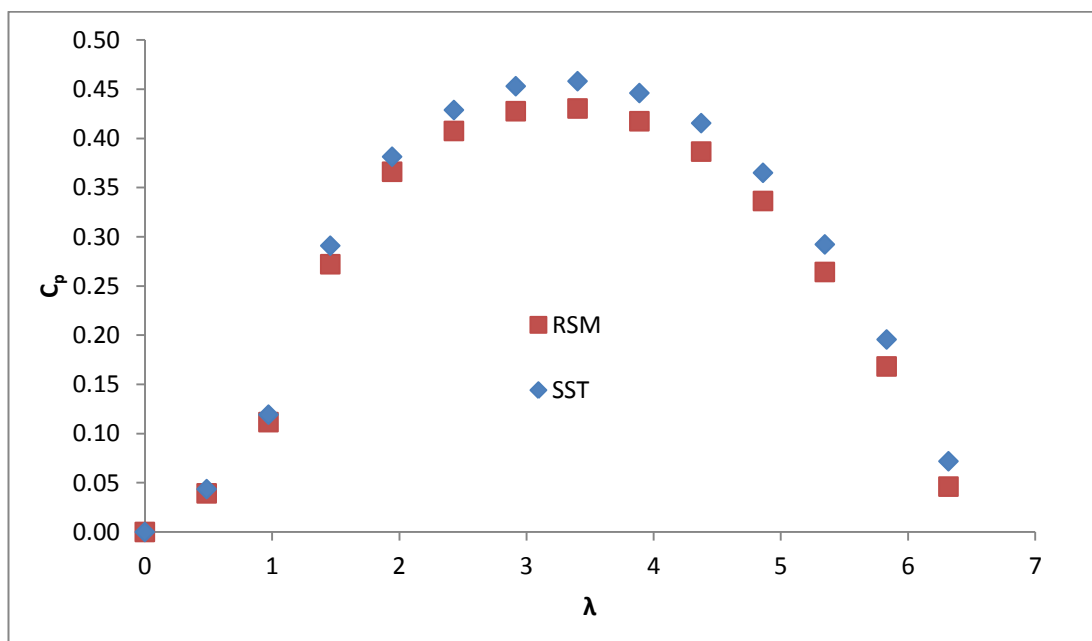


Figure 6.8 C_p vs λ for the 4 bladed turbine

As seen in Figure 6.9, peak power increases with the number of blades and the tip speed ratio at which peak power occurs decreases. The difference in both peak power and the λ at which it occurs is greater between the 2 and 3 bladed turbines than between the 3 and 4 bladed turbine, with diminishing returns from each additional blade as expected from Hau (2006). In this case the peak C_p values are 0.37, 0.41 and 0.43, occurring at λ of 4.37, 3.65 and 3.40 for the 2, 3 and 4 bladed turbines respectively. These values fall within the range given in the literature for peak C_p of a HATT (Mason-Jones, 2010, Jo et al., 2013, Faudot et al., 2013, Walker et al., 2013).

The operating range is shown to increase with decreasing number of blades, with freewheeling occurring around a λ of 8.1 for the 2 bladed turbine, 7.3 for the 3 bladed turbine and 6.4 for the 4 bladed turbine. This trend has also been shown to occur for HAWTs and VAWTs (Hau, 2006, Roh and Kang, 2013).

The increasing C_p , at a lower λ , and the reduced operating range, with increasing number of blades also occurs with the SST model albeit with slightly higher values predicted for each turbine at all values of λ and slightly larger operational ranges, as given in Appendix A.

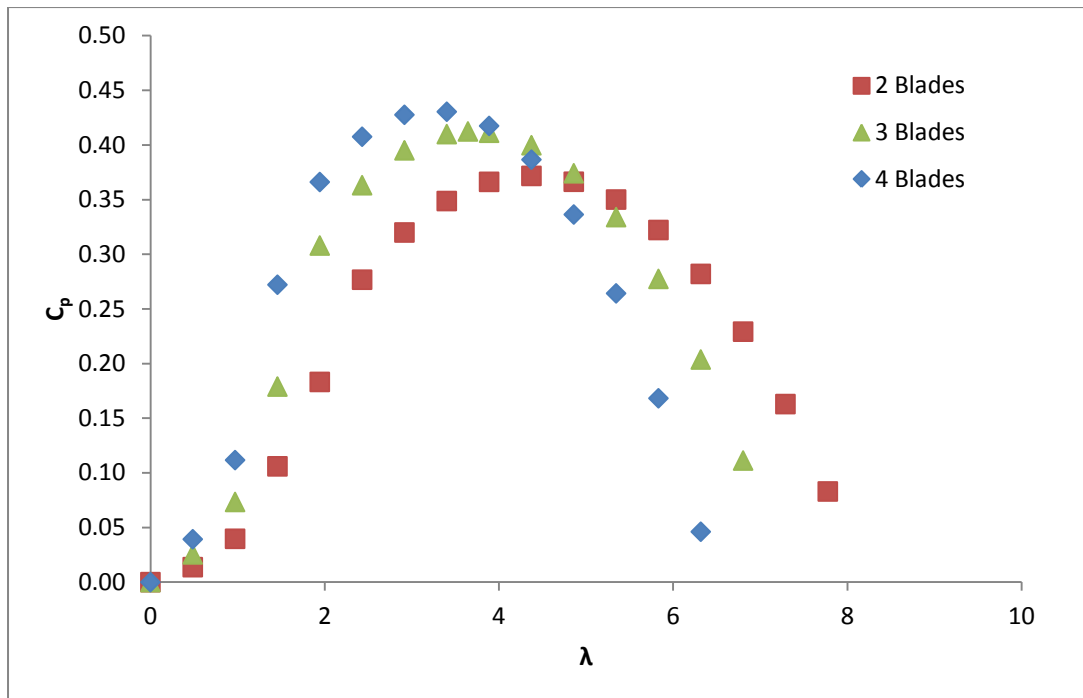


Figure 6.9 C_p vs λ for the 2, 3 and 4 bladed turbines

Normalising the C_p curves with respect to maximum λ and maximum C_p gives the curves shown in Figure 6.10. As with the normalised C_θ curves, the data show good correlation for all three turbines, particularly from peak C_p to freewheeling. The λ at which peak C_p occurs could be estimated to within 6% from the knowledge of the freewheeling λ for any of the configurations. It should be noted that the asymmetry of the correlation is simply due to λ being normalised against λ_{max} , whereas if the normalisation was based on λ at peak C_p the correlation would be symmetrical. The same trends are again shown for the normalised SST results and are again given in Appendix A.

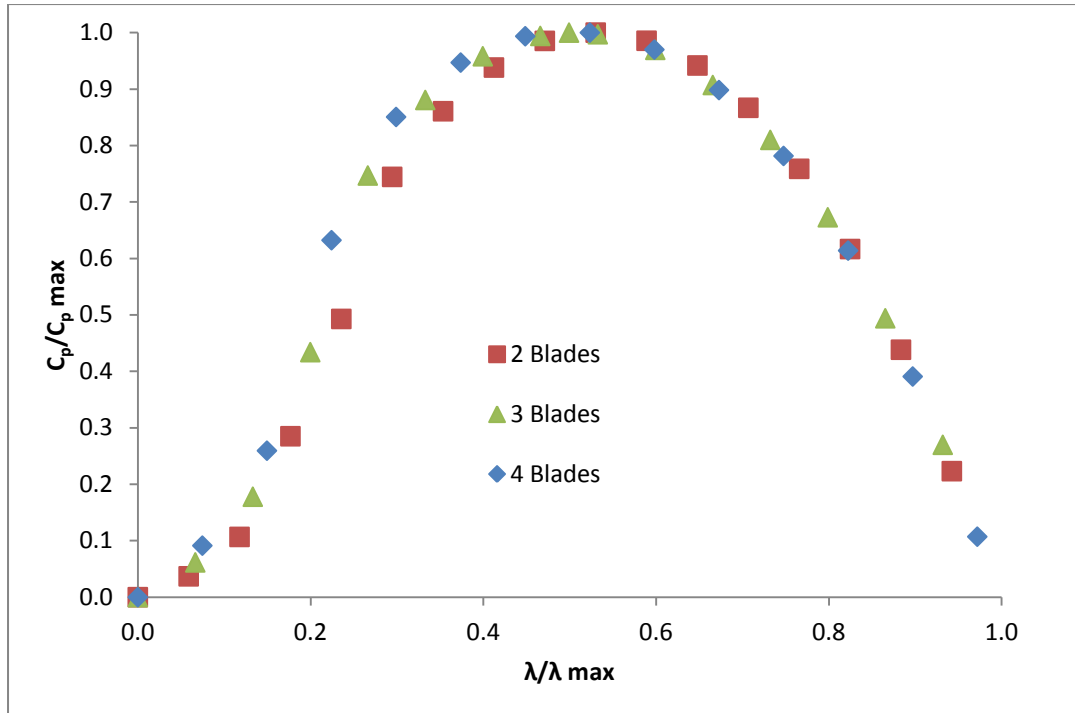


Figure 6.10 Normalised C_p vs normalised λ for the 2, 3 and 4 bladed turbines

6.3 Thrust

With the RSM, the C_t of the 2 bladed turbine when it is stationary is 0.17, as shown in Figure 6.11. This then increases with λ , reaching a maximum of 1.06 at freewheeling. Since operating at peak power would result in the greatest quantity of electricity being produced, it is assumed that this would be the normal operating condition. If the 2 bladed turbine was operated at peak power, i.e. a λ of 4.4, the C_t would be 0.82.

At λ below 5 the thrust predictions are very similar for both the RSM and SST models with the SST model giving slightly higher values. Above this λ the difference between the values of C_t , predicted by both models, increases with λ . However, the maximum difference, at a λ of 7.8, is 5.3% between both models. At peak C_p the predicted C_t is 0.03, or 3.4%, higher for the SST model.

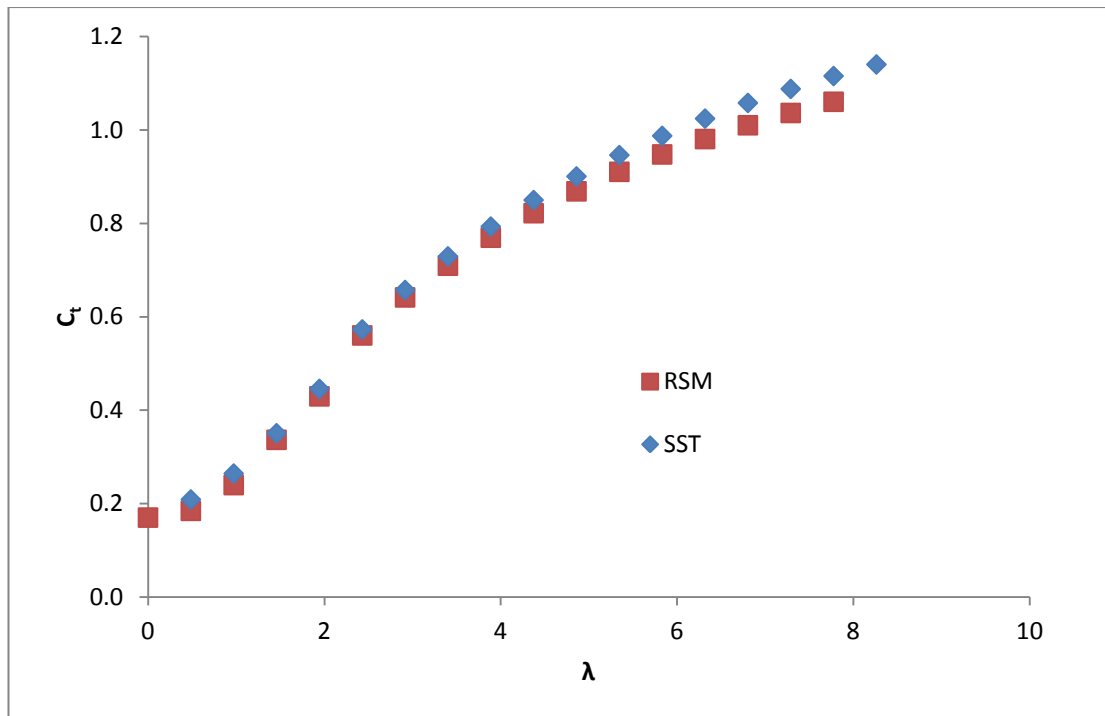


Figure 6.11 C_t vs λ for the 2 bladed turbine

As expected the C_t of the 3 bladed turbine, Figure 6.12, is higher when stationary than the C_t of a stationary 2 bladed turbine due to the higher solidity, with a C_t predicted by the RSM of 0.25. The RSM prediction of C_t for the 4 bladed turbine, Figure 6.13, is higher again, at 0.34, due to its even higher solidity.

For the 3 bladed turbine the C_t predicted by the RSM at the λ corresponding to maximum C_p is 0.85 which is slightly higher than under the same condition for the 2 bladed turbine. Unlike with the 2 bladed turbine, the C_t of the 3 bladed turbine does not continue to increase with λ to freewheeling but instead reaches a maximum at a λ of 5.8, before decreasing slightly to freewheeling. Peak C_t is lower at 0.94, compared with 1.06 for the 2 bladed turbine.

As with the 3 bladed turbine, the C_t for the 4 bladed does not continue to increase with λ to freewheeling. It reaches a maximum of 0.86, the lowest of the three configurations, at a λ of 3.9 before falling to 0.77 at freewheeling. The C_t of the 4 bladed turbine at peak power is 0.85, which is the same as that of the 3 bladed turbine at peak power.

It is clear from Figures 6.12 and 6.13 that at all λ ; the SST model predicts a slightly higher C_t than the RSM model. As with the 2 bladed turbine, the difference predicted by each model increases at higher λ for the 3 and 4 bladed turbines. For the 3 bladed turbine the difference at peak C_t is 0.06, or 6.5%, at a λ of 6.8. At peak C_p the difference is lower at 0.035, or 4.2%. For the 4 bladed turbine peak C_t predicted by the SST is 0.91 compared with 0.86 for the RSM. This is a 4.6% increase. At peak power the SST model predicts a C_t which is 5.0% higher than the RSM model, at 0.90. Again, given the $\pm 5\%$ uncertainty in the flume velocity measurements, these differences are of the same magnitude and therefore considered reasonable.

As with the RSM, the SST model also predicts that for the 3 bladed turbine the C_t does not continue to increase with λ but instead reaches an almost constant value above $\lambda=5.8$, with a slight reduction at the highest value of λ . The SST model also predicts the drop in thrust at high λ , near freewheeling, for the 4 bladed turbine.

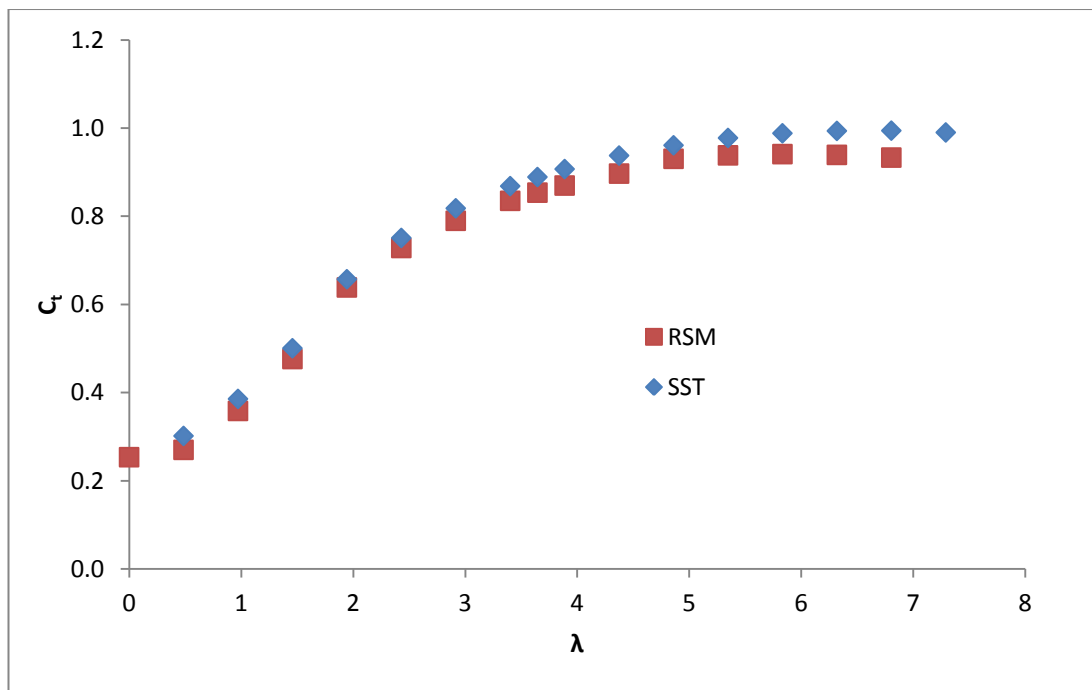


Figure 6.12 C_t vs λ for the 3 bladed turbine

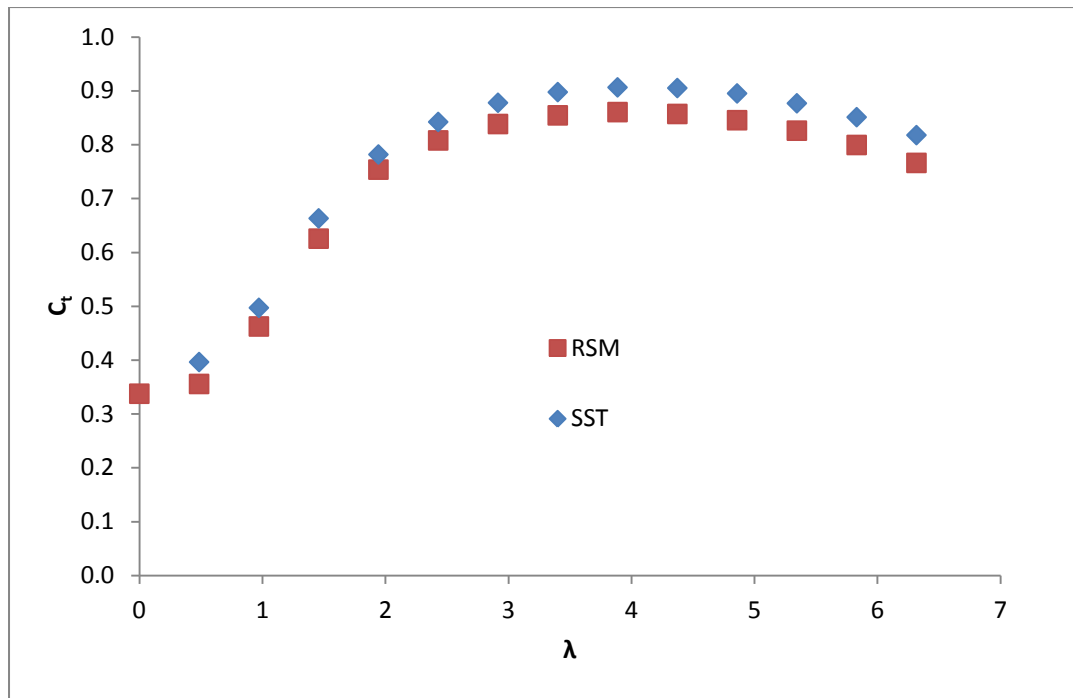


Figure 6.13 C_t vs λ for the 4 bladed turbine

Figure 6.14 compares C_t against λ for the 2, 3 and 4 bladed turbines. It shows that at lower λ the C_t of the 4 bladed turbine is highest and the C_t of the 2 bladed turbine is lowest but that at higher λ this is reversed. It also shows that at the freewheeling λ for each turbine the C_t of the 2 bladed turbine is still increasing, the C_t of the 3 bladed turbine is steady and the C_t of the 4 bladed turbine is decreasing. This is because the pitch angle increases with the number of blades. Mason-Jones et al. (2012) investigated the effect of changing the pitch angle of a 3 bladed turbine, using the same blade design as used in this work. The findings showed that pitch angle had little effect on C_t at λ less than 1.2 but with a pitch angle less than 6° , C_t continues to increase with λ to freewheeling whereas with a pitch angle above 6° , C_t reaches a maximum before decreasing toward freewheeling.

The consequences of this behaviour at high λ would be important when designing the turbine to withstand loads in the event of a failure of the control or braking system with the steady load on the 3 bladed turbine and the decreasing load on the 4 bladed turbine being an advantage. The peak C_t for each turbine over the operating range are 1.06, 0.94 and 0.86 for the 2, 3 and 4 bladed turbines

respectively. It is therefore clear that the peak C_t is highest for the 2 bladed turbine and lowest for the 4 bladed turbine. This means that if these blades were used for a fixed pitch 2 bladed rotor, the control system would need to be very reliable or the blade roots strong enough to withstand the high bending moments that would result from the high thrust in the event of a failure. The alternatives would be to have:

- 1) variable pitch blades, which could increase the cost and complexity of the device and potentially reduce reliability.
- 2) bend-twist coupled blades where the tip pitch angle would increase with deflection.

In order to assess the C_t for each turbine under normal operating conditions it is necessary to compare the C_t of each turbine at the λ at which it is run. If each turbine is run at peak power the C_t values predicted by the RSM for the 2, 3 and 4 bladed turbines are 0.82, 0.85 and 0.85 respectively. Hence it can be seen that under normal conditions the C_t of each turbine is 0.84 ($\pm 2\%$).

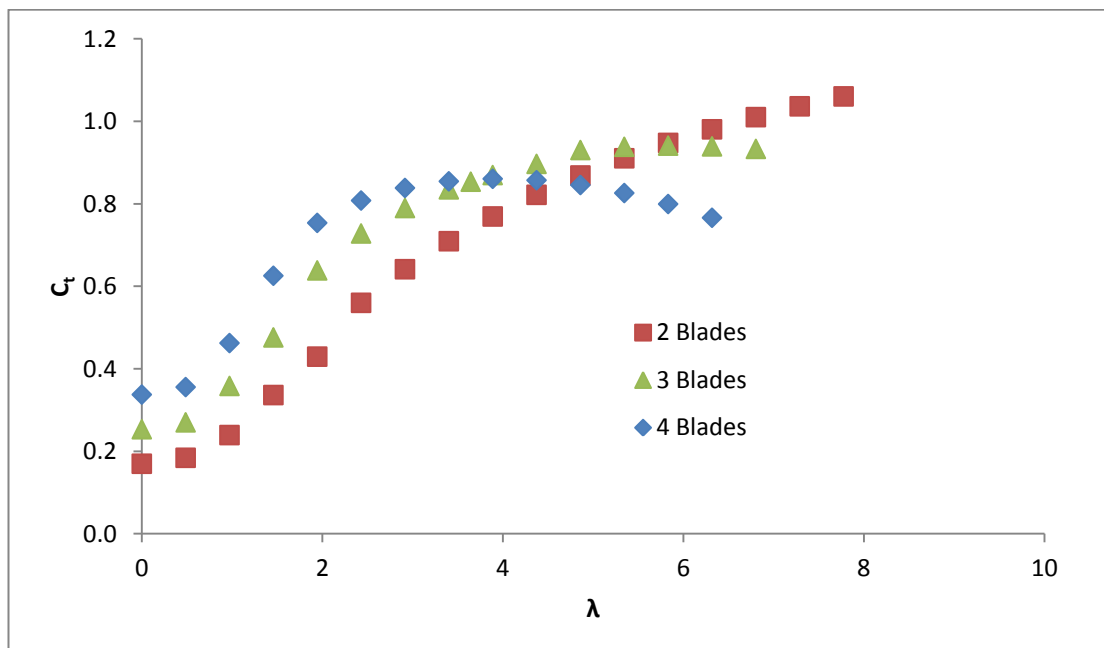


Figure 6.14 C_t vs λ for the 2, 3 and 4 bladed turbines

When comparing the normalised C_t curves for each turbine, shown in Figure 6.15, it is clear that unlike the C_p and C_θ characteristics none of the curves overlay and that the C_t curve of one configuration cannot be estimated from the C_t curve of another.

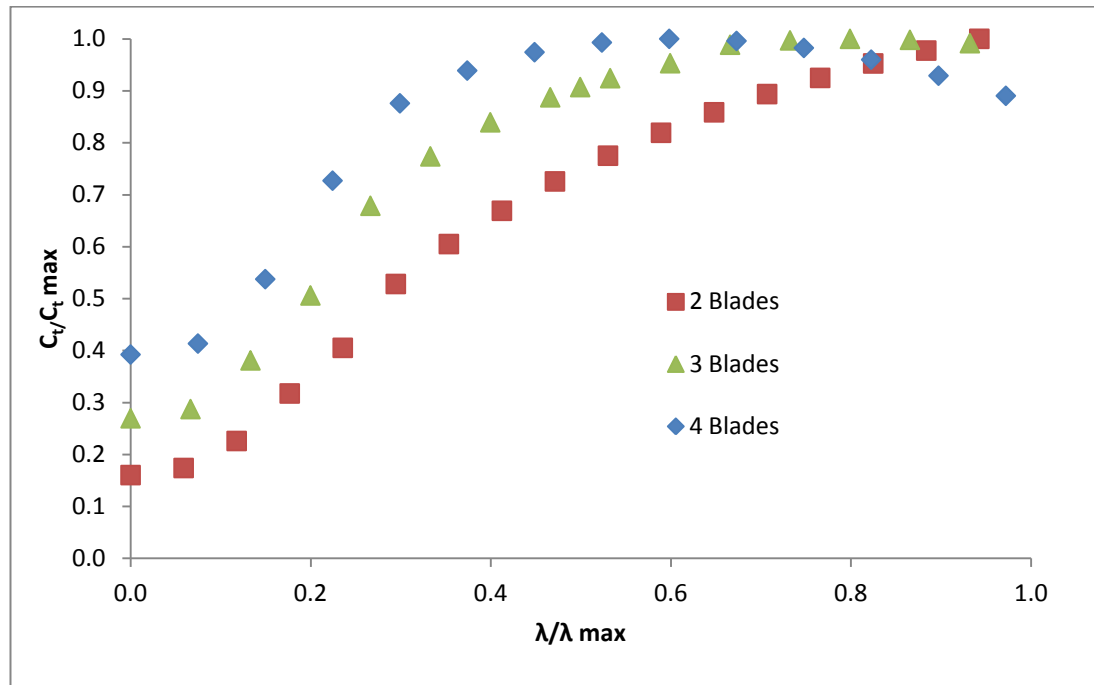


Figure 6.15 Normalised C_t vs normalised λ for the 2, 3 and 4 bladed turbines

Although the thrust load on each turbine is of a similar magnitude under normal operating conditions, when the number of blades is considered, the thrust per blade is as shown in Figure 6.16. It is clear that at λ below 2, the thrust per blade is very similar for all three turbine configurations. At λ above 2, the curves diverge with the thrust per blade on the 2 bladed turbine highest and the thrust per blade on the 4 bladed turbine lowest. The thrust per blade on the 4 bladed turbine peaks at 79.2 kN at a λ of 3.9 before falling to 70.5 kN at the freewheeling λ . Peak thrust per blade on the 3 bladed turbine is 116.0 kN at a λ of 6.3 and this remains fairly steady to freewheeling with only a slight decrease to 115.0 kN. The thrust per blade on the 2 bladed turbine keeps increasing to freewheeling at which it reaches 200.3 kN. Comparing the thrust per blade with that of the 4 bladed turbine, there is an increase of a factor of approximately 1.5 for the 3 bladed turbine and 2.5 for the 2 bladed turbine. Under normal operating conditions, which are assumed to be at peak power, the thrust per blade is 151.0 kN, 104.6 kN and 78.5 kN for the 2, 3 and

4 turbines respectively. Therefore, even under these conditions, the thrust per blade is 1.3 times greater for the 3 bladed turbine and 1.9 times greater for the 2 bladed turbine when comparing with the thrust per blade on the 4 bladed turbine. This blade design is therefore better suited to a 3 or 4 bladed rotor since, even at peak power the load on each blade of a 2 bladed rotor is much greater and, in the case of a failure, continues to increase to freewheeling.

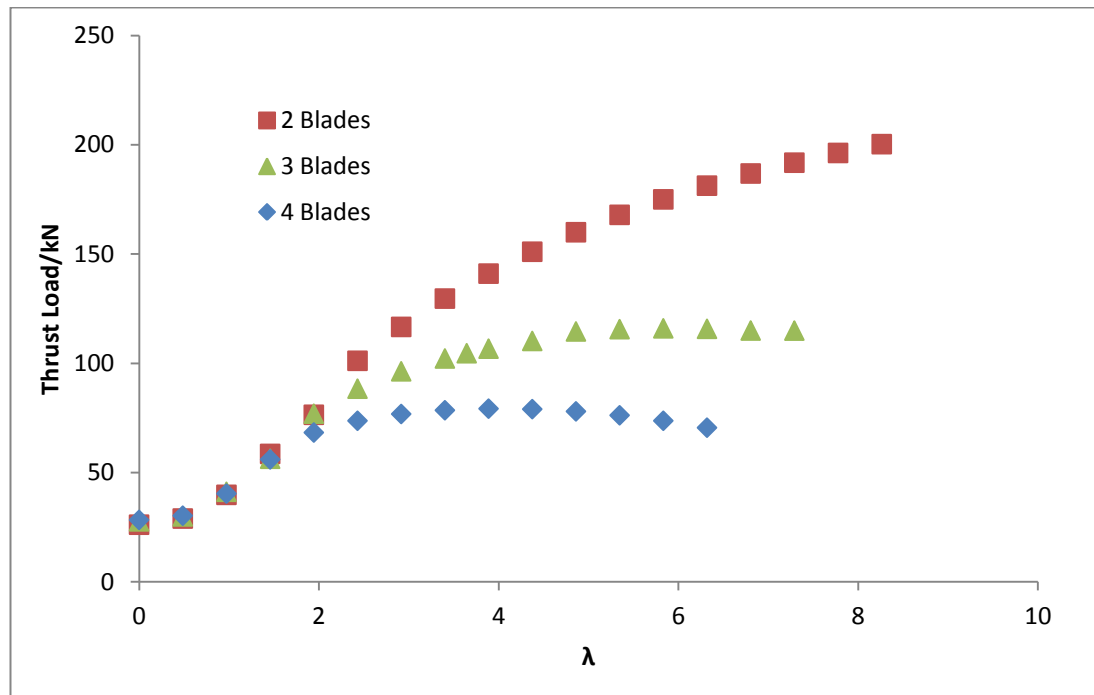


Figure 6.16 Thrust per blade vs λ for the 2, 3 and 4 bladed turbines

6.4 Summary of Performance Characteristics

Sections 6.1 to 6.3 have shown that there is an increase in torque, and hence power, with an increasing number of blades, as shown in the literature (Hau, 2006, Roh and Kang, 2013). There is also a reduction in the λ at which peak power occurs which could be beneficial from an environmental viewpoint, particularly for fish and marine mammals, as discussed in Chapter 2.

It has also been shown that although under normal operating conditions, C_t is slightly higher for 3 and 4 bladed turbines, the thrust per blade is much higher for 2 bladed turbine. Therefore the loads which the stanchion, drive train etc. must

withstand would be of a similar magnitude regardless of the number of blades. The blades themselves would, though, need to be designed for much greater loads with fewer blades. However, more blades would mean an increased cost of manufacture, increased cost and complexity of installation and maintenance, and more parts resulting in more areas of potential failure. It is also worth considering that an even number of blades may suffer from tower shadow problems for certain designs, as discussed in Chapter 2, which could result in torque fluctuations.

6.5 Effect of Different Turbulence Decay

Having established that the trends are the same for each turbine with the RSM and SST model, possible reasons for the, albeit small, differences in actual predictions were considered. It became apparent that although the same settings were used for the turbulence at the inlet for both the RSM and SST models, due to the slower decay in turbulence with the SST model, the turbulence immediately upstream of the turbine was much greater with the SST model. As shown in Figure 6.17, the turbulent intensity around 1 turbine diameter upstream of the rotational plane of the turbine was between 9.1 and 12.9%, which is thought to be realistic for conditions in marine environment suitable for placement of tidal stream turbines (McCann et al., 2008, Osalusi et al., 2009, McCaffrey et al., 2013). Figure 6.18 shows that with the SST model the turbulent intensity around 1 turbine diameter upstream of the rotational plane of the turbine is between 43.3% and 47.0%.

Therefore, rather than trying to match the turbulence immediately upstream of the turbine by trial and error through varying the turbulence at the inlet, a minimum turbulence level was set throughout the entire domain. This may be considered more realistic since the turbulence in the ocean would not decay as in an idealised domain as it would constantly be generated by waves, seabed topography, marine life etc. Setting a minimum turbulence level throughout the domain may therefore be considered as the background turbulence in a realistic setting. Fixing the minimum background turbulence was achieved by setting a minimum turbulent kinetic energy of $0.05 \text{ m}^2\text{s}^{-2}$ through the domain. This resulted in a turbulent intensity, at 1 turbine diameter upstream of the rotational plane of the turbine, of 18% for both the RSM and SST models. This value is at the upper end of the range

found in the literature (McCann et al., 2008, Osalusi et al., 2009, McCaffrey et al., 2013) and between the values in the original models.

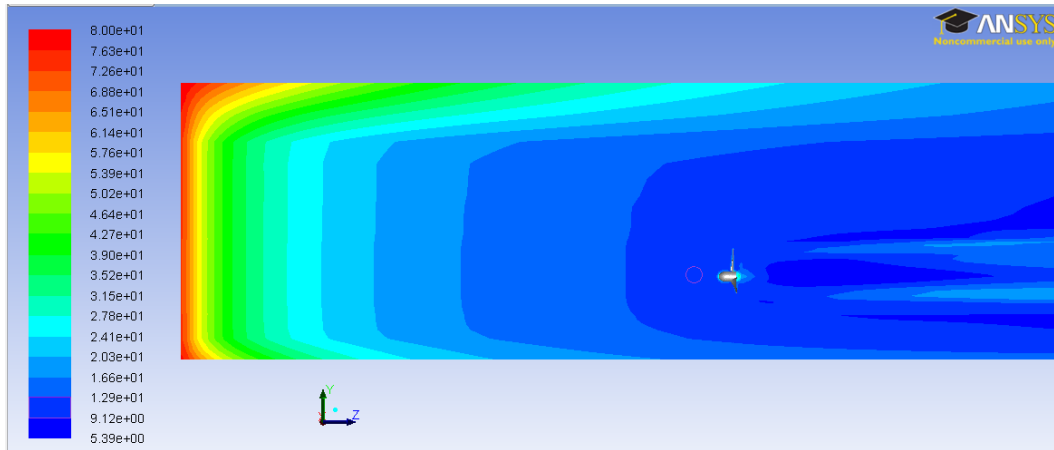


Figure 6.17 Contours of Turbulent Intensity with the RSM model

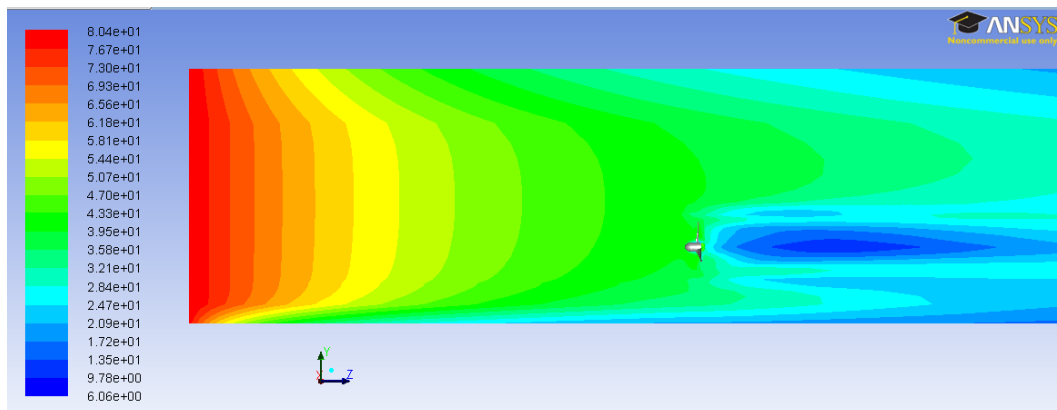


Figure 6.18 Contours of Turbulent Intensity with the SST model

Figures 6.19, 6.20 and 6.21 compare the C_θ , C_p and C_t at peak power of the 2, 3 and 4 bladed turbines for each of the fixed minimum turbulence models with the results from the original RSM and SST models.

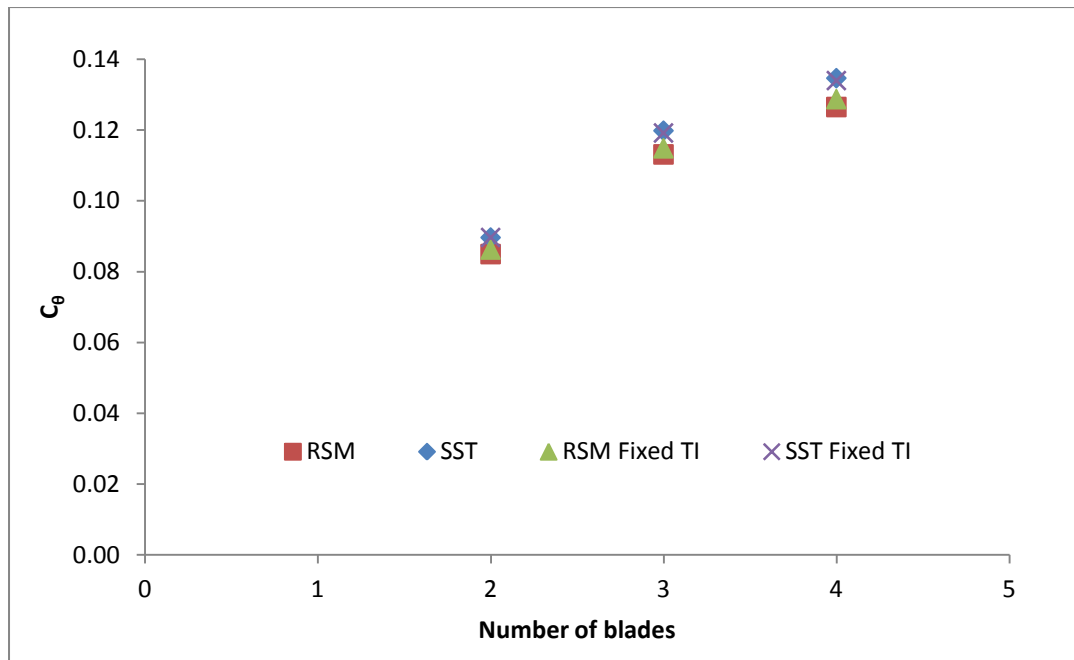


Figure 6.19 C_θ vs Number of Blades at peak C_p (normal operating condition)

Figure 6.19 shows that the difference in C_θ predicted by the fixed minimum turbulence models is less than the difference between the original RSM and SST models for all three turbine configurations. The differences between C_θ predicted by the original models were 0.0047, 0.0067 and 0.0082, or 5.5%, 5.9% and 6.5% for the 2, 3 and 4 bladed turbines respectively. With fixed minimum turbulence these differences have reduced to 0.0034, 0.0043 and 0.0052 or 4.0%, 3.8% and 4.1%. Since the turbulence intensity in the fixed minimum turbulence model is closer to the value immediately upstream of the turbine in the original RSM model than the original SST model, it would be expected that there would be a greater effect on the values predicted by the SST models than those predicted by the RSM models. However, there is a greater difference between the values predicted by the two RSM models than between those predicted by the two SST models. This suggests that either the SST model is less sensitive to changes in turbulence intensity or that changes in turbulence intensity have a greater effect at low values of turbulence than at high values. It is also possible that limiting the minimum turbulence also limits the anisotropy of the turbulence in the RSM model. However, further work would be required to determine if any of these suggestions are true. The difference

in predicted values increases with the number of blades. This is due to the small changes in the predicted forces on each blade, hence a greater difference with more blades.

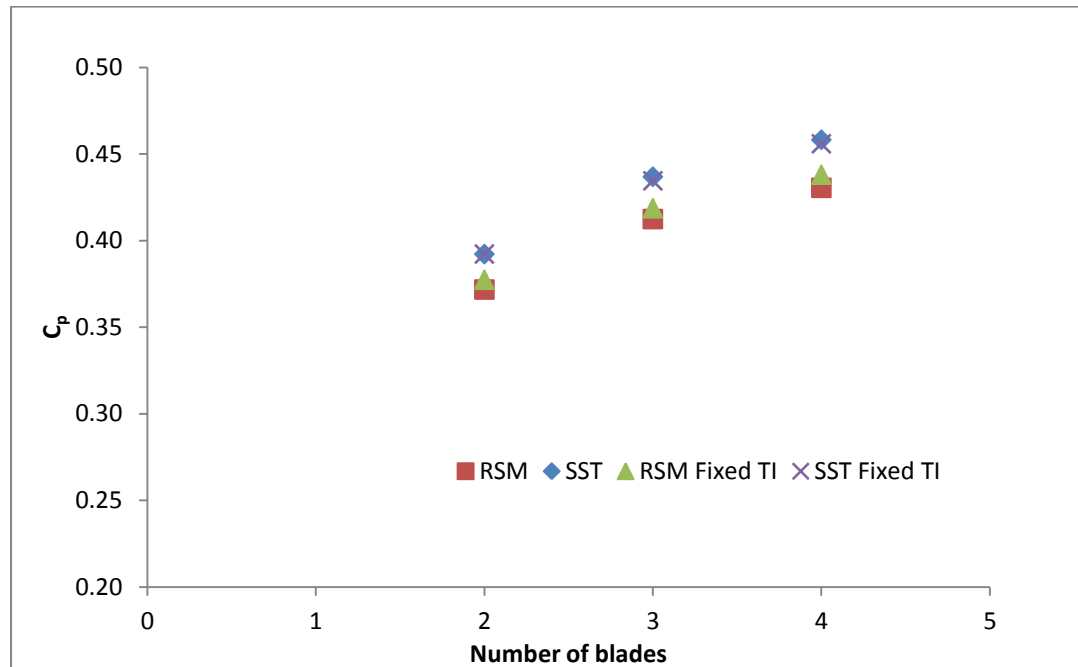


Figure 6.20 C_p vs Number of Blades at peak C_p (normal operating condition)

Since the difference in C_θ predicted by the fixed turbulence models is less than that predicted by the original models, it follows that the difference in predicted values of C_p must also be less. Figure 6.20 shows that this is the case and that fixing a minimum turbulence has a greater effect on the power predicted by the RSM model than that predicted by the SST model. This is despite the turbulent intensity immediately upstream of the turbine being closer in the fixed minimum turbulence models to the RSM model than to the SST model and again suggests a non-linear dependence of the predicted C_p on the turbulence. As stated above, further values of turbulent intensity would need to be modelled to establish the nature of this relationship.

The variations between C_p predicted by the original models were 0.020, 0.024 and 0.028, or 5.4%, 5.9% and 6.6% for the 2, 3 and 4 bladed turbines respectively. With fixed minimum turbulence these variations have reduced to 0.015, 0.016 and 0.018

or 4.1%, 4.3% and 4.9%. As for C_θ there is again an increasing disparity with an increasing number of blades due to the difference per blade resulting in a greater total difference with more blades.

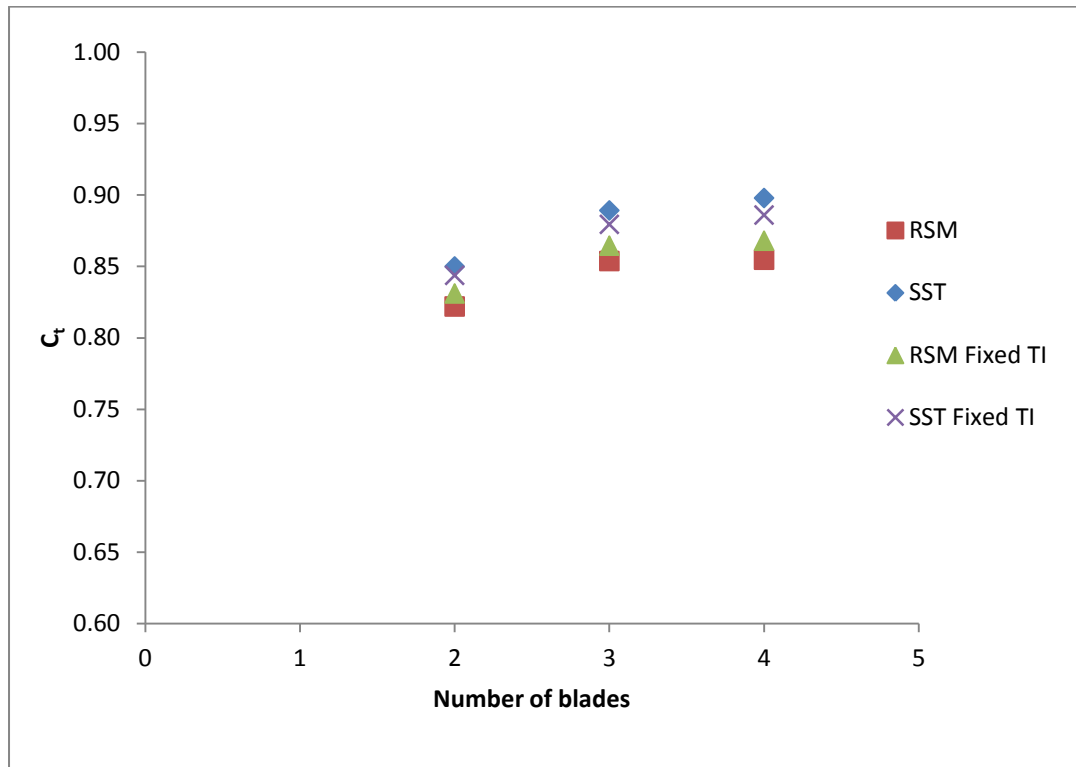


Figure 6.21 C_t vs Number of Blades at peak C_p (normal operating condition)

Figure 6.21 shows that as with the C_θ and the C_p , the difference in the C_t values predicted by the fixed minimum turbulence models is less than the difference in the C_t values predicted by the original models. The differences have reduced from 0.028, 0.035 and 0.033 between the original 2, 3 and 4 bladed models respectively to 0.013, 0.015 and 0.018 between the fixed minimum turbulence models. This equates to reductions from 3.4%, 4.1% and 3.9% to 1.6%, 1.8% and 2.1%. There is a greater reduction in the differences between the C_t predictions than between the C_θ and C_p predictions indicating that thrust is more sensitive than torque or power to differences in turbulence. Unlike the values of C_θ and C_p , fixing the minimum turbulence is shown to alter the C_t values predicted by the SST model by a similar magnitude to those predicted by the RSM model, suggesting that the dependence

of thrust on turbulence is different to that of torque. Again, further values of turbulent intensity would need to be modelled to investigate this further.

Fixing the minimum turbulence has reduced the difference in predictions of each performance characteristic for each turbine showing that the differences in the values predicted by the original RSM and SST models were partly due to the difference in turbulent intensity immediately upstream of the turbine. The results suggest a non-linear dependence on turbulence, with a different relationship between thrust and turbulence to the relationship between torque and turbulence. More modelling would be required at different turbulent intensities to establish these relationships. Even with a fixed minimum turbulence there are still differences in the predictions of each model. These are due to differences inherent within each model such as the ability to model anisotropic turbulence with the RSM model which is particularly relevant in near wall regions, as discussed in Chapter 3. Given that the differences in predictions are small, especially where the turbulence is specified so as to give a similar level in the vicinity of the turbine; it is not considered necessary, or economical, to use the RSM model with its much longer run time if only the performance characteristics of the turbine are of interest. Chapters 7 and 8 will investigate whether there is a considerable difference in the swirl and wake characteristics predicted by each model.

7 Swirl Characteristics

This chapter evaluates the swirl characteristics in the wake of each turbine by considering the swirl number, the swirl decay, the decay of maximum tangential velocity, the vortex type and the dynamic pressure profiles.

As discussed in Section 4.4, the swirl number, S , is calculated over the swept area of the turbine at a number of x/D positions, where x is the downstream distance and D is the turbine diameter. Since the level of swirl was unknown, both the RSM and SST models were used for this work. The RSM model is recommended for highly swirling flows, whilst the SST model, incorporating isotropic turbulence is suitable for low swirl. Comparisons between the two models are given for the main points of interest.

7.1 Swirl Number

Figure 7.1a shows how the Swirl number varies with λ and downstream distance for the 2 bladed turbine, based on the RSM model. Close to the turbine, at $x/D=0.1$, the swirl varies with λ with a similar trend to that of C_{θ} , peaking at the same λ of 2.43, with a swirl number of 0.17. However, at very low values of λ , below 1, the swirl is in the same direction as the rotation of the turbine and the opposite direction to the flow further downstream of the turbine. This is due to recirculation zones behind the turbine blades which occur at very low rotational speeds as shown in Figure 7.1b. Equation 3.7 shows the equation for the calculation of swirl number. If the negative axial velocities were removed from the calculation then the swirl number would be 0 at a λ of 0.49 and 0.03 at a λ of 0.97. At values of λ of 1.45 and above, the only recirculation zone is behind the hub. At all values of λ above 1, the swirl is highest at $x/D=0.1$, decreasing with increasing downstream distance. At downstream distances between $x/D=10$ and $x/D=40$, the λ at which peak swirl occurs has increased to around 4, before decreasing with further increases in downstream distance, again reaching 2.43 at $x/D=25$.

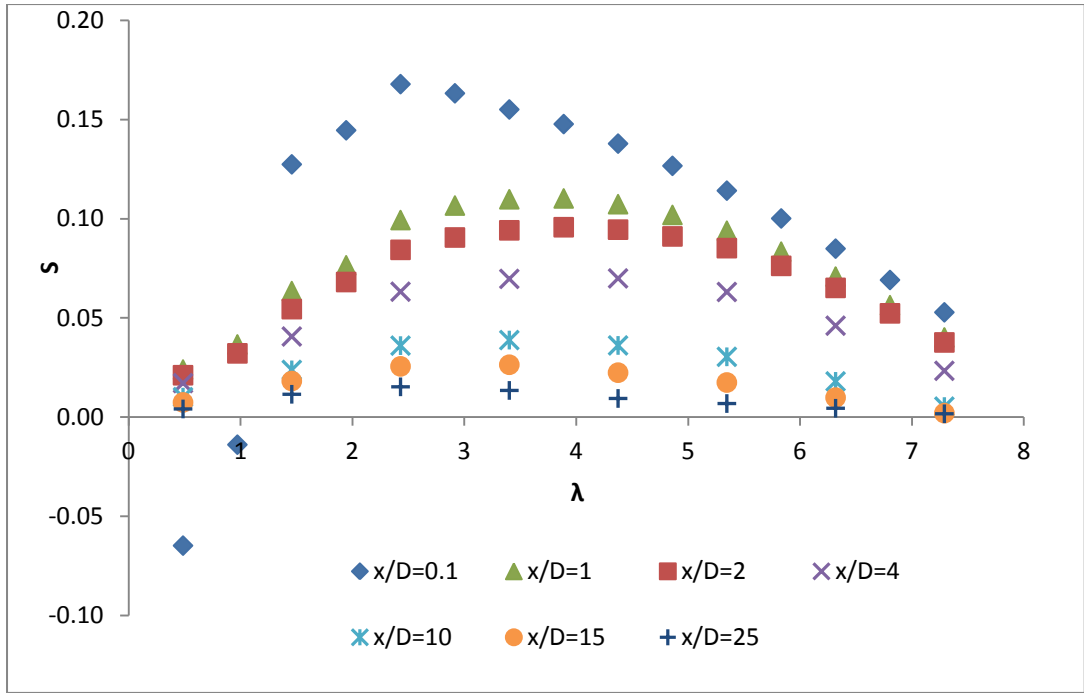


Figure 7.1a Variation of swirl number with downstream distance for the 2 bladed turbine

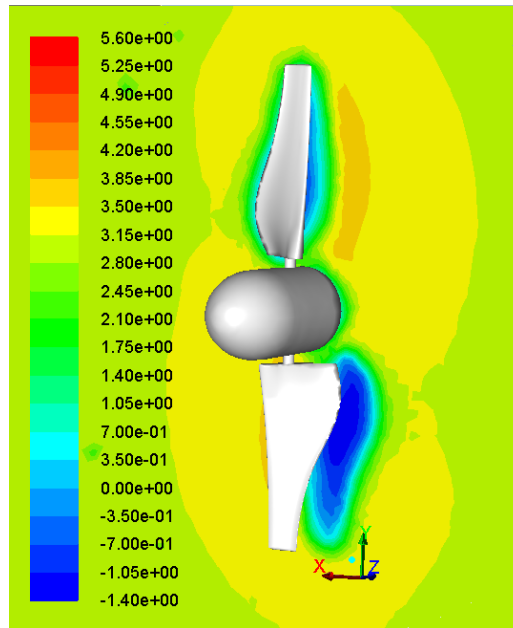


Figure 7.2b Recirculation zones behind turbine blades at $\lambda=0.49$

Figure 7.2 compares the swirl number at $x/D=0.1$ downstream of the rotational plane of the turbine, for both the RSM and SST models. The peak swirl number predicted by the SST model is slightly lower, at 0.156, compared with 0.167 for the RSM, i.e. a reduction of 6.6%. As with the RSM model, at a λ of 0.49, the swirl

predicted by the SST model is of the opposite direction to that at λ above 1 but its magnitude is slightly reduced. At a λ of 0.97, the direction of swirl predicted by the SST model is opposite to that predicted by the RSM model but the magnitude is similar and is again small. The differences at these low values of λ are likely to be mostly due to the difference in turbulent intensity in each model since the blades are moving so slowly that the ambient flow conditions are dominant. At all values of λ above 1, the values of S predicted by each model are very similar, with the SST predicting slightly lower swirl numbers at λ between 1 and 5 and slightly higher swirl numbers at λ above 6. This indicates that the difference in turbulent intensity has less effect at these values of λ as the flow field is dominated by the presence of the turbine.

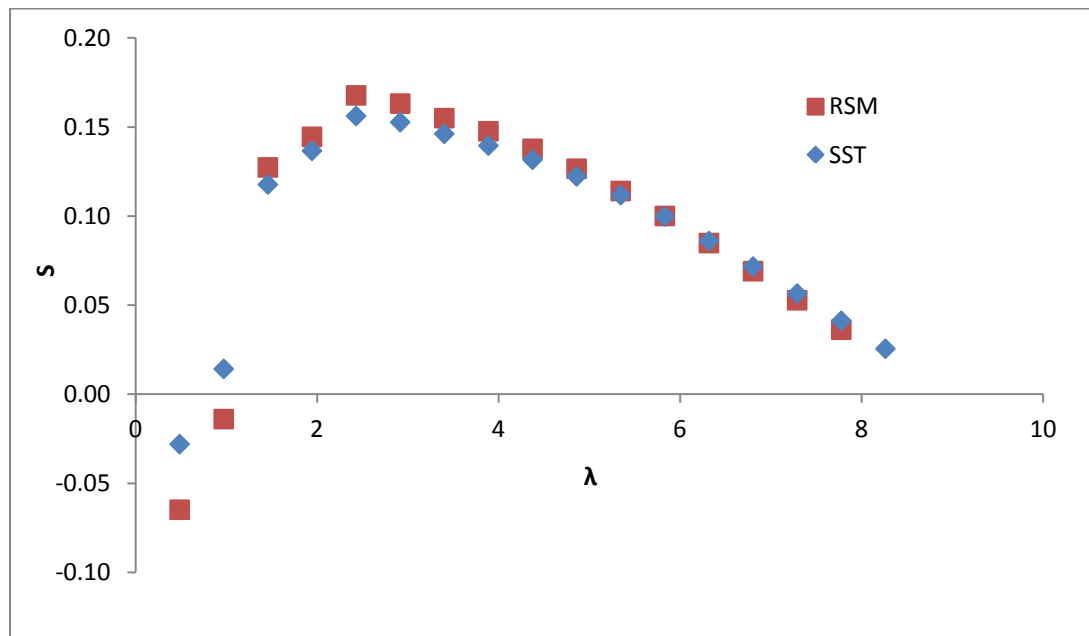


Figure 7.3 Swirl Number vs λ at $x/D=0.1$ with RSM and SST for the 2 bladed turbine

Figures 7.3 and 7.4 show how the swirl number varies with λ and downstream distance for the 3 and 4 bladed turbines.

Close to the turbine, at $x/D=0.1$, the swirl again varies with λ with a similar trend to that of C_θ , peaking at the same λ of 1.94 for the 3 bladed turbine, with a swirl number of 0.23, and λ around 1.8 for the 4 bladed turbine, with a swirl number of 0.28.

As with the 2 bladed turbine, at the lowest λ , 0.49, the swirl at $x/D=0.1$ downstream of the 3 bladed turbine is in the same direction as the rotation of the turbine and the opposite direction to the flow further downstream of the turbine. This is again due to recirculation zones which occur at very low rotational speeds. The size of these zones has decreased due to the increased blade pitch angle and the positive swirl imparted to the flow has increased due to the additional blade. Therefore, the relative effect of the recirculation zones is reduced resulting in a lower magnitude of negative swirl at a λ of 0.49 and positive swirl at a λ of 0.97. However, unlike the 2 and 3 bladed turbines, even at the lowest λ , 0.49, the swirl at $x/D=0.1$ downstream of the 4 bladed turbine is in the opposite direction to the rotation of the turbine and the same direction as the flow further downstream. This can be attributed to the further reduction in size of recirculation zones from the increased blade pitch angle and an increase in positive swirl imparted by another additional blade.

For the 3 bladed turbine, at values of λ between 0.9 and 5, the swirl is highest at $x/D=0.1$, again decreasing with increasing downstream distance. At values of λ above 5, the highest swirl no longer occurs at $x/D=0.1$ but is instead further downstream, although the degree of swirl at $x/D=0.1$, 1 and 2 is very similar. This is because, although the tangential velocity has reduced from $x/D=0.1$ to $x/D=1$, the axial velocity has also reduced (within the swept area of the turbine), and by a greater amount, so the ratio of angular momentum to linear momentum is higher. The same is true for the 4 bladed turbine, although it is found to occur over more of the operational range, at values of λ above 3. This is because the reduction in axial velocity increases with the number of blades due to a higher proportion of energy extraction.

The λ at which peak swirl occurs increases with downstream distance to around 3 at $x/D=4$, for both the 3 and 4 bladed turbines, before decreasing with further increases in downstream distance, following the same trend as the 2 bladed turbine.

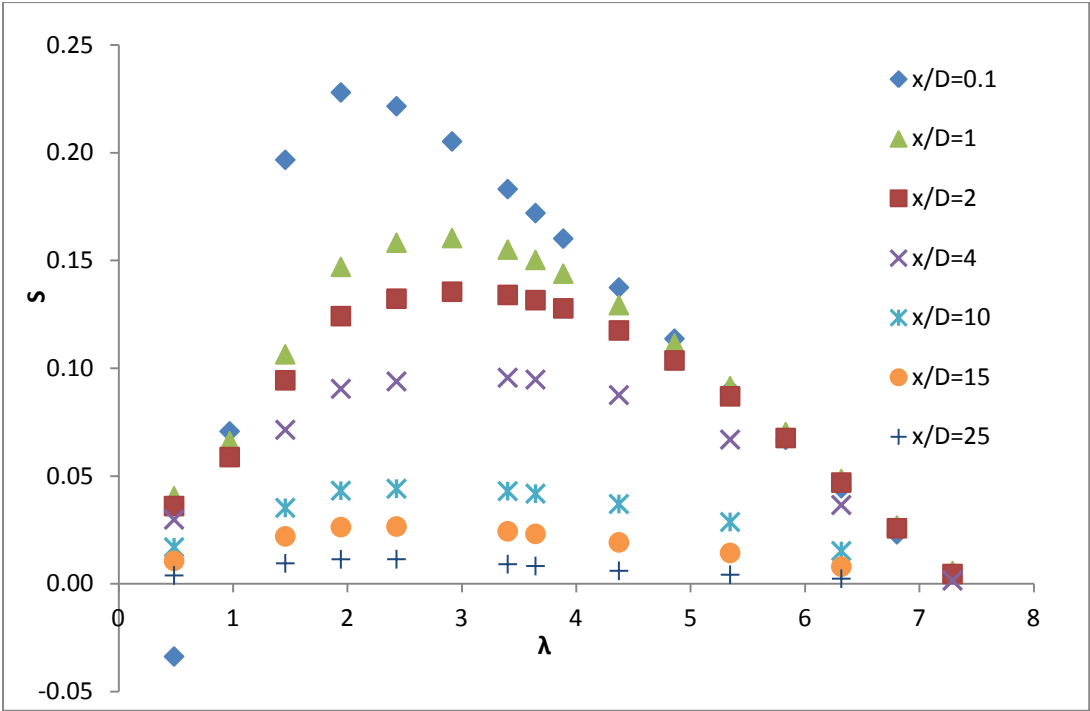


Figure 7.4 Variation of swirl number with downstream distance for the 3 bladed turbine

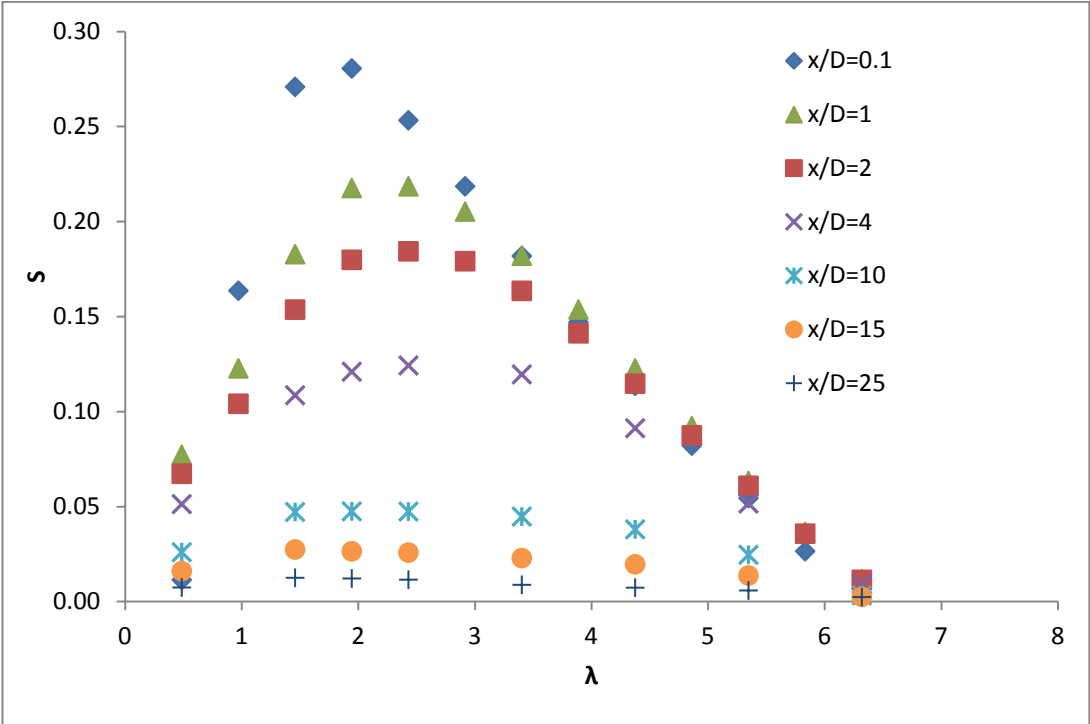


Figure 7.5 Variation of swirl number with downstream distance for the 4 bladed turbine

As for the 2 bladed turbine, Figures 7.5 and 7.6 show that the peak swirl predicted by the SST model at 1m downstream of the turbine is lower than that predicted by the RSM model for the 3 and 4 bladed turbines. The peak swirl number predicted by the SST model for the 3 and 4 bladed turbines are 0.21 and 0.37 respectively, 6.4% and 5.1% lower than with the RSM model.

The trends shown for the 2 bladed turbine are again evident with the SST model predicting higher swirl numbers than the RSM model for values of λ near start up and freewheeling, with higher predictions at λ below 1 and above 5.5 for the 3 bladed turbine and below 1 and above 4 for the 4 bladed turbine. Again, the difference in predicted S is greater at the lowest values of λ and again is likely to be due to the greater effect of differing turbulence predictions at these low rotational speeds.

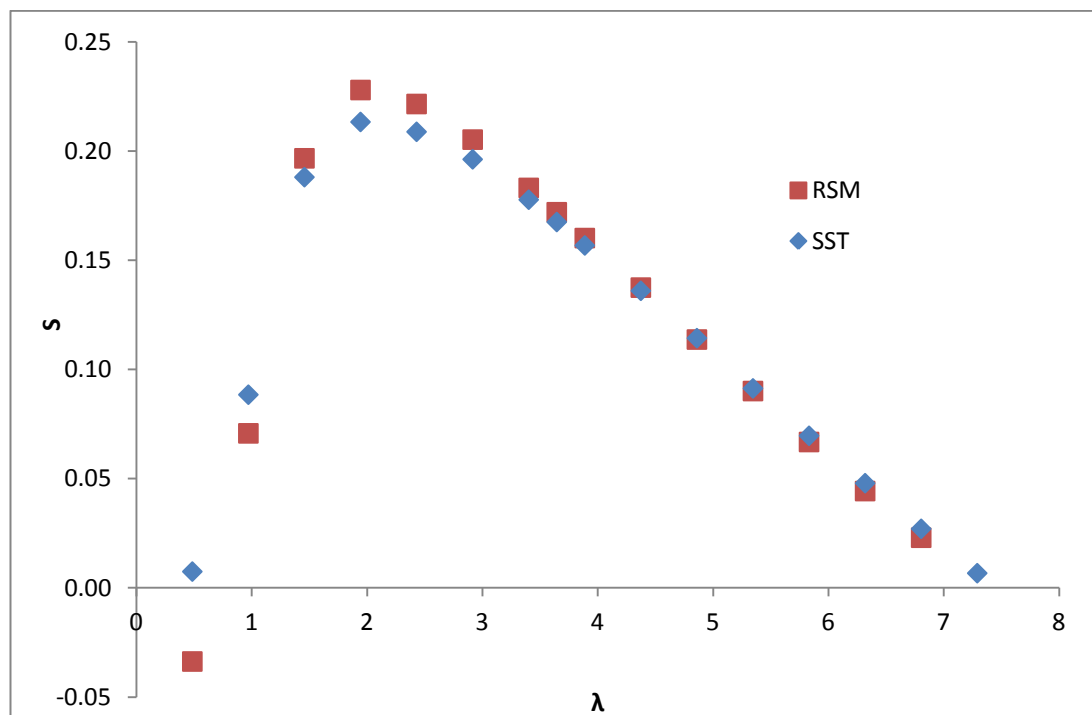


Figure 7.6 Swirl Number vs λ at $x/D=0.1$ with RSM and SST for the 3 bladed turbine

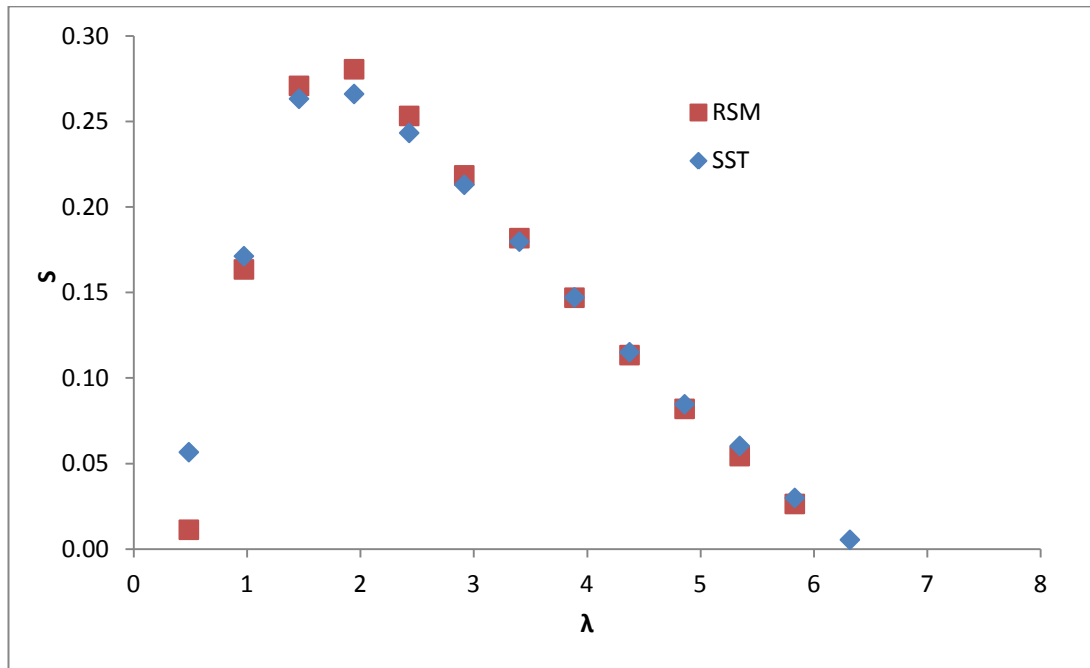


Figure 7.7 Swirl Number vs λ at $x/D=0.1$ with RSM and SST for the 4 bladed turbine

Figure 7.7 compares the swirl number against λ at $x/D=0.1$ for the 2, 3 and 4 bladed turbines with the RSM model. Maximum swirl number is shown to increase with the number of blades. The maximum calculated values of S are 0.168, 0.228 and 0.281 for the 2, 3 and 4 bladed turbines respectively, indicating that the turbine generates either a very weak swirl ($S < 0.2$) or weak swirl ($0.2 < S < 0.5$). As discussed in Chapter 3, this means that the tangential component of velocity is decoupled from that of the axial velocity; hence the length of the wake cannot be inferred from knowledge of the swirl number. However, Gupta et al (1984) have shown that for a stronger swirl flow, i.e. $S \geq 0.3$ the tangential velocity starts to become coupled with the axial velocity, hence the stronger the swirl, the faster the decay in the wake length. The swirl number of the 4 bladed turbine is close to this threshold and therefore it is possible that for some turbine designs, the wake recovery will be related to the swirl number. Furthermore, since this work is based on a constant velocity, it is not possible to state whether S is independent of u from this particular

study, as C_θ , C_p and C_t have been shown to be by Mason-Jones et al. (2012). Higher levels of swirl could therefore occur at different flow velocities.

Figure 7.7 also shows the negative values of S at the two lowest values of λ for the 2 bladed turbine and the lowest value of λ for the 3 bladed turbine with no negative values for the 4 bladed turbine. As discussed above, this is due to the decreasing ratio of negative swirl in the recirculation zones behind the blades to positive swirl imparted by the blades, with an increasing number of blades. Similar trends are observed with the SST model as shown in Appendix B.

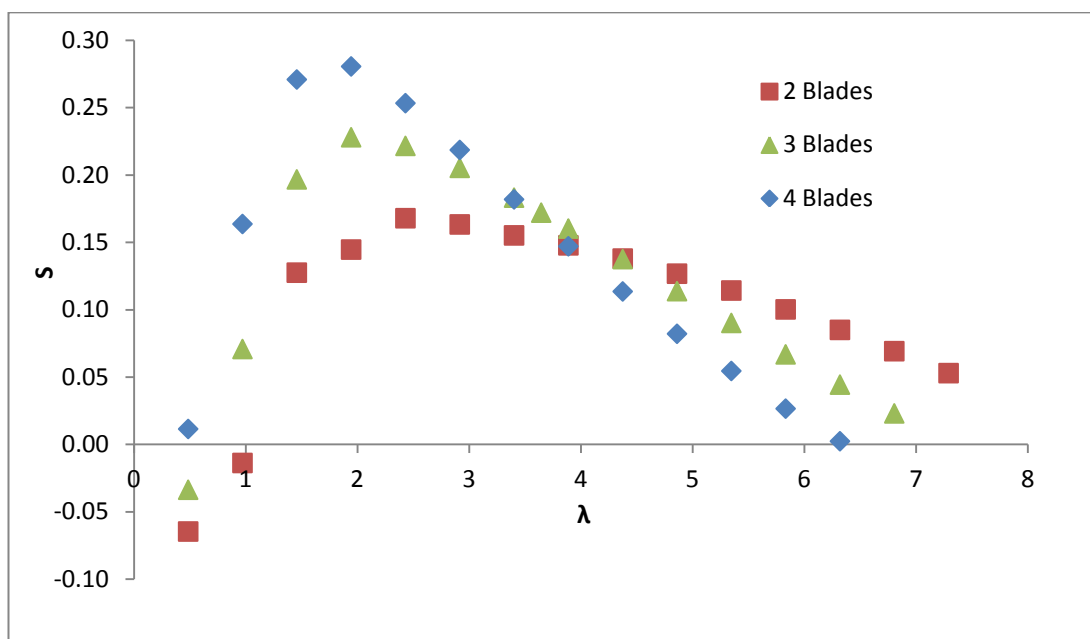


Figure 7.8 Swirl Number vs λ at $x/D=0.1$ for the 2, 3 and 4 bladed turbines

Figure 7.8 shows the λ at which peak swirl occurs for each downstream location for the 2, 3 and 4 bladed turbines with the RSM. It is clear that all three turbines follow the same trend where the λ which produces the maximum swirl at $x/D=0.1$, does not produce the highest swirl at downstream distances between $x/D=1$ and $x/D=10$. This is because the λ which produces the highest swirl at $x/D=0.1$ also results in a more rapid decay in swirl than at other values of λ . The λ at which peak swirl occurs reaches a maximum at around $x/D=4$ for all three turbines, before decreasing with a further increase in downstream distance. The λ which produces the most swirl at downstream distances of $x/D=15$ and above is slightly higher than that which

produces maximum swirl at $x/D=0.1$ for the 2 and 3 bladed turbines, and slightly lower for the 4 bladed turbine.

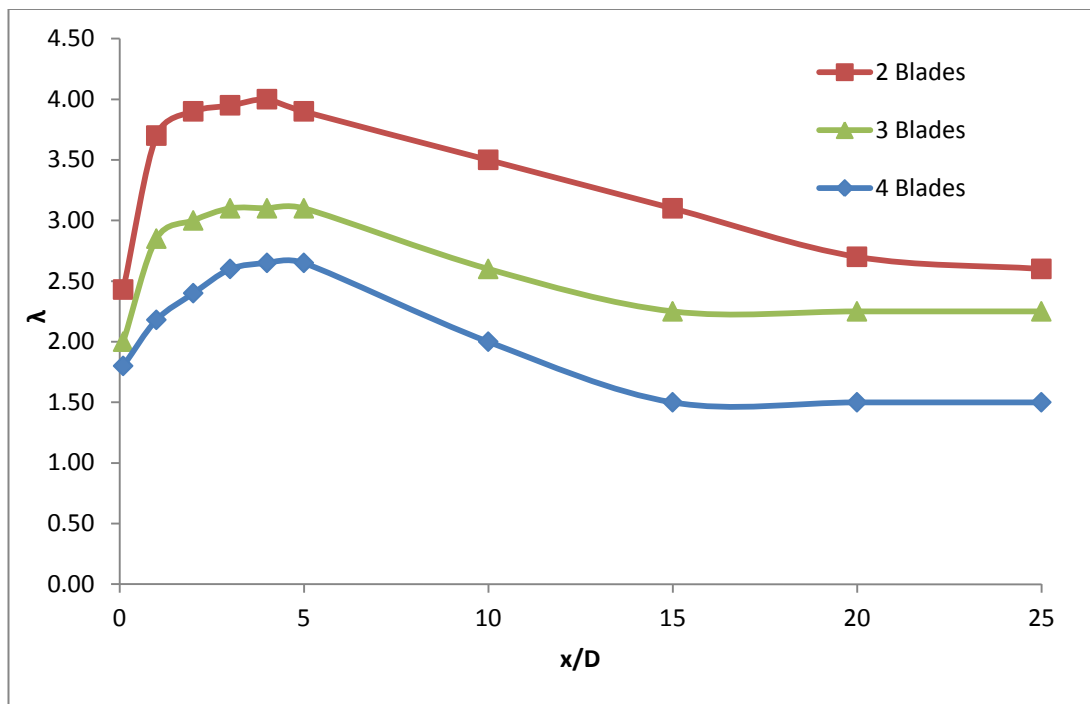


Figure 7.9 λ at which peak swirl occurs for each downstream location for the 2, 3 and 4 bladed turbines

As stated in Chapter 6, the models with a fixed minimum turbulence were run at peak power. In addition, they were also run at peak swirl to investigate the effect of ambient turbulence on swirl predictions. Figure 7.9 shows peak swirl predicted by the minimum turbulence models along with the predictions of the original models for each turbine configuration. The maximum swirl numbers predicted by each model are close, and they all show an increase in S with increasing number of blades. The largest relative difference in values predicted by the two original models is 6.6% for the 2 bladed turbine. For both of the original models and the SST fixed minimum turbulence model the increase in S with number of blades is almost linear although there is a slight reduction in the increase between 3 and 4 blades compared with the increase from 2 to 3 blades. This is to be expected since it is not feasible for the swirl number to increase linearly with a continually increasing number of blades. However, the RSM fixed minimum turbulence model shows a

greater increase in S from 3 to 4 blades than from 2 to 3 blades. This suggests that the sensitivity of S to the turbulence intensity, at $x/D=0.1$, increases with the number of blades when using the RSM model as the results get further from those predicted by the other models. This could be because S is more sensitive to turbulence at lower values of λ with the RSM model, than with the SST model

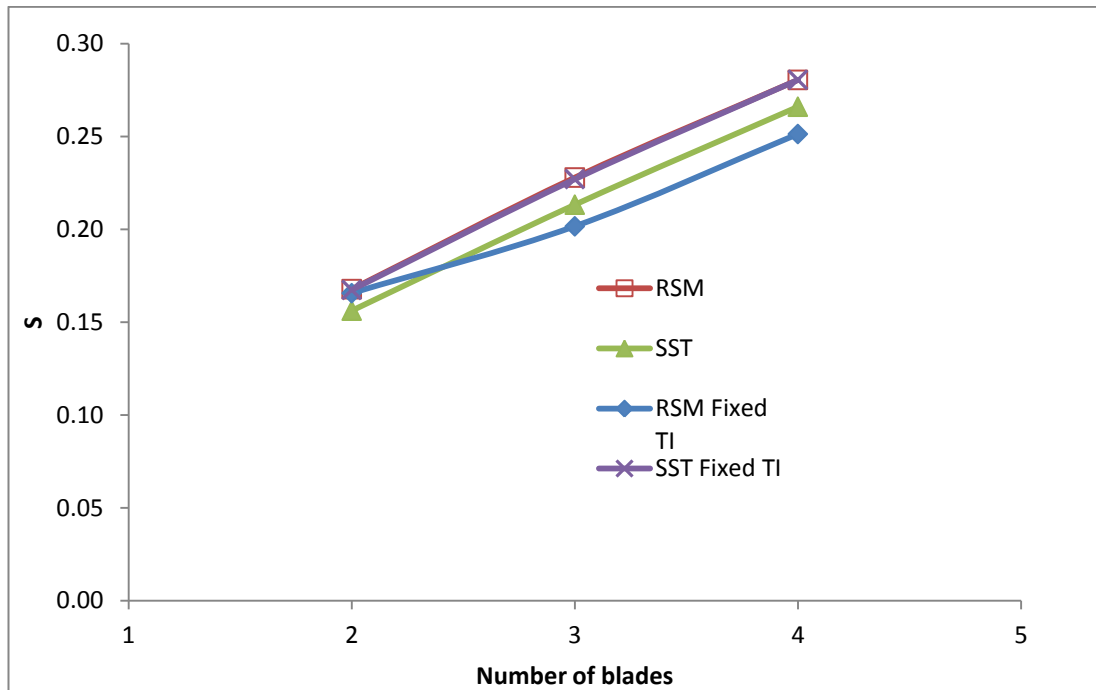


Figure 7.10 Peak swirl number vs number of blades for each model

At peak power the predicted swirl numbers are very close, and again, all models show an increase in S with the number of blades, as seen in Figure 7.10. Unlike at peak swirl, at peak power, there is a reduction in the rate of increase from 3 to 4 blades shown for all models and the change in this rate is much greater. The greater change in rate at peak power is expected since there is a greater difference in λ for each turbine than at peak swirl. The RSM fixed minimum turbulence results are closer to those of the other models than at peak swirl, indicating a reduction in the dependence of S on turbulence at higher rotational speeds.

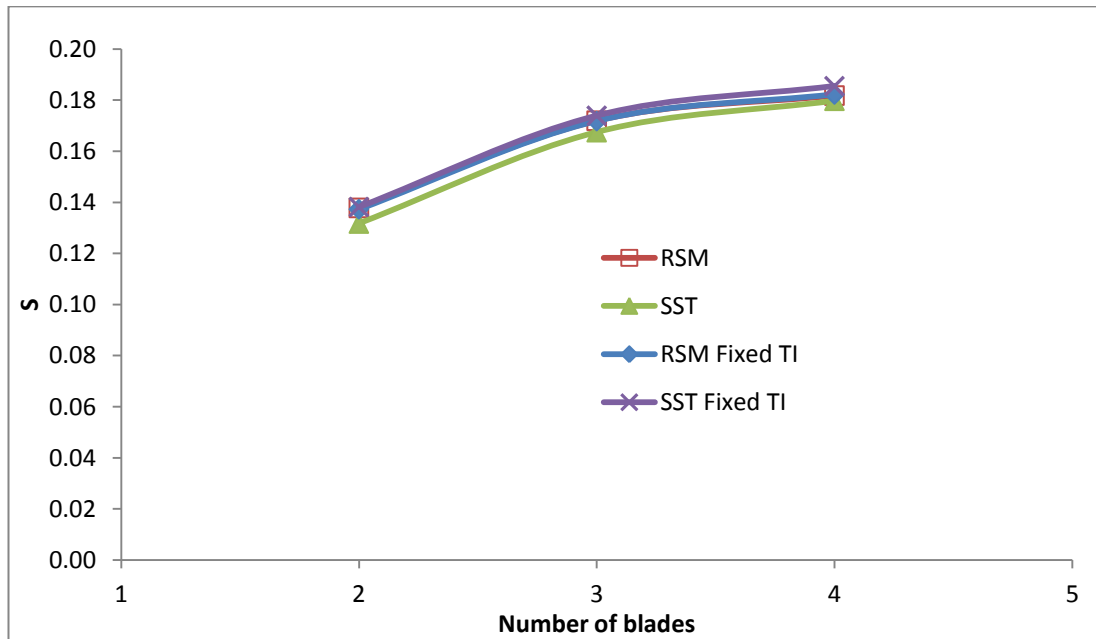


Figure 7.11 Swirl at peak power vs number of blades for each model

7.2 Swirl Decay

Figure 7.11 compares the swirl decay for the λ which coincide with peak S , $\lambda=2.4$ and peak C_p , $\lambda=4.4$, for the 2 bladed turbine using the RSM model. At $\lambda=2.4$ the swirl at $x/D=0.1$ is higher, at 0.17, compared with 0.14 at $\lambda=4.4$. However, the initial decay in swirl is more rapid at $\lambda=2.4$ and hence the swirl is lower for downstream distances between $x/D=1$ and $x/D=5$. At downstream distances above $x/D=5$, the predicted swirl numbers are close for both values of λ and above $x/D=15$ the differences between the predictions are negligible. This suggests that S is only affected, marginally, by λ in the near wake region.

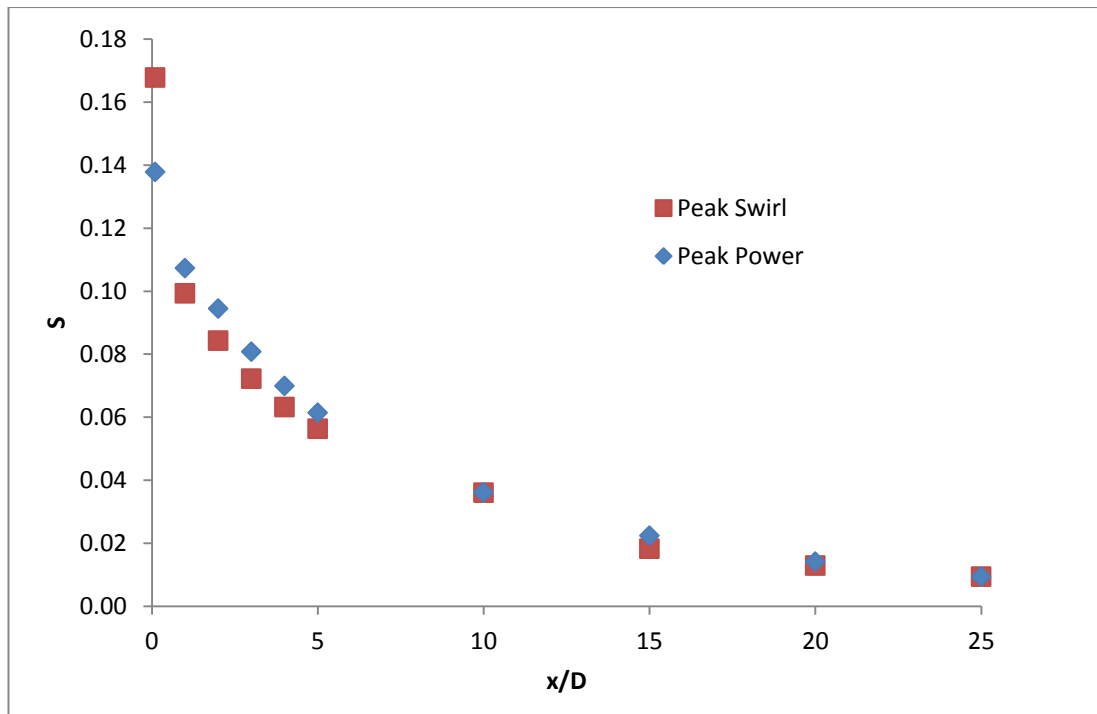


Figure 7.12 Swirl decay at peak swirl and peak power for the 2 bladed turbine

Figures 7.12 and 7.13 compare the swirl decay for the λ which coincide with peak C_θ and peak C_p , for the 3 and 4 bladed turbines.

At $x/D=0.1$ downstream of the 3 bladed turbine, the swirl at peak power is 0.17 compared with a peak swirl of 0.23. For the 4 bladed turbine the swirl at $x/D=0.1$ is 0.18, 0.1 lower than the peak swirl of 0.28. The difference between S at peak swirl and at peak power is therefore increasing with the number of blades meaning that S is more sensitive to λ at higher σ , as also shown by Figure 7.14.

For the 3 bladed turbine the initial decay in swirl is again more rapid at peak swirl. However, unlike with the 2 and 3 bladed turbines, at peak power, the swirl downstream of the 4 bladed turbine shows very little decay at downstream distances close to the turbine. This is again because although the tangential velocity has reduced from $x/D=0.1$ to $x/D=1$, the axial velocity has also reduced, and by a greater amount, so the ratio of angular momentum to linear momentum is higher at $x/D=1$. This occurs over more of the operational range for the 4 bladed turbine than for the 3 bladed turbine and does not occur within the operational range for the 2 bladed turbine as the 4 bladed turbine extracts the highest proportion of

energy from the flow, and therefore has the greatest axial velocity deficit, as discussed further in Chapter 8.

As with the 2 bladed turbine, other than immediately downstream of the turbine, the predicted swirl numbers are close at peak swirl and peak power for both the 3 and 4 bladed turbines. There is very little difference in S at downstream distances of $x/D=1$ and above for the 3 bladed turbine and $x/D=3$ and above for the 4 bladed turbine again suggesting that S is not dependent on λ outside the near wake region.

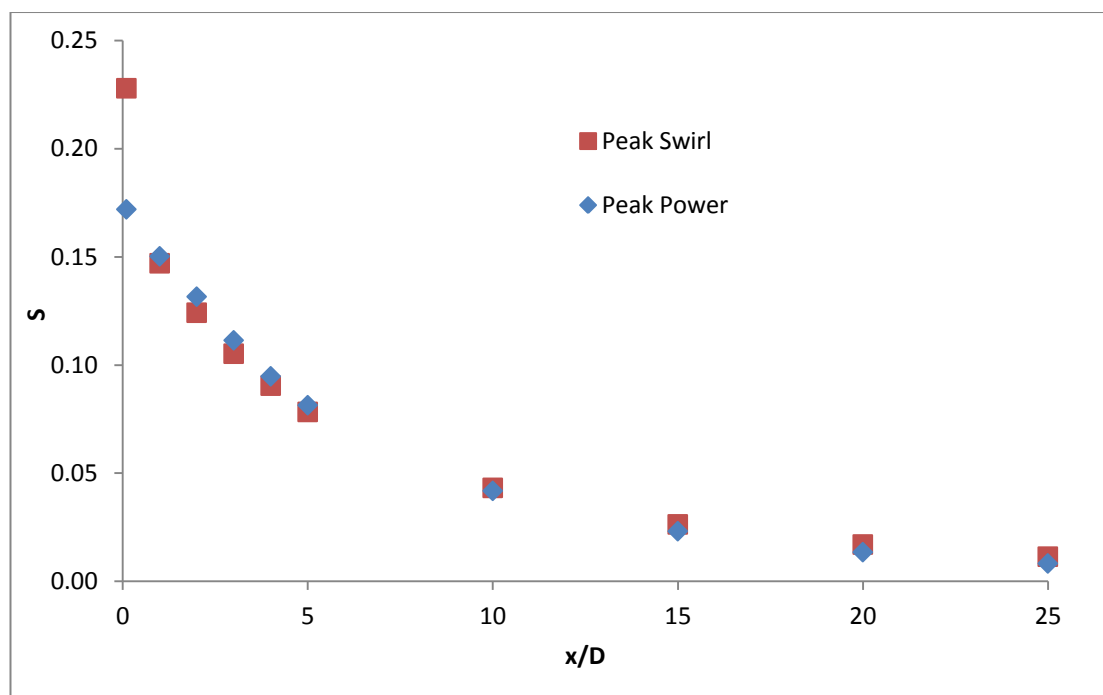


Figure 7.13 Swirl decay at peak swirl and peak power for the 3 bladed turbine

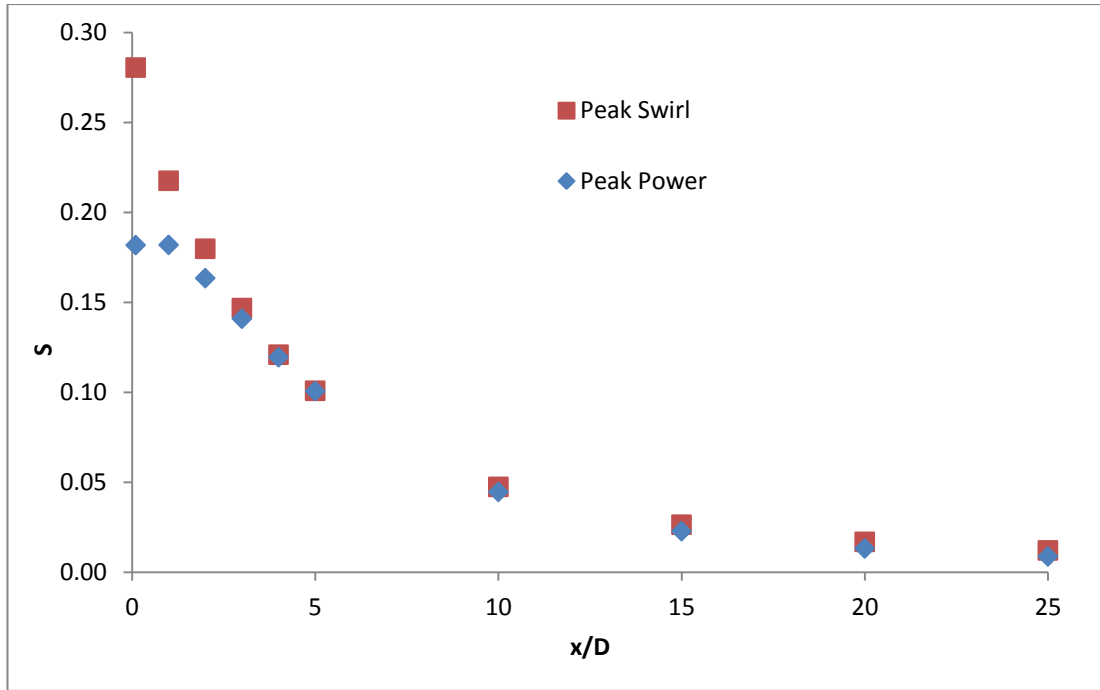


Figure 7.14 Swirl decay at peak swirl and peak power for the 4 bladed turbine

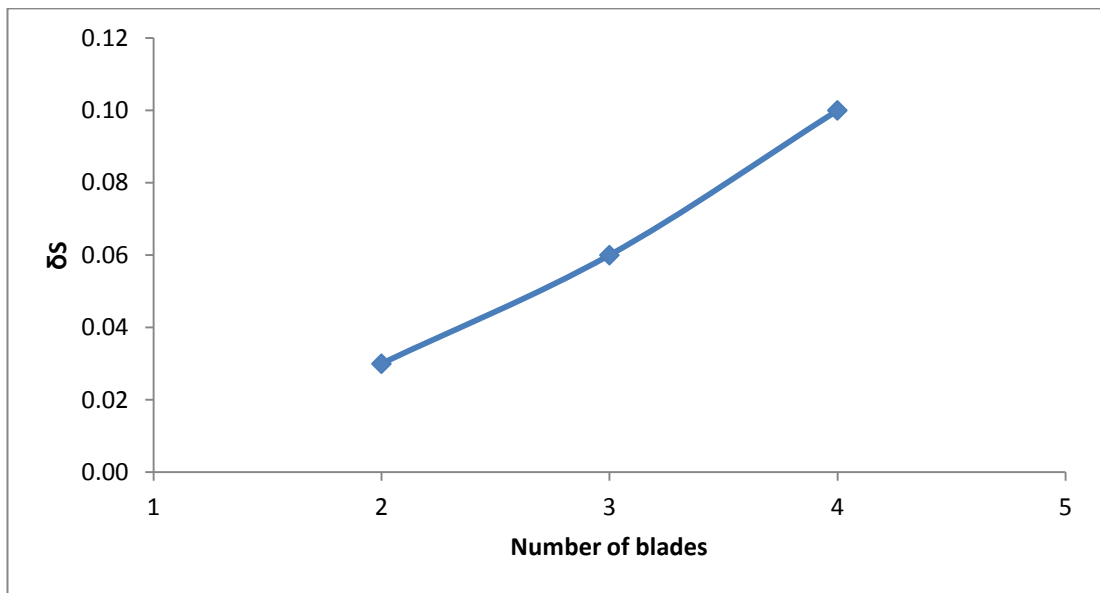


Figure 7.15 Difference between peak swirl and swirl at peak power vs number of blades at $x/D=0.1$

At the λ at which peak swirl was found to occur, the predicted decay in swirl downstream of the 2 bladed turbine is shown in Figure 7.15 for both the RSM and SST models, along with the models with fixed minimum turbulence. As stated

above, the peak swirl predicted by the SST model is lower than that predicted by the RSM. The decay in swirl predicted by the SST model is more rapid with the difference in predicted values increasing with downstream distance to $x/D = 10$ before decreasing to $x/D = 25$. The more rapid decay predicted by the SST model results in the swirl number being close to 0 by $x/D = 15$. It is clear that when the minimum turbulence is fixed, the results from each model are very close with a rate of decay between those of the original models. This is to be expected since the turbulent intensity immediately upstream of the turbine is greater than with the original RSM model and less than with the original SST model. The rate of decay is closer to that of the original RSM model for downstream distances of $x/D = 5$ and below but then moves further from the RSM and closer to the SST predictions. This is because the turbulent intensity continues to decay with downstream distance for the RSM and SST models so whilst the turbulence in the RSM model is closer to that in the fixed minimum turbulence models close to the turbine, the turbulence in the SST models becomes closer for greater values of x/D . It is therefore clear that the difference in swirl decay predicted by the RSM and SST models is mostly due to the difference in turbulence predicted by each model.

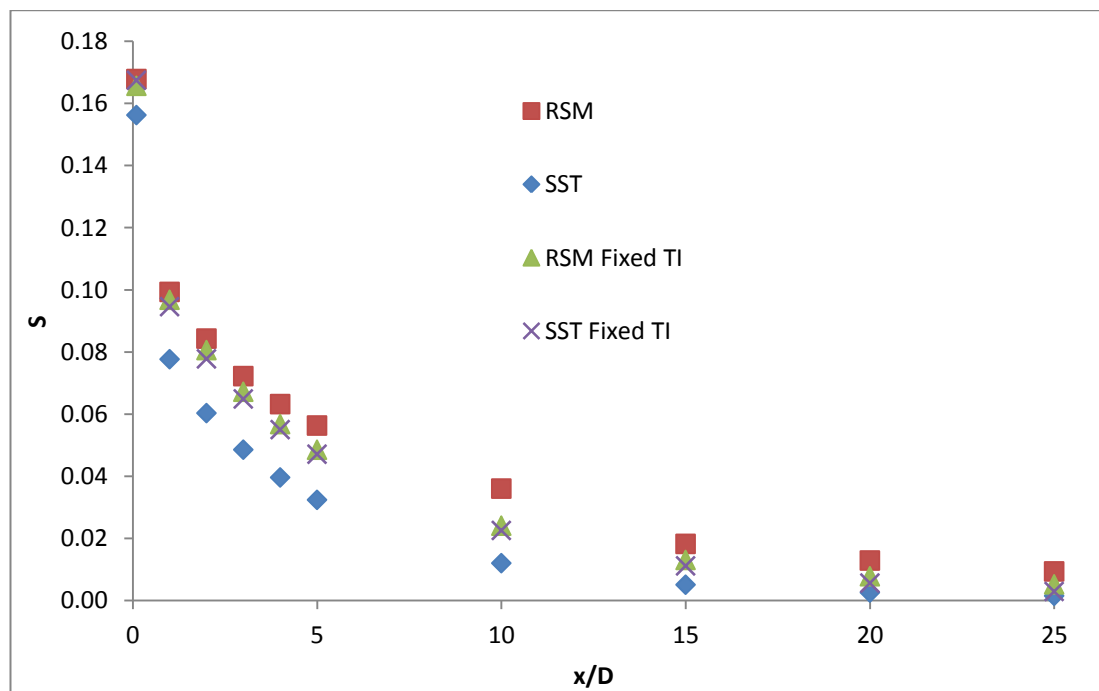


Figure 7.16 Swirl decay at peak swirl for the 2 bladed turbine with each model

Figures 7.16 and 7.17 show the decay in swirl downstream of the 3 and 4 bladed turbines at the λ at which peak swirl occurs for the each of the original models along with the fixed minimum turbulence models. As with the 2 bladed turbine, the SST model predicts a lower Swirl number at $x/D=0.1$ and a more rapid decay in swirl than the RSM model for each of the other configurations with a swirl number again close to 0 by $x/D=15$.

The difference in swirl decay predicted by the models with fixed minimum turbulence is again less than the difference in decay predicted by the original models with the decay rates predicted with fixed minimum turbulence falling between those of the original models at most downstream distances. However, at $x/D=0.1$, the swirl predicted by the RSM model with fixed minimum turbulence is slightly lower than either of the original models indicating that, close to the turbine, S is affected both by the predicted forces on the blades and the turbulent intensity.

As with the 2 bladed turbine, the decay predicted by the fixed minimum turbulence models moves further from the original RSM predictions and closer to the original SST predictions with increasing downstream distance due to the continuing decay of turbulence seen with both of the original models.

The values for the SST model with fixed minimum turbulence are higher than those for the RSM model with fixed minimum turbulence due to the higher torque and hence greater S , predicted by the SST models. The difference is greater with the 4 bladed turbine than with the 3 bladed turbine as would be expected since the difference in predicted torque also increases with the number of blades due to the disparity in the forces on each blade being multiplied by the number of blades as discussed in Chapter 6.

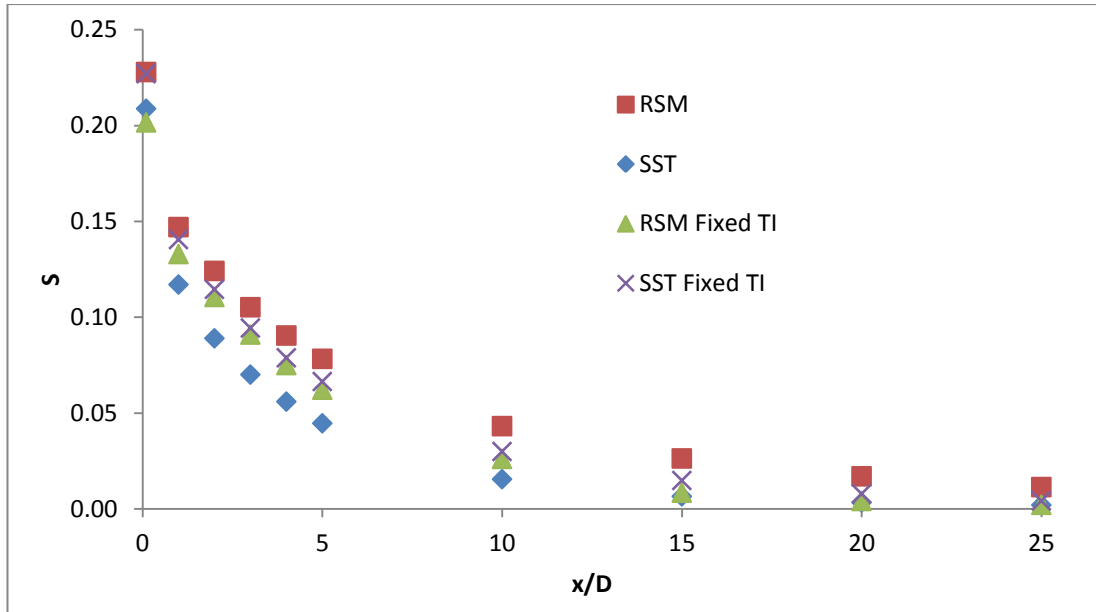


Figure 7.17 Swirl decay at peak swirl for the 3 bladed turbine with each model

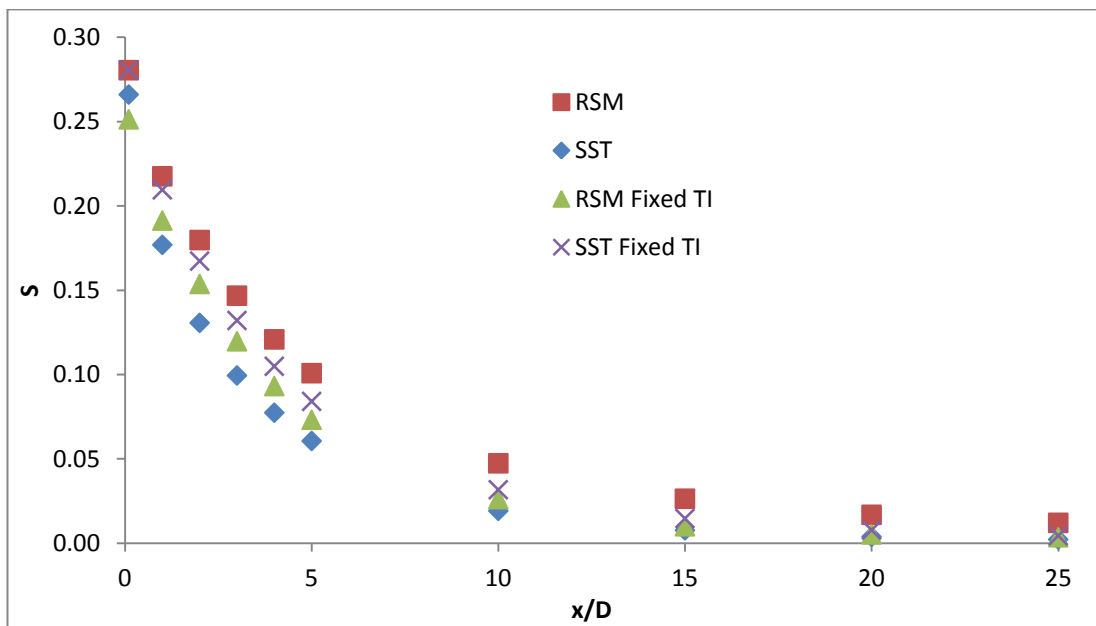


Figure 7.18 Swirl decay at peak swirl for the 4 bladed turbine with each model

Figure 7.18 compares the decay in swirl at the λ coinciding with peak swirl for the 2, 3 and 4 bladed turbines using the RSM model. It is clear that for all three turbines there is a rapid decay in swirl immediately downstream of the turbine, followed by a slow, steady decline. The peak swirl number is highest for the 4 bladed turbine and lowest for the 2 bladed turbine. This indicates that more tangential momentum

is generated compared to the axial momentum when the number of blades is increased. However, the rate of decay slows closer to the turbine for the 2 bladed turbine and further from the turbine for the 4 bladed turbine so that by $x/D=10$ the values of S for each turbine are close and by $x/D=20$ are approximately the same. Therefore the swirl number is only affected by the number of blades in the near wake region. Similar trends can be seen with the SST, and fixed minimum turbulence models as given in Appendix B.

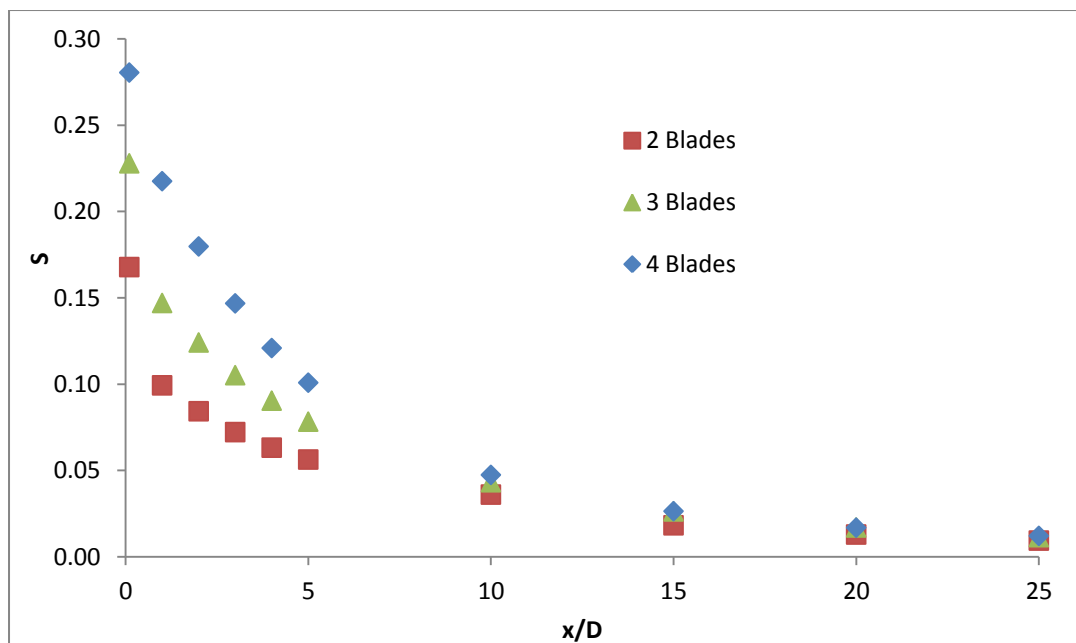


Figure 7.19 Swirl decay at peak swirl for the 2, 3 and 4 bladed turbines

At the λ which coincides with peak C_p , the swirl number predicted by the SST model at $x/D=0.1$ downstream of the 2 bladed turbine is close to that predicted by the RSM model with a difference of 4.5%, Figure 7.19. However, as at peak swirl, the decay in swirl predicted by the SST model is again more rapid than the RSM with the difference in predicted values increasing to $x/D = 10$ and the swirl number predicted by the SST model being close to 0 by $x/D=15$.

At peak power, the predicted values are again very close for both of the models with fixed minimum turbulence. As at peak swirl, the rate of decay is between those of the original models but is closer to the rate of decay of the original SST model for downstream distances of $x/D=3$ and above, whereas at peak swirl this

does not happen until much further downstream. This is because the decay in downstream turbulence is dependent on the rotational speed of the turbine, as illustrated by Figure 7.20, and therefore the point at which the turbulence in the SST model becomes closer than the RSM model to the fixed minimum turbulence models moves closer to the turbine.

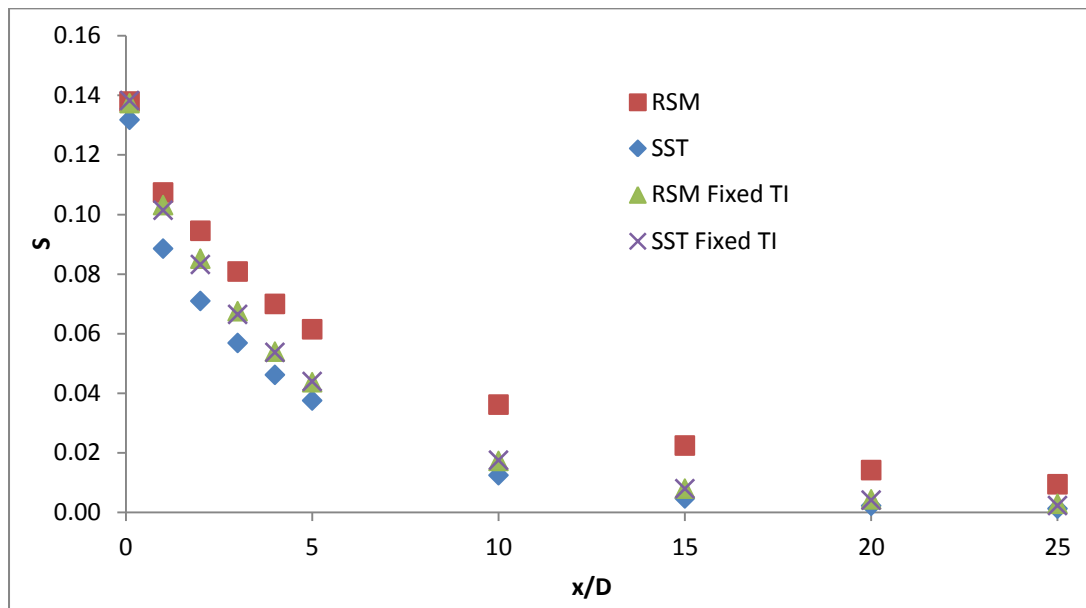


Figure 7.20 Swirl decay at peak power for the 2 bladed turbine with each model

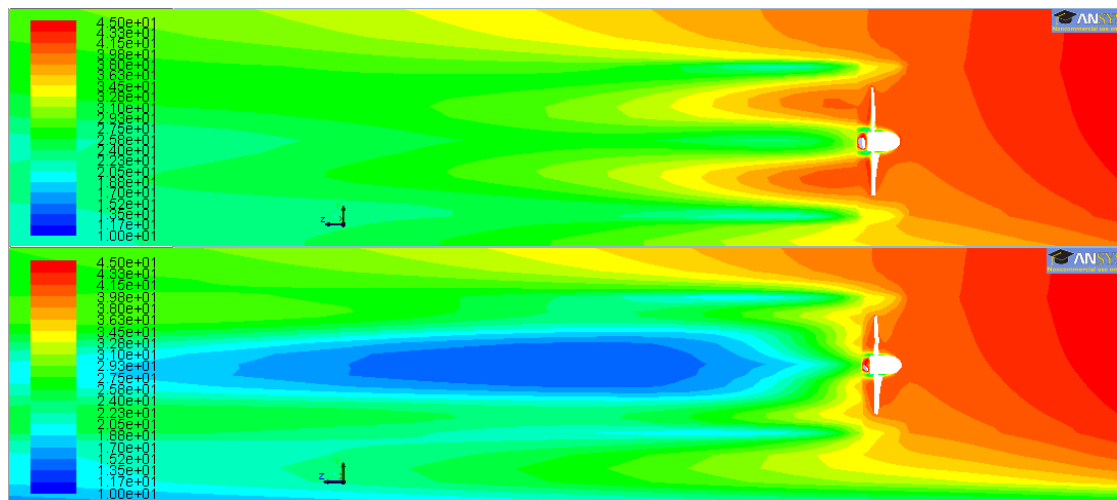


Figure 7.21 Turbulent Intensity downstream of the 2 bladed turbine at peak swirl (top) and peak power (bottom)

Figures 7.21 and 7.22 show the swirl decay downstream of the 3 and 4 bladed turbines, at the λ which coincides with peak C_p for each of the original models, along with the fixed minimum turbulence models. As for the 2 bladed turbine the swirl numbers predicted by the SST model at $x/D=0.1$ are very close to those predicted by the RSM model, with differences of 2.6% and 1.1% respectively. The decay in swirl predicted by the SST model is once again more rapid with the difference in predicted values increasing to $x/D = 5$ and the swirl number predicted by the SST model being close to 0 by $x/D=15$.

Again the difference between the predictions of each of the models with fixed minimum turbulence is very small and again the rates of decay fall between the rates predicted by the original models, confirming that the difference in S predicted by each of the original models is mostly due to differences in turbulence. As with the 2 bladed turbine the rates predicted by the fixed minimum turbulence models are closer to the rates predicted by the original RSM models at $x/D=2$ and below and closer to those predicted by the SST models for $x/D=3$ and above for both the 3 and 4 bladed turbines.

Although the lack of swirl decay between $x/D=0.1$ and $x/D=1$ downstream of the 4 bladed turbine predicted by the original RSM model is not shown with the SST or fixed minimum turbulence models, the fixed minimum turbulence models show a slower decay predicted between these downstream distances than at distances between $x/D=1$ and $x/D=5$. This is because the reduction in axial velocity between $x/D=0.1$ and $x/D=1$ is greater for lower turbulence levels as will be discussed further in Chapter 8.

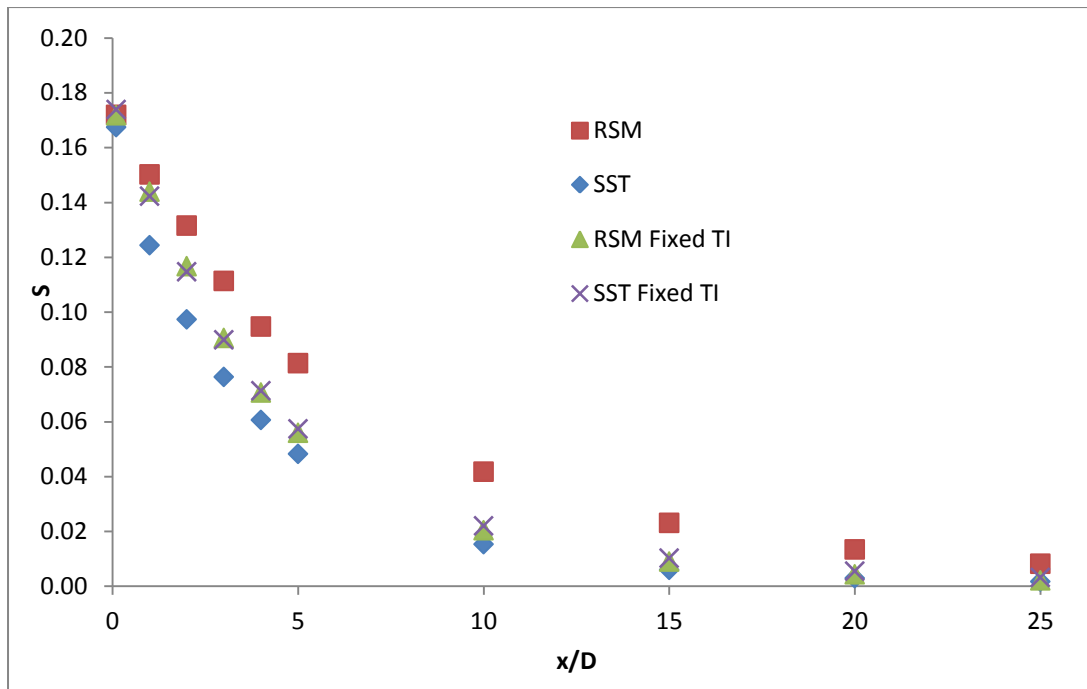


Figure 7.22 Swirl decay at peak power for the 3 bladed turbine with each model

From Figures 7.13 and 7.22 the RSM prediction of swirl number, for $x/D = 0.1$ and 1, show a lack of decay compared to all the other models. The flow off the back of the turbine for this condition must be anisotropic as the SST does not show this detail. Also the level of the fixed minimum turbulence intensity must drive the RSM to also simulate that of an isotropic flow. By fixing the minimum turbulence intensity there are clearly advantages by not allowing the turbulence to decay when in reality it wouldn't, but this also raises a possible disadvantage of anisotropic characteristics being smothered.

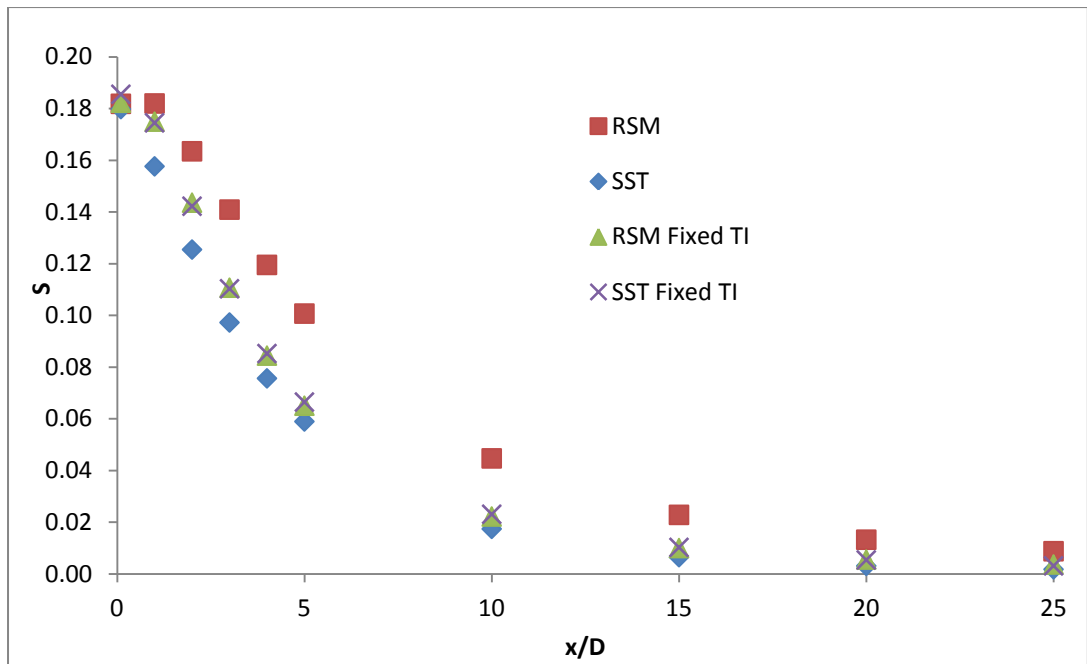


Figure 7.23 Swirl decay at peak power for the 4 bladed turbine with each model

Figure 7.23 shows that at peak power the swirl number is still highest for the 4 bladed turbine and lowest for the 2 bladed turbine. However, the difference between the peak swirl numbers has decreased from those at peak torque, with swirl numbers of 0.14, 0.17 and 0.18 for the 2, 3 and 4 bladed turbines respectively compared with 0.17, 0.23 and 0.28 at peak torque. S is therefore more dependent on σ in the near wake region at peak swirl than at peak power, due to greater differences in C_{θ} .

At downstream distances of $x/D=1$ and above, similar trends to those found at peak torque are apparent, with the most rapid decay in swirl occurring for the 4 bladed turbine and the least rapid for the 2 bladed turbine. However, the decay in swirl from $x/D=0.1$ to $x/D=1$ is greatest for the 2 bladed turbine, with a smaller decay for the 3 bladed turbine and no decay for the 4 bladed turbine. As discussed above, this is because at higher rotational speeds there is a more rapid reduction in axial velocity than in tangential velocity between $x/D=0.1$ and $x/D=1$. This effect increases with the number of blades, as more energy is extracted from the flow, as discussed further in Chapter 8. Similar trends can again be seen with the SST, and fixed minimum turbulence models, as given in Appendix B.

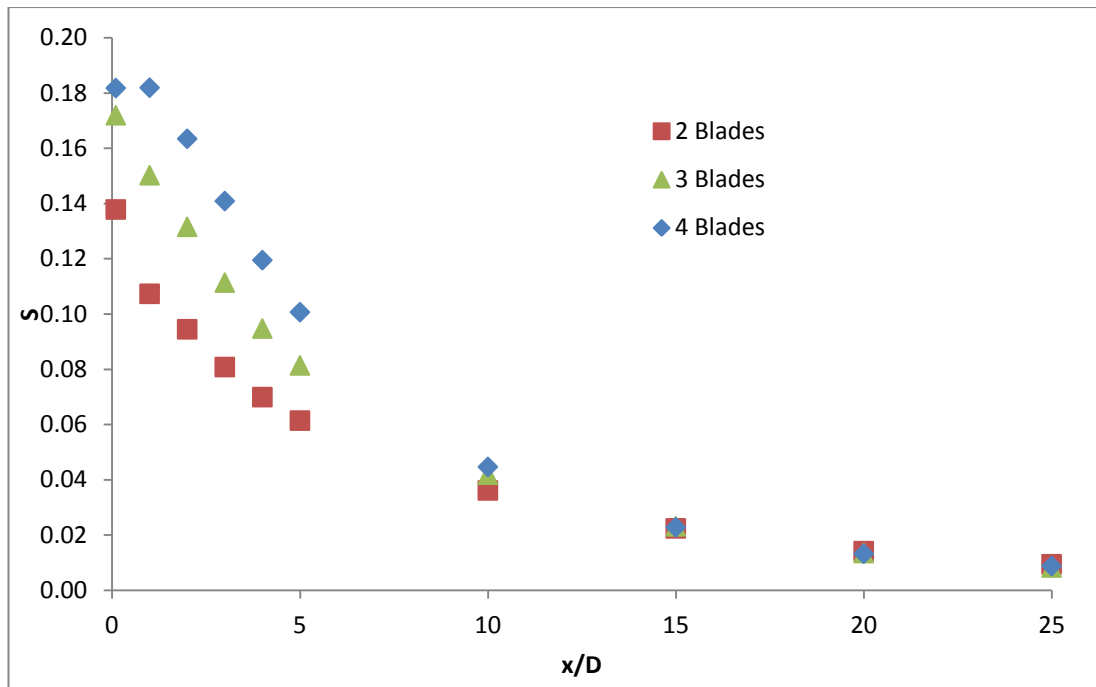


Figure 7.24 Swirl decay at peak power for the 2, 3 and 4 bladed turbines

7.3 Tangential velocity decay, W_m/W_{m0}

Overall flow characterisation of swirling flows is provided by Gupta et al. (1984) based upon experimental time-mean data provided by Chigier and Chervinsky (1967). The work presents curves detailing the downstream decay and cross-stream profiles of axial and swirl velocities and static pressure. Swirling flows can be produced by a number of methods within industry and include a wide range of applications, i.e. swirl burners, cyclones, etc. However no matter what method used to produce the swirl, the characteristics seem to collapse onto reasonably well defined profiles. The findings of this work are no different to any swirl generator where the swirl number defines a very weak swirl as can be seen in Figure 7.24, which superimposes the maximum tangential velocity at peak swirl and peak power for each turbine at each x/D , normalised to that at $x/D = 0.1$, onto the curves of Chigier and Chervinsky (1967).

It should be reiterated at this point that the swirl decay being compared in this figure represent significantly different types of swirl generators, with the curve of

Chigier and Chervinsky (1967) based upon data from swirling jets as supposed to a turbine wake. That said; similarities can be seen between the decay in maximum tangential velocities of the turbine wake and jets. With D assumed to be the turbine diameter, the decay of the turbine wake swirl velocity maximum appears to replicate that of the jet very well, with the principle characteristics of an exponential fall when x/D is small and a subsequent slow but steady decline with increasing x/D . Furthermore the majority of this decay has occurred by $x/D = 5$.

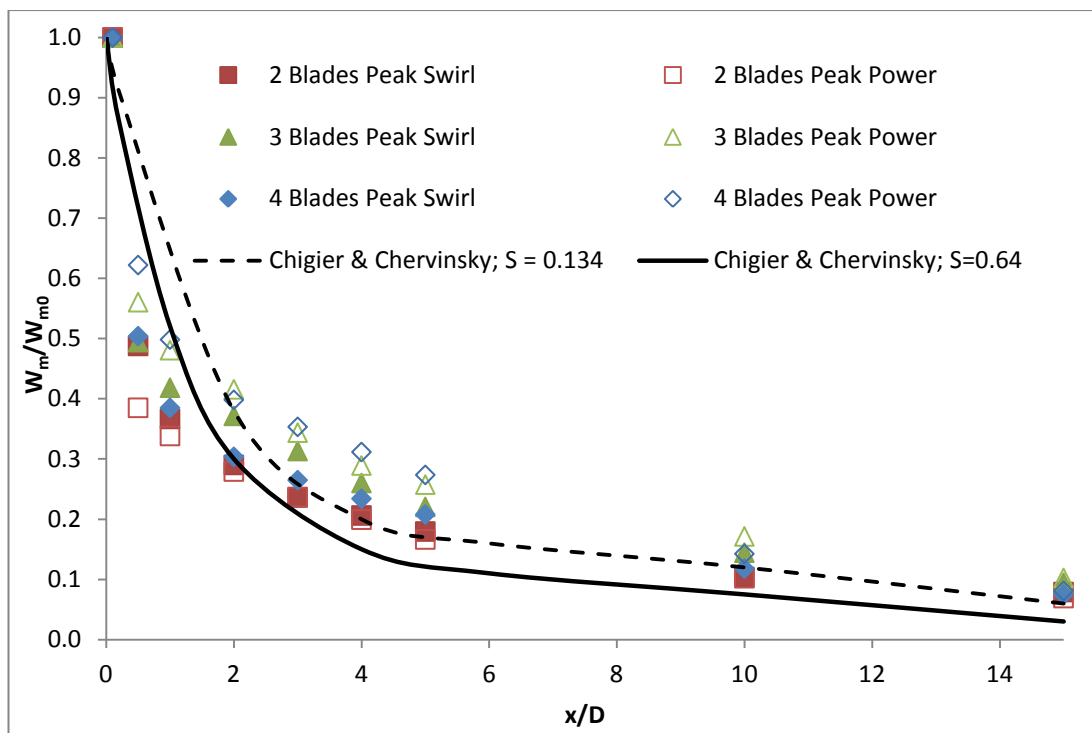


Figure 7.25 Decay of maximum tangential velocity along axis of swirling jets (Chigier & Chervinsky, 1967) & in the wake of 2, 3 and 4 bladed turbines at peak swirl & peak power

Figure 7.25 shows that the decay in maximum w follows the same trend with the SST model as with the RSM and fits even more closely with the experimental data of Chigier and Chervinsky (1967).

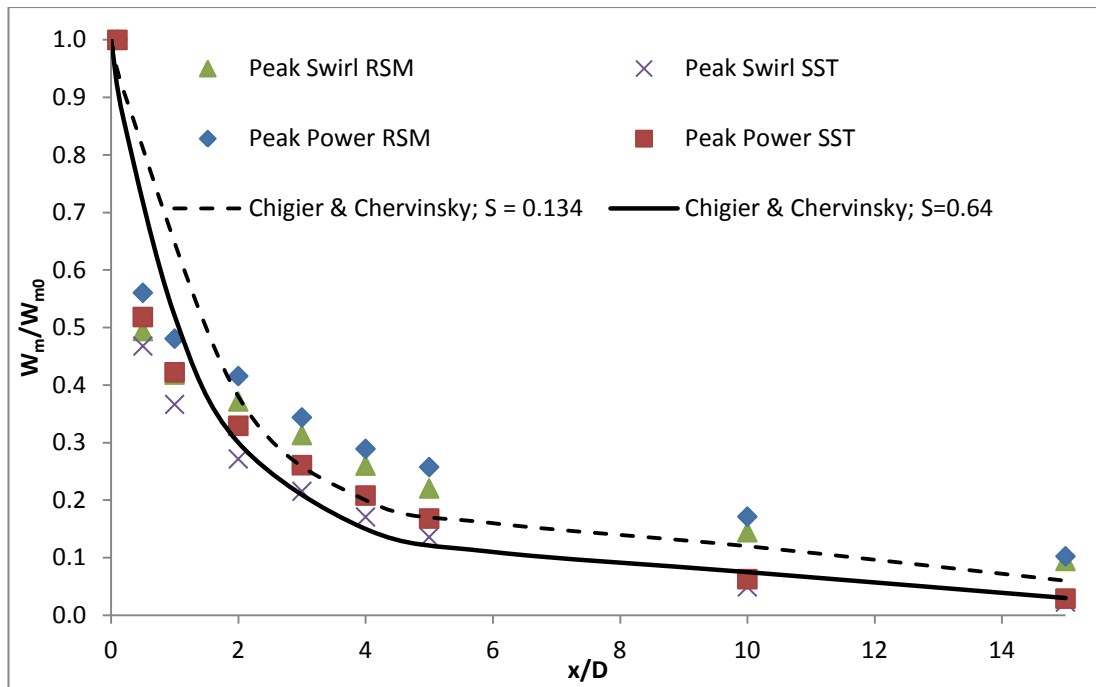


Figure 7.26 Decay of maximum tangential velocity along axis of swirling jets (Chigier & Chervinsky, 1967) and in the wake of the 3 bladed turbine at peak swirl and peak power with the RSM and SST models

7.4 Type of Vortex

Figure 7.26 shows the tangential velocity profiles taken at $x/D=1$ downstream of the 2 bladed turbine along a vertical line (y axis) and a horizontal line (x axis) at peak swirl and peak power. Maximum w is clearly higher at peak swirl than at peak power along both axes. At peak swirl maximum w along the y axis is higher than along the x axis but at peak power this is reversed as the area of maximum w rotates as the flow moves downstream and is closer to the x axis at peak power than at peak swirl, as shown in Figure 7.27 (note: maximum tangential velocity given as negative since turbine rotation is defined as positive). This is because, although the maximum tangential velocity over the swept area is higher at peak swirl than at peak power, average axial velocity is also higher meaning the area of maximum w reaches the x axis further downstream. At both peak power and peak swirl, and along both axes, w increases from $r/R=0$, reaches a maximum between $r/R=0.35$ and $r/R=0.55$ and then decreases to $r/R=1.5$, showing a classical Rankine vortex profile. On the x axis, at r/R above 1.25, the tangential velocity becomes

negative, indicating a small rotation in the opposite direction to that in the wake due to eddies shedding off the blades, before recovering towards 0 with increasing r/R . On the y axis, w remains close to 0 at r/R above 1.5.

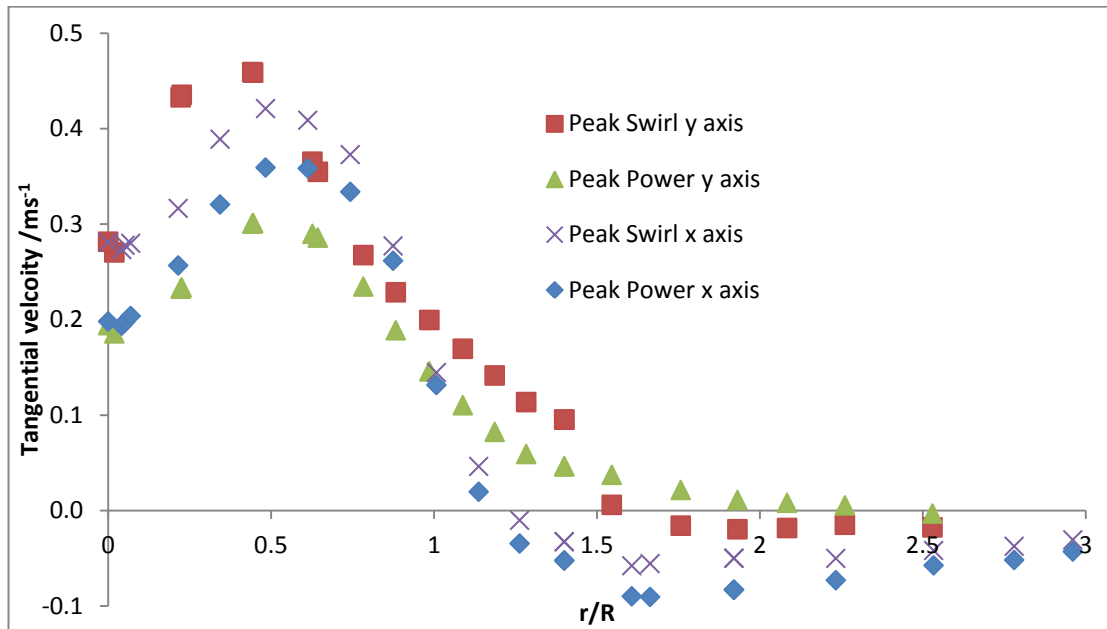
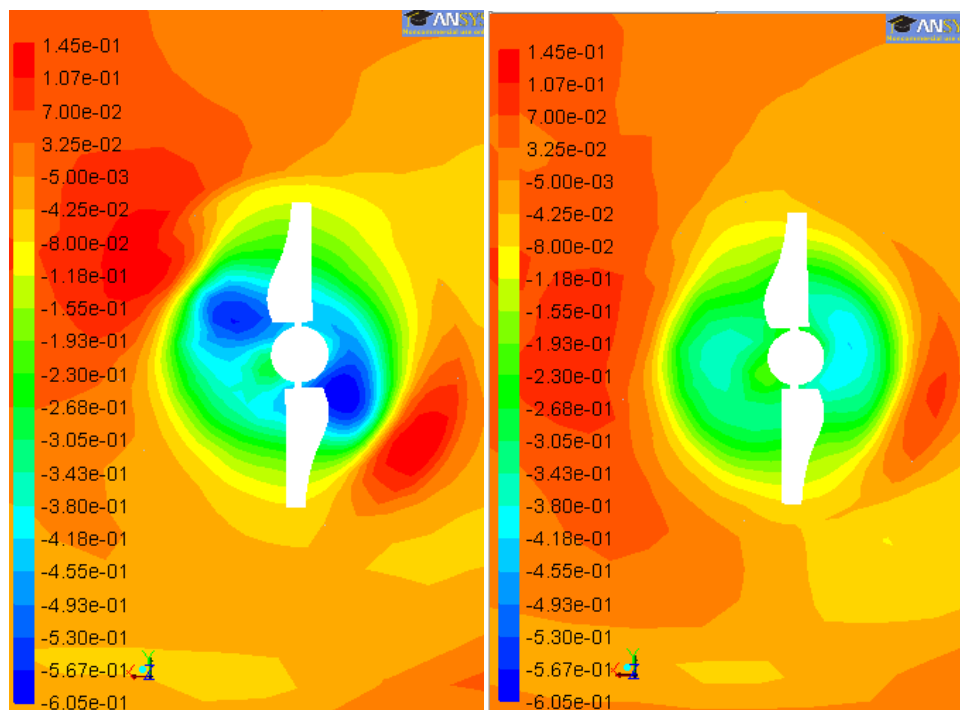


Figure 7.27 Tangential velocity profile at $x/D=1$ downstream of the 2-bladed turbine on x and y axes



(a) Peak Swirl

(b) Peak Power

Figure 7.28 Tangential Velocity Contours at $x/D=1$ downstream of the 2-bladed turbine

Figures 7.28 and 7.29 show the tangential velocity profiles taken at $x/D=1$ downstream of the 3 and 4 bladed turbines along the y and x axes at peak swirl and peak power. As with the 2 bladed turbine, maximum w is higher at peak swirl than at peak power along both axes for both of the other turbine configurations. Unlike the 2 bladed turbine, there is little difference between the profiles along the x axis and the y axis for the 3 or 4 bladed turbine. This is because the blades are physically closer and therefore the tangential velocity profile becomes more uniform over the swept area of the turbine. The tangential velocity profiles follow the same trend as those of the 2 bladed turbine but there is less variation in the radial position at which maximum w occurs, which is around $r/R=0.5$ for both the 3 and 4 bladed turbines at peak swirl and peak power along both axes. The profiles therefore demonstrate a Rankine vortex in the wake of each turbine at both peak swirl and peak power. Outside the wake region, at r/R above 1.5, w is close to 0 for both turbines.

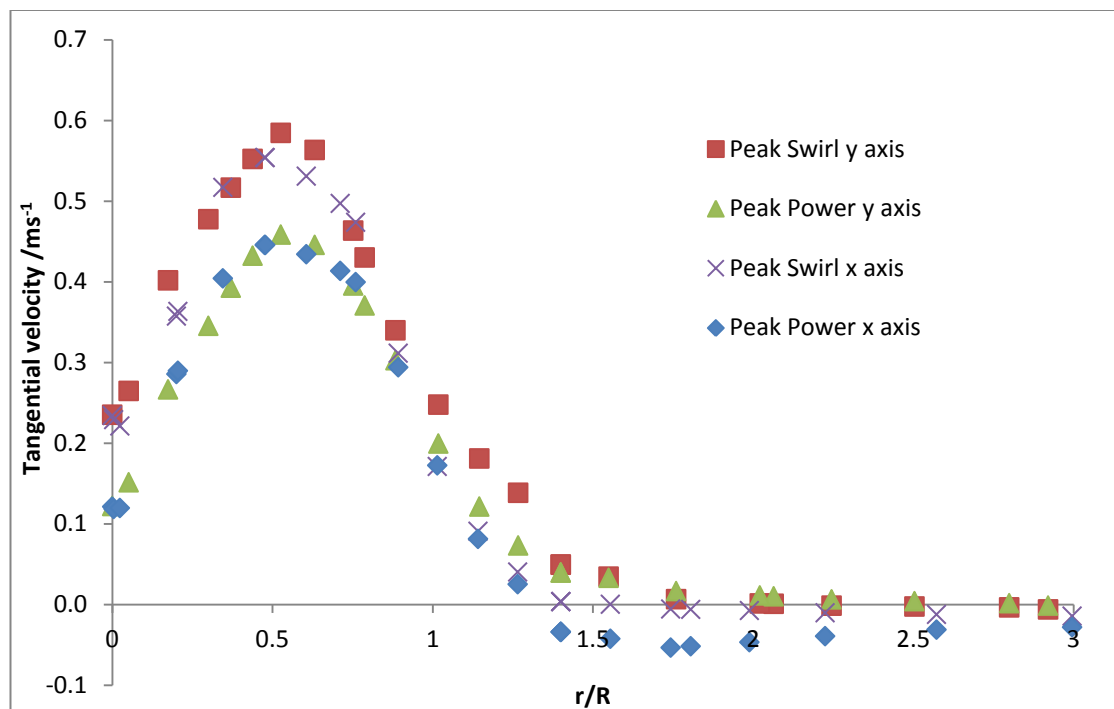


Figure 7.29 Tangential velocity profile at $x/D=1$ downstream of the 3 bladed turbine on x and y axes

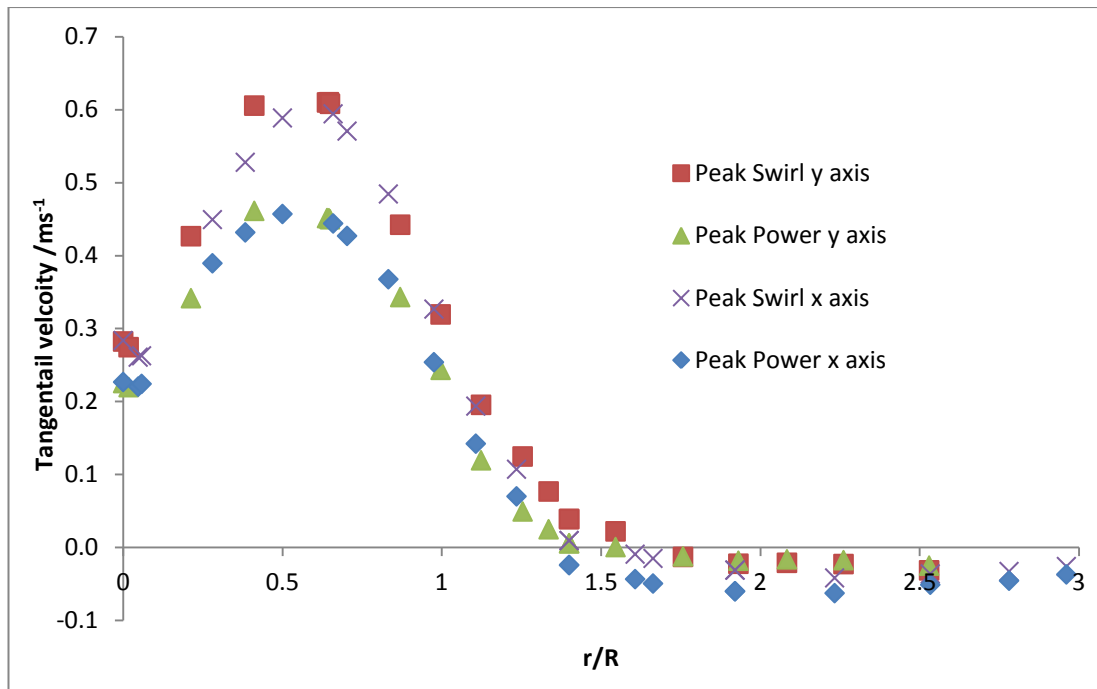


Figure 7.30 Tangential velocity profile at $x/D=1$ downstream of the 4 bladed turbine on x and y axes

7.5 Dynamic Pressure

It has been shown in this chapter that the turbine generates either a very weak swirl or a weak swirl, depending on the number of blades, and it is known that very low swirl flows should result in a significant lateral (or radial), but a low axial, pressure drop (Gupta et al, 1984). To ensure that the results were in agreement with swirl theory for all three turbine configurations, the dynamic pressure was examined for the 2, 3 and 4 bladed turbines at λ at which peak Swirl occurred and peak power since this is assumed to be the normal operating λ . Since the results at $x/D=0.1$ were found to be heavily influenced by the hub, the pressure gradient in the radial direction was calculated at $x/D=1$. The dynamic pressure at $x/D=25$ was also extracted to enable the pressure gradient in the axial direction to be calculated. The results shown in Figures 7.27 to 7.29 are based on the RSM models with a sample comparison with an SST model given in Figure 7.30.

Figure 7.30 shows that, at peak swirl, the minimum dynamic pressure at $x/D=1$ downstream of the 2 bladed is around 1680 Pa at the rotational axis of the turbine. This has recovered to around 4750 Pa at $r/R \sim \pm 1.55$, giving a radial pressure gradient

of 396 Pa/m. In the axial direction, the dynamic pressure has recovered to 3730 Pa at $x/D=25$ which results in a much smaller axial pressure gradient of ~ 8.5 Pa/m. At peak power, the minimum dynamic pressure at $x/D=1$ downstream of the 2 bladed turbine is around 1400 Pa at $r/R \sim \pm 0.65$, also shown in Figure 7.30. This has recovered in the radial direction to 4860 Pa at $r/R \sim \pm 1.5$ and in the axial direction to 3160 Pa at $x/D=25$. As at peak swirl, the pressure gradient is therefore much greater, at 814 Pa/m in the radial direction, compared with 7.3 Pa/m in the axial direction.

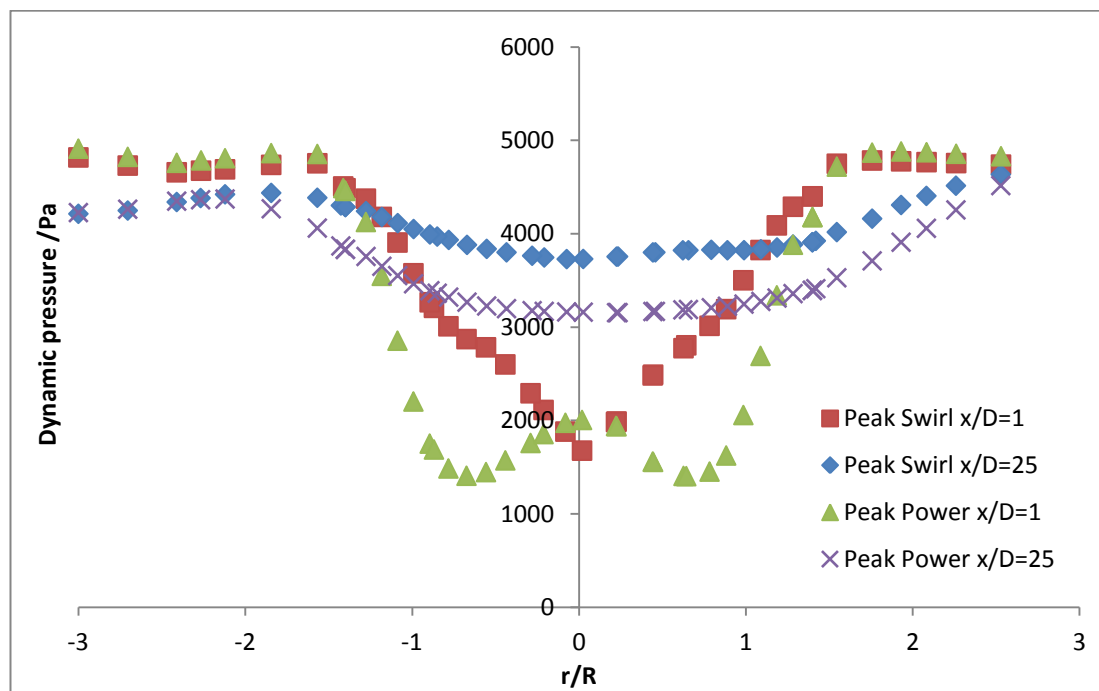


Figure 7.31 Dynamic pressure profiles downstream of the 2 bladed turbine

Figure 7.31 shows the dynamic pressure profiles at $x/D=1$ and $x/D=25$ downstream of the 3 bladed turbine at peak swirl and peak power. At $x/D=1$ at peak swirl the minimum dynamic pressure is around 1000 Pa. At $x/D=25$ the pressure has recovered, so that the minimum pressure is now 3370 Pa, thus giving an average pressure drop of ~ 10.5 Pa/m in the axial direction. In the radial direction the maximum pressure difference can be seen to be ~ 4000 Pa at $x/D=1$ over a radial distance of ~ 7 m, giving a pressure drop of ~ 560 Pa/m. By $x/D=25$ the maximum

pressure drop in the radial direction has reduced to ~ 110 Pa/m showing that the radial pressure drop is still dominant relative to the axial pressure drop.

At peak power the minimum dynamic pressures at $x/D=1$ and $x/D=25$ are around 1000 Pa, at $r/R \sim \pm 0.7$, and 3000 Pa, at $r/R=0$, respectively. This is an axial pressure gradient of 8.3 Pa/m. The dynamic pressure at $x/D=1$ is around 4670 Pa at $r/R \sim \pm 1.4$, giving a radial pressure gradient of ~ 1050 Pa/m.

As with the 2 and 3 bladed turbines, the 4 bladed turbine also produces a wake with a much greater pressure gradient in the radial direction than in the axial direction. Figure 7.29 shows that, at peak swirl, the pressure difference in the radial direction is around 3920 Pa over a radial distance of $r/R \sim 1.4$, or 7 m, and in the axial direction the pressure difference is around 2450 Pa over $x/D=24$, or 240 m. These pressure differences give gradients of 560 Pa/m and 10.2 Pa/m in the radial and axial directions respectively.

Again, at peak power, the pressure gradient in the wake of the 4 bladed turbine is much greater in the radial direction than the axial direction. From Figure 7.32 the pressure difference in the radial direction is 3660 Pa over a distance of 4.25 m giving a pressure gradient of 861 Pa/m. In the axial direction the pressure difference is 1880 Pa over 240 m giving a pressure gradient of 7.8 Pa/m.

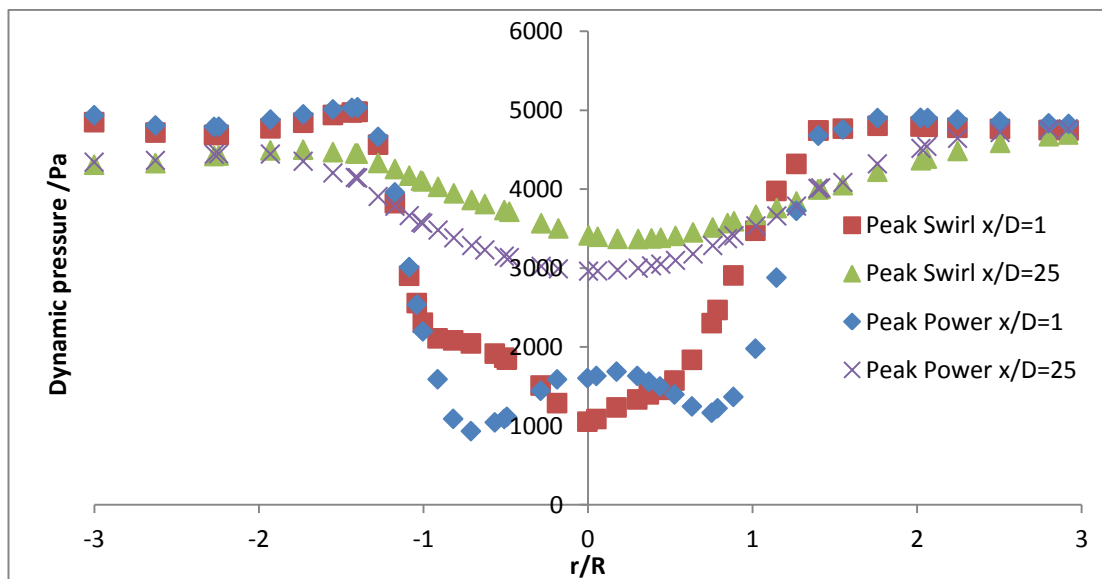


Figure 7.32 Dynamic pressure profiles downstream of the 3 bladed turbine

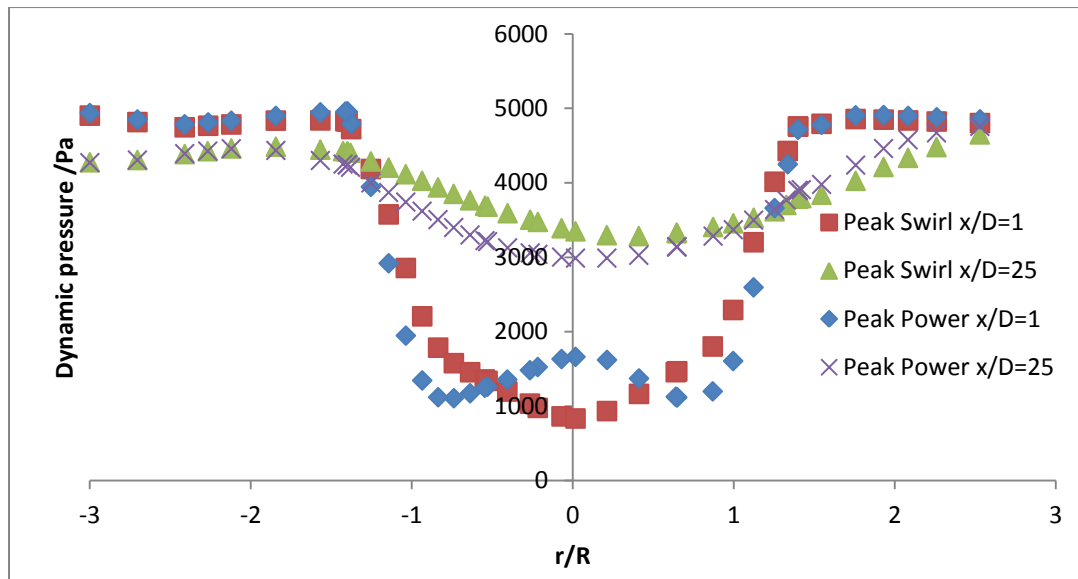


Figure 7.33 Dynamic pressure profiles downstream of the 4 bladed turbine

Figure 7.33 shows the dynamic pressure profiles at $x/D=1$ and $x/D=25$ downstream of the 3 bladed turbine at peak power for the RSM and SST models. At $x/D=1$ the profiles are very similar and whilst at $x/D=25$ the dynamic pressure has recovered more with the SST model, due to the higher ambient turbulence discussed in Chapter 6, the radial pressure gradient is still much greater than the axial pressure gradient. Similar observations were seen at peak swirl and for the 2 and 4 bladed turbines and are given in Appendix C. It is therefore clear that the condition of a large dynamic pressure gradient in the radial direction when compared with that in the axial direction is satisfied by all three turbine configurations at peak swirl and under normal operating conditions.

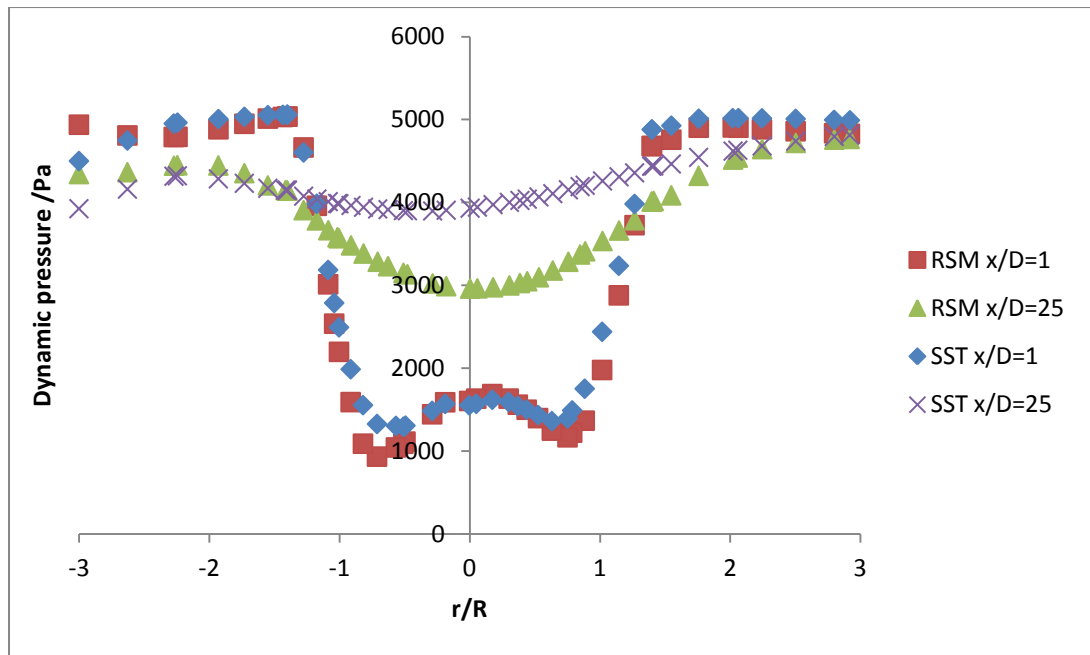


Figure 7.34 Dynamic pressure profiles downstream of the 3 bladed turbine with the RSM and SST models

7.6 Summary of Swirl Characteristics in Wake

This chapter has shown that close to the turbine, at $x/D=0.1$, S varies with λ with a similar trend to the turbine's C_{θ} , peaking at the same λ , for each of the turbine configurations. Further downstream, maximum of S occurs at a λ which varies with x/D but follows the same trend for each turbine.

Although the maximum swirl numbers, close to the turbine, are similar for each model at both peak swirl and peak power, the predicted decay in swirl is more rapid with the SST model than the RSM model for all cases. It is clear that the difference in swirl decay is largely due to the difference in turbulence resulting from the more rapid decay in turbulence with the RSM model since when the minimum turbulence is fixed, both models give very similar rates of swirl decay.

The difference in swirl decay between both of the models with fixed minimum turbulence is smallest for the 2 bladed turbine and largest for the 4 bladed turbine. As with the performance characteristic results presented in Chapter 6, this is due to the difference in swirl imparted to the flow by each blade being multiplied by the

number of blades. With a fixed minimum turbulence, the results at peak power are very close. For each turbine configuration the results move away from RSM and toward SST with increases in x/D as the turbulence intensity in the original models continues to decay along the length of the domain. With fixed minimum turbulence, the rate of decay is approximately the same for RSM and SST for all 3 turbines but SST gives higher values at all $x/D=0.1$ due to the higher predictions of torque shown in Chapter 6 and hence higher swirl imparted to the flow.

Since the swirl was found to be weak or very weak, the RSM did not offer a significant advantage over the SST model with very similar predictions for the models with fixed minimum turbulence. Hence, for a turbine with weak or very weak swirl the SST model is sufficient for analysing the swirl characteristics, provided the turbulence can be accurately matched to the proposed site. However, for a turbine with a higher swirl it may be necessary to use the RSM.

Peak swirl increases with the number of blades but is weak or very weak in all cases. However, peak S for the 4 bladed turbine is close to the threshold of 0.3 stated by Gupta et al (1984) at which axial velocity starts to become coupled with tangential velocity and therefore wake recovery may be related to S for some turbine designs. It is also possible that this may occur for this turbine design with a different mean flow velocity since the ratio of axial to tangential momentum may not be independent of flow velocity.

Swirl is only affected by the number of blades in the near wake region with values converging after $x/D=10$. In the far wake the ambient turbulence is of much greater significance to the swirl than the number of blades. Accurate turbulence data from a proposed site is therefore crucial if the swirl in the far wake is of importance.

Since the wakes of all three turbines, at both peak swirl and peak power compare well with the experimental work of Chigier and Chervinsky (1967), demonstrate a classical Rankine vortex and follow the principle of a much greater pressure drop in the radial direction than in the axial direction it is reasonable to state that they fit classical swirl theory.

8 Wake Recovery

In areas where more than one row of turbines can be sited, in an array, an estimation of the wake length of each device is critical when determining the spacing of the devices in order to make the most efficient use of the available area. This chapter considers the wake length predicted by each model for the 2, 3 and 4 bladed turbines at their respective normal operating λ , again assumed to be at peak C_p , and then compares the wake length for each configuration.

8.1 Centre Line Velocity

Figure 8.1 shows the normalised axial velocity downstream of the 2 bladed turbine along its rotational axis for each of the models, where x/D is as defined in Chapter 6 and u/U is the axial velocity, normalised to the inlet velocity, 3.086ms^{-1} . Negative values in the recirculation zone immediately behind the hub have been removed for clarity. Each of the models predicts an initial rapid recovery to between 65% and 69% of the upstream value at $x/D \sim 0.5$, followed by a drop to between 53% and 56% at $3.6 < x/D < 5.2$, and then a gradual recovery through the remainder of the domain.

There is a clear difference between the recovery predicted by each of the original models with an 80 % recovery at $x/D=23$ with the RSM model and the same recovery at a much reduced downstream distance of $x/D=14$ with the SST model. It is also evident that the difference in predicted recovery is almost entirely due to the difference in turbulence since the recovery predicted by each of the models with fixed minimum turbulence is very similar. The recovery predicted by both of the models with fixed minimum turbulence is closer to that predicted by the original SST model than the RSM model. This is because downstream of the turbine the turbulence intensity is closer to that predicted by the original SST model due to the continual decay of turbulence throughout the domain with both of the original models. The centre line velocity is insensitive to the viscous model from $x/D=0$ to $x/D \sim 2.5$ as the turbulence immediately behind the turbine is much higher than the ambient turbulence and is similar for all of the models.

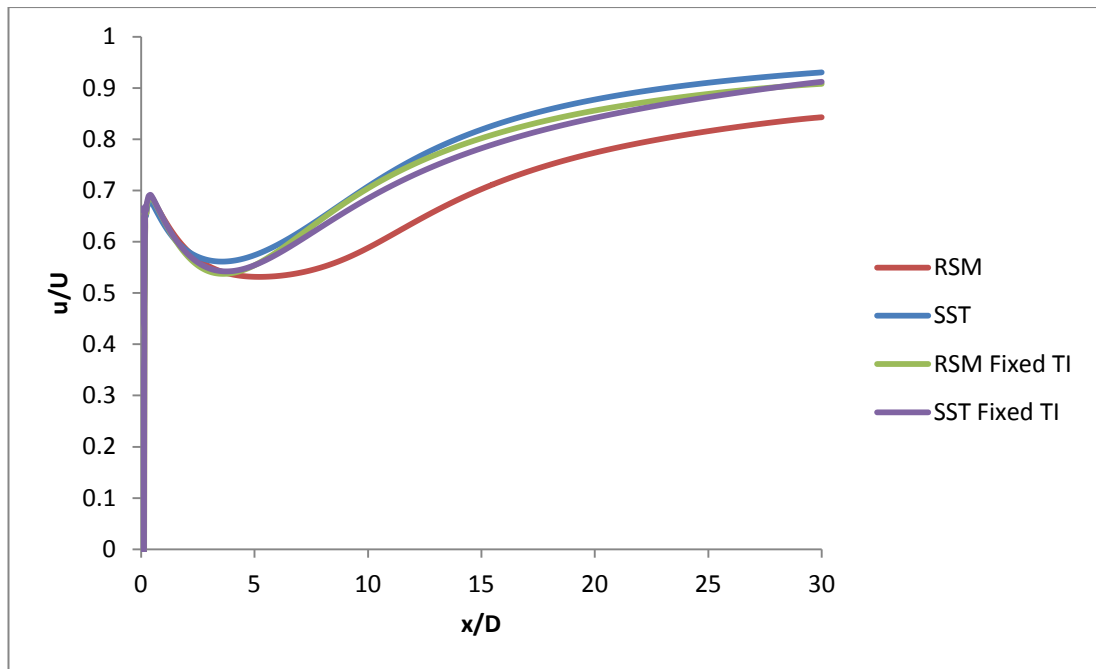


Figure 8.1 Normalised centre line axial velocity downstream of the 2 bladed turbine

Figures 8.2 and 8.3 show the normalised axial velocity downstream of the 3 and 4 bladed turbines along their rotational axes for each of the models. Again, negative values in the recirculation zone immediately behind the hub have been removed for clarity. The trends follow the pattern of the 2 bladed wake, with an initial rapid recovery, followed by a drop in velocity and then a gradual recovery.

Immediately downstream of the 3 bladed turbine the initial rapid recovery reaches 61% to 62% of the upstream value at $x/D \sim 0.4$, lower than the 2 bladed turbine but occurring closer to the turbine. The initial rapid recovery downstream of the 4 bladed turbine reaches 66% to 67% of the upstream value at $x/D \sim 0.3$, between the values of the 2 bladed turbine and 3 bladed turbines but occurring closer to the turbine. It is unclear why this occurs but it is possibly due to difference in accelerated flow between blades and hub and also between blades themselves as they get closer together.

The minimum axial velocity downstream of the 3 bladed turbine, outside the recirculation zone, is between 46% and 49% of the upstream value at $3.7 < x/D < 6.2$, lower than for the 2 bladed turbine and slightly further downstream. Downstream

of the 4 bladed turbine, after the initial rapid recovery, the axial velocity drops to between 44% and 47% at $3.8 < x/D < 7.1$, lower than for the 2 and 3 bladed turbines and slightly further downstream. This is because the 4 bladed turbine extracts the most energy from the flow and the 2 bladed turbine the least, as discussed in Chapter 5.

There is again a clear difference between the recovery predicted by each of the original models with an 80 % recovery at $x/D=26$ downstream of the 3 bladed turbine with the RSM model and at $x/D=14$ with the SST model. Downstream of the 4 bladed turbine an 80 % recovery is seen at $x/D=26$ with the RSM model and at $x/D=15$ with the SST model.

As with the 2 bladed turbine, the difference in predicted recovery downstream of the 3 and 4 bladed turbines is almost entirely due to the difference in turbulence since the recovery predicted by each of the models with fixed minimum turbulence is very similar. Again, the recovery predicted by both of the models with fixed minimum turbulence is closer to that predicted by the original SST model than the RSM model due to the turbulence being closer to that predicted by the original SST model.

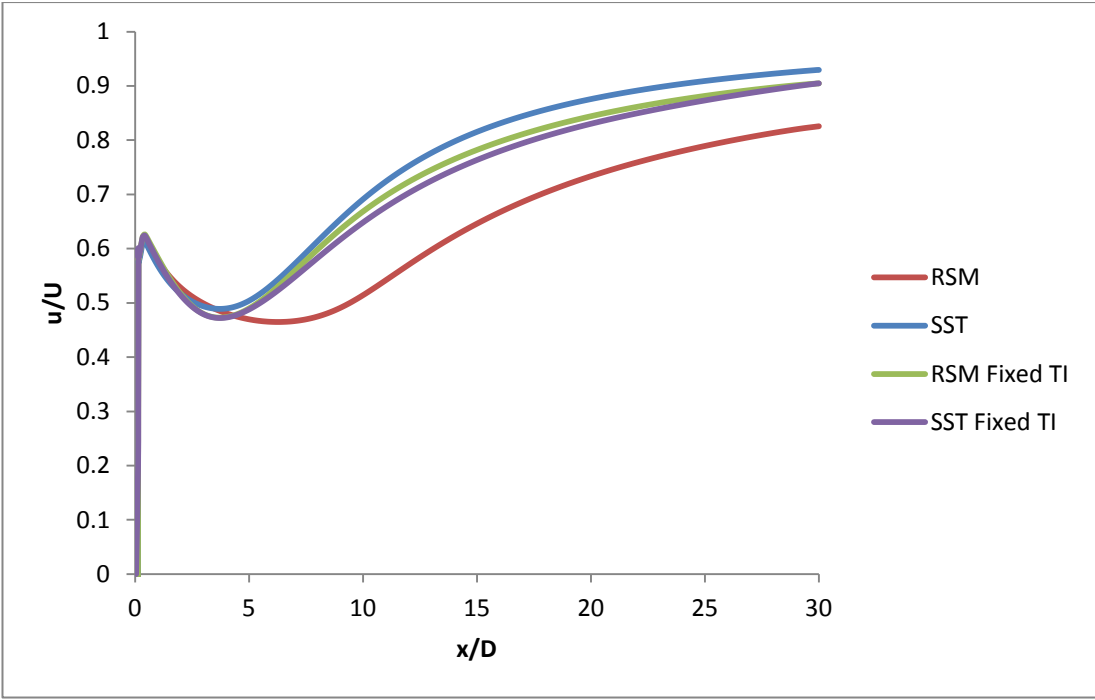


Figure 8.2 Normalised centre line axial velocity downstream of the 3 bladed turbine

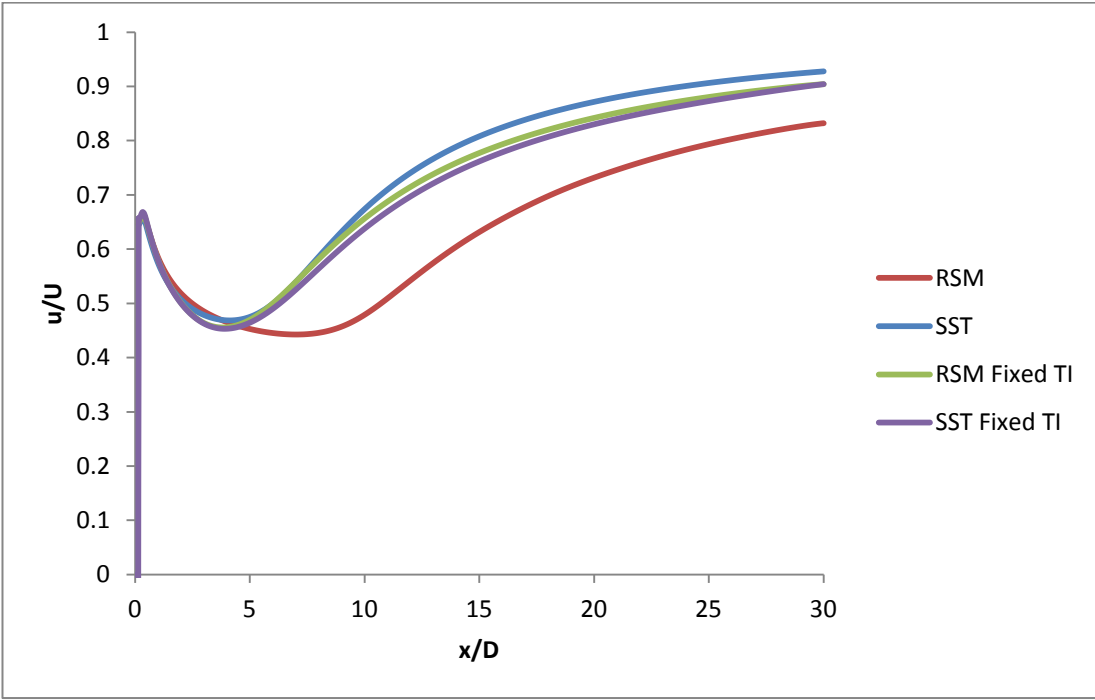


Figure 8.3 Normalised centre line axial velocity downstream of the 4 bladed turbine

Analysis of the centre line axial velocity and the swept area average axial velocity for the 2, 3 and 4 bladed turbines has shown that the differences in wake predictions are almost entirely due to the difference in turbulence in each model since there is negligible difference in the results of the models with fixed minimum turbulence. Therefore the comparison between 2, 3 and 4 blades is based on the original RSM and SST models as these give the upper and lower values with those of the fixed minimum turbulence models falling between the original models in every case.

Figure 8.4 compares the normalised centre line axial velocity for the 2, 3 and 4 bladed turbines, as predicted by the RSM and SST models. For each turbine, the centre line axial velocity is shown to be insensitive to the viscous model from $x/D=0$ to $x/D=2.5$ due to similar turbulence, as discussed previously. Both models show a greater drop in velocity in the near wake with an increasing number of blades and both show a greater difference between 2 and 3 blades than between 3 and 4 blades. This is to be expected since at peak C_p for each turbine, the C_θ and C_p are highest for the 4 bladed turbine and lowest for the 2 bladed turbine, with a larger difference in both of these values between 2 and 3 blades than between 3 and 4 blades, as shown in Chapter 6. The higher values of C_θ and C_p with an increase in the number of blades means that more of the energy is extracted and hence the lower axial velocity seen in the wake. The differences in the RSM and SST predictions for each turbine can be explained by the difference in turbulence, as discussed above, but there is also a difference in the trend for varying numbers of blades. Both models show a reduction in the dependence on the number of blades with increasing downstream distance. This is a similar finding to that of Myers and Bahaj (2010), who compared the wake recovery for differing C_t values and found that the far wake was insensitive to C_t . However the SST model shows a convergence in recovery for all 3 turbine configurations at the same downstream distance whereas the RSM model shows a convergence of the 3 and 4 bladed centre line velocities much further upstream than where they converge with the 2 bladed turbine. This suggests that the centre line wake recovery is more sensitive to the number of blades at low turbulence levels and that low solidity rotors may offer

higher overall array efficiencies in areas of low turbulent intensity. At $x/D=10$ and above, the differences in velocity recovery as a result of the number of blades are smaller than the differences caused by different turbulence levels meaning that the far wake is more dependent on turbulence than solidity and reinforcing the importance of having accurate turbulence data for a proposed array site.

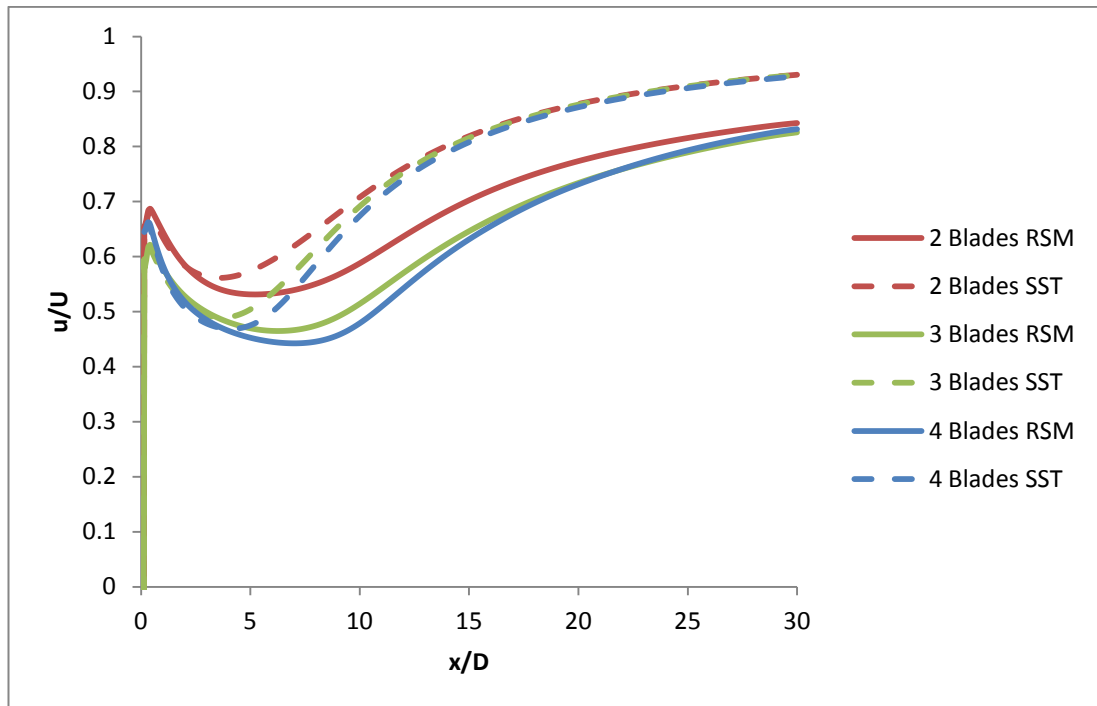


Figure 8.4 Normalised centre line axial velocity downstream of the 2, 3 and 4 bladed turbines

8.2 Swept Area Average Velocity

Since the power output of a turbine is based on the energy available in the swept area, basing the spacing between turbines on the centre line recovery may be over conservative, especially since the hub will not produce any torque and the majority of the torque comes from the area of the blade nearest the tip. Due to the cone shaped nature of a wake, the minimum velocity is found on the centre line with a radial increase in velocity. Therefore, a more accurate estimate of the power available to a turbine positioned downstream of another may be found by considering the average velocity over its swept area.

Figure 8.5 shows the normalised average axial velocity over the swept area of the 2 bladed turbine at downstream distances of x/D between 0.1 and 25 for each of the models. The trends are similar to those of the centre line values but there are no negative values immediately behind the turbine since the effect of the recirculation zone behind the hub is negated. As with the centre line values there is a drop from 66% to 68% of the free stream value close to the turbine to a minimum shortly downstream followed by a gradual recovery. The minimum value for the average velocity is slightly higher than the centre line value at 54% to 57% and occurs closer to the turbine at $x/D=1$ to $x/D=2$. The gradual recovery is also shifted closer to the turbine with an 80% recovery at $x/D=18$ for the RSM and $x/D=10$ for the SST, compared with $x/D=23$ and $x/D=14$ for the centre line values. This is a 22% to 29% reduction in the distance to this recovery. The models with fixed minimum turbulence again show a recovery that falls between those of the original models and closer to the SST than RSM. With the swept area average there is almost no difference in predictions for each of the fixed minimum turbulence models, again confirming that the difference in the predictions of recovery of the original models is almost entirely due to differences in turbulence. As with the centre line velocity, immediately downstream of the turbine the average axial velocity over the swept area of the turbine is insensitive to the viscous models but differences are seen by $x/D=1$ indicating that there is more variance in the turbulence in each model over the swept area than at the centre line.

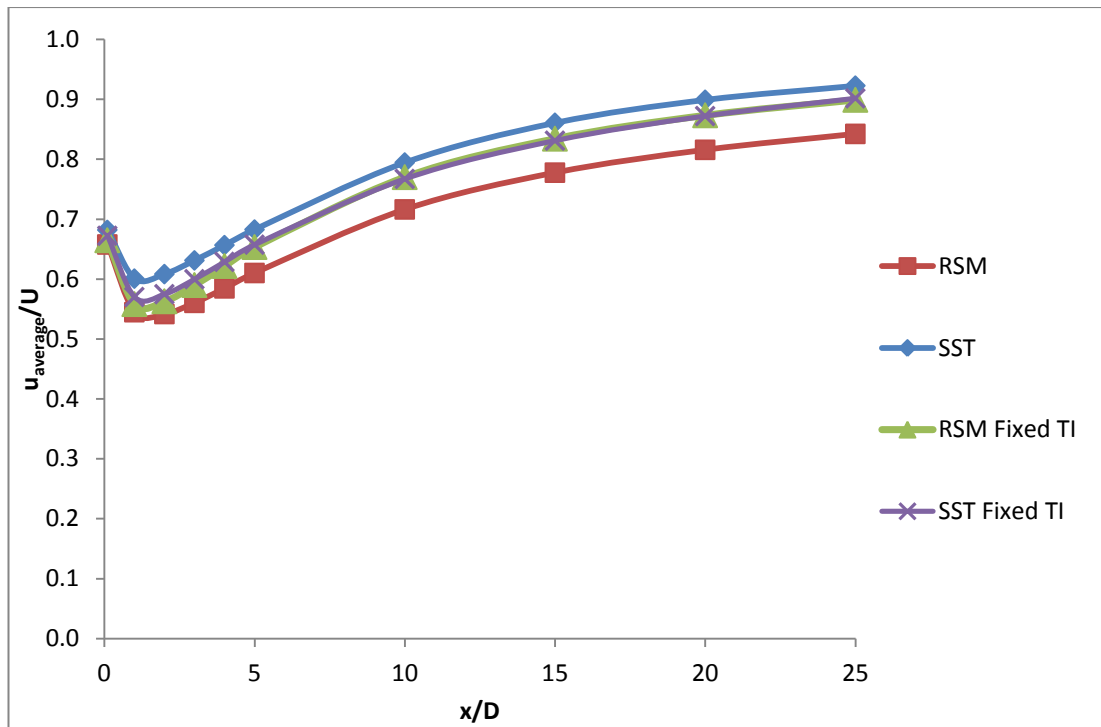


Figure 8.5 Normalised swept area average axial velocity downstream of the 2 bladed turbine

Figures 8.6 and 8.7 show the average axial velocity over the swept area of the downstream of the 3 and 4 bladed turbine at distances of x/D between 0.1 and 25 for each of the models. As with the 2 bladed turbine the trends are similar to those of the centre line values but again there are no negative values as the recirculation zone behind the hub is negated.

The average axial velocity at $x/D=0.1$ is 64% to 67% of the free stream value for the 3 bladed turbine and 64% to 66% for the 4 bladed turbine. The minimum values for the average velocity are again higher than the centre line values and occur closer to the turbine, reaching 50% to 56% at $x/D=1$ to $x/D=2$ for the 3 bladed turbine and 47% to 54% at $x/D=1$ to $x/D=2$ for the 4 bladed turbine.

The gradual recovery is also shifted closer to the turbine. For the 3 bladed turbine there is an 80% recovery at $x/D=22$ for the RSM and $x/D=11$ for the SST, compared with $x/D=26$ and $x/D=14$ for the centre line values. This is a 15% to 21% reduction in the distance to this recovery. Similarly, for the 4 bladed turbine, an 80% recovery

occurs at $x/D=22$ for the RSM and $x/D=12$ for the SST, compared with $x/D=26$ and $x/D=15$ for the centre line values. This is a 15% to 20% reduction in the distance to this recovery.

The models with fixed minimum turbulence again show a recovery that falls between those of the original models and closer to the SST than RSM. As with the 2 bladed turbine, the average axial velocity immediately downstream of the 3 and 4 bladed turbines is insensitive to the viscous model and differences between the models occur closer to the turbine than for the centre line values.

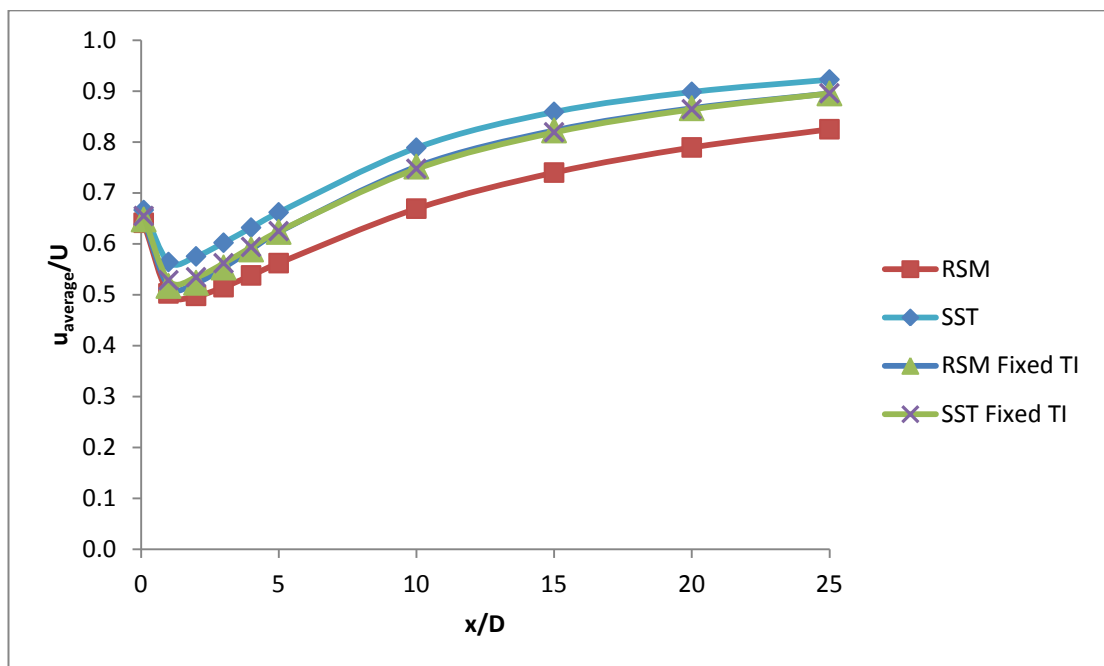


Figure 8.6 Normalised swept area average axial velocity downstream of the 3 bladed turbine

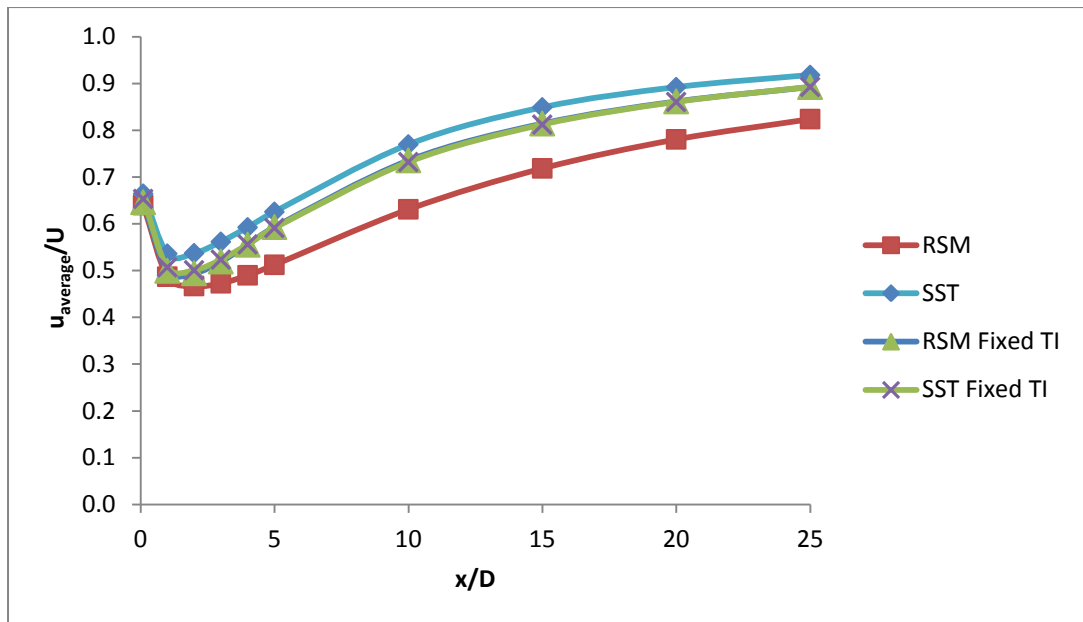


Figure 8.7 Normalised swept area average axial velocity downstream of the 4 bladed turbine

The recovery of average axial velocity over the swept area of the turbine is shown in Figure 8.8 for the 2, 3 and 4 bladed turbines with the RSM and SST models. As with the centre line values, both models show a reduction in the minimum average velocity with an increasing number of blades for the same reasons. However, there is no longer a significantly greater difference between 2 and 3 blades than between 3 and 4 blades. Both models again show a decreasing dependence on the number of blades with increasing downstream distance and the recovery of all 3 turbines converge further upstream with the SST model than with the RSM model, again showing a higher dependence on the number of blades at a lower turbulent intensity. The recovery of the average axial velocity for the 3 and 4 bladed turbines with the RSM model converge further downstream than the centre line values suggesting that the average velocity is more sensitive than the centre line velocity to the number of blades at low turbulence levels.

Again, at $x/D=10$ and above, the differences in velocity recovery as a result of the number of blades are smaller than the differences caused by different turbulence levels. As discussed above, this means that the far wake is more dependent on turbulence than on solidity.

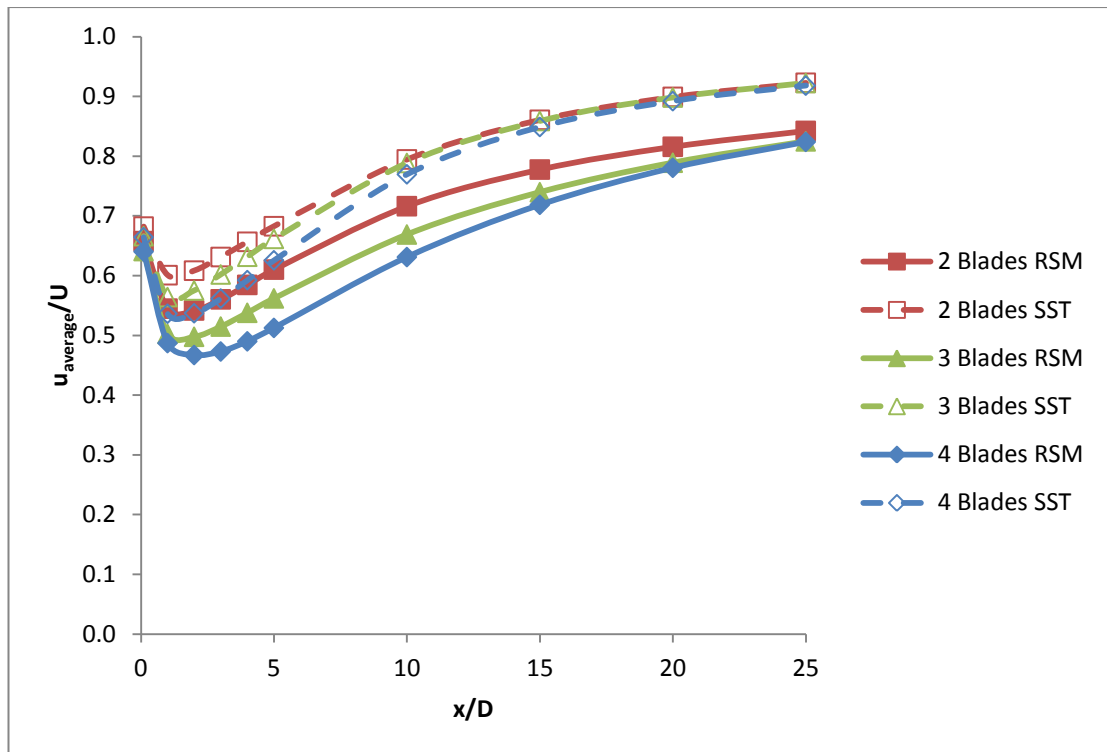


Figure 8.8 Normalised swept area average axial velocity downstream of the 2, 3 and 4 bladed turbines

8.3 Comparison of centre line and swept area average velocity

Figure 8.9 gives a comparison of the centre line and swept area average axial velocities for each turbine with both the RSM and SST models. It is clear that basing the calculation on the swept area rather than the centre line reduces the downstream distance at which the velocity reaches a given velocity. This effect is most pronounced at downstream distances between $x/D=5$ and $x/D=8$, depending on the model, and decreases with downstream distance above this. Therefore if device spacing is based on a 90% recovery, using the swept area average axial velocity will have less effect than if it is used where spacing is based on an 80% recovery. Although it is not possible to make a comparison at 90% recovery as the RSM models have not reached this by the end of the domain, at 80% recovery, there is a greater difference between the centre line velocity and the swept area average velocity with the RSM model than with the SST model. This shows that at lower turbulence levels, there is a greater variation in u with radial distance from the centre and therefore, a more conservative recovery given by the centre line value.

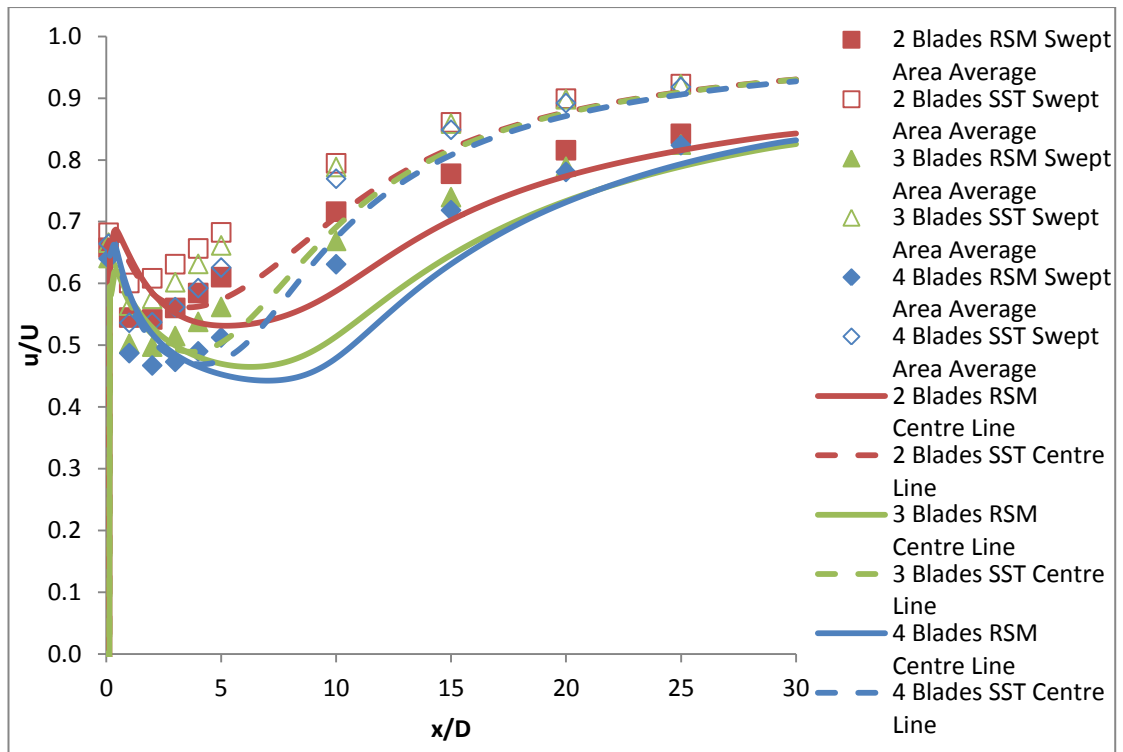


Figure 8.9 Normalised centre line and swept area average axial velocity downstream of the 2, 3 and 4 bladed turbines

Figure 8.10 shows the swept are average velocity against the centre line velocity for the wake recovery downstream of the 2, 3 and 4 bladed turbines with each of the models. It is clear that, in general, the difference between the centre line and swept area average values decreases with increasing velocity. This would be expected since the highest velocities are found toward the end of the wake where the velocity across the whole of the swept area has recovered to close to the free stream value. Only the values for $x/D=4$ and above are shown since those closer to the turbine are of little interest. It is interesting to note that the difference between swept area average velocity and centre line velocity shows good correlation for all three turbine configurations with very similar values where the centre line velocity is at 0.6ms^{-1} and above.

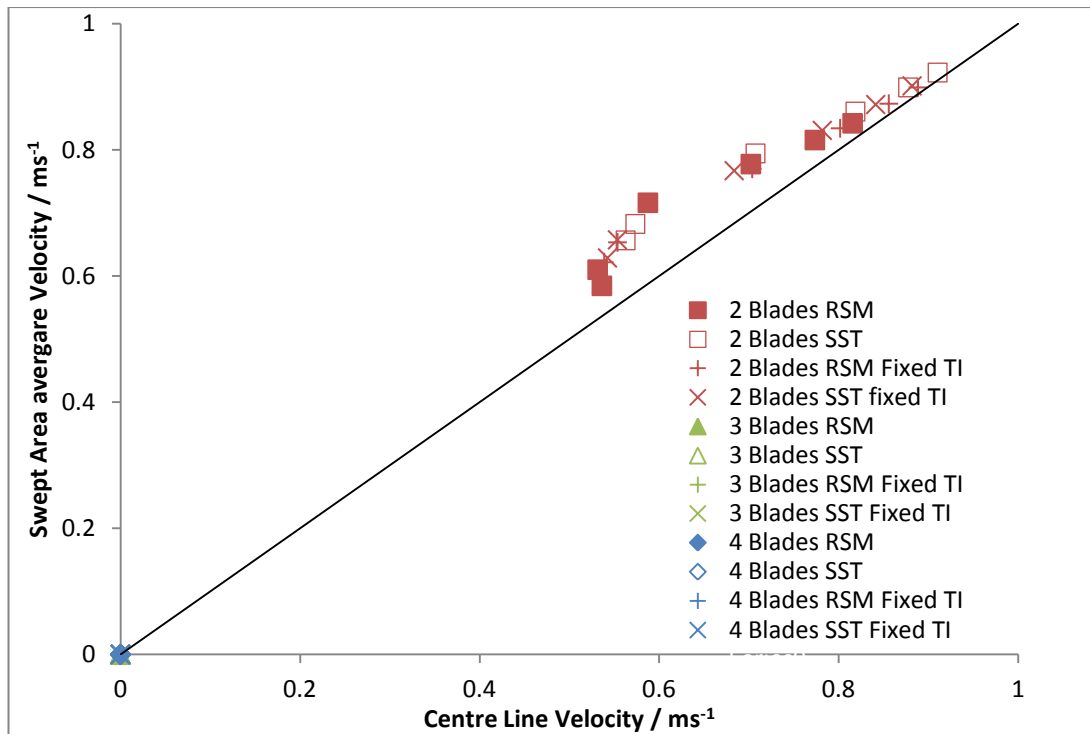


Figure 8.10 Swept area average axial velocity v centre line axial velocity at $x/D=4$ and above downstream of the 2, 3 and 4 bladed turbines

8.4 Summary of Wake Study

All of the models for each of the turbines show the same trend of a rapid recovery in axial velocity very close to turbine, a drop shortly downstream and then a gradual recovery. The SST model predicts a shorter wake length than RSM for each turbine and when based on the centre line as well as the swept area average value. This is almost entirely due to the difference in turbulence as there was negligible difference between the results of the fixed minimum turbulence models. The axial velocity immediately behind the turbine is insensitive to turbulence. This extends to $x/D \sim 2.5$ for the centre line values but is only true at $x/D=0.1$ with the swept area average.

The swept area average velocity can give a better estimate of the available energy, and gives a shorter wake length than the centre line value. The effect of this method of defining wake recovery is most pronounced between $x/D=5$ and $x/D=8$ and reduces with x/D beyond this. There is also a greater effect at low turbulence than at high.

The minimum axial velocity in the wake, outside the recirculation zone behind the hub, decreases with increasing number of blades since more energy is extracted from the flow. The difference in this minimum velocity is significantly greater from 2 to 3 blades than from 3 to 4 for the centre line values but the decrease is approximately linear with the swept area average values.

There is a reduction in the dependence of the recovery on solidity with increasing downstream distance. The centre line recovery is more sensitive to the number of blades at low turbulence than at high turbulence, and the swept area average more sensitive than the centre line value. The far wake is more dependent on turbulence than on solidity. However, at low turbulence there is still some dependence on the number of blades at $x/D=25$, with the 2 bladed turbine showing the greatest recovery. Low solidity devices may therefore be better suited to low turbulence areas than high solidity devices and in some sites it may be beneficial to have a combination of different rotor solidities within an array.

9 Blade Deflection

The performance characteristics, swirl and wake discussed so far in Chapters 6, 7 and 8 are all based on a rigid turbine. In reality the hydrodynamic forces would cause the blades to deflect and possibly alter some of these findings. This chapter presents the results of the 2 way coupled FSI models which account for blade deflection. Only the performance characteristics at peak power for each turbine are analysed. The SST model was used for all of the FSI work since the SST and RSM models showed little difference in predictions of performance characteristics and the RSM models required a much longer run time.

9.1 Torque

Figure 9.1 shows the torque output against modulus for the 2 bladed turbine configuration. It is clear that the torque increases with decreasing modulus, reaching a maximum of 184.8 kNm at a modulus of 20 GPa. This is an increase of 1.5% from 182.1 kNm at a modulus of 200 GPa. This suggests that the blade is not in its optimum position for the rigid turbine design. It is expected that at lower values of modulus, which would result in an increase in blade deflection, the torque would continue to increase but would eventually decrease due to the reduction in swept area, additional tip losses and change in angle of attack as the blade tip moves further from the plane of rotation. However, at lower values of modulus the model became unstable due to problems with inverted cells caused by dynamic meshing and convergence was not possible.

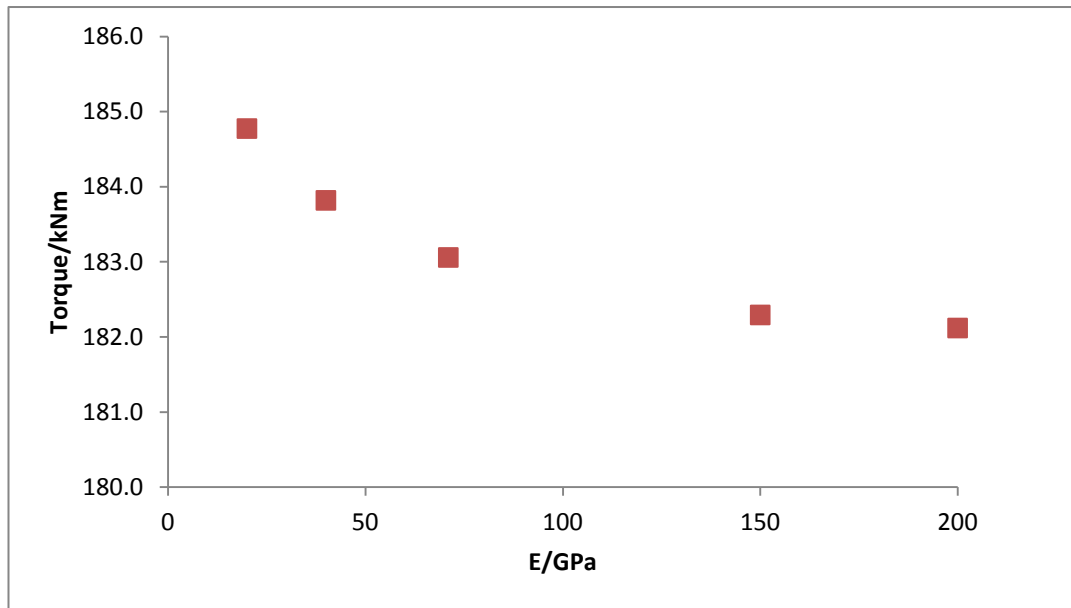


Figure 9.1 Torque vs E for the 2 bladed turbine

The torque output against modulus for the 3 and 4 bladed turbines is shown in Figures 9.2 and 9.3. Unlike the 2 bladed turbine, the torque produced by the 3 bladed turbine is shown to decrease with decreasing modulus. The torque at a modulus of 200 GPa is 242.1 kNm and this has dropped by 0.4% to 241.1 kNm at a modulus of 40 GPa. It is expected that the torque would continue to decrease with further reductions in modulus. This suggests that the blade is close to optimum in its original position.

The torque generated by the 4 bladed first increases with decreasing modulus, following a similar trend to the 2 bladed turbine, before eventually falling at very small values of modulus. Peak torque is 257.0 kNm and occurs at a modulus of around 20 GPa. This is 0.3% higher than the torque of 256.2 kNm which occurs at a modulus of 200 GPa. At a modulus of 10 GPa, the torque has then reduced to 256.5 kNm and it is expected that at lower values of modulus this would continue to decrease. As with the 2 bladed turbine the results suggest that the blade is not in its optimum position for the rigid turbine design.

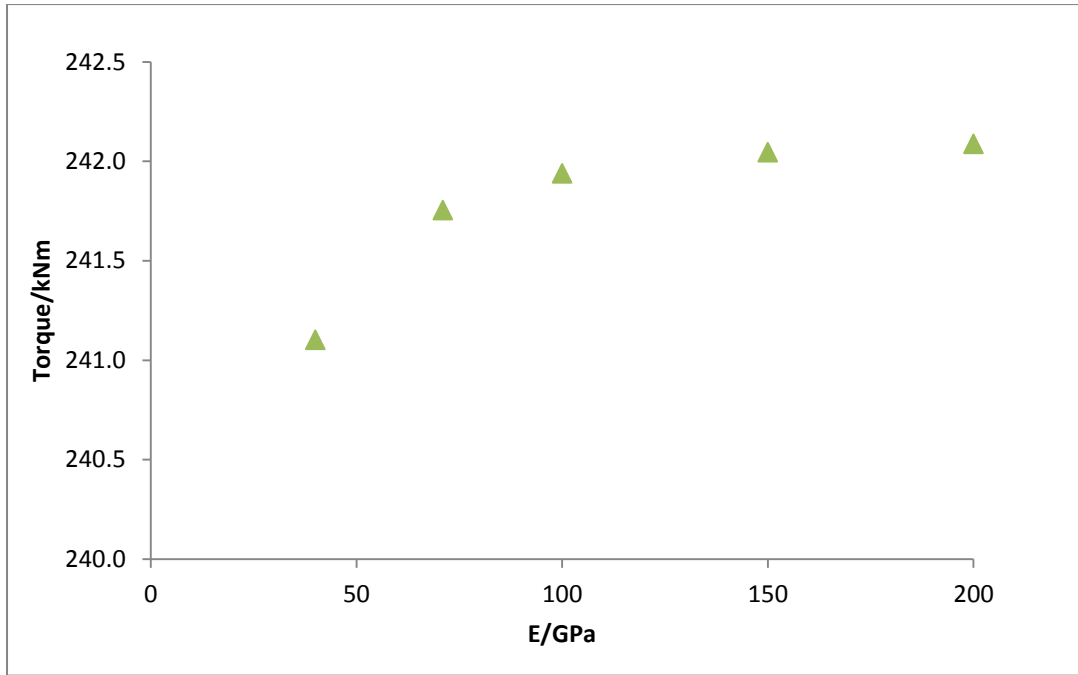


Figure 9.2 Torque vs E for the 3 bladed turbine

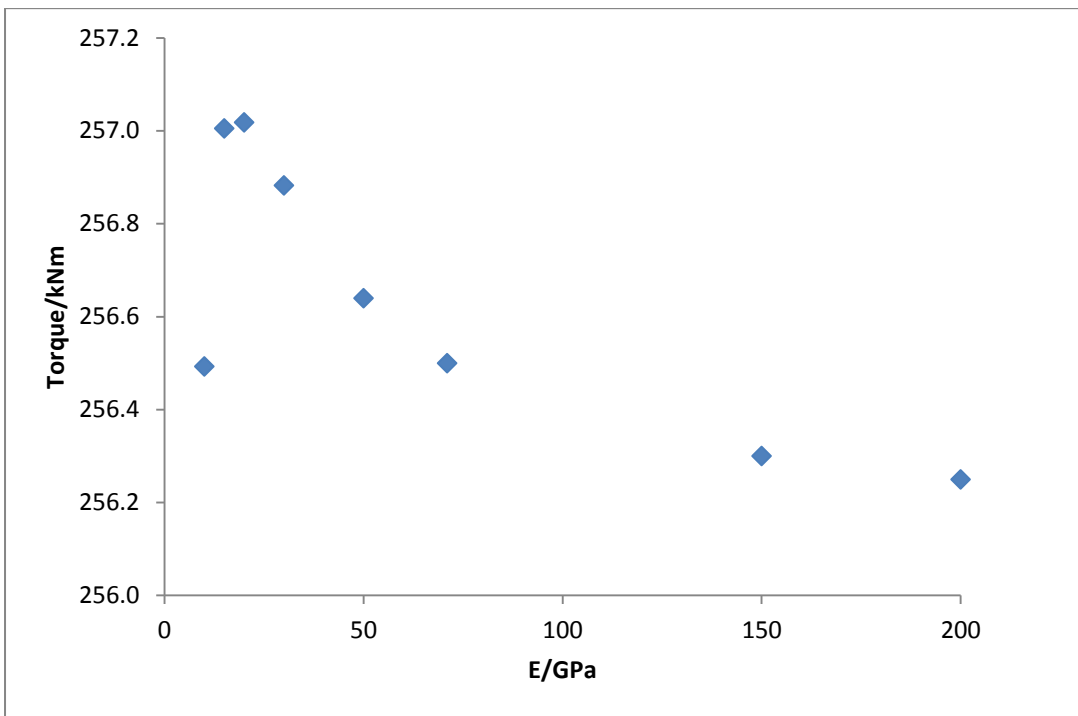


Figure 9.3 Torque vs E for the 4 bladed turbine

9.2 Thrust

The thrust load on the 2 bladed turbine is shown in Figure 9.4 for the range of moduli considered. The thrust is shown to follow a similar trend to the torque produced by the 2 bladed turbine, in that it increases with decreasing modulus. The maximum thrust found was 325.8 kN at a modulus of 20 GPa which is 2.0% higher than the thrust of 319.4 kN at a modulus of 200 GPa. As with the torque, the thrust would also be expected to first increase and finally decrease at lower values of modulus, again due to the lower swept area.

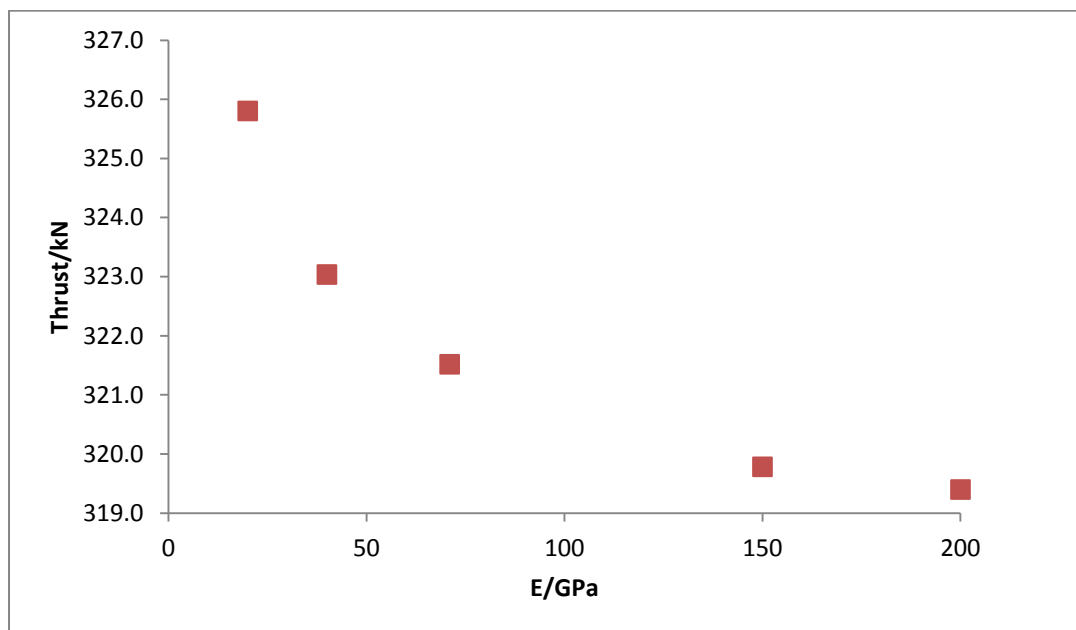


Figure 9.4 Thrust vs E for the 2 bladed turbine

Figures 9.5 and 9.6 show the thrust load against modulus on the 3 and 4 bladed turbines. Unlike the 2 bladed turbine, the thrust load on the 3 bladed turbine decreases with decreasing modulus. The thrust load at a modulus of 200 GPa is 328.7 kN. At a modulus of 40 GPa this has dropped by 0.3% to 327.8 kN and it is expected that further reductions in modulus would result in further reductions in thrust. This shows that where blades are fully optimised, a reduced modulus can result in lower loads as the projected area of each blade decreases as it deflects.

The thrust load on the 4 bladed turbine follows a similar trend to the 2 bladed turbine, increasing with decreasing modulus. However, at the lowest value of

modulus considered, which is 10 GPa, the rate of increase is slowing. At this modulus, the thrust load is 330.4 kN which is 1% higher than the thrust of 327.0 kN seen at a modulus of 200 GPa. It is expected that the thrust would continue to increase at values of modulus just below 10 GPa but would then decrease at lower modulus values.

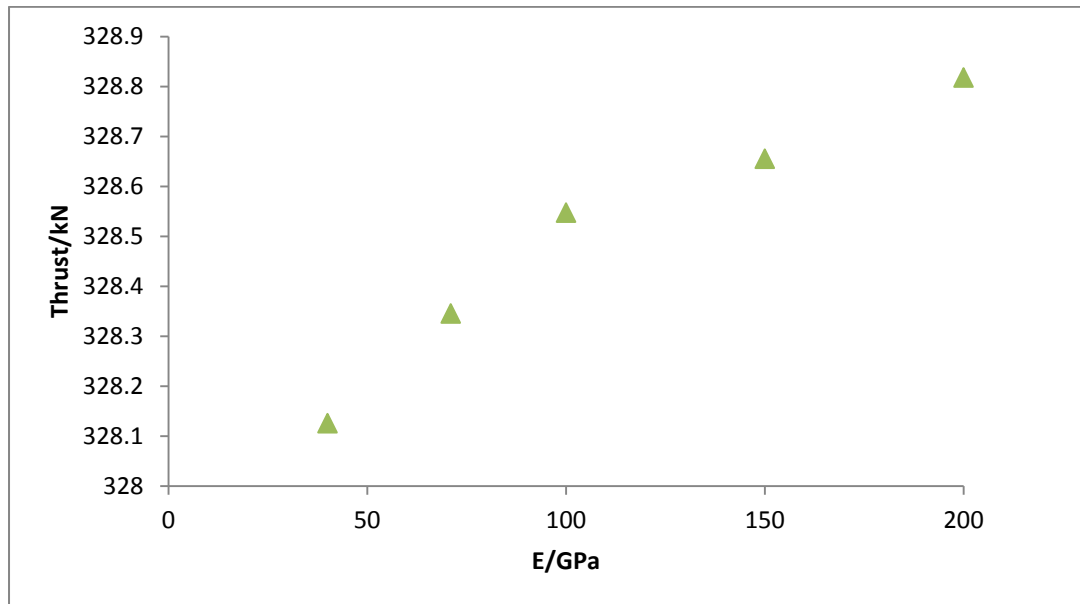


Figure 9.5 Thrust vs E for the 3 bladed turbine

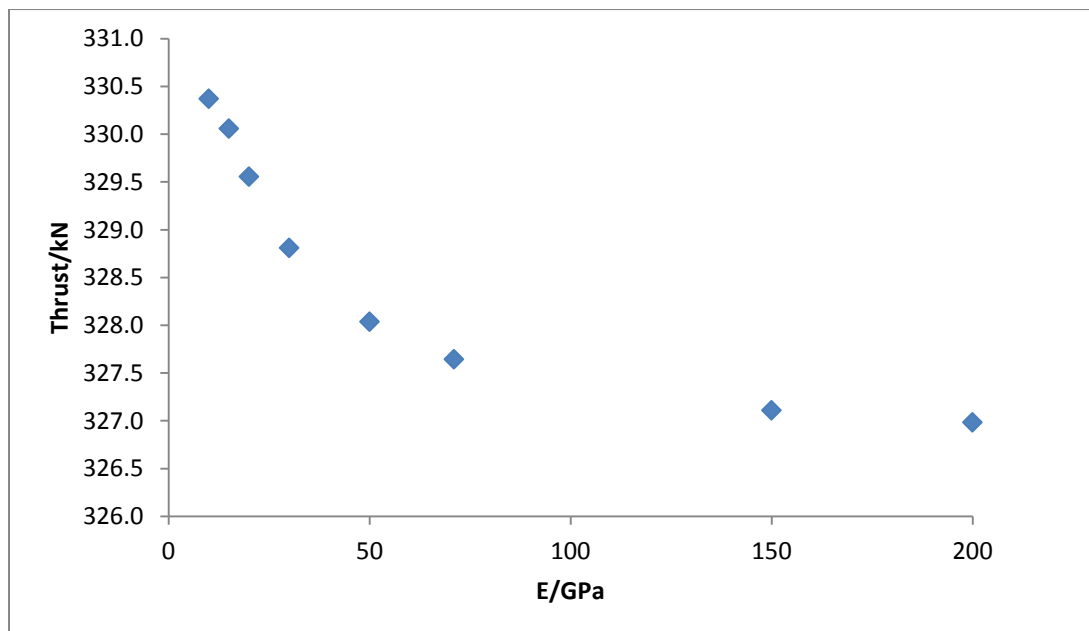


Figure 9.6 Thrust vs E for the 4 bladed turbine

9.3 Blade Deflection

The maximum blade deflection for the 2 bladed turbine for each value of modulus studied is shown in Figure 9.7. Clearly, the blade deflection increases with decreasing modulus as expected. It is shown to follow a power law, where the deflection changes by a factor which is the inverse of that by which the modulus is changed. The deflection at 200 GPa is 0.035 m and this has increased to 0.35 m at a modulus of 20 GPa.

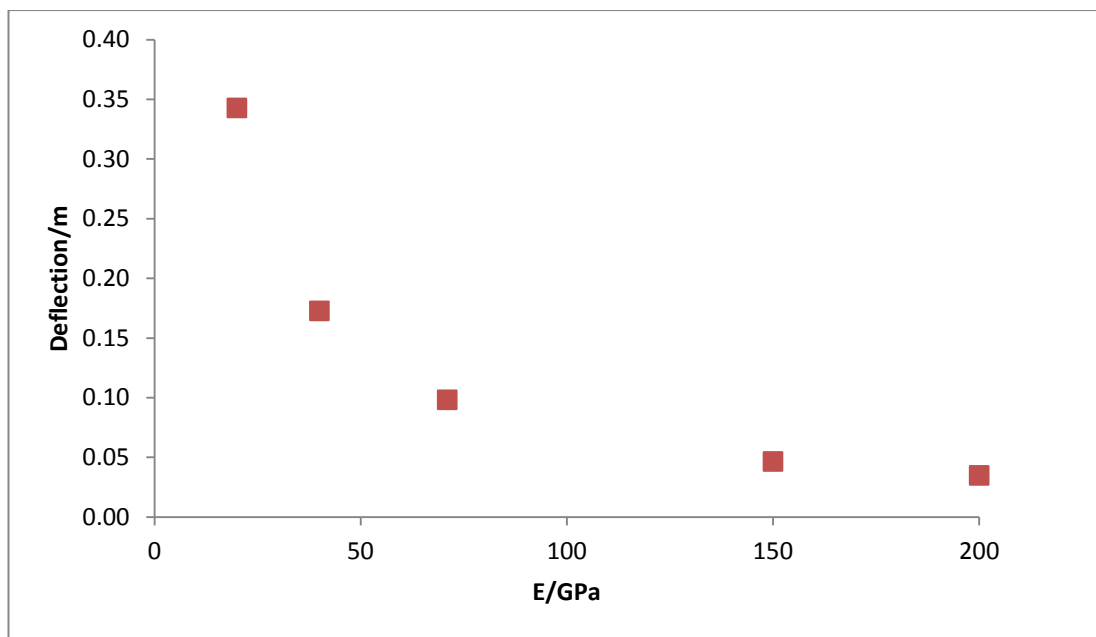


Figure 9.7 Deflection vs E for the 2 bladed turbine

Figures 9.8 and 9.9 show that, as for 2 Bladed turbine, deflection increases with decreasing modulus for the 3 and 4 bladed turbines. For the 3 bladed turbine a deflection of 0.12 m is shown at a modulus of 40 GPa, compared with a deflection of 0.024 m at a modulus of 200 GPa. The largest deflection for the 4 bladed turbine for the range of moduli considered was 0.36 m at a modulus of 10 GPa compared with a deflection of 0.018 m at a modulus of 200 GPa. Therefore the deflection of the 3 and 4 bladed turbines follow the same power law as the 2 bladed turbine.

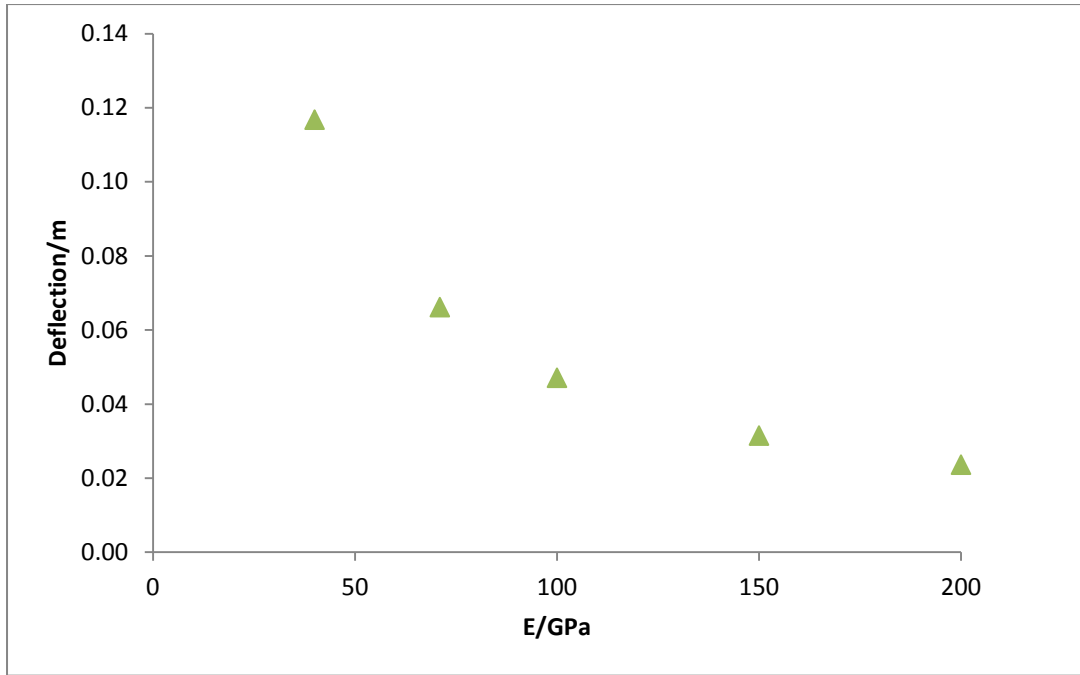


Figure 9.8 Deflection vs E for the 3 bladed turbine

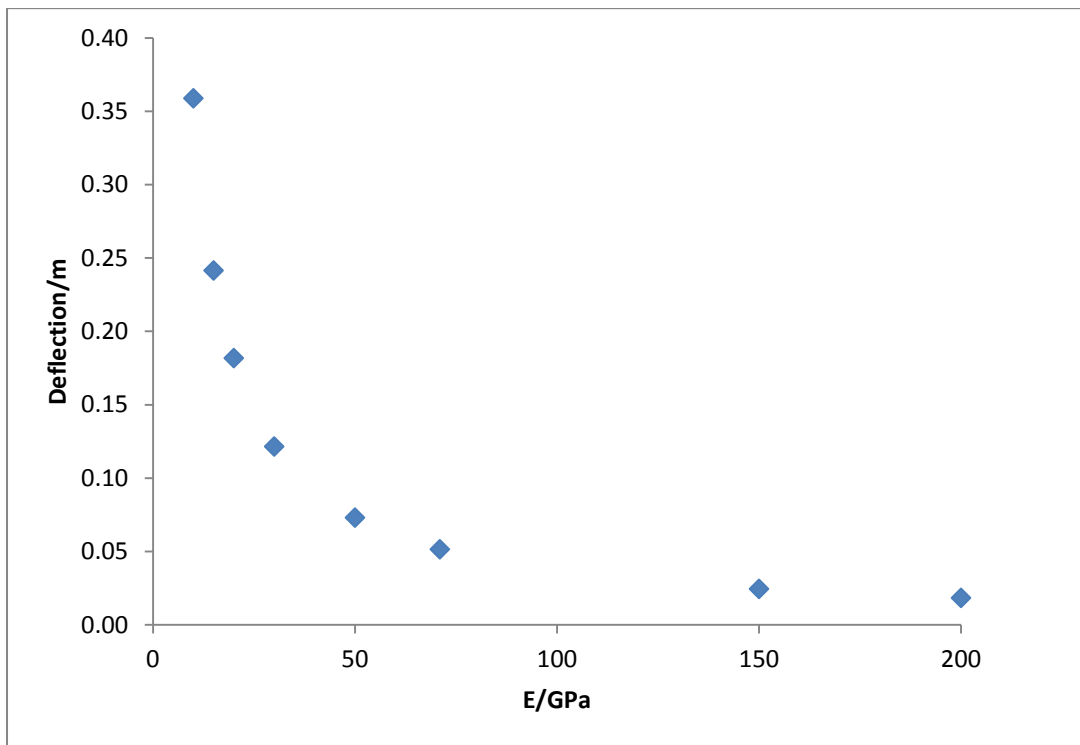


Figure 9.9 Deflection vs E for the 4 bladed turbine

For all three blade configurations the deflection increases with decreasing modulus or increasing flexibility, as shown in Figure 8.10. For all values of modulus, the 2 bladed turbine has the highest deflection and the 4 bladed turbine the lowest. This is expected since although the 2 bladed turbine has the lowest overall thrust, the thrust load on each blade is greater as discussed in Chapter 5.

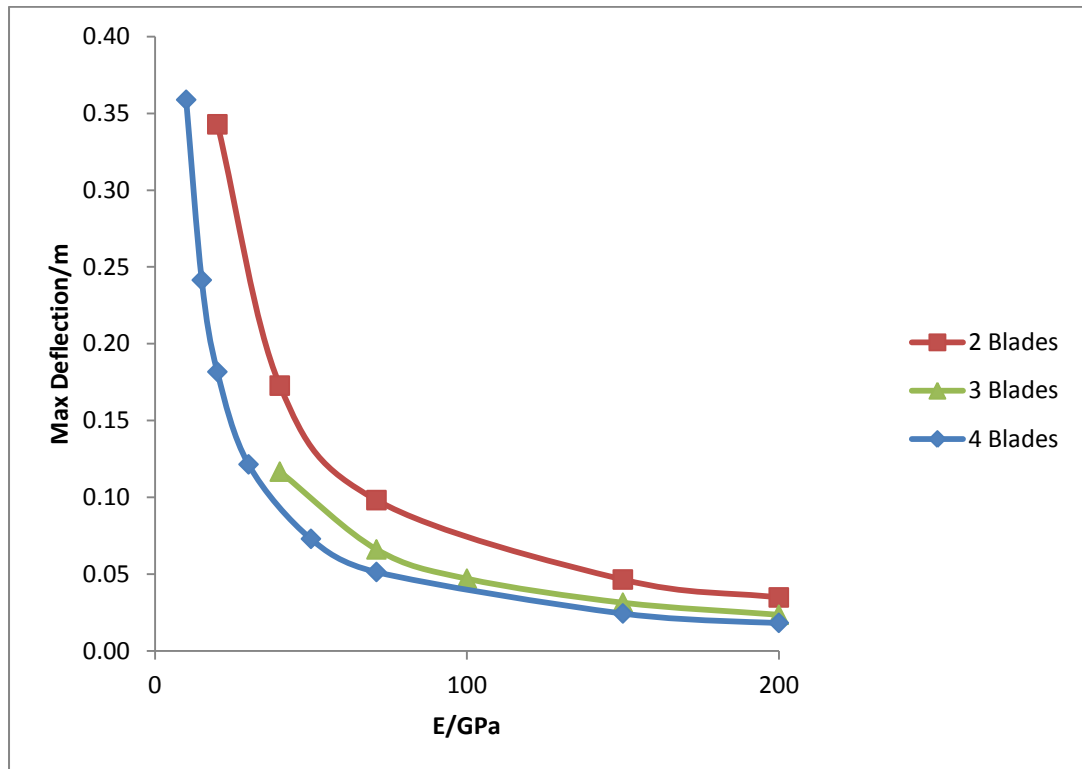


Figure 9.10 Deflection vs E for the 2, 3 and 4 bladed turbines

9.4 Change in Power with Deflection

Figure 9.11 gives the power output against deflection for the 2 bladed turbine model. The power is shown to increase with increasing blade deflection, reaching 499 kW at a deflection of 0.35 m, from a baseline of 490 kW at 0 m deflection. This is a 1.7% increase. However, the rate of increase in power is slowing at a deflection of around 0.35 m and would be expected to decrease with further deflection, eventually becoming negative. Since the model became unstable at lower values of modulus, it was not possible to run models with a greater deflection. The increase in power with blade deflection suggests that blade is not fully optimised in its original position. An explanation for this could be that the blade was designed for a

3 Bladed turbine configuration. The twist along the length of the blade is therefore based on the tip speed ratio at which peak power is achieved for the 3 Bladed configuration. In addition the blade pitch angle was found to the nearest whole degree during previous work but in reality the optimum may be slightly above or below this value.

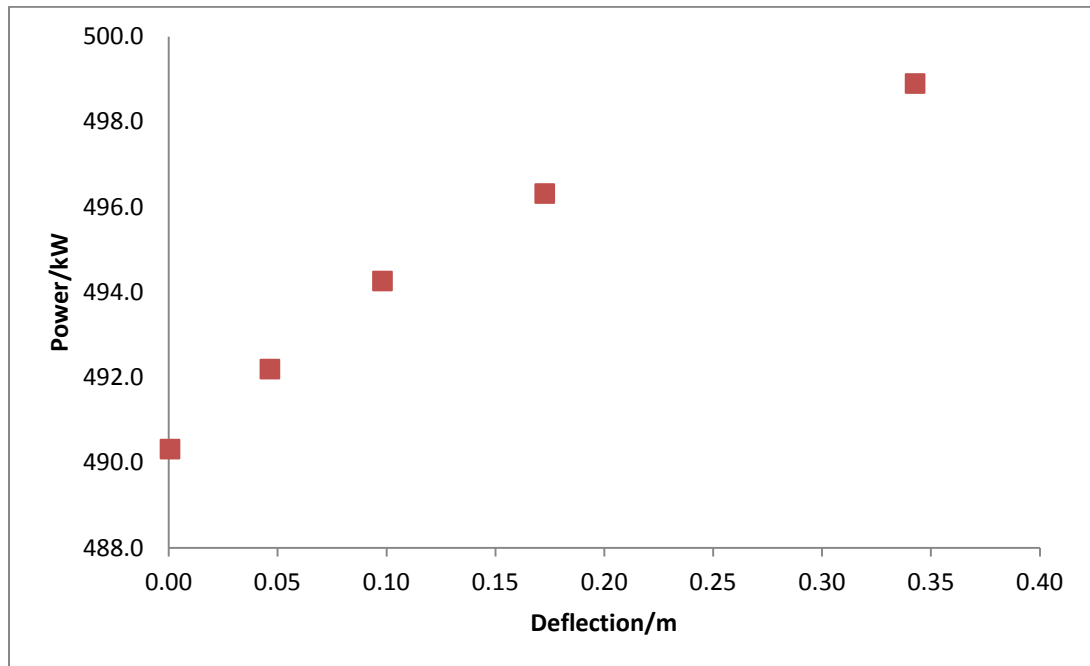


Figure 9.11 Power vs deflection for the 2 bladed turbine

Figures 9.12 and 9.13 give the power output against deflection for the 3 and 4 bladed turbines. The power output of the 3 bladed turbine first increases marginally for a small blade deflection and then decreases for larger blade deflections. This again suggests that although the original blade design may not be fully optimised, it is close to the optimum design for the 3 bladed configuration. Peak power is shown to occur at a deflection of approximately 0.02 m. At this deflection the power increases by 0.04% from the baseline of 544.5 kW to 544.7 kW before falling by 0.4% from the baseline to 542.5 kW. It is expected that the power would continue to fall at higher values of deflection. As for the 3 Bladed turbine, the power output of the 4 bladed turbine first increases with blade deflection before finally decreasing at larger deflections. However, peak power occurs at a much larger blade deflection of around 0.2 m, compared with 0.02 m for the 3 bladed turbine

again suggesting that the 4 bladed turbine is further from optimum in its original position. Peak power of the 4 bladed turbine is 539.7 kW which is 0.4% higher than the baseline of 537.8 kW.

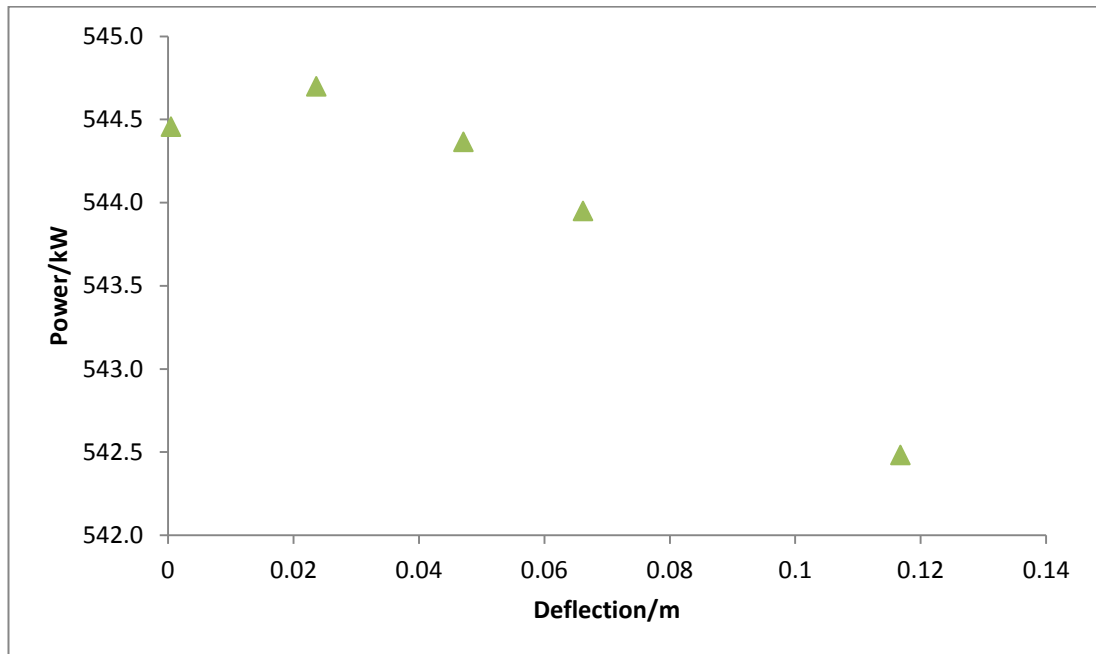


Figure 9.12 Power vs deflection for the 3 bladed turbine

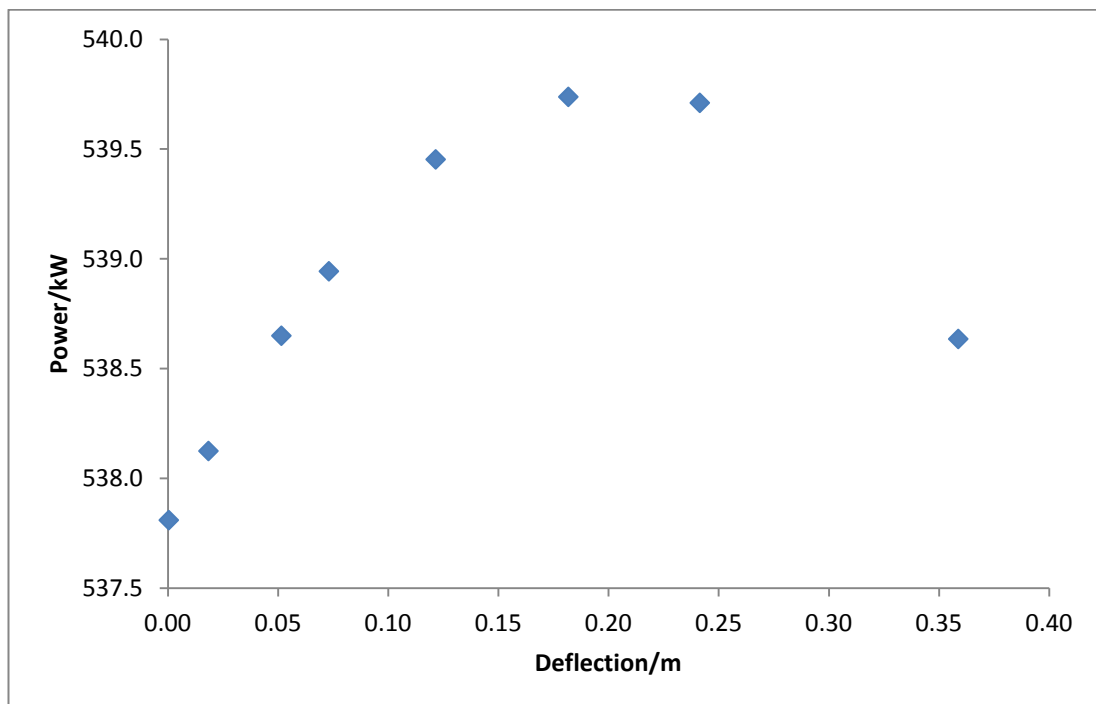


Figure 9.13 Power vs deflection for the 4 bladed turbine

The FSI models with a very high modulus (10 000 GPa), and hence no deflection, predict a slightly different power output than their respective uncoupled CFD models with a variance of $\pm 2\%$. This is thought to be due to the higher convergence and hence greater accuracy that was achieved with the uncoupled CFD models since the problem is inherently transient but has been modelled here as a static case as part of the development of transient models. Therefore the magnitude of power output may be slightly over or under predicted by the FSI models but since these were all run with the same convergence criteria, and each turbine configuration was run with the same mesh for all moduli, it is reasonable to assume that the trends are correct. This can explain why the predicted power output of the 3 bladed turbine is higher than the 4 bladed turbine, as shown in Figures 9.12 and 9.13, whereas the uncoupled models presented in Chapter 5 show that the 4 bladed turbine has the highest power output.

To enable a comparison between the 2, 3 and 4 bladed turbines, the power was normalised against the value given at a modulus of 10 000 GPa and is shown in Figure 9.14 for each of the configurations. It is clear that the greatest effect is on the 2 bladed turbine, although even this is small, with a maximum increase of less than 2% for a blade deflection of around 0.35 m. In comparison with the 2 bladed turbine, the power output of the 4 bladed turbine increases by a much smaller amount, reaching a maximum of 0.4% above the baseline value at a blade deflection of around 0.2 m before falling at greater deflections. The power output of the 3 bladed turbine falls below the baseline level at a blade deflection of 0.04 m and continues to decrease at blade deflections above this reaching 99.6% of its original value at a deflection of 0.12 m; a reduction of 0.4%. At blade deflections below 0.04 m, the power output increases marginally, reaching a maximum of 0.04% above the baseline value at a blade deflection of around 0.02 m. The results for the 3 bladed turbine agree with Jo Chul-Hee et al (2013) and Se Wan Park et al (2013), with blade deflection resulting in a power reduction. The reductions given by these studies were higher than in this work, at 2.2% and 1.7% respectively but were based on different blade profiles. In addition, neither of these studies

investigated whether there was any increase in power at smaller deflections, since only one case was considered with no change in material properties of the blade or flow velocity. The results of the 2 and 4 bladed turbine show that it is possible that blade deflection can result in an increase in power as also shown by Nicholls-Lee et al, who found an improvement of up to 5%. This means that blades could be designed to reach their optimum position at a given deflection.

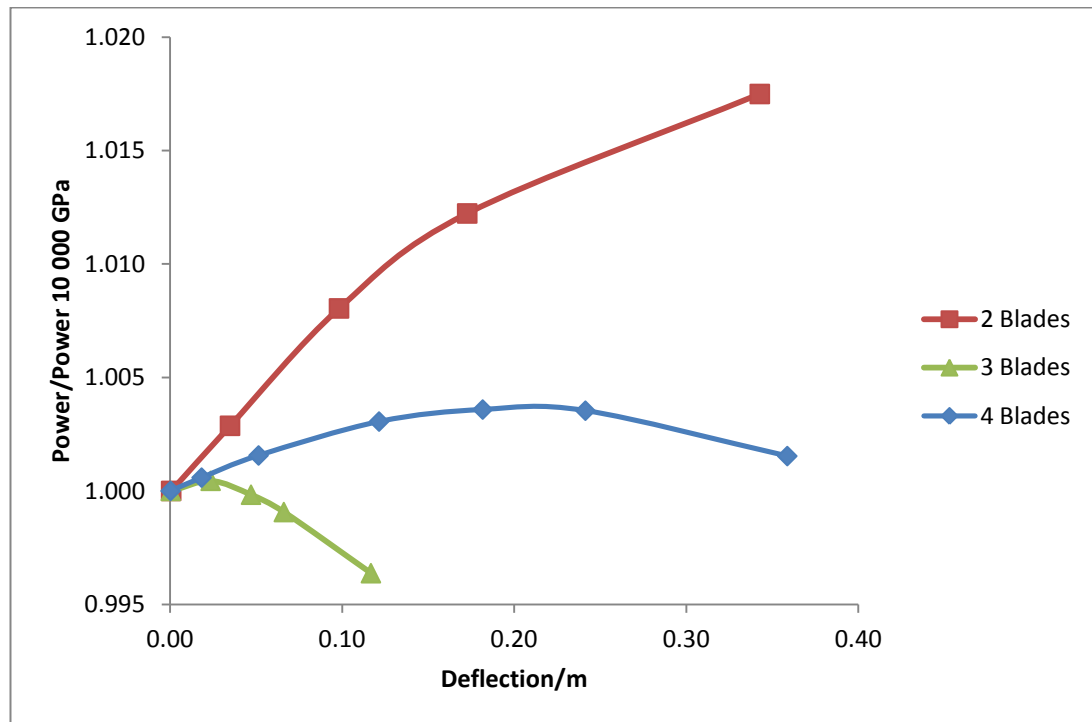


Figure 9.14 Normalised power vs deflection for the 2, 3 and 4 bladed turbines

9.5 Change in Pitch Angle

As the blades deflect as a result of the thrust loading, the tip pitch angle increases. Figure 9.15 shows how the power changes with the increase in pitch angle for the 2, 3 and 4 bladed turbines. The trends are similar to the curves of power against deflection and suggest that the 3 bladed turbine is close to optimum pitch angle in its original undeflected state, whereas the 4 bladed turbine is around 0.3° out and the 2 bladed turbine is at least 0.4° out. This could explain why the power output of the 2 and 4 bladed turbines increases with blade deflection despite the small reduction in swept area. Jo et al. (2013) also found an increase in the tip pitch angle of 0.25° and suggest that this attributed to the loss of power. To confirm that the

change in power output was due to the change in pitch angle and not caused by errors in the coupling, the 2 bladed CFD model was re-run with modified pitch angles, since this configuration showed the largest power change. Figure 9.16 shows reasonable correlation between the FSI results and the modified CFD results, giving confidence in the coupled models. It should be noted that while there is a difference between the results of the FSI and modified CFD results, the CFD results do not include any blade deflection or change in twist along the length of the blade.

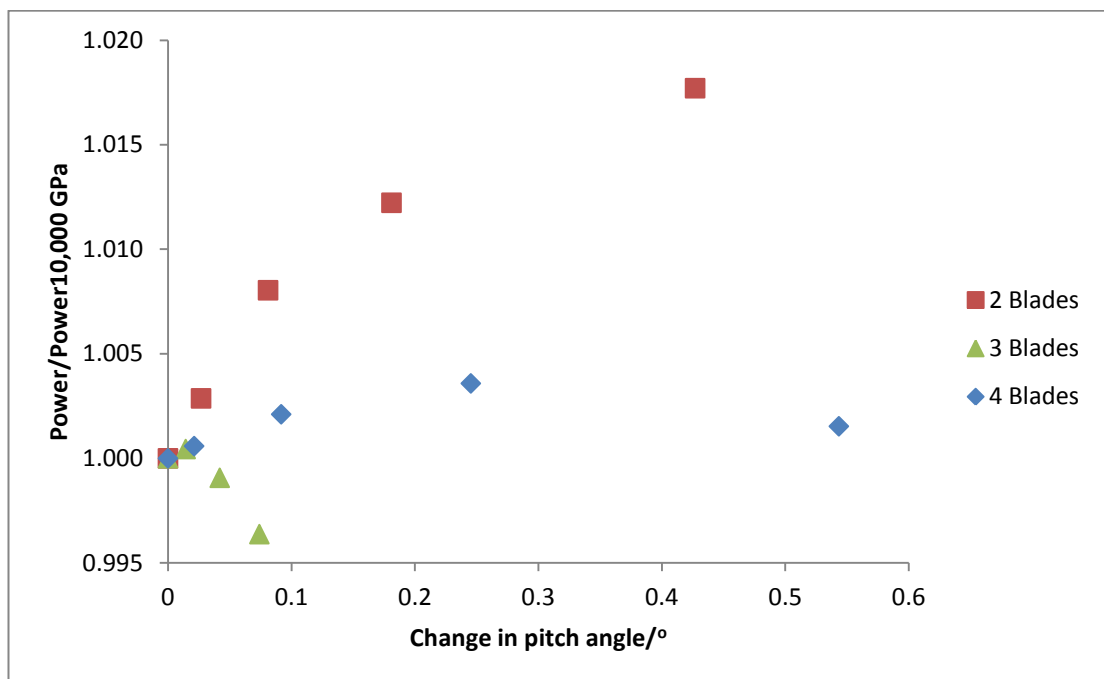


Figure 9.15 Normalised power vs change in pitch angle for the 2, 3 and 4 bladed turbines

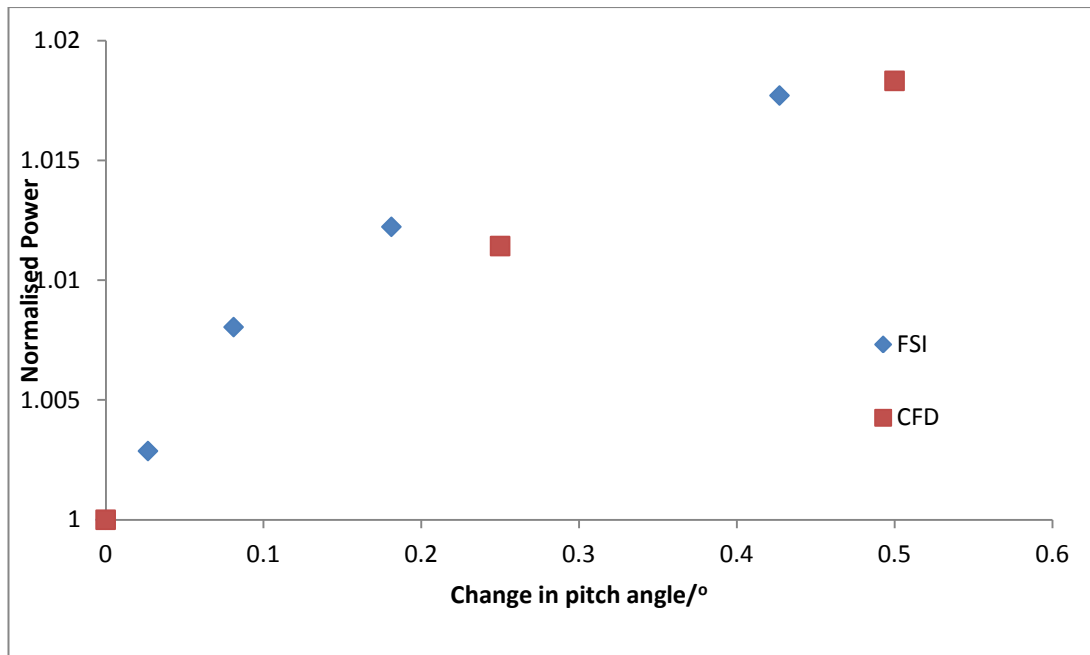


Figure 9.16 Normalised power vs change in pitch angle for the 2, 3 and 4 bladed turbines

9.6 Change in Twist

Along with the change in tip pitch angle, there is also a change in the twist along the length of the blade, reducing the difference between the angle at the tip of the blade and the base of the blade. Figure 9.17 shows how the power changes as the twist from base to tip reduces. It is not possible to separate the effect of the change in pitch angle from the change in twist or to determine how much influence each of these variables has on the power. However, since the power output of the 3 bladed turbine increases slightly and then decreases with changes of pitch angle and of twist, it is likely the original position is close to optimum for both variables.

Figure 9.18 shows the variation in angle along a blade that would be required to maintain a constant angle of attack based on the values of λ associated with peak C_p for each turbine, as presented in Chapter 5. The required twist based on the λ at C_p of the 4 bladed turbine is very close to that required for the 3 bladed turbine. However, there is a difference in the required twist of the 2 bladed turbine, with a

reduction in comparison to that of the 3 and 4 bladed turbines. This would make very little difference to the power output if the tip pitch angle was set to optimum since the inner part of the blade, nearest the hub, contributes a small proportion of the torque. Although the effect of the reduction in twist may be small, when combined with the increase in tip pitch angle, could explain the 1.7% increase in power seen for the 2 bladed turbine. Since the required twist is slightly higher for the 4 bladed turbine than for the 3 bladed turbine, the reduction in twist with deflection would be expected to result in a reduction in power. This could explain why the change in power output of the 4 bladed turbine is smaller than that of the 2 bladed turbine as the tip pitch angle moves closer to optimum but the twist moves further from optimum. The reduction in power seen for the 3 bladed turbine could be a result of both tip pitch angle and twist moving away from the optimum position as the blade deflects.

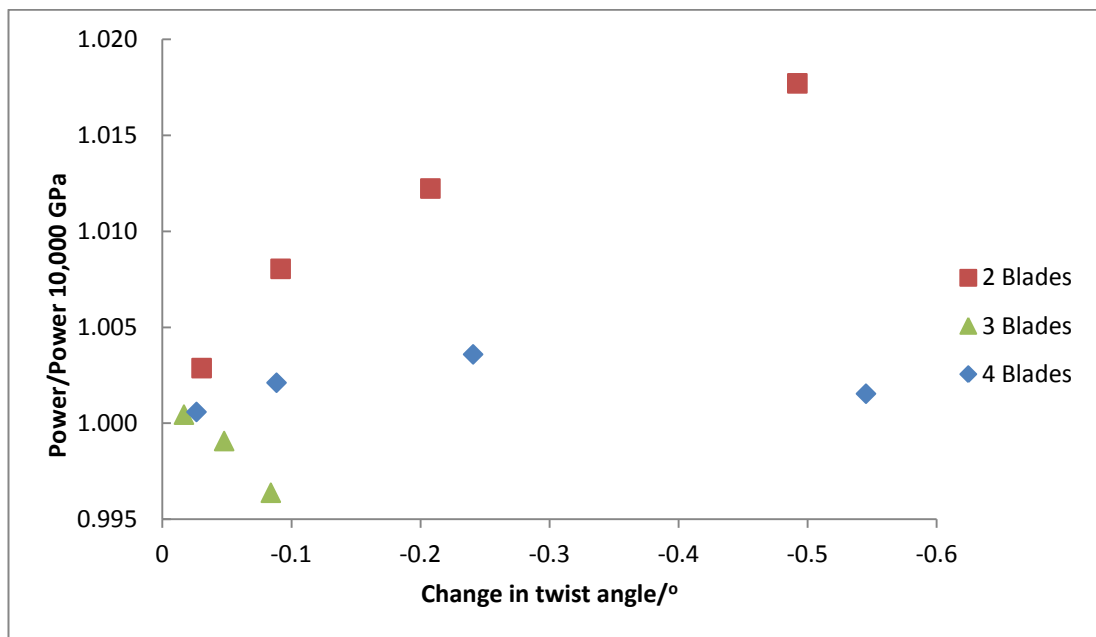


Figure 9.17 Normalised power vs change in twist angle for the 2, 3 and 4 bladed turbines

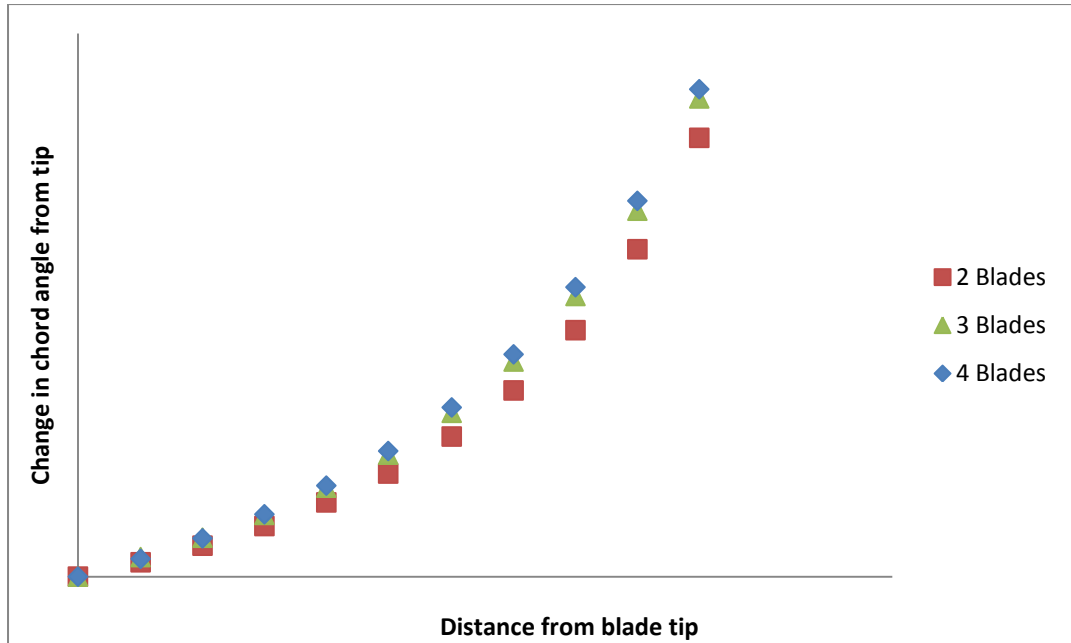


Figure 9.17 Twist required to maintain a constant angle of attack at λ for peak power found in this study

9.7 Summary of Blade Deflection

It is clear that modulus has little effect on power with the greatest change in power over the range of moduli studied found to be around 1.7% for the 2 bladed turbine. Deflections up to 0.35 m also have little effect on the power output of the 2 and 4 bladed turbines. Peak power output occurs at a deflection of around 0.04 m for the 3 bladed turbines, 0.2 m for the 4 bladed turbine and has not yet been reached at 0.35 m for the 2 bladed turbine, although the results indicate that the peak is close to this. These deflections suggest that the original, undeflected blade is closest to optimum for the 3 bladed configuration and furthest from optimum for the 2 bladed configuration. This can be expected since the blade was designed for the 3 bladed configuration and the tip speed ratio at which peak power occurs for the 2 bladed configuration is furthest from this. The results show that where a blade is in its optimum position in its undeflected state, blade deflection will result in a reduction in power but that it is possible to design blades so that they will reach their optimum position at a given deflection.

The thrust load on the 2 and 4 bladed turbines show similar trends although the thrust on 4 bladed turbine starts to taper off around a modulus of 15 GPa. It was not possible to run the 2 bladed model at a modulus below 20 GPa due to the large deflection that occurs, as discussed in Section 9.1. It is therefore not possible to determine whether the same reduction in the rate of increase would be seen for the 2 bladed turbine. Unlike the 2 and 4 bladed configurations the 3 bladed turbine shows a decrease in thrust with blade deflection indicating that a reduction in thrust can be achieved with blade deflection where the blade is at, or close to, optimum in its original position.

10 Conclusions and recommendations

This chapter summarises the findings of the work that has been presented in this thesis, which investigated the effect of solidity on the performance, swirl characteristics, wake recovery and blade deflection of a HATT. The main conclusions are given, followed by specific observations and finally, recommendations for further work.

10.1 Conclusions

Increasing the solidity of a HATT by increasing the number of blades has been found to increase the peak C_θ and peak C_p and reduce the λ at which these occur. C_t was found to be approximately the same at peak C_p , which has been assumed to be the normal operating condition. At λ above peak C_p , near freewheeling, C_t continued to increase for the 2 bladed turbine, remained approximately constant for the 3 bladed turbine and decreased for the 4 bladed turbine, indicating that with the blade profile used in this work, higher solidity rotors would have to withstand lower loads in the event of a failure. In addition, the thrust per blade was shown to increase with a reduction in the number of blades. Additional costs associated with additional blades may therefore be offset by the lower loads which they must be designed to withstand.

The swirl characteristics in the wake were found to agree with swirl theory and the swirl was found to increase with solidity whilst being weak or very weak in each case. Swirl number was found to be dependent on solidity only up to distances of 10 diameters downstream.

At higher turbulent intensities, the wake recovery was only influenced by solidity up to 15 diameters downstream of the HATT but at low turbulence intensities the wake length increased with solidity indicating that low solidity rotors may offer higher overall array efficiencies in areas of low turbulent intensity. Depending on site conditions, it may also be beneficial to have different solidity rotors at different locations within an array.

Blade deflection was shown to increase with a reduction in solidity, due to the increased thrust per blade. The power output of the 3 bladed turbine was shown to decrease with deflection, whereas for the 2 and 4 bladed turbines it was found to first increase as it was subsequently found that the pitch settings found in a previous study were not fully optimised. The power output of the 4 bladed turbine was found to initially increase with deflection and then decrease with further deflection. It is expected that the power output of the 2 bladed turbine would eventually decrease with further deflections but no decrease was found for the maximum deflection achieved in this work. It was therefore found that blade deflection will alter the power output and that blades could be designed so as to reach their optimum setting at a given blade deflection.

10.2 Specific Observations

10.2.1 Validation Data

The modifications made to the laboratory scale prototype HATT resulted in greatly reduced scatter in the angular velocity measurements, giving more confidence in the data. However, the replacement of the motor with a physically smaller version meant that the motor cut out at a current of around 3 A, and therefore the peak C_p was not captured.

10.2.2 Performance Characteristics

Of the two turbulence models used in this work, the SST model predicted higher values than the RSM for C_θ , C_p and C_t over the entire operating range of each turbine but the trends were the same with each model. The difference is thought to be due to the ability of the RSM to model anisotropic turbulent viscosity which is particularly relevant in the near wall region, near the surface of the blades. The RSM predicted peak C_θ values of 0.114, 0.158 and 0.188 for the 2, 3 and 4 bladed turbines respectively, with the SST predicting values of 0.116, 0.163 and 0.199. Predictions of peak C_p for the 2, 3 and 4 bladed turbines of 0.37, 0.41 and 0.43 were found with the RSM compared with 0.39, 0.44 and 0.46 with the SST. Maximum C_t for each turbine was 1.06, 0.94 and 0.86 with the RSM and 1.14, 0.99 and 0.91 with

the SST. The C_t at peak power is similar for each turbine at 0.82, 0.85 and 0.85 with the RSM and 0.85, 0.89 and 0.90 with the SST.

The increase in C_p shows diminishing returns with an increase of between 4.5% and 4.8% from 3 to 4 blades compared with between 10.8% and 11.5 % from 2 to 3 blades. Normal operating λ , which was assumed to be at peak C_p was found to be around $\lambda=4.4$, $\lambda=3.65$ and $\lambda=3.4$ for the 2, 3 and 4 bladed turbines respectively.

Setting a minimum turbulence made very little difference to the performance characteristics.

10.2.3 Swirl

Maximum swirl numbers of 0.17, 0.23 and 0.28 were predicted by the RSM for the 2, 3 and 4 bladed turbines. The maximum swirl numbers predicted by the SST are slightly lower at 0.16, 0.21 and 0.27. The weak or very weak swirl means that the tangential component of velocity is decoupled from axial component and hence wake length cannot be inferred from the swirl number.

Immediately downstream of the turbine, peak swirl occurs at approximately the same λ as peak torque. Further downstream, at distances between 1 and 5 turbine diameters, the swirl is greater with a higher rotational speed of the turbine. At downstream distances above this, the λ which produces maximum swirl is reduced.

Although the maximum swirl close to the turbine occurs at peak torque, the decay is more rapid than at peak power and therefore at distances of 10 diameters or more downstream of the turbine, the swirl produced at peak torque is very close to that produced at peak power.

The difference in max swirl number for each turbine design is greater at peak torque than at peak power . At peak torque swirl number increases almost linearly with the number of blades with only a slight decrease in gradient between 3 and 4 blades compared to that between 2 and 3 blades. At peak power the increase in swirl between 3 and 4 blades is much less than the increase between 2 and 3 blades.

The SST model predicts a more rapid decay in swirl than the RSM model as the turbulent decay is much less rapid. With a fixed minimum background turbulence level, the differences in predictions of swirl and swirl decay were reduced with the models showing very similar predictions at peak power. There were still small differences between the swirl decay at peak torque although the difference was very small for the 2 bladed model. The difference in predictions increased with the number of blades due to the small difference in the swirl imparted per blade being multiplied by the number of blades.

10.2.4 Wake

The velocity recovery in the wake is highly dependent on the ambient turbulence, with higher turbulence intensity resulting in a shorter wake length. The difference in turbulence almost entirely accounted for the difference between the RSM and SST wake recovery predictions, with negligible difference in predictions when a fixed minimum turbulence was set.

The swept area average velocity can give a better estimate of the available energy at a given position downstream of a turbine and gives a shorter wake length than the centre line value.

The minimum axial velocity, outside the recirculation zone, decreases with increasing solidity. The dependence of the velocity recovery on solidity decreases with increasing downstream distance with the far wake being more dependent on turbulent intensity than on solidity.

10.2.5 Blade Deflection

The 3 bladed turbine shows a very small increase in torque, and hence a 0.04% increase in power, with a very small blade deflection of 0.02 m. There is then a reduction in torque and power with a reduction in modulus and an increase in blade deflection, giving a reduction in power of 0.4% at a deflection of 0.12 m.

Unlike the 3 bladed turbine, the 2 and 4 bladed turbines show a small increase in power with a relatively large blade deflection. The 4 bladed turbine reaches

maximum power at a blade deflection of around 0.2m whereas the power for the 2 bladed turbine continues to increase at the maximum deflection modelled of 0.35m. The maximum increase in power found was 1.7% for the 2 bladed turbine and 0.4% for the 4 bladed turbine, although the results indicate that for the 2 bladed turbine the maximum is slightly above that found in this study.

The results indicate that the torque, power and thrust are relatively insensitive to changes in modulus and blade deflections. They also indicate that the 3 bladed turbine is close to its optimum setting, whereas the 2 and 4 bladed turbine reach their optimum settings with blade deflections of at least 0.35m and around 0.2m respectively. It is suggested that this may be partly due to the 3 bladed being closest to its optimum blade pitch angle in its undeflected state with the 4 bladed turbine being around 0.3° below its optimum and the 2 bladed turbine at least 0.4° below optimum. The change in twist along the blade may also alter the performance although it is not possible to state whether the change in pitch or the change in twist has a greater effect.

10.3 Recommendations and future work

Further modifications should be made to the laboratory scale HATT to include instrumentation such as strain gauges, which would enable validation of the FEA models. It would also be beneficial to include a motor with a higher rated current so that more of the power curve could be covered by the experimental testing.

The influence of solidity on the various parameters considered could be investigated by changing the chord length instead of the number of blades. This would enable comparisons to be made and hence the effect of blade number separated from the effect of solidity.

The effect of ambient turbulence on the swirl and the wake recovery could be further assessed by testing a range of values of fixed minimum turbulence. This could help to inform array spacing based on the turbulence measured at a site.

Field measurements of the far wake are required to validate wake modelling and improve confidence in the predicted recovery.

A series of CFD models should be run with changes in pitch angles in small increments of around 0.1° to establish a more exact optimum position for a rigid blade before any further FSI modelling which is focussed on changes in performance.

Transient FSI models with the inclusion of a support stanchion could be developed to explore the dynamic loading and fluctuations in blade deflection as the blades pass in front of, or behind the stanchion. Velocity profiles could also be included in these models.

The blades should be redesigned so they are more realistic for a full scale turbine, with a larger diameter tapered root, and composite materials with internal blade structure. This would allow realistic stress and strain outputs from the FEA models and hence would inform fatigue and life predictions.

Finally, the drive train could also be included in the FEA models to study the load distribution on the various internal components, again informing life predictions and contributing to estimation of required maintenance cycles.

References

ABP mer, 2007. *Quantification of Exploitable Tidal Energy Resources in UK Waters*. Southampton: ABP Marine Environmental Research Ltd.

Afgan, I., McNaughton, J., Rolfo, S., Apsley, D.D., Stallard, T., Stansby, P., 2013. Turbulent Flow and Loading on a Tidal Stream Turbine by LES and RANS. *International Journal of Heat and Fluid Flow* 43, pp. 96-108.

Alstom, 2013. *Alstom's tidal turbine generates 100MWh of electricity on the grid* [Online]. Available at: <http://www.alstom.com/press-centre/2013/10/alstoms-tidal-turbine-generates-100mwh-of-electricity-on-the-grid/> [Accessed 20 Jan 2014]

ANSYS, 2010. FLUENT Theory Guide. ANSYS Academic Research Release 13. ANSYS, Inc.

ANSYS, 2011a. *Mechanical APDL Theory Reference*. ANSYS Academic Research Release 14. ANSYS, Inc.

ANSYS, 2011b. *System Coupling User's Guide*. ANSYS Academic Research Release 14. ANSYS, Inc.

Appleyard, D., 2012. *Tide Mill Institute* [Online]. Available at: <http://www.tidemillinstitute.org/35.html> [Accessed 20 April 2012]

Arnold, M., Biskup, F., Cheng, P. W., 2013. Simulation of Fluid-Structure-Interaction on Tidal Current Turbines Based on Coupled Multibody and CFD Methods. *Proc. Twenty-third International Offshore and Polar Engineering*. Anchorage, 30 June-5 July 2013.

Ashby, M.F. and Jones, D.R.H., 1980. *Engineering Materials, An Introduction to their Properties and Applications*. Oxford: Pergamon Press Ltd.

Bahaj, A.S., Batten, W.M.J. and McCann, G., 2007a. Experimental verifications of numerical predictions for the hydrodynamic performance of horizontal axis marine current turbines. *Renewable Energy* 32 (15), pp. 2479-2490.

Bahaj, A.S., Molland, A.F., Chaplin, J.R., Batten, W.M.J., 2007b. Power and thrust measurements of marine current turbines under various hydrodynamic flow

conditions in a cavitation tunnel and a towing tank. *Renewable Energy* 32, pp. 407-426.

Batten, W.M.J., Harrison, M.E., Bahaj, A.S., 2013. Accuracy of the actuator disc-RANS approach for predicting the performance and wake of tidal turbines. *Philosophical Transactions of The Royal Society A, Mathematical, Physical & Engineering Sciences* 371, 20120293

BBC, 2002. *Tidal Energy Power Plan* [Online]. Available at: <http://news.bbc.co.uk/1/hi/scotland/2254701.stm> - [Accessed: 25 March 2012]

Bercin, K., Lloyd, T., Xie, Z., Turnock, S.R., 2013. Efficient method for analysing fluid-structure interaction of horizontal axis tidal turbine blades. *10th European Wave and Tidal Energy Conference*. Aalborg, 2-5 September 2013.

BERR, 2008. *Atlas of UK Marine Renewable Energy Resources: Atlas Pages, A Strategic Environmental Assessment Report*. Southampton: ABP mer.

Betz, A., 1996. *Introduction to the Theory of Flow Machines*. (D.G.Randall, Trans.) Oxford: Pergamon Press.

Bhushan, S., Alam, M. F., Walters, D.K., 2013- Evaluation of hybrid RANS/LES models for prediction of flow around surface combatant and Suboff geometries. *Computers & Fluids* 88, pp. 834-849.

BioPower Systems, 2013. *bioStream* [Online] Available at: <http://www.biopowersystems.com/biostream.html> [Accessed 22 Feb 2013]

Black and Veatch, 2005. *Phase II UK Tidal Stream Energy Resource Assessment*. London: Carbon Trust

Black and Veatch, 2011. *UK Tidal Current Resource & Economics*. London: Carbon Trust

Byrne, C., Cherrett, W., Grosvenor, R., Mason-Jones, A., Morris, C., O'Doherty, D., O'Doherty, T., Prickett, P., 2011. An Investigation into the Possible Effects of Cavitation on a Horizontal Axis Tidal Turbine. *9th European Wave and Tidal Energy Conference*. Southampton, 5-9 September 2011.

Chigier, N.A. and Chervinsky, A., 1967. Experimental Investigation of Swirling Vortex Motion in Jets, *Fifth United States National Congress of Applied Mechanics*, Minnesota, 1966. *J. Applied Mechanics, Trans. ASME, Series E* 3, pp. 443-451.

Cho, R., 2011. Is Biomass Really Renewable? [Online] Available at: <http://blogs.ei.columbia.edu/2011/08/18/is-biomass-really-renewable/> [Accessed 15 Nov 2013]

Clarke, J.A., Connor, G., Grant, A.D., Johnstone, C., Ordonez-Sanchez, S., 2008. A contra-rotating marine current turbine on a flexible mooring: Development of a scaled prototype. *Proceedings of the 2nd international conference on Ocean Energy*, 15-17 Oct 2008, Brest, France. Clarke JA, Connor G, Grant A.D, Johnstone C, Ordonez-Sanchez S.

Clarke, J., Connor, G., Grant, A.D., Johnstone, C., Ordonez-Sanchez, S., 2010. Analysis of a single point tensioned mooring system for station keeping of a contra-rotating marine current turbine. *IET Renewable Power Generation* 4(6)

Collier, W. and Way, S.P., 2013. Full Scale validation study of a numerical tool for the prediction of loading and hydrodynamic performance of axial flow tidal turbines. *10th European Wave and Tidal Energy Conference*. Aalborg, 2-5 September 2013.

Consul, C.A., Willden, R.H.J., Ferrer, E., McCulloch, M.D. 2009. Influence of Solidity on the Performance of a Cross-Flow Turbine. *8th European Wave and Tidal Energy Conference*, Uppsala, 7-10 September 2009.

Cottrell, J., 2002. The mechanical design, analysis and testing of a two-bladed wind turbine hub. National Renewable Energy Laboratory. Technical Report. NREL/TP-500-26645. [Online] Available at: <http://www.nrel.gov/docs/fy02osti/26645.pdf> [Accessed 6 April 2013]

Daly, B.J. and Harlow, F.H., 1970. Transport Equations in Turbulence. *Phys. Fluids* 13, pp.2634–2649.

DECC, 2011. *UK Renewable Energy Roadmap*. London: Crown copyright, Department of Energy & Climate Change

DECC, 2012. *UK Renewable Energy Roadmap Update 2012*. London: Crown copyright, Department of Energy & Climate Change

DECC, 2013. *UK Renewable Energy Roadmap Update 2013*. London: Crown copyright, Department of Energy & Climate Change

DTI, 2007. *Economic viability of a simple tidal stream energy capture device*. London: Department of Trade and Industry.

Duquette, M. and Visser, K.D., 2003- Numerical implications of solidity and blade number on rotor performance of horizontal-axis wind turbines. *Journal of Solar Energy Engineering* 125(4), pp. 425-432.

Duquette, M.M., Swanson, J., Visser, K.D., 2003- Solidity and blade number effects on a fixed pitch, 50W horizontal axis wind turbine. *Wind Engineering*, 27(4), pp.299-316.

Egarr, D.A., O'Doherty, T., Morris, S., Ayre, R.G., 2004. Feasibility study using Computational Fluid Dynamics for the use of a turbine for extracting energy from the tide. *Proceedings of the 15th Australasian Fluid Mechanics Conference*. Sydney, 13-17 December 2004.

EMEC, 2012. *Tidal Devices* [Online] Available at: <http://www.emec.org.uk/marine-energy/tidal-devices/> [Accessed 14 April 2012]

Environment Agency, 2009. *Biomass: Carbon sink or carbon sinner?* [Online] Available at: http://www.environment-agency.gov.uk/static/documents/Leisure/Biomass__carbon_sink_or_carbon_sinner_summary_report.pdf [Accessed 15 Nov 2013]

Eriksson, S., Bernhoff, H., Leijon, M., 2008. Evaluation of different turbine concepts for wind power. *Renewable and Sustainable Energy Reviews* 12(5), pp. 1419-1434.

European Union Committee, 2008. *27th Report of Session 2007–08 - The EU's Target for Renewable Energy: 20% by 2020*. London : The Stationery Office Limited

Faudot, C., Dahlhaug, O.G., Holst, M.A., 2013. Tidal Turbine Blades in runaway situation: experimental and numerical approaches. *10th European Wave and Tidal Energy Conference*. Aalborg, 2-5 September 2013.

Fleming, C.F., McIntosh, S.C., Willden, R.H.J., 2013. Tidal Turbine Performance in Sheared Flow. EWTEC 2013. Simon C McIntosh, Richard H.J. Willden. *10th European Wave and Tidal Energy Conference*. Aalborg, 2-5 September 2013.

Flumill, 2012. *Power Tower, The future of renewable energy* [Online] Available at: <http://www.flumill.com> [Accessed 25 August 2013].

- Frankel, P.L.**, 2002. Power from marine currents. *Proceedings of the Institution of Mechanical Engineers 216 Part A: J Power and Energy*, pp. 1-14.
- Frid, C. and Andonegi, E.**, 2012. The environmental interactions of tidal and wave energy generation devices. *Environmental Impact Assessment Review* 32(1), pp.133-139.
- Frost, C., Morris, C.E., Mason-Jones, A., O'Doherty, D.M., O'Doherty, T.**, 2014. The Effect of Tidal Flow Directionality on Tidal Turbine Performance Characteristics. *Renewable Energy*. Submitted Feb 2014.
- Gant, S. and Stallard, T.**, 2008. Modelling a tidal turbine in unsteady flow. Proceedings of the 18th International Offshore and Polar Engineering Conference. Vancouver, 6-11 July 2008.
- Gibson, M.M. and Launder, B.E.**, 1978. Ground Effects on Pressure Fluctuations in the Atmospheric Boundary Layer. *J. Fluid Mech* 86, pp. 491–511.
- Gupta, A.K., Lilley, D.G., Syred, N.**, 1984, *Swirl flows*, Tunbridge Wells, Abacus Press.
- Han, S.H., Park, J.S., Lee, K.S.**, 2013. In-situ demonstration test for tidal current power generation with a helical turbine- 10th *European Wave and Tidal Energy Conference*. Aalborg, 2-5 September 2013.
- Hansen, M.O.L.**, 2001. Aerodynamics of wind turbines: Rotors, loads and structure. London; James & James (Science publishers) Ltd.
- Harris, R.E., Johanning, L., Wolfram, J.**, 2004. Mooring systems for wave energy converters: A review of design issues and choices. 3rd *International Conference on Marine Renewable Energy*, Blyth, 6-9 July 2004
- Hau, E.**, 2006. *Wind Turbines: Fundamentals, technologies, application, economics*. 2nd edition.
- Helmis, C.G., Papadopoulos, K.H., Asimakopoulos, D.N., Papageorgas, P.G., Soilemes, A.T.**, 1995. An experimental study of the near wake structure of a wind turbine operating over complex terrain. *Solar Energy* 54(6), pp. 413-28.
- Hinze, J.O.**, 1975. *Turbulence*. 2nd edition. New York: McGraw-Hill.

- Jo, C.H., Lee, J.H., Kim, D.Y., Lee, K.H.,** 2013. Performance of a Horizontal Axis Tidal Current Turbine with Blade Deformation. *10th European Wave and Tidal Energy Conference*. Aalborg, 2-5 September 2013.
- Keyes, J.J.,** 1960, An experimental study of gas dynamics in high velocity vortex flow. *Proceedings of the 1960 Heat Transfer and Fluid Mechanics Institute*, Stanford.
- Khan, M.J., Bhuyan, G., Iqbal, M.T., Quaicoe, J.E.,** 2009. Hydrokinetic energy conversion systems and assessment of horizontal and vertical axis turbines for river and tidal applications: A technology status review. *Applied Energy* 86, pp. 1823-1835.
- Lauder, B.E. and Spalding, D.B.,** 1974. The Numerical Computation of Turbulent Flows. *Computer Methods in Applied Mechanics and Engineering* 3, pp. 269–289.
- Lee, Y.J. Jhan, Y.T., Chung, C.H.,** 2012- Fluid-structure interaction of FRP wind turbine blades under aerodynamic effect. *Composites Part B: Engineering* 43(5), pp. 2180-2191.
- Lien, F.S. and Leschziner, M.A.,** 1994. Assessment of Turbulent Transport Models Including Non-Linear RNG Eddy-Viscosity Formulation and Second-Moment Closure. *Computers and Fluids* 23(8), pp. 983–1004.
- Lilley, D.G.,** 1973. Prediction of inert turbulent swirl flows, *AIAA Journal* 11(7), pp. 955-960.
- Liu, P., Veitch, B.,** 2012. Design and Optimization for Strength and Integrity of Tidal Turbine Rotor Blades. *Energy* 46, pp. 393-404.
- Lucca-Negro, O.,** 1999. *Modelling of swirling flow instabilities*. PhD Thesis, University of Wales, Cardiff.
- Lucca-Negro, O. and O'Doherty, T.,** 2001. Vortex breakdown: a review. *Progress in Energy and Combustion Science* 27, pp. 431-481.
- Lunar Energy,** 2012. *Technology. LTT-The Product* [Online] Available at: <http://www.lunarenergy.co.uk/productOverview.htm> [Accessed 4 Mar 2012].
- Mackay, D.J.C.,** 2007. *Under-estimation of the UK tidal resource* [Online]. Available at: www.inference.phy.cam.ac.uk/mackay/abstracts/TideEstimate.html. [Accessed 20 Nov 2012]

Malki, R., Williams, A.J., Croft, T.N., Togneri, M., Masters, I., 2013. A coupled blade element momentum – Computational fluid dynamics model for evaluating tidal stream turbine performance. *Applied Mathematical Modelling* 37, pp. 3006-3020

Mason-Jones, A., Evans, P.S., O'Doherty, T., O'Doherty, D.M., 2008. Characterisation of a tidal stream turbine design using CFD and ADCP, *Proceedings of the World Renewable Energy Congress*. Glasgow, 19-25 July 2008.

Mason-Jones, A., 2010. *Performance Assessment of a Horizontal Axis Tidal Turbine in a High Velocity Shear Environment*. PhD thesis, Cardiff University.

Mason-Jones, A., O'Doherty, D.M., Morris, C.E., O'Doherty, T., 2013. Influence of a velocity profile & support structure on tidal stream turbine performance. *Renewable Energy* 52, pp. 23-30.

Mason-Jones, A., O'Doherty, D. M., Morris, C. E., O'Doherty, T., Byrne, C. B., Prickett, P. W., Grosvenor, R. I., Owen, I., Tedds, S., Poole, R. J., 2012. Non-dimensional scaling of tidal stream turbines. *Energy* 44(1), pp. 820-829.

Massey, B.S., (Revised by J Ward-Smith), 2006. *Mechanics of Fluids*, 8th Edition. London: Taylor and Francis

Masters, I. Malki, R. Williams, A.J. Croft, T.N., 2013. The influence of flow acceleration on tidal stream turbine wake dynamics: A numerical study using a coupled BEM-CFD model. *Applied Mathematical Modelling* 37, pp. 7905-7918

McCaffrey, K., Fox-Kemper, B., Hamlington, P., Thomson, J., 2013. Characterization of Turbulence Anisotropy, Coherence, and Intermittency at a Prospective Tidal Energy Site: Observational Data Analysis. Submitted to *Renewable Energy* October 2013.

McCann, G. Thomson, M., Hitchcock, S., 2008. Implications of Site-Specific Conditions on the Prediction of Loading and Power Performance of a Tidal Stream Device. 2nd *International Conference on Ocean Energy*, Brest, 15-17 October 2008.

McCombes, T, Grant, A., Johnstone, C., 2008. Unsteady hydrodynamic modelling of rotor systems used in marine current turbines. *Proceedings of the World Renewable Energy Congress*. Glasgow, 19-25 July 2008.

McNaughton, J., Rolfo, S., Apsley, D., Stallard, T., Stansby, P., 2013. CFD Power and Load Prediction on a 1MW Tidal Stream Turbine with Typical Velocity Profiles from the EMEC Test Site. 10th *European Wave and Tidal Energy Conference*. Aalborg, 2-5 September 2013.

McSherry, R., Grimwade, J., Jones, I., Mathias, S., Wells, A., Mateus, A., 2011. 3D CFD modelling of tidal turbine performance with validation against laboratory experiments. *9th European Wave and Tidal Energy Conference*. Southampton, 5-9 September 2011.

Menter, F.R., 1994. Two-Equation Eddy-Viscosity Turbulence Models for Engineering Applications. *AIAA Journal* 32(8), pp. 1598–1605.

Menter, F.R., Langtry, R.B., Likki, S.R., Suzen, Y.B., Huang, P.G., Volker, S., 2004. A Correlation Based Transition Model Using Local Variables Part 1-Model Formulation. ASME Turbo Expo. Vienna, 14-17 June 2004.

Millward, A. and Rositer, J., 1983. The Design of a Multi-purpose Multicomponent Strain Gauge Dynamometer. *Strain* 19 (7), pp 27-30.

Minesto, 2012. *Deep Green Technology* [Online] Available at: <http://www.minesto.com/deepgreentechnology/index.html> [Accessed 25 Feb 2012]

Murdoch University, 2008. *Tidal Barrage & Tidal Turbines* [Online]. Available at: <http://www.see.murdoch.edu.au/resources/info/Tech/tidal/> [Accessed 20 Jan 2014]

Myers, L.E., and Bahaj, A.S., 2010. Experimental analysis of the flow field around horizontal axis tidal turbines by use of scale mesh disk rotor simulators. *Ocean Engineering* 37(2-3), pp. 218-227.

National Archives, 2008. *Climate Change Act 2008* [Online]. Available at: <http://www.legislation.gov.uk/ukpga/2008/27/contents> [Accessed 15 Nov 2013]

Nicholls-Lee, R.F., Turnock, S.R., Boyd, S.W., 2011. A method for analysing FSI on a HATT. *9th European Wave and Tidal Energy Conference*. Southampton, 5-9 September 2011.

Nicholls-Lee, R.F., 2011- Adaptive Composite Blades for Horizontal Axis Tidal Turbines. PhD Thesis, University of Southampton.

Olczak, A., Stallard, T., Stansby, P., 2013. The influence of waves on Tidal Stream Turbine Wake Recovery- 10th *European Wave and Tidal Energy Conference*. Aalborg, 2-5 September 2013.

OpenHydro, 2012. *Technology* [Online] Available at: <http://www.openhydro.com/news/100908.html> [Accessed 4 Feb 2012]

Orme, J.A.C. and Masters, I., 2004. Design and testing of a direct drive tidal stream generator. 3rd *International Conference on Marine Renewable Energy*. Blyth, 6-9 July 2004.

Osalusi, E., Side, J., Harris, R., 2009. Structure of turbulent flow in EMEC's tidal energy test site. *International Communications in Heat and Mass Transfer* 36(5), pp. 422-431.

Park, S.W., Park, S, Rhee, S.H., 2013. Performance Predictions of a Horizontal Axis Tidal Stream Turbine Considering the Effects of Blade Deformation. 3rd *International Symposium on Marine Propulsors*. Launceston, 5-8 May 2013.

Renewabl, 2010. *OSD to being testing of tidal energy device in Humber estuary* [Online]. Available at: <http://www.renewabl.com/2010/09/03/osd-to-being-testing-of-tidal-energy-device-in-humber-estuary.html> [Accessed 25 March, 2012].

Renewable Energy World, 2010. *Flaw Hits Hundreds of EU Offshore Wind Turbines* [Online]. Available at: <http://www.renewableenergyworld.com/rea/news/article/2010/04/flaw-hits-hundreds-of-eu-offshore-wind-turbines> [Accessed 26 Mar 2012].

Renewable UK, 2011. *Wave and Tidal Energy in the UK*. [pdf] London:Renewable UK. Available at http://www.bwea.com/pdf/marine/Wave-Tidal_energy_UK.pdf [Accessed 20 Nov 2012]

Riegler, H., 2003. HAWT versus VAWT: Small VAWTs find a clear niche. *Refocus* 4 (4), pp. 44-46

Roh, S.C., and Kang, S.H., 2013. Effects of a blade profile, the Reynolds number, and the solidity on the performance of a straight bladed vertical axis wind turbine. *Journal of Mechanical Science and Technology* 27 (11), pp. 3299-3307.

Roschke, E.J. and Pivrotto, J.J., 1965. Similarity in Confined Vortex Flows. *Jet Propulsion Lab. Tech. Report, no. 32-789*.

Royal Haskoning, 2011. *SeaGen Environmental Monitoring Programme Final Report* [Online]. Available at: <http://www.marineturbines.com/sites/default/files/SeaGen-Environmental-Monitoring-Programme-Final-Report.pdf> [Accessed 2 March 2013]

Salter, S.H., 2005. Possible under-estimation of the UK tidal resource [Online]. Available at: www.berr.gov.uk/files/file31313.pdf. [Accessed 20 Nov 2012].

Sea Generation, 2007. *Sea Gen Fact Sheet* [Online] Available at: <http://www.seageneration.co.uk/downloads/asp> Accessed 22 Feb 2012].

Shiono, M., Suzuki, K., Kiho, S., 2000. An Experimental Study of the Characteristics of a Darrieus Turbine for Tidal Power Generation. *Electrical Engineering in Japan* 132(3), pp. 38-47.

Sloan, D.G., Smit, P.J. and Smoot, L.D., 1986. Modelling of swirl in turbulent flow systems. *Progress in Energy and Combustion Science* 12, pp. 163-250.

SMD, 2012-Renewables Design & Development [Online] Available at: <http://www.smd.co.uk/products/renewables/design-devlopment.htm> [Accessed 22 Feb 2012]

Sozou, C. and Swithenbank, J., 1969. Adiabatic transverse waves in a rotating fluid, *J. Fluid Mech.* 38(4), pp. 657-671.

Spall, R.E., Gatski, T.B., Grosch, C.E., 1987. A criterion for vortex breakdown, *Physics of Fluids* 30(11), pp. 3434-3440.

Starzmann, R., Baldus, M., Groh, E., Hirsch, N., Lange, N.A., Scholl S., 2013- Full Scale Testing of a Tidal Energy Converter Using a Tug Boat. *10th European Wave and Tidal Energy Conference*. Aalborg, 2-5 September 2013.

Sustainable Development Commission, 2007. *Turning the tide- Tidal Power in the UK* [Online]. Available at: <http://www.sd-commission.org.uk/publications.php?id=607> [Accessed 4 Mar 2012]

Switzer, T., and Meggitt, D., 2010. Review of Literature and Studies on Electromagnetic Fields (EMF) Generated by Undersea Power Cables and Associated

Influence on Marine Organisms. *Oceans- Innerspace: A Global Responsibility*, Seattle, 20-23 September 2010.

Syred, N., 2006. A review of oscillation mechanisms and the role of the precessingvortex core (PVC) in swirl combustion systems. *Progress in energy and Combustion Science* 32, pp.93-161.

Taylor, P., 2007. SeaGen Tidal Power Installation [Online] Available at: <http://www.alternative-energy-news.info/seagen-tidal-power-installation/> [Accessed 27 Mar 2012].

Tedds S.C., de Jesus Henriques, T.A., Owen, I., Poole, R.J., 2013. Near wake characterisation of Horizontal Axis Tidal Stream Turbines in non-uniform steady flow. *10th European Wave and Tidal Energy Conference*. Aalborg, 2-5 September 2013.

Tedds, S.C., Poole, R.J., Owen, I., Najafian, G., Bode, S.P., Mason-Jones, A., Morris, C., O'Doherty, T., O'Doherty, D.M., 2011. Experimental Investigation of Horizontal Axis Tidal Stream Turbines. *9th European Wave and Tidal Energy Conference*. Southampton, 5-9 September 2011.

The Engineering Business, 2005. *Stingray Tidal Stream Device-Phase 3* [Online] Available at: <http://www.inference.phy.cam.ac.uk/sustainable/refs/tide/StingrayPhase3r.pdf> [Accessed 29 Feb 2012]

Tidal Energy, 2012a- *The technology* [Online]. Available at http://tidalenergyltd.com/?page_id=640 [Accessed 20 May 2012].

Tidal Energy, 2012b *Our History* [Online]. Available at: http://www.tidalenergyltd.com/?page_id=21 [Accessed 20 May 2012]

Tidal Generation, 2010. *Product Development* [Online] Available at: <http://www.tidalgeneration.co.uk/products/> [Accessed 20 Jan 2012].

U.S. Department of Energy, 2009. *Report to Congress on the Potential Environmental Effects of Marine and Hydrokinetic Energy Technologies* [Online]. Available at: http://www1.eere.energy.gov/water/pdfs/doe_eisa_633b.pdf [Accessed 12 Dec 2011]

University of Naples, 2012. *Aircraft design and Aeroflight Dynamics Group-Renewable energy* [Online]. Available at:

http://www.adag.unina.it/english/research/renewable_energy.html [Accessed 20 Nov 2012].

VerdErg, 2012. *SMEC Technology, Basic Principles* [Online] Available at: http://www.verderg.com/index.php?option=com_content&view=article&id=95&Itemid=66 [Accessed 25 Feb 2012]

Vermeer, L.J., Sorensen, J.N., Crespo, A., 2003. Wind turbine wake aerodynamics. *Progress in Aerospace Sciences* 39 pp. 467-510

Versteeg H.K., and Malalasekara, W., 2007. *An Introduction to Computational Fluid Dynamics, The Finite Volume Method*. 2nd Edition. Harlow: Pearson Education Limited.

Wadia, M., Meunier, M., Olsen, D., McEwen, L., 2011. Composite Blades for Tidal Turbines Versus Wind Turbines at Multi-Megawatt Scale. *9th European Wave and Tidal Energy Conference*. Southampton, 5-9 September 2011.

Walker, J.M., Flack, K.A., Lust, E.E., Schultz, M.P., Luznik, L., 2013. The Effects of Blade Roughness and Fouling on Marine Current Turbine Performance. *10th European Wave and Tidal Energy Conference*. Aalborg, 2-5 September 2013.

Wilcox, D.C., 1998. *Turbulence Modelling for CFD*. La Canada: DCW Industries, Inc.

Appendix A Performance Characteristics with SST model

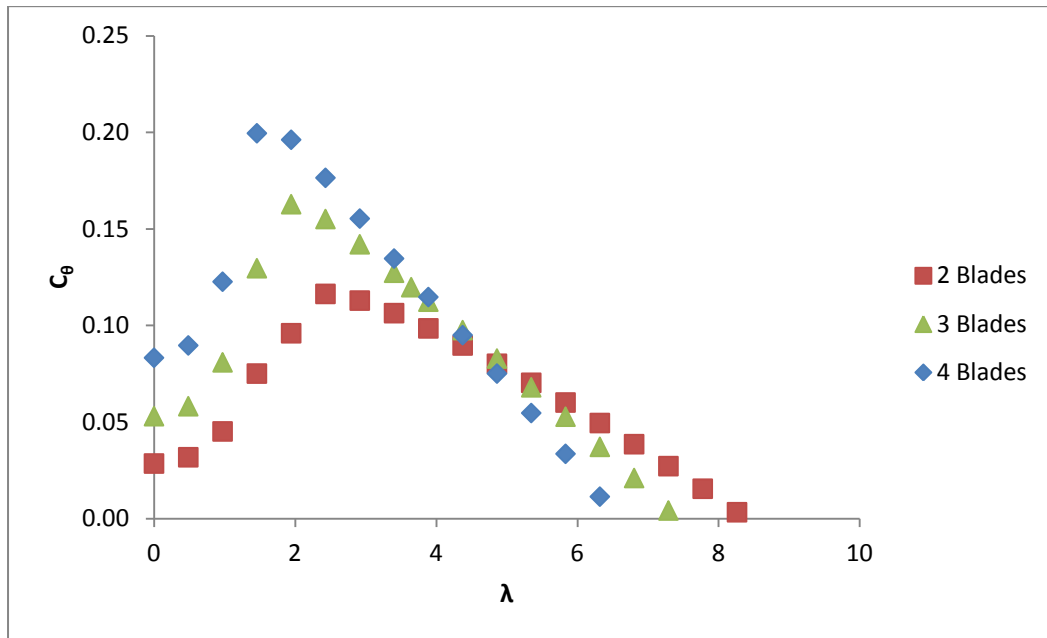


Figure A-1 C_p vs λ for the 2,3 and 4 bladed turbines

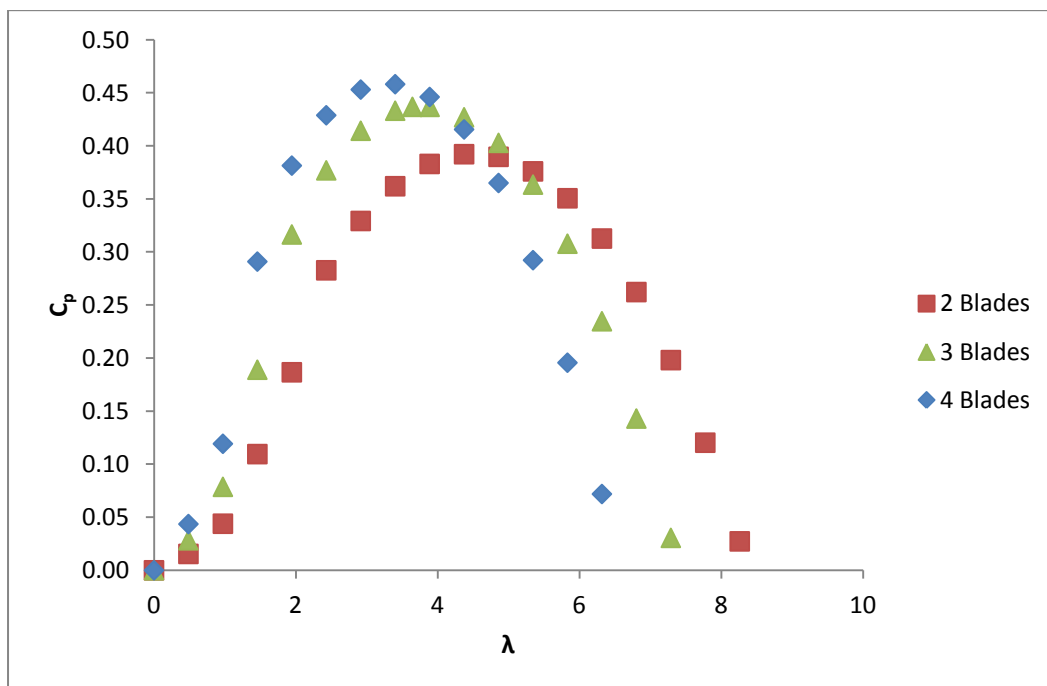


Figure A-2 C_p vs λ for the 2,3 and 4 bladed turbines

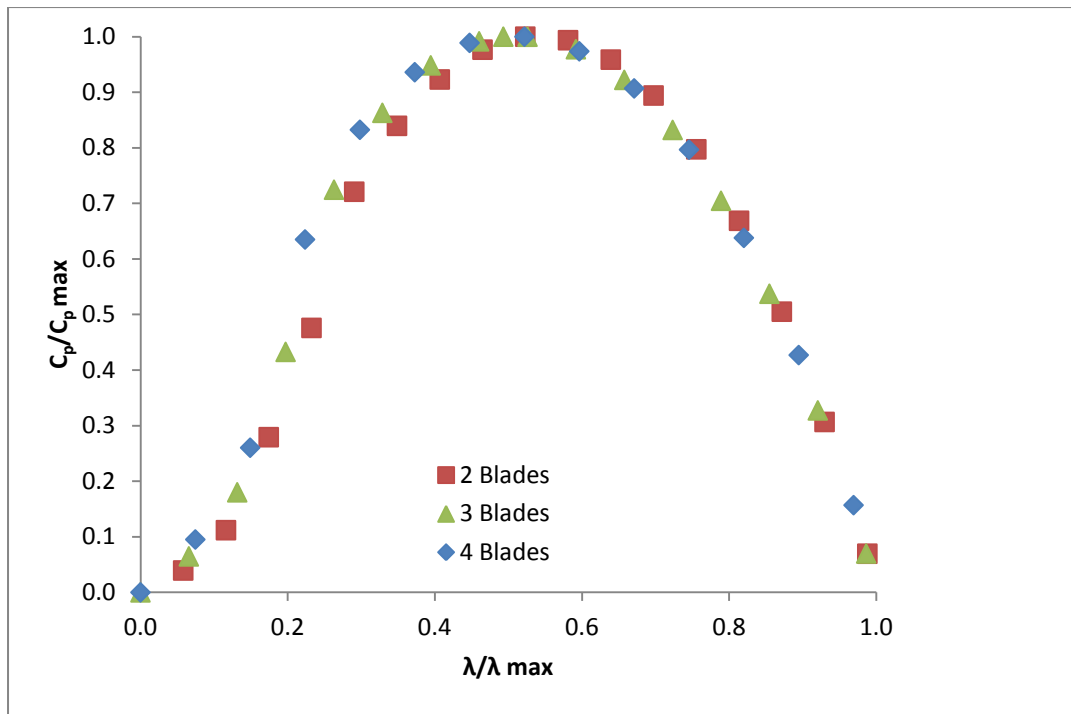


Figure A-3 $C_p/C_{p,max}$ vs λ/λ_{max} for the 2,3 and 4 bladed turbines

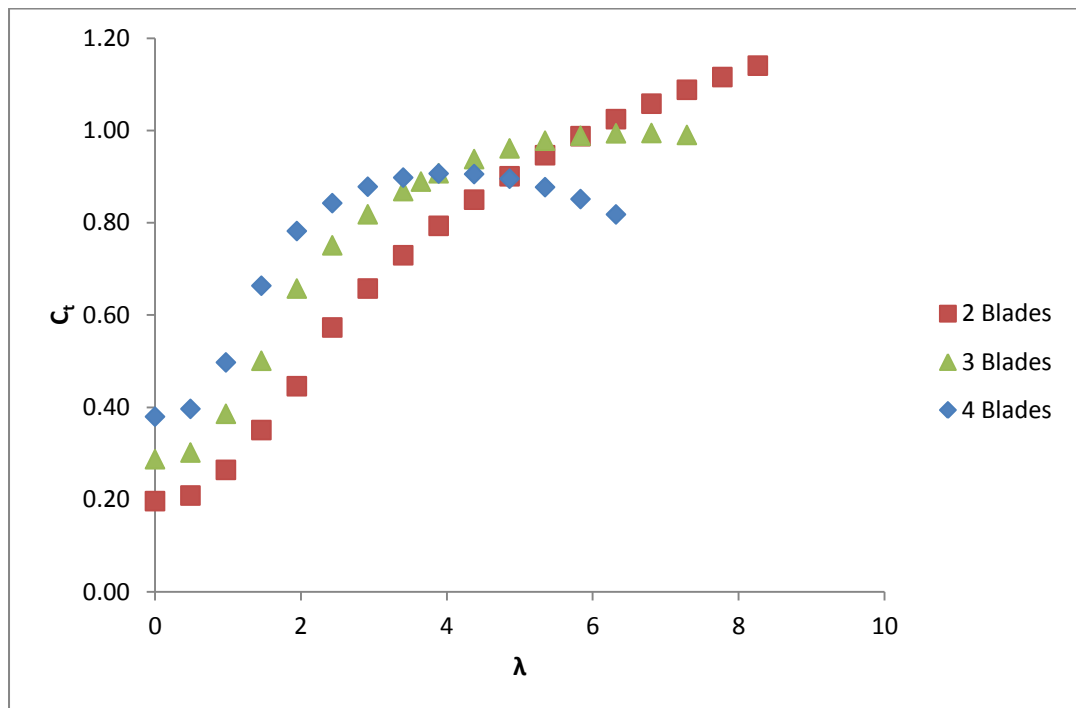


Figure A-4 C_t vs λ for the 2,3 and 4 bladed turbines

Appendix B Swirl Characteristics with SST model

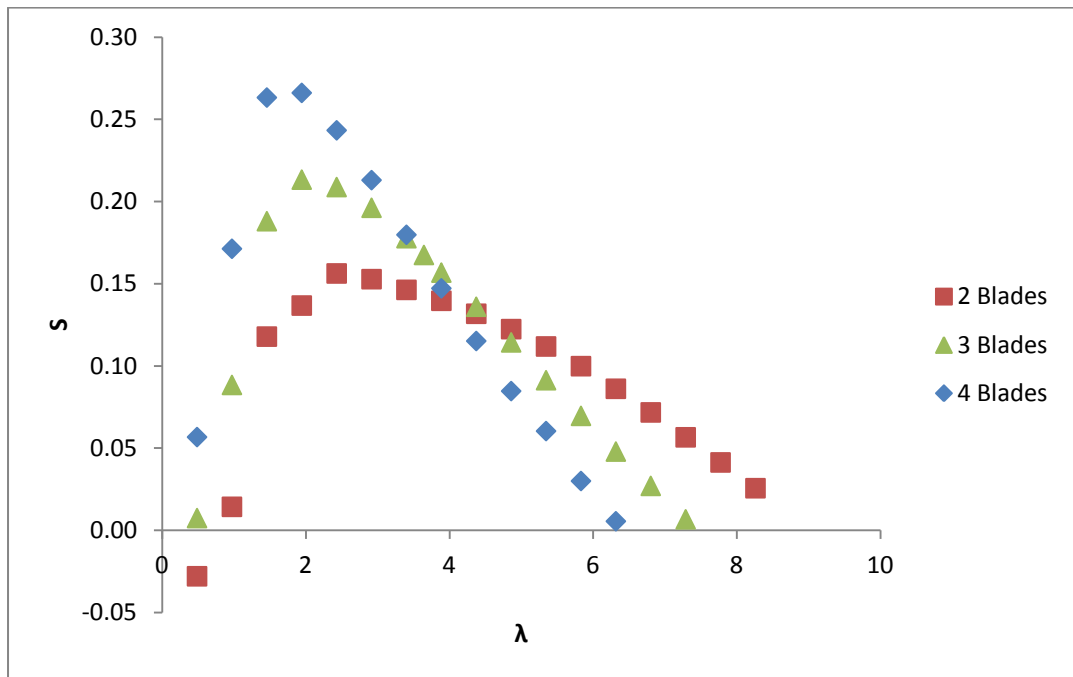


Figure B-1 Swirl Number vs λ at $x/D=0.1$ for the 2, 3 and 4 bladed turbines

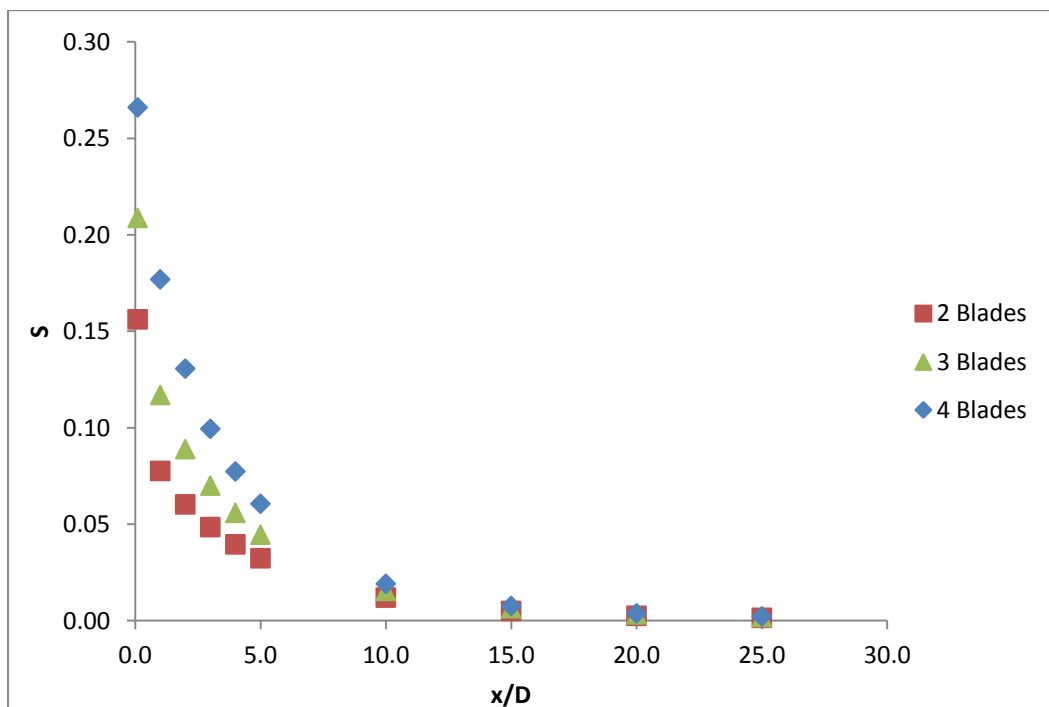


Figure B-2 Swirl decay at peak swirl for the 2, 3 and 4 bladed turbines

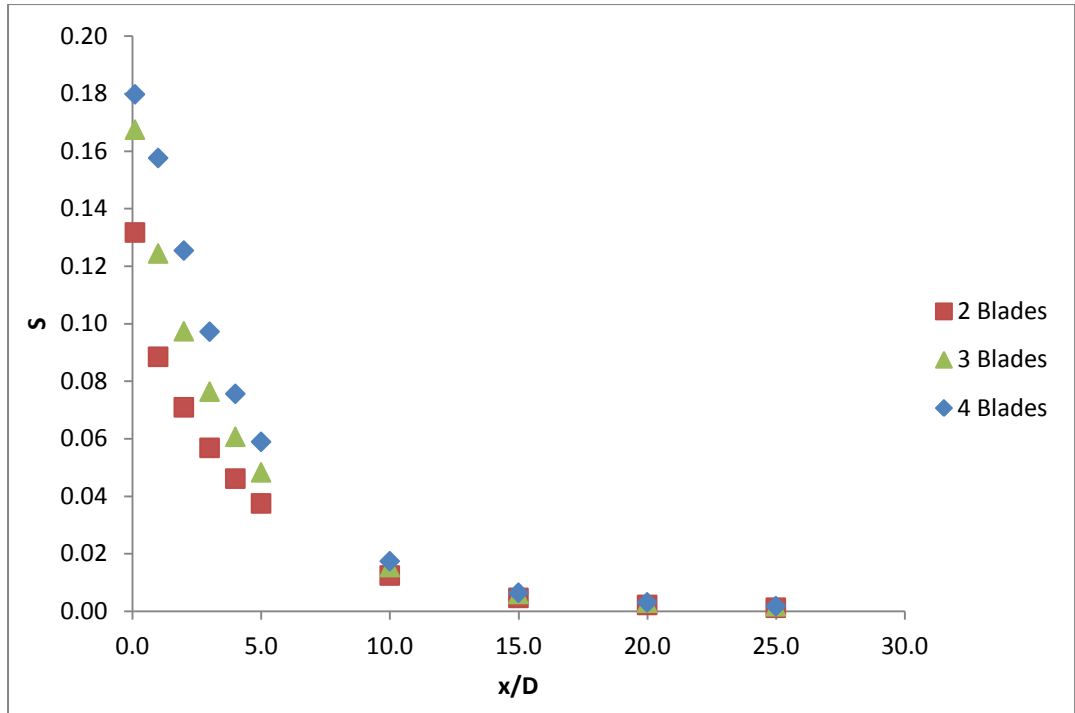


Figure B-3 Swirl decay at peak power for the 2, 3 and 4 bladed turbines

Appendix C Dynamic Pressure Profiles with SST model

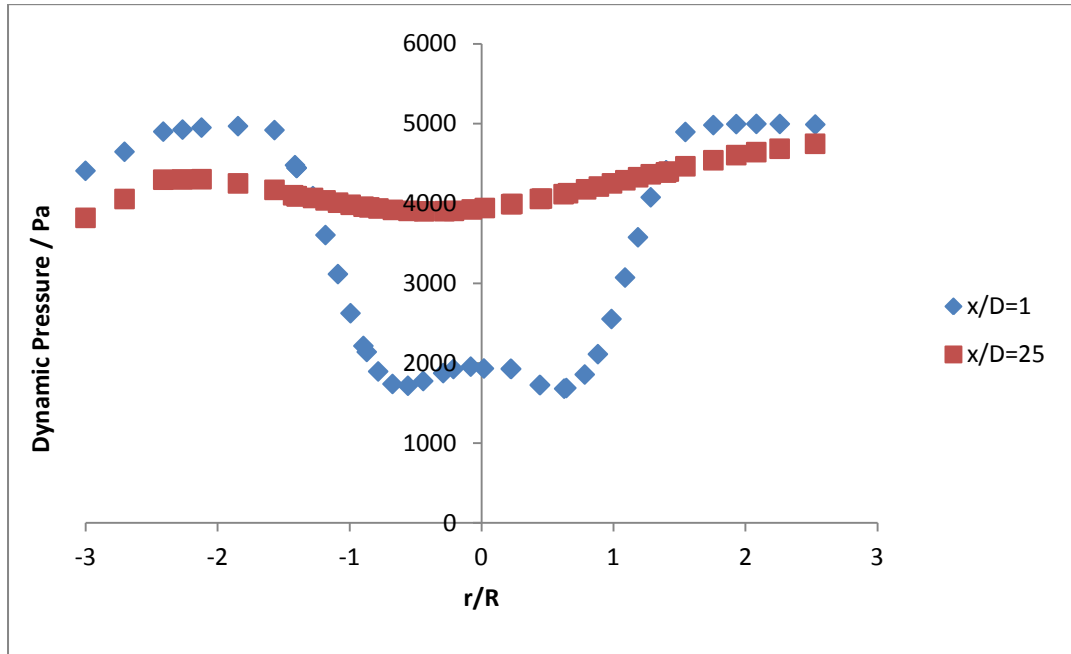


Figure C-1 Dynamic pressure profiles downstream of the 2 bladed turbine at peak power

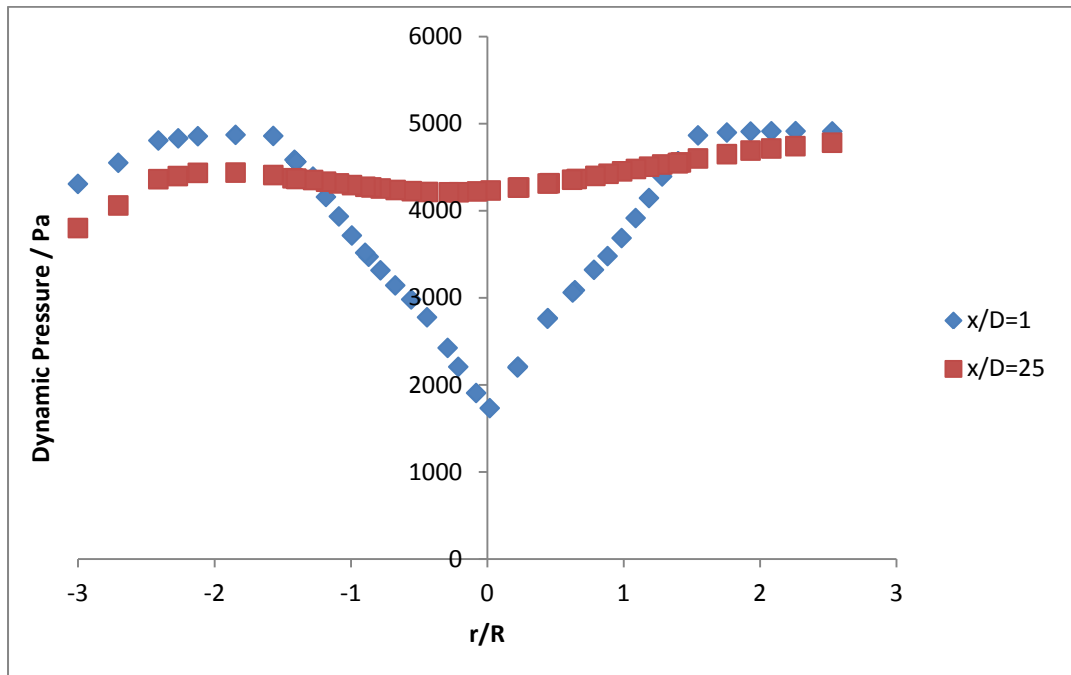


Figure C-2 Dynamic pressure profiles downstream of the 2 bladed turbine at peak swirl

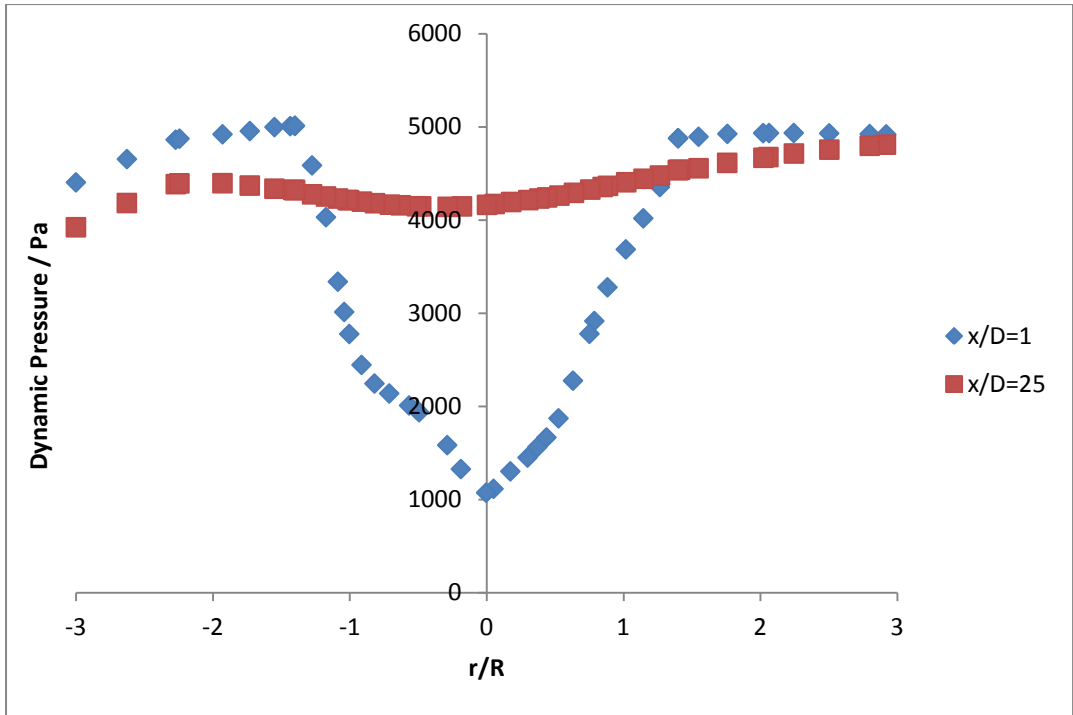


Figure C-3 Dynamic pressure profiles downstream of the 3 bladed turbine at peak swirl

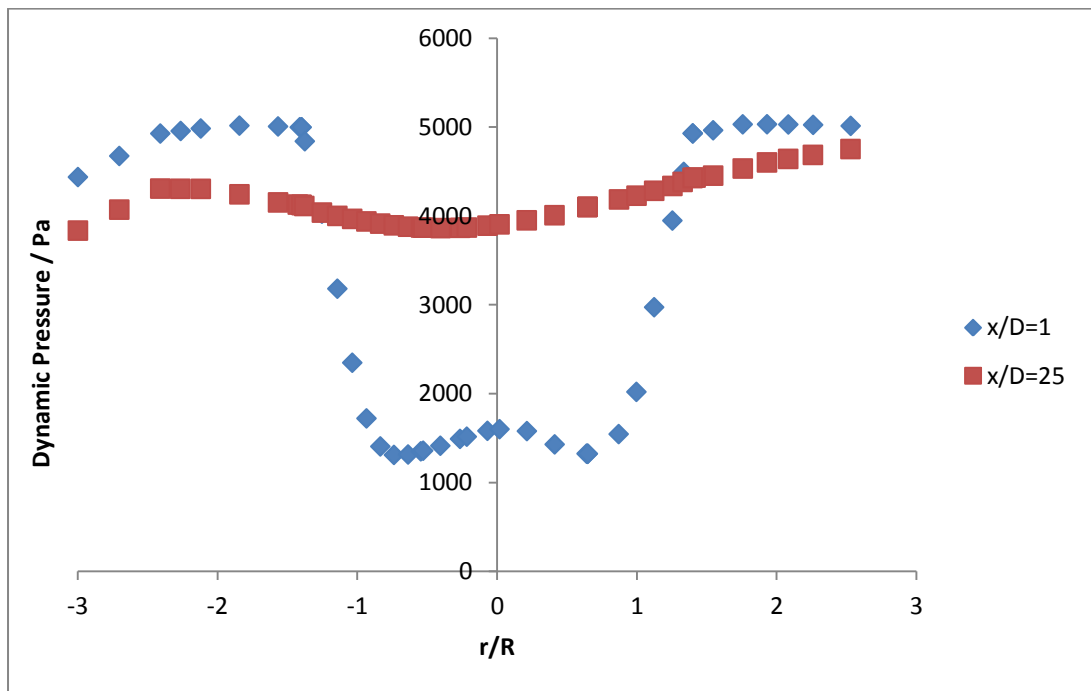


Figure C-4 Dynamic pressure profiles downstream of the 4 bladed turbine at peak power